Journal of Quantitative Spectroscopy & Radiative Transfer 353 (2026) 109807

Contents lists available at ScienceDirect

Journal of Quantitative Spectroscopy and Radiative Transfer

journal homepage: www.elsevier.com/locate/jqsrt

The HITRAN2024 molecular spectroscopic database☆

I.E. Gordon [1,*], L.S. Rothman [1], R.J. Hargreaves [1], F.M. Gomez [1], T. Bertin [1], C. Hill [2], R.V. Kochanov [3], Y. Tan [1,4], P. Wcisło [5], V. Yu. Makhnev [1], P.F. Bernath [6], M. Birk [7], V. Boudon [8], A. Campargue [9], A. Coustenis [10], B.J. Drouin [11,12], R.R. Gamache [13], J.T. Hodges [14], D. Jacquemart [15], E.J. Mlawer [16], A.V. Nikitin [17], V.I. Perevalov [3], M. Rotger [18], S. Robert [19], J. Tennyson [20], G.C. Toon [11], H. Tran [45], V.G. Tyuterev [3,49], E.M. Adkins [14], A. Barbe [18], D.M. Bailey [14], K. Bielska [5], L. Bizzocchi [26], T.A. Blake [34], C.A. Bowesman [20], P. Cacciani [23], P. Čermák [24], A.G. Császár [27], L. Denis [1,25], S.C. Egbert [44], O. Egorov [3], A. Yu. Ermilov [39], A.J. Fleisher [14], H. Fleurbaey [9], A. Foltynowicz [28], T. Furtenbacher [27], M. Germann [28,29], E.R. Guest [20], J.J. Harrison [30,31], J.-M. Hartmann [21], A. Hjältén [28], S.-M. Hu [4], X. Huang [32,33], T.J. Johnson [34], H. Jóźwiak [5], S. Kassi [9], M.V. Khan [15], F. Kwabia-Tchana [46], T.J. Lee [33,a], D. Lisak [5], A.-W. Liu [4], O.M. Lyulin [3], N.A. Malarich [44], L. Manceron [35], A.A. Marinina [3], S.T. Massie [36], J. Mascio [16], E.S. Medvedev [37], V.V. Meshkov [39], G. Ch. Mellau [38], M. Melosso [26], S.N. Mikhailenko [3], D. Mondelain [9], H.S.P. Müller [40], M. O'Donnell [1,41], A. Owens [20], A. Perrin [45], O.L. Polyansky [20,47], P.L. Raston [42,43], Z.D. Reed [14], M. Rey [18,8], C. Richard [8], G.B. Rieker [44], C. Röske [7], S.W. Sharpe [34], E. Starikova [3], N. Stolarczyk [5], A.V. Stolyarov [39], K. Sung [11], F. Tamassia [22], J. Terragni [48], V.G. Ushakov [37], S. Vasilchenko [3], B. Vispoel [19,25], K.L. Vodopyanov [50], G. Wagner [7], S. Wójtewicz [5], S.N. Yurchenko [20], N.F. Zobov [47]

[1] *Center for Astrophysics/Harvard & Smithsonian, Atomic and Molecular Physics Division, Cambridge MA 02138, USA*
[2] *Nuclear Data Section, International Atomic Energy Agency, Vienna International Centre, PO Box 100, A-1400 Vienna, Austria*
[3] *V.E. Zuev Institute of Atmospheric Optics, Russian Academy of Sciences, 634055 Tomsk, Russia*
[4] *Hefei National Research Center for Physical Science at Microscale, University of Science and Technology of China, Hefei, China*
[5] *Institute of Physics, Faculty of Physics, Astronomy and Informatics, Nicolaus Copernicus University in Torun, Grudziadzka 5, 87-100 Torun, Poland*
[6] *Old Dominion University, Department of Chemistry, Norfolk VA, USA*
[7] *German Aerospace Center (DLR), Remote Sensing Technology Institute, Wessling, Germany*
[8] *Université Bourgogne Europe, CNRS, Laboratoire Interdisciplinaire Carnot de Bourgogne ICB UMR 6303, F-21000 Dijon, France*
[9] *University of Grenoble Alpes, CNRS, LIPhy, F-38000 Grenoble, France*
[10] *Laboratoire d'Etudes Spatiales et d'Instrumentation en Astrophysique, Paris Observatory, CNRS, PSL Univ., Sorbonne Univ., Paris, France*
[11] *Jet Propulsion Laboratory, California Institute of Technology, Pasadena CA, USA*
[12] *California Institute of Technology, Division of Astronomy, Pasadena CA, USA*
[13] *University of Massachusetts Lowell, Department of Environmental, Earth & Atmospheric Sciences, Lowell MA, USA*
[14] *National Institute of Standards and Technology, Material Measurement Laboratory, Gaithersburg MD, USA*
[15] *Sorbonne Université, CNRS, De la MOlécule aux NAno-objets : Réactivité, Interactions et Spectroscopies, MONARIS, 75005 Paris, France*
[16] *Atmospheric and Environmental Research, Lexington MA, USA*
[17] *Technion - Israel Institute of Technology, Haifa, Israel*
[18] *Groupe de Spectrométrie Moléculaire et Atmosphérique, UMR CNRS 7331, BP 1039, F-51687, Reims Cedex 2, France*
[19] *Royal Belgian Institute for Space Aeronomy (BIRA-IASB), 1180 Brussels, Belgium*
[20] *Department of Physics and Astronomy, University College London, London, WC1E 6BT, UK*
[21] *Laboratoire de Météorologie Dynamique/IPSL, CNRS, École polytechnique, Sorbonne Université, École normale supérieure, PSL Research University, F-91120 Palaiseau, France*
[22] *Dipartimento di Chimica Industriale "Toso Montanari", Università di Bologna, P. Gobetti 85, Bologna 40129, Italy*
[23] *Univ. Lille, CNRS, UMR 8523 - PhLAM - Physique des Lasers, Atomes et Molécules, 59000 Lille, France*
[24] *Department of Experimental Physics, Faculty of Mathematics, Physics and Informatics, Comenius University, Mlynská dolina F2, Bratislava 842 48, Slovakia*

☆ This article is part of a Special issue entitled: 'HITRAN 2024' published in Journal of Quantitative Spectroscopy and Radiative Transfer.

* Corresponding author.
E-mail address: igordon@cfa.harvard.edu (I.E. Gordon).

[a] Deceased in November, 2022.

https://doi.org/10.1016/j.jqsrt.2026.109807
Received 2 October 2025; Received in revised form 18 December 2025; Accepted 4 January 2026
Available online 15 January 2026

[25] Research Unit Lasers and Spectroscopies (LLS), Institute of Life, Earth and Environment (ILEE), University of Namur (UNamur), B-5000, Namur, Belgium
[26] Dipartimento di Chimica "Giacomo Ciamician", Università di Bologna, Via P. Gobetti 85, Bologna 40129, Italy
[27] ELTE Eötvös Loránd University, Institute of Chemistry, Budapest, Hungary
[28] Department of Physics, Umeå University, 901 87 Umeå, Sweden
[29] Experimental Physics Department, CERN European Organization for Nuclear Research, 1211 Geneva 23, Switzerland
[30] National Centre for Earth Observation, Space Park Leicester, Leicester, UK
[31] University of Leicester, School of Physics and Astronomy, Leicester, UK
[32] SETI Institute, Mountain View, CA 94043, USA
[33] Astrophysics Branch, Space Science and Astrobiology Division, NASA Ames Research Center, Moffett Field, CA 94035, USA
[34] Pacific Northwest National Laboratory, Richland, WA, USA
[35] Synchrotron SOLEIL, Beamline AILES, Saint-Aubin, France
[36] University of Colorado, Laboratory for Atmospheric and Space Physics, Boulder CO, USA
[37] Federal Research Center of Problems of Chemical Physics and Medicinal Chemistry (former Institute of Problems of Chemical Physics), Russian Academy of Sciences, 142432 Chernogolovka, Russia
[38] Physikalisch-Chemisches Institut, Justus-Liebig-Universität Giessen, Heinrich-Buff-Ring 58, D-35392 Giessen, Germany
[39] Department of Chemistry, Lomonosov Moscow State University, Moscow 119991, Russia
[40] Astrophysik/I. Physikalisches Institut, Universität zu Köln, 50937 Köln, Germany
[41] Bates College, Lewiston ME, USA
[42] Department of Chemistry, University of Hawai'i at Mānoa, Honolulu HI 96822, USA
[43] Department of Chemistry, University of Adelaide, Adelaide, SA 5005, Australia
[44] Precision Laser Diagnostics Laboratory, University of Colorado Boulder, Boulder CO, USA
[45] Laboratoire de Météorologie Dynamique/IPSL, CNRS, Sorbonne Université, École normale supérieure, PSL Research University, École polytechnique, F-75005 Paris, France
[46] Université Paris Cité and Univ. Paris Est Creteil, CNRS, LISA, F-75013 Paris, France
[47] Institute of Applied Physics of Russian Academy of Sciences, Nizhny Novgorod, Russia
[48] NASA Goddard Space Flight Center, Greenbelt MD, 20771, USA
[49] Physics Department, Tomsk State Research University, Tomsk, 634050, Russia
[50] CREOL, College of Optics and Photonics, University of Central Florida, Orlando FL, USA

ARTICLE INFO

Keywords:
HITRAN
Spectroscopic database
Molecular spectroscopy
Spectroscopic line parameters
Absorption cross-sections
Collision-induced absorption
Aerosols
Molecular opacities

ABSTRACT

The HITRAN database is a curated compilation of validated molecular spectroscopic parameters, established in the early 1970s. It is used by various computer codes to predict and simulate the transmission and emission of light in gaseous media (with an emphasis on terrestrial and planetary atmospheres). The HITRAN compilation is composed of six major components. These components include the line-by-line spectroscopic parameters required for high-resolution radiative-transfer codes, experimentally derived absorption cross-sections (for molecules where it is not yet feasible for representation in a line-by-line form), collision-induced absorption data, aerosol indices of refraction, and general tables (including partition sums) that apply globally to the data. Responding to community requests, HITRAN2024 also incorporates — for the first time — a water-vapor continuum model.

This paper describes the details of the choices of data and their compilation for the 2024 quadrennial edition of HITRAN. The HITRAN2024 edition takes advantage of recent experimental and theoretical data that were meticulously validated, in particular, against laboratory and atmospheric spectra. The new edition replaces the previous HITRAN edition of 2020 (including various updates during the intervening years).

The extent of the updates of the line-by-line section in the HITRAN2024 edition ranges from updating a few lines of specific molecules/isotopologues to complete replacements of the lists, and also the introduction of additional isotopologues and six new (to HITRAN) molecules: H_3^+, CH_3, S_2, COFCl, HONO, $ClNO_2$. Many new vibrational bands were added, extending the spectral coverage and completeness of the line lists. In addition, the accuracy of the parameters for major atmospheric absorbers has been increased substantially, often bringing the uncertainties down to unprecedented levels below 0.1%.

The HITRAN2024 edition is available through www.hitran.org as well as the HITRAN Application Programming Interface (HAPI). The functionality of the tools to work with the HITRAN data has been extended for the new edition.

1. Introduction

The HITRAN molecular spectroscopic database was established over half a century ago [1] and has consistently served as a necessary input in radiative transfer codes that model and interpret the interaction of light with gaseous media. It is important to emphasize that the main component of the database (the line-by-line sections) is not a collection of spectra itself, but rather the fundamental parameters that allow for the generation of high-resolution spectra at different thermodynamic conditions. HITRAN is indispensable in atmospheric and planetary studies, but it is also actively used in education, engineering, surveillance, safety (e.g. outgassing of toxic gases in working environments), medicine (e.g. patient breath monitoring), and many other applications.

The database is being updated regularly thanks to the contributions and feedback from an extensive scientific network that includes spectroscopists, atmospheric scientists, planetary scientists, and data scientists across the globe. The project makes use of new experimental or theoretical data that undergo thorough validations before being accepted into the database. Public "reference" editions of HITRAN have been released on a regular (in the last two decades, quadrennial) basis. These editions are described in dedicated, highly-cited papers [2–17], and the standardized format and curation of the database make it an accepted international standard. The HITRAN2020 paper [17] has summarized many of the terrestrial and planetary radiative transfer codes that rely on HITRAN. The number of these codes grows rapidly. Interestingly, MacDonald and Batalha [18] have identified 50 radiative transfer codes that are being used in the exoplanetary community alone. The launch of the James Webb Space Telescope (JWST) [19] enabled the possibility of getting high-resolution spectra not only from exoplanets, brown dwarfs, and comets but also from protoplanetary disks where the individual rovibrational lines are much better resolved and HITRAN has proven to be an indispensable tool (see, for instance, Refs. [20,21]).

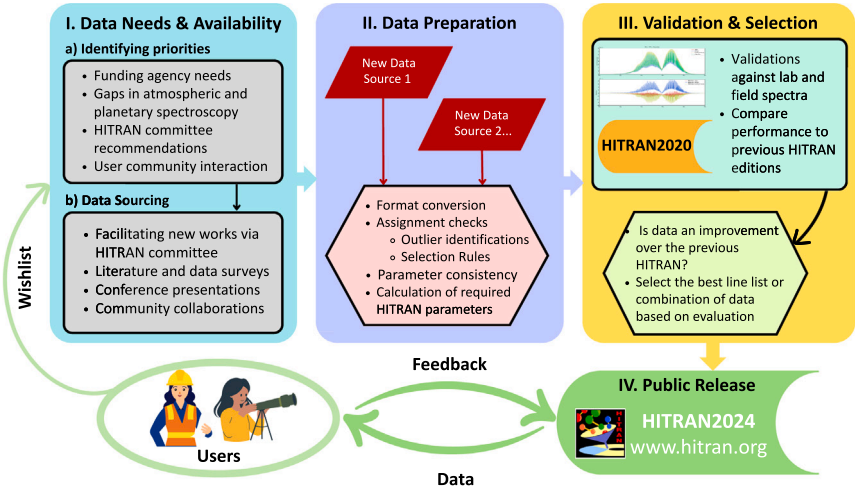

Fig. 1. Flow diagram of the path of the data incorporated in HITRAN2024. The diagram highlights setting priorities; obtaining new data, which could be theoretical or experimental, or semi-empirical; calculating parameters necessary for these data to be converted into the HITRAN format; validating the data against each other, previous HITRAN, and laboratory and field data; and finally identifying the best set of parameters to be included in HITRAN2024.

With the rapid advances in instrumentation and computational resources, the applications require more and more critical updates from HITRAN. Following a PACT (Practicality, Accuracy, Completeness, and Traceability) philosophy, these updates include, but are not limited to, substantial improvement of the accuracy of the existing parameters, extending spectral and dynamic coverage, adding more molecules and isotopologues, adding new line-shape representations and associated parameters, and parametrizations of "new" (to HITRAN) phenomena, such as water-vapor continuum, that are required to reduce the residuals of atmospheric retrievals. As will be evident from the subsequent sections, the HITRAN2024 edition described in this paper makes substantial advances in all of these directions, thanks to the state-of-the-art experimental and theoretical (or semi-empirical) values that became available in recent years. The data have gone through validation by cross-comparisons of alternative sources, if they exist, and comparisons against laboratory and field data when available. Fig. 1 provides a flow diagram of how the data is typically collected and curated by HITRAN, including the validation process.

The HITRAN2024 compilation provides a diverse set of spectroscopic data separated into six components (vs. five in HITRAN2020) that provide different parametrizations of various molecular phenomena required as spectroscopic input into the radiative-transfer models. The updates to these portions of HITRAN with respect to HITRAN2020 [17] (and the inclusion of a new one: water-vapor continuum), as well as the underlying system of data structure with accompanying internet user interface and an application programming interface (API), will be discussed in the following sections. (1) Section 2 is dedicated to the line-by-line component of HITRAN, the original and most widely-used component, which provides spectroscopic parameters for high-resolution molecular absorption and radiance calculations. For many molecules, the data span the microwave through to the ultraviolet region of the spectrum. (2) Section 3 relates to experimental absorption cross-sections, where over 300 molecules have been added (bringing the total number to 644) and data for multiple existing molecules updated. These cross-sections generally represent absorption by molecules that have very dense spectra, thanks to their molecular weight or multiple low-lying vibrational modes. (3) Collision-induced absorption data for multiple collisional pairs are described in Section 4. (4) Updated tables of aerosol refractive indices are described in Section 5. (5) The water-vapor continuum has been introduced to the database for the first time due to high demand from the community. The incorporation of this new parametrization is effectively described by Mlawer et al. [22], with a brief summary and future prospects described in Section 6. (6) Global data and tools that apply in a general manner to the archive are another integral part of the database and are described in Section 7. This includes, but is not limited to, information on molecular/isotopologue masses, abundances, Total Internal Partition Sums (TIPS), as well as updates to the HITRAN website, underlying structure, and HITRAN Application Programming Interface (HAPI) [23], which are also described in Section 7.

Starting from the HITRAN2016 edition [16], the database has been cast into a relational database format, which enabled seamless incorporation of additional parameters and flexibility of their representation. These parameters can be retrieved from the dynamic and user-friendly web interface HITRAN*online* (at www.hitran.org) [24]. Since the inception of the website, over 40 000 unique users have registered (as of early January 2026). It is important to stress that the default output is still the familiar HITRAN-formatted ASCII files, but the versatility of a relational structure allows one to request user-defined formats that can accommodate new features and parameters. The examples of such parameters include non-Voigt line-shape parameters [25–27], broadening by gases other than air (e.g. by water vapor [28], H_2, He and CO_2 [29,30]), along with corresponding references and uncertainties. The HITRAN Application Programming Interface (HAPI) [23], a very efficient and popular tool that was released with HITRAN2016 [16] has also been updated for increased capabilities and speed of calculations.

The knowledge of HITRAN definitions of the parameters and formalisms can aid substantially in the comprehension of this paper. These details can be found in the documentation section of the HITRAN website https://hitran.org/docs/definitions-and-units/. For a complete description of quantum number identifications of energy levels or states provided for each molecule in the line-by-line section of the HITRAN database, users are referred to https://hitran.org/quanta/ where the global and local quanta are described. Note that these descriptions are kept up to date, and therefore supersede Tables S1 and S2, from the HITRAN2020 paper [17] and especially those previously described in HITRAN2004 (i.e., Tables 3 and 4 of Ref. [13]).

New users of the database should also be aware that all of the HITRAN editions (including this one) do not strictly adhere to the Système International (SI) units for both historical and application-specific reasons. Thus cm^{-1} (reciprocal centimeter, the unit of the quantity wavenumber) is seen throughout, as is atm (atmosphere) for pressure (1 atm is 101 325 Pa in SI units). Also, the symbol ν is used throughout for line position in cm^{-1}, thereby dropping the tilde ($\tilde{\nu}$) that is the official designation of wavenumber. The HITRAN unit for intensity is traditionally expressed as $cm^{-1}/(molecule \times cm^{-2})$ (e.g. wavenumber per column density) rather than simplifying to the equivalent

cm × molecule^{-1}. However, both notations are used throughout this paper.

Many abbreviations have been used throughout this paper when describing data, instruments, missions, collaborations, and methods. Although these are explained in the text, for the readers' convenience, a list of these abbreviations is also provided in the Appendix.

2. Line-by-line modifications

An overview of changes and additions to the line-by-line section for each molecule and their isotopologues in the database with respect to the HITRAN2020 edition is provided in Table 1. For each molecule, isotopologues are presented in order of their descending abundance. The molecular abundance values in HITRAN are calculated based on the terrestrial atomic abundances selected from Ref. [31]. Users should be aware that the line intensities in the HITRAN database are scaled by these abundances. Note that although the number of lines and spectral ranges has not changed for some molecules, some parameters of corresponding lines may have been updated or added. The subsequent subsections of this line-by-line section are dedicated to individual molecules (note that a small fraction of the HITRAN "molecules" are actually radicals, molecular ions, and a single atom). These subsections detail the updates/additions that were carried out in the new edition.

The definitions of the uncertainty indices used in HITRAN for spectral parameters in the line-by-line representation are defined in Table 2. Uncertainty and reference indices are now given for all parameters in HITRAN except for the Einstein-*A* coefficients (which usually share the same source and uncertainty as the intensities), lower-state energies, and quantum numbers. It should be remarked that the code 0 in Table 2 might lend itself to two different meanings in the case of line position or air pressure-induced shift. It means that either the uncertainty in the reported line position is greater than 1 cm^{-1} or was not reported, with the former being a very rare case. The word "default" or "constant" (code 1 in Table 2) means a constant value, and the word "average" or "estimate" (code 2 in Table 2) means an average or empirical value. In this new edition, we have added a new code (9) for the parameters that are given uncertainties in percentages. Code 9 refers to the uncertainties below 0.1%, while code 8 implies that the uncertainties are between 0.1% and 1%. Table 2 will be frequently referred to across different subsections of Section 2.

2.1. H_2O: Water vapor (molecule 1)

2.1.1. Principal isotopologue

After the release of the official edition of HITRAN2020, evaluations performed using TCCON [32] atmospheric spectra from the Lamont site identified a number of issues for the line list for water vapor above 4340 cm^{-1}. This prompted the issuance of an update in the summer of 2022. For instance, the line-shift parameters in HITRAN2020 that originated from Ref. [33] were found to have errors for certain bands (especially those that involved bending vibrations), resulting in a large number of positive values. At that point, the issue was fixed in the following way. The shifts that affected the quality of the residuals have been reverted back to the HITRAN2016 values or replaced with those from the AER list "aer3.8.1" [34], which contains manual modifications of the HITRAN2016 parameters to match the TCCON spectra better. Similarly, the air-broadened half-widths that affected the quality of the residuals have been reverted to HITRAN2016 values or replaced with those from the AER list. In addition, the intensities in the $4\nu_2 + \nu_3$ band were scaled down by 22%, while individual intensities (of *ab initio* origin) in different bands had to be scaled to provide a better fit of the TCCON spectra. Finally, it was found [35] that a large percentage of the lines in HITRAN2020 that had line positions attributed to the W2020 MARVEL (Measured Active Rotation-Vibration Energy Levels) line list [36] deviated slightly from the line positions in the original W2020 work. This was fixed in the 2022 update. Since then, more data for improvements have become available and the further updates toward HITRAN2024 are described below.

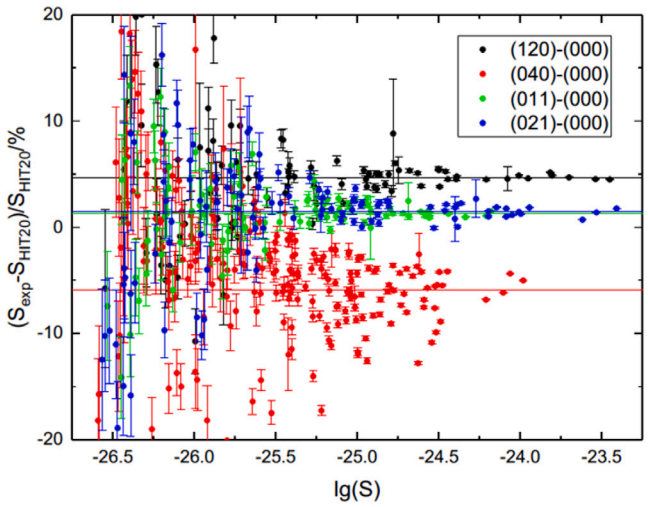

Fig. 2. Percentage intensity differences of Ref. [47] compared to HITRAN2020 for the strongest bands in the observed region 5970–6575 cm^{-1}. Plotted against HITRAN2020 intensities on a logarithmic scale. 1σ statistical error bars are shown. Average differences are shown as horizontal lines.

2.1.1.1. Line positions. Recently, a new MARVEL analysis resulted in improved empirical energy levels for the principal isotopologue [37]. This study considered both the corrections proposed in Ref. [35] and a number of additional references to those used to construct the W2020 dataset, including Refs. [38–43]. This analysis resulted in the W2024 dataset and the associated composite CW2024 line list [37].

In HITRAN2024, the CW2024 line positions and assignments were employed whenever possible, except for the 6600–7500 cm^{-1} region, where an updated version of W2024 [44] was used.

A small percentage of weak lines in HITRAN2020 had variationally-calculated line positions [45], which cannot yet achieve experimental accuracy, especially toward the visible part of the spectrum (see, for instance, the discussion in Ref. [43]). The use of empirically derived W2024 line positions could replace these first-principles values only for a few dozen lines (although some of them were strong, and this improvement was important). Therefore, in place of the remaining variational line positions, we used the line positions from the newly-calculated *ab initio* line list, which appeared to reproduce the real spectra somewhat better. For instance, the unassigned lines from Ref. [43] could now be straightforwardly assigned using the new variational values. Unfortunately, the new line list extends only up to 25 000 cm^{-1}; above that region, the HITRAN2020 line positions were retained.

2.1.1.2. Line intensities. The HITRAN2020 $H_2{}^{16}O$ line list provides primarily *ab initio* intensities [45], supplemented with the most accurate experimental values where possible, or for some bands, the variational intensities were scaled to limited experimental observations where the differences were systematic. New experimental data in the 1-μm region [46] have shown that in HITRAN2020 the *ab initio* intensities in bands involving highly-excited bending motion are systematically off by 7–19%, depending on the band, while for the $\nu_1 + 4\nu_2$ band, there are substantial non-systematic differences for the different lines. Less drastic, 1–5%, but also predominantly systematic differences have been identified in other spectral regions [47] (see Fig. 2). For the $4\nu_2$ band, a larger scatter was observed, with the differences ranging from −12% to +18%.

For HITRAN2024, these bands were scaled to match the experimental values, while for the $\nu_1+4\nu_2$ and $4\nu_2$ bands, experimental intensities were used wherever possible. In the case of the $4\nu_2$ band, a scaling factor was applied to the lines not measured experimentally. Table 3 lists the bands and the scaling factors that were applied to variational intensities in different bands.

Table 1
Molecules and isotopologues represented in the line-by-line portion of HITRAN.

Molecule	Isotopologue	Abundance[a]	HITRAN2024		HITRAN2020	
			Spectral range[b]	# of lines	Spectral range[b]	# of lines
(1) H_2O	$H_2^{16}O$	9.973×10^{-1}	0–42 000	324 121	0–42 000	319 887
	$H_2^{18}O$	2.000×10^{-3}	0–19 991	42 305	0–19 991	42 178
	$H_2^{17}O$	3.719×10^{-4}	0–19 945	27 520	0–19 945	27 544
	$HD^{16}O$	3.107×10^{-4}	0–19 935	56 444	0–19 935	56 430
	$HD^{18}O$	6.230×10^{-7}	0–10 729	10 664	0–10 729	10 664
	$HD^{17}O$	1.159×10^{-7}	0–10 703	6360	0–10 703	6360
	$D_2^{16}O$	2.420×10^{-8}	0–12 796	23 195	0–12 796	23 195
(2) CO_2	$^{12}C^{16}O_2$	9.842×10^{-1}	158–17 697	173 129	158–19 909	174 412
	$^{13}C^{16}O_2$	1.106×10^{-2}	332–13 735	69 865	332–13 735	69 870
	$^{16}O^{12}C^{18}O$	3.947×10^{-3}	1–13 832	122 354	1–12 678	122 142
	$^{16}O^{12}C^{17}O$	7.340×10^{-4}	0–12 727	73 993	0–12 727	73 942
	$^{16}O^{13}C^{18}O$	4.434×10^{-5}	2–9213	41 050	2–9213	41 059
	$^{16}O^{13}C^{17}O$	8.246×10^{-6}	9–8062	23 608	9–8062	23 607
	$^{12}C^{18}O_2$	3.957×10^{-6}	482–8163	10 498	482–8163	10 498
	$^{17}O^{12}C^{18}O$	1.472×10^{-6}	498–8193	14 605	498–8194	15 623
	$^{12}C^{17}O_2$	1.368×10^{-7}	535–6933	6493	535–6933	6493
	$^{13}C^{18}O_2$	4.446×10^{-8}	539–6687	2926	539–6687	2926
	$^{18}O^{13}C^{17}O$	1.654×10^{-8}	549–4915	3980	549–4915	3980
	$^{13}C^{17}O_2$	1.538×10^{-9}	575–3615	1501	575–3615	1501
(3) O_3	$^{16}O_3$	9.929×10^{-1}	0–6997	314 163	0–6997	304 262
	$^{16}O^{16}O^{18}O$	3.982×10^{-3}	0–3165	57 907	0–3165	57 907
	$^{16}O^{18}O^{16}O$	1.991×10^{-3}	1–2739	18 887	1–2739	18 887
	$^{16}O^{16}O^{17}O$	7.405×10^{-4}	0–2122	65 467	0–2122	65 467
	$^{16}O^{17}O^{16}O$	3.702×10^{-4}	0–2102	31 022	0–2101	31 022
(4) N_2O	$^{14}N_2^{16}O$	9.903×10^{-1}	0–14 018	286 881	0–7797	33 265
	$^{14}N^{15}N^{16}O$	3.641×10^{-3}	0–10 612	62 581	5–5086	4222
	$^{15}N^{14}N^{16}O$	3.641×10^{-3}	0–10 721	68 563	4–4704	4592
	$^{14}N^{14}N^{18}O$	1.986×10^{-3}	0–10 790	62 673	0–10364	116 694
	$^{14}N_2^{17}O$	3.693×10^{-4}	1–8937	35 426	550–4430	1705
(5) CO	$^{12}C^{16}O$	9.865×10^{-1}	3–14 478	1344[c]	3–14 477	1344
	$^{13}C^{16}O$	1.108×10^{-2}	3–12 231	1042[c]	3–12 230	1042
	$^{12}C^{18}O$	1.978×10^{-3}	3–12 205	920[c]	3–12 204	920
	$^{12}C^{17}O$	3.679×10^{-4}	3–10 295	800[c]	3–10 294	800
	$^{13}C^{18}O$	2.223×10^{-5}	3–8078	674[c]	3–8078	674
	$^{13}C^{17}O$	4.133×10^{-6}	3–8168	601[c]	3–8168	601
(6) CH_4	$^{12}CH_4$	9.883×10^{-1}	0–13 923	323 311	0–11 502	325 431
	$^{13}CH_4$	1.110×10^{-2}	0–11 319	85 439	0–11 319	79 931
	$^{12}CH_3D$	6.158×10^{-4}	7–6531	60 536	7–6511	54 550
	$^{13}CH_3D$	6.918×10^{-6}	959–1695	4236	959–1695	4213
(7) O_2	$^{16}O_2$	9.953×10^{-1}	0–57 028	16 474	0–57 028	15 367
	$^{16}O^{18}O$	3.991×10^{-3}	1–56 670	2975[c]	1–56 670	2975
	$^{16}O^{17}O$	7.422×10^{-4}	0–14 538	11 313[c]	0–14 538	11 313
(8) NO	$^{14}N^{16}O$	9.940×10^{-1}	0–23 726	251 898	0–23 726	251 898
	$^{15}N^{16}O$	3.654×10^{-3}	0–15 631	67 370	0–15 631	67 370
	$^{14}N^{18}O$	1.993×10^{-3}	0–15 503	65 037	0–15 503	65 037
(9) SO_2	$^{32}S^{16}O_2$	9.457×10^{-1}	0–4160	549 425	0–4160	549 425
	$^{34}S^{16}O_2$	4.195×10^{-2}	0–3466	141 665	0–3466	141 665
	$^{33}S^{16}O_2$	7.464×10^{-3}	0–2626	75 785	0–2626	75 785
	$^{16}O^{32}S^{18}O$	3.792×10^{-3}	0–2974	208 183	0–2793	208 183
(10) NO_2	$^{14}N^{16}O_2$	9.916×10^{-1}	0–7978	230 147	0–7978	171 057
	$^{15}N^{16}O_2$	3.646×10^{-3}	1500–2891	9657	1500–1660	5860
	$^{16}O^{14}N^{18}O$	3.976×10^{-3}	1508–1642	9623	–	–
(11) NH_3	$^{14}NH_3$	9.959×10^{-1}	0–12 810	92 117	0–10 349	76 605
	$^{15}NH_3$	3.661×10^{-3}	0–6842	24 008	0–5180	13 791
(12) HNO_3	$H^{14}N^{16}O_3$	9.891×10^{-1}	0–4167	1 066 364	0–1770	950 863
	$H^{15}N^{16}O_3$	3.636×10^{-3}	0–923	58 108	0–923	58 107
(13) OH	^{16}OH	9.975×10^{-1}	0–43 408	55 696[c]	0–43 408	55 698

(*continued on next page*)

Table 1 (*continued*).

Molecule	Isotopologue	Abundance[a]	HITRAN2024		HITRAN2020	
			Spectral range[b]	# of lines	Spectral range[b]	# of lines
	^{18}OH	2.000×10^{-3}	0–329	295	0–329	295
	^{16}OD	1.554×10^{-4}	0–332	912	0–332	912
(14) HF	H^{19}F	9.998×10^{-1}	24–32 351	8090	24–32 351	8088
	D^{19}F	1.557×10^{-4}	13–20 829	11 920	13–20 829	11 920
(15) HCl	H^{35}Cl	7.576×10^{-1}	8–20 231	8892[c]	8–20 231	8892
	H^{37}Cl	2.423×10^{-1}	8–20 218	8908[c]	8–20 218	8908
	D^{35}Cl	1.180×10^{-4}	5–15 265	17 762[c]	5–15 265	17 762
	D^{37}Cl	3.774×10^{-5}	5–15 246	17 690[c]	5–15 246	17 690
(16) HBr	H^{79}Br	5.068×10^{-1}	13–16 033	3039	13–16 033	3028
	H^{81}Br	4.931×10^{-1}	13–16 031	3031	13–16 031	3029
	D^{79}Br	7.894×10^{-5}	7–8780	1455	7–8780	1453
	D^{81}Br	7.680×10^{-5}	7–8777	1455	7–8777	1455
(17) HI	H^{127}I	9.998×10^{-1}	10–13 907	3161	10–13 907	3160
	D^{127}I	1.557×10^{-4}	5–7625	1590	5–7625	1588
(18) ClO	^{35}Cl^{16}O	7.559×10^{-1}	0–1208	5721	0–1208	5721
	^{37}Cl^{16}O	2.417×10^{-1}	0–1200	5780	0–1200	5780
(19) OCS	^{16}O^{12}C^{32}S	9.374×10^{-1}	0-13 957	530 134	0–7822	21 776
	^{16}O^{12}C^{34}S	4.158×10^{-2}	0-12 028	237 065	0–7796	7424
	^{16}O^{13}C^{32}S	1.053×10^{-2}	0–9834	172 871	0–6660	3395
	^{16}O^{12}C^{33}S	7.399×10^{-3}	0-10 086	146 060	0–6632	3005
	^{18}O^{12}C^{32}S	1.880×10^{-3}	0–7668	97 656	0–4046	1640
	^{16}O^{13}C^{34}S	4.675×10^{-4}	0–6946	68 736	1951–2039	221
(20) H_2CO	H$_2$^{12}C^{16}O	9.862×10^{-1}	0–5000	346 546	0–3100	40 670
	H$_2$^{13}C^{16}O	1.108×10^{-2}	0–117	2309	0–117	2309
	H$_2$^{12}C^{18}O	1.978×10^{-3}	0–101	1622	0–101	1622
(21) HOCl	H^{16}O^{35}Cl	7.558×10^{-1}	1–3800	8877	1–3800	8877
	H^{16}O^{37}Cl	2.417×10^{-1}	1–3800	7399	1–3800	7399
(22) N_2	^{14}N$_2$	9.927×10^{-1}	11–9355	1107	11–9355	1107
	^{14}N^{15}N	7.478×10^{-3}	11–2578	161	11–2578	161
(23) HCN	H^{12}C^{14}N	9.851×10^{-1}	0–17 586	128 215	0–17 586	131 031
	H^{13}C^{14}N	1.107×10^{-2}	0–8000	22 599	0–8000	22 599
	H^{12}C^{15}N	3.622×10^{-3}	2–3420	646	2–3420	646
(24) CH_3Cl	^{12}CH$_3$^{35}Cl	7.489×10^{-1}	0–3198	110 462	0–3198	110 462
	^{12}CH$_3$^{37}Cl	2.395×10^{-1}	0–3198	109 113	0–3198	109 113
(25) H_2O_2	H$_2$^{16}O$_2$	9.950×10^{-1}	0–1731	126 983	0–1731	126 983
(26) C_2H_2	^{12}C$_2$H$_2$	9.776×10^{-1}	13–10737	81 454	13–10 737	74 335
	H^{12}C^{13}CH	2.197×10^{-2}	613–9857	3064	613–9857	2120
	H^{12}C^{12}CD	3.046×10^{-4}	1–2666	8204	1–789	7512
(27) C_2H_6	^{12}C$_2$H$_6$	9.770×10^{-1}	225–3071	63 516[c]	225–3071	63 516
	^{12}CH$_3$^{13}CH$_3$	2.195×10^{-2}	285–919	7107	285–919	7107
(28) PH_3	^{31}PH$_3$	9.995×10^{-1}	0–4763	121 786	0–3660	104 759
(29) COF_2	^{12}C^{16}O^{19}F$_2$	9.865×10^{-1}	696–2002	168 793	697–2001	168 793
	^{13}C^{16}O^{19}F$_2$	1.108×10^{-2}	686–815	15 311	687–815	15 311
(30) SF_6	^{32}S^{19}F$_6$	9.502×10^{-1}	319–965	336 027[c]	319–965	336 027
(31) H_2S	H$_2$^{32}S	9.499×10^{-1}	1–11 330	90 507	3–11 330	36 556
	H$_2$^{34}S	4.214×10^{-2}	6–11 227	11 452	6–11 227	11 452[c]
	H$_2$^{33}S	7.498×10^{-3}	6–11 071	6220	6–11 071	6220[c]
(32) HCOOH	H^{12}C^{16}O^{16}OH	9.839×10^{-1}	10–1889	187 596	10–1889	187 596
	H^{13}C^{16}O^{16}OH	1.105×10^{-2}	0–178	13 573	–	–
(33) HO_2	H^{16}O$_2$	9.951×10^{-1}	0—3676	38 804	0–3676	38 804
(34) O	^{16}O	9.976×10^{-1}	68–159	2[c]	69–158	2

(*continued on next page*)

Table 1 (*continued*).

Molecule	Isotopologue	Abundance[a]	HITRAN2024		HITRAN2020	
			Spectral range[b]	# of lines	Spectral range[b]	# of lines
(35) $ClONO_2$	$^{35}Cl^{16}O^{14}N^{16}O_2$	7.496×10^{-1}	763—798	21 988	763—798	21 988
	$^{37}Cl^{16}O^{14}N^{16}O_2$	2.397×10^{-1}	765—791	10 211	765—791	10 211
(36) NO^+	$^{14}N^{16}O^+$	9.940×10^{-1}	3—2531	1270	3–2530	1270
(37) HOBr	$H^{16}O^{79}Br$	5.056×10^{-1}	0—316	2177	0–316	2177
	$H^{16}O^{81}Br$	4.919×10^{-1}	0—316	2181	0–316	2181
(38) C_2H_4	$^{12}C_2H_4$	9.773×10^{-1}	620–3242	59 536	620–3242	59 536
	$^{12}CH_2{}^{13}CH_2$	2.196×10^{-2}	615–3180	18 095	615–3180	18 095
(39) CH_3OH	$^{12}CH_3{}^{16}OH$	9.859×10^{-1}	0–1408	21 213	0–1407	19 897
(40) CH_3Br	$^{12}CH_3{}^{79}Br$	5.010×10^{-1}	794–1706	18 692	794–1706	18 692
	$^{12}CH_3{}^{81}Br$	4.874×10^{-1}	795–1697	18 219	795–1967	18 219
(41) CH_3CN	$^{12}CH_3{}^{12}C^{14}N$	9.739×10^{-1}	0–964	47 675	890–946	3572
(42) CF_4	$^{12}C^{19}F_4$	9.889×10^{-1}	2–1519	926 064	582–1519	842 709
(43) C_4H_2	$^{12}C_4H_2$	9.560×10^{-1}	0–3365	251 490	0–1303	251 245
(44) HC_3N	$H^{12}C_3{}^{14}N$	9.633×10^{-1}	0–3361	249 763	0–3361	226 369
(45) H_2	H_2	9.997×10^{-1}	15–27 185	4591	15–27 185	3480
	HD	3.114×10^{-4}	3–36 406	13 649	3–36 406	11 575
(46) CS	$^{12}C^{32}S$	9.396×10^{-1}	1–2586	1088	1–2586	1088
	$^{12}C^{34}S$	4.168×10^{-2}	1–1359	396	1–1359	396
	$^{13}C^{32}S$	1.056×10^{-2}	1–1331	396	1–1331	396
	$^{12}C^{33}S$	7.417×10^{-3}	1–156	198	1–156	198
(47) SO_3	$^{32}S^{16}O_3$	9.434×10^{-1}	0–2825	14 295	0–2825	14 295
(48) C_2N_2	$^{12}C_2{}^{14}N_2$	9.708×10^{-1}	200–307	71 775	200–307	71 775
(49) $COCl_2$	$^{12}C^{16}O^{35}Cl_2$	5.664×10^{-1}	793–900	164 437	793–900	164 437
	$^{12}C^{16}O^{35}Cl^{37}Cl$	3.622×10^{-1}	800–892	145 477	800–892	145 477
(50) SO	$^{32}S^{16}O$	9.479×10^{-1}	0-12 631	64 819	0-12 631	42 916
	$^{34}S^{16}O$	4.205×10^{-2}	0–372	671	0–372	671
	$^{32}S^{18}O$	1.901×10^{-3}	0–363	677	0–363	677
(51) CH_3F	$^{12}CH_3{}^{19}F$	9.884×10^{-1}	945–1291	9069	1067–1291	1499
	$^{13}CH_3{}^{19}F$	1.110×10^{-2}	954–1074	1337	–	–
(52) GeH_4	$^{74}GeH_4$	3.652×10^{-1}	648–2270	12 209	648–2270	12 209
	$^{72}GeH_4$	2.741×10^{-1}	649–2270	12 141	649–2270	12 141
	$^{70}GeH_4$	2.051×10^{-1}	649–2271	12 092	649–2271	12 092
	$^{73}GeH_4$	7.755×10^{-2}	649–2270	12 170	649–2270	12 170
	$^{76}GeH_4$	7.755×10^{-2}	648–2270	12 266	648–2270	12 266
(53) CS_2	$^{12}C^{32}S_2$	8.928×10^{-1}	64–7550	354 910	23–6467	45 758
	$^{32}S^{12}C^{34}S$	7.921×10^{-2}	191–6430	343 902	196–4543	7237
	$^{32}S^{12}C^{33}S$	1.409×10^{-2}	204–5948	202 208	611–4567	3401
	$^{13}C^{32}S_2$	1.003×10^{-2}	159–5789	110 264	1–4426	27 024
(54) CH_3I	$^{12}CH_3{}^{127}I$	9.884×10^{-1}	693–3274	178 247	693–3274	178 247
(55) NF_3	$^{14}N^{19}F_3$	9.963×10^{-1}	2–2201	2 717 795	2–2201	2 717 795
(56) H_3^+	H_3^+	9.995×10^{-1}	7–25 000	75 241	–	–
(57) CH_3	$^{12}CH_3$	9.884×10^{-1}	3–8000	342 893	–	–
(58) S_2	$^{32}S_2$	9.028×10^{-1}	21 905–41 298	387 432	–	–
(59) COFCl	$^{12}C^{16}O^{19}F^{35}Cl$	7.475×10^{-1}	734–1913	153 481	–	–
	$^{12}C^{16}O^{19}F^{37}Cl$	2.390×10^{-1}	737–1908	62 158	–	–
(60) HONO	$H^{16}O^{14}N^{16}O$	9.915×10^{-1}	0–236	31 171	–	–

(*continued on next page*)

Table 1 (*continued*).

Molecule	Isotopologue	Abundance[a]	HITRAN2024		HITRAN2020	
			Spectral range[b]	# of lines	Spectral range[b]	# of lines
(61) $ClNO_2$	$^{35}Cl^{14}N^{16}O_2$	7.514×10^{-1}	341–387	5001	–	–
	$^{37}Cl^{14}N^{16}O_2$	2.403×10^{-1}	336–381	4999	–	–

[a] Abundances are calculated from terrestrial atomic abundances in Ref. [31]. Line intensities in the HITRAN database have been scaled by these isotopologue abundances.

[b] Spectral ranges are given in cm^{-1}.

[c] There are cases in which the spectral ranges and number of lines are unchanged with respect to HITRAN2020, but there have been changes to the spectral parameters of lines for these isotopologues.

Table 2

The uncertainty codes used by the HITRAN database (as presented in HITRAN*online*) are based on Table 5 of the HITRAN2004 paper [13], although they are expanded to allow for smaller uncertainties. There are two types of uncertainty codes corresponding to absolute uncertainty in cm^{-1} (used for the line position and pressure-induced line shift parameters) and relative uncertainty in % (used for the line intensity and line-shape parameters).

Code	Absolute uncertainty range	Code	Relative uncertainty range
0	≥ 1 or Unreported	0	Unreported or unavailable
1	≥ 0.1 and < 1	1	Default or constant
2	≥ 0.01 and < 0.1	2	Average or estimate
3	≥ 0.001 and < 0.01	3	≥ 20%
4	≥ 0.0001 and < 0.001	4	≥ 10% and < 20%
5	≥ 0.00001 and < 0.0001	5	≥ 5% and < 10%
6	≥ 0.000001 and < 0.00001	6	≥ 2% and < 5%
7	≥ 0.0000001 and < 0.000001	7	≥ 1% and < 2%
8	≥ 0.00000001 and < 0.0000001	8	≥ 0.1% and < 1%
9	≥ 0.000000001 and < 0.00000001	9	< 0.1%

Table 3

Bands for which intensities of variational origin were scaled by factors (SF) determined from experimental studies (referenced in the table).

Band	SF	Source
$4\nu_2$	0.9411[a]	[47]
$2\nu_2+\nu_3$	1.0189	[47]
$\nu_1+2\nu_2$	1.0487	[47]
$\nu_2+\nu_3$	1.0129	[47]
$\nu_2+2\nu_3$	0.9171	[46]
$\nu_1+\nu_2+\nu_3$	0.9632	[46]
$4\nu_2+\nu_3$	1.0747[b]	[46]
$\nu_1+4\nu_2$	0.7378[a]	[46]

[a] Due to non-systematic scatter of ratios, if the experimental intensities were available, they were taken directly; if not, they were scaled by the factors in the Table.

[b] This factor is with respect to the updated HITRAN2020 (see text for details).

2.1.1.3. Line-shape parameters. As mentioned earlier, in the NIR and visible regions, many air-broadening and shift parameters in the official release of HITRAN2020 had to be corrected based on a comparison with the TCCON retrievals. The majority of the issues have been traced back to the prediction routine from Ref. [33] and, to a lesser extent, experimental outliers. For the HITRAN2024 edition, we have developed a new (with respect to the previous effort [48]) "Diet" to filter out the outliers in broadening, their temperature dependencies, and shifts. The new Diet incorporates a filtering algorithm conceived to identify the most probable outliers based on the general tendencies of the dataset. When plotted against J, shifted by $0.9 \times K_c''/J''$ to highlight the change of parameters through the oblate ($K_c'' = 0$) to prolate ($K_c'' = J$) regime, line broadening, and their temperature dependencies, follow a multi-parabolic tendency. This pattern is illustrated in Fig. 3(a), in which each set of values sharing the same J'' has been fitted by separate third-order polynomials. The standard deviation around this polynomial is significantly stronger for larger $|K_a - K_c|$ values, highlighting the spread induced by the vibrational dependence of these parameters. This approach is inherently dependent on the quantity and quality of the available data.

To accommodate this dependence and smooth the disparities of available data, for each polynomial fit, the parameters are sorted by vibrational group instead of vibrational band. Following [49], a vibrational group is defined by the number of quanta exchanged in bending and stretching modes, assuming that, in the first approximation, vibrational dependencies of the symmetric and asymmetric stretching modes are the same. This filtering technique has been tested on several bands, including the $4\nu_1$ band. In the last update of the H_2O line list, many of the HITRAN2020 air-broadening coefficients in this band had to be adjusted based on the TCCON spectra residuals. The evaluation of the original HITRAN2020 line list is presented in Fig. 3(a). The values identified by the filter are highlighted in orange, and the values modified in the updated version of HITRAN2020 are in dark blue. The algorithm has no safe way to judge the quality of the values within the average spread of the data, but it is successful in the identification of most of the especially-offending outliers outside of this range. In this regard, the filter assembles a basic list of transitions requiring investigation. In an iterative approach, the tendency fitted on pre-existing data can serve as a guide to pre-filter new experimental data, disregarding the quantity of transitions covered by the new dataset. Once these new data are filtered and incorporated into the database, the freshly updated line list can be used to fit a new general tendency, providing a more average and accurate template for filtering future data.

In the end, the following approach has been used to improve the line-shape parameters in HITRAN.

For air broadening, the new experimental laboratory data [47,51–55] were pre-filtered using the new "Diet" and used when available, unless a lower uncertainty measurement already existed in the database for a particular transition. In cases where the latest experimental data could not replace the outliers originating from the prediction algorithm from Ref. [33], they were replaced by the values from the so-called ATM24 line list [56]. The ATM line lists are designed to minimize residuals from TCCON retrievals and combine different HITRAN data in the 650–15 000 cm^{-1} with *ad hoc* fixes that are designed to minimize residuals in atmospheric spectra [57]. One should note that Refs. [47,54,55] also provided speed-dependent Voigt parameters, and they were added to the database wherever possible, making use of the HITRAN relational structure. The temperature dependencies were retained as in HITRAN2020, as they agree well with recent experiments (see, for example, Ref. [54]).

For air shifts, the procedure was similar to that for broadening, noting that the procedure was more heavily based on the ATM24 line

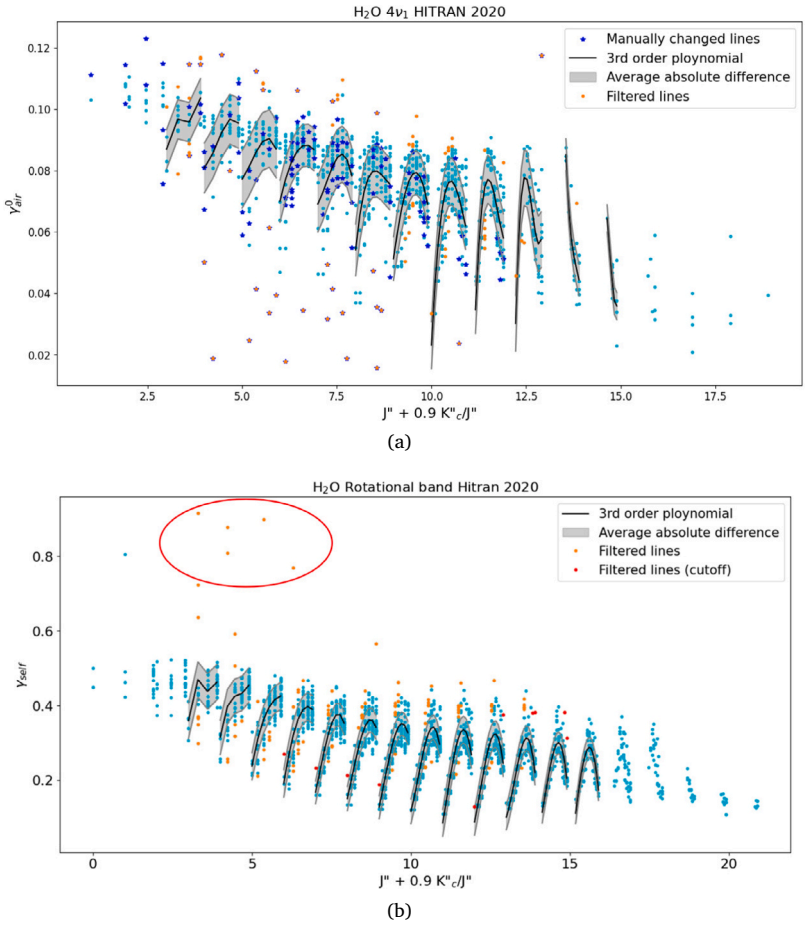

Fig. 3. Demonstration of the filtering procedure to identify outliers in pressure-broadened half-widths of water vapor lines. (a) Identifying outliers in the $H_2^{16}O$ air-broadened values for the $4\nu_1$ band in HITRAN2020. (b) Identifying outliers in the self-broadened values in the pure-rotational band in HITRAN2020. Circled values are from Ref. [50], where FWHM values were reported and were not divided by 2 when taken to HITRAN.

list [56]. Above, 15 000 cm^{-1}, an improved prediction routine was used.

Self-broadening improvements included eliminating identified outliers. Fig. 3(b) demonstrates how the new "Diet" helps to "catch" erroneous values. For instance, transitions circled in the figure correspond to values from Podobedov et al. [50], which were FWHM but mistakenly taken as HWHM when compiling the HITRAN2024 database. New measurements from Refs. [47,58,59] were incorporated, where possible, including non-Voigt parameters.

2.1.2. $H_2{}^{18}O$ and $H_2{}^{17}O$

Recent experiments in the FIR region by Toureille et al. [41] have demonstrated deficiencies in the MARVEL-based line positions of oxygen-substituted isotopologues in HITRAN2020. For $H_2{}^{18}O$, a new effective Hamiltonian was recently built for the five lowest-lying vibrational states [60], based on validated empirical data. For transitions involving these states in the 2–5000 cm^{-1} region, we have updated the line positions to those calculated by Coudert et al. [60]. Similar work on the $H_2{}^{17}O$ lines is ongoing and will be used in future updates. In addition, precision-spectroscopy line-position results, with uncertainties at the kHz level, have been reported recently for $H_2{}^{18}O$ and $H_2{}^{17}O$ [40,61,62] and were adapted where available. Finally, some of the line positions from W2020 that were not properly transferred to HITRAN2020 were fixed.

The line-shape parameters of the principal isotopologue species were transferred to the corresponding transitions of $H_2{}^{18}O$ and $H_2{}^{17}O$, ignoring the weak isotopic dependence in oxygen-substituted species.

2.1.3. Deuterated isotopologues

The line positions and intensities for all deuterated water isotopologues in HITRAN2020 (the same in HITRAN2016) are based on the line list from Kyuberis et al. [63], featuring *ab initio* intensities and a mixture of variational and empirically-derived line positions. In addition to the intensity cutoff, it was calculated for transitions that involved only energy levels with a total angular momentum $J \leq 20$.

Recent experimental work on $HD^{16}O$ in the FIR region has shown that there are a lot of fairly intense lines with $J > 20$ that were missing in HITRAN2020. They also found that for many lines, the line positions can be improved. For HITRAN2024, we have included the missing lines identified in Ref. [64] and updated the line positions of the transitions between the first five vibrational states of $HD^{16}O$ using the same reference. Precision-spectroscopy line-center positions have been published for $HD^{16}O$ [65], but they need further investigation.

A very recent study [66] has been conducted on the analysis of FIR experimental data of doubly-deuterated water isotopologues. We have not used it yet to update the $D_2{}^{16}O$ line list, except to add a couple of strong lines missing in the ν_2 band. More work on this will be done for the next edition.

In Ref. [47], the following HDO line-shape parameters were determined in the range 5970–6575 cm^{-1}: $\gamma_{0,air}$, $\delta_{0,air}$, $\gamma_{0,self}$. Except for very weak lines and a few lines where $\gamma_{2,self}$ and $\gamma_{2,air}$ were fitted, these values were set applying polynomials of γ_2/γ_0 vs γ_2 fitted from the main isotopologue values. No other changes were made to the line-shape parameters of deuterated isotopologues.

2.2. CO_2: Carbon dioxide (molecule 2)

The update of the carbon dioxide line list in HITRAN2020 provided a significant overall improvement for the spectroscopy of CO_2 in comparison to previous editions [67,68]. The update was carried out for the line positions and intensities (explained in Karlovets et al. [69]) as well as improvements in the line-shape parameters (including the addition of the speed-dependent Voigt parameters [26] and broadening by gases other than air [28,30]). While the HITRAN2020 carbon dioxide line list was very successful, new high-quality experimental and theoretical works have since been published, allowing for further improvements. In addition, some issues were identified with the HITRAN2020 line list, including a number of bands with variational intensities added in HITRAN2020 above 8000 cm^{-1} that have since been shown to have overestimated intensities [70–72]. Here we outline the changes made to the carbon dioxide line list for HITRAN2024.

2.2.1. Line positions

Line positions of the principal isotopologue ($^{12}C^{16}O_2$) for HITRAN2024 have been taken from the updated Carbon Dioxide Spectroscopic Databank for the principal isotopologue: CDSD-2024-PI [73]. This is an improvement over the previous version of CDSD (CDSD-2019 [74]), which was a primary source for line position values in HITRAN2020. CDSD-2024-PI provides a new global fit of the effective Hamiltonian parameters for $^{12}C^{16}O_2$, which accounts for the most recent line position measurements (references from Table 2 of Ref. [73]). These new measurements include very high-precision data (see for instance Refs. [75–78]) and bands that were not observed before, including the 2005i–00001 (i = 1, 2, 3) bands near 718 nm [79] and 30052–00001, 30053–00001 and 60031–00001 bands near 660 nm [80]. The vibrational assignments[1] are given as $v_1\ v_2\ \ l_2\ v_3\ r$ for the upper and lower states, referring to the vibrational quanta in each mode (v_i), the angular momentum of the degenerate bend (l_2), and a ranking index (r). For the minor isotopologues of carbon dioxide, the line positions remain unchanged from HITRAN2020. There are values from the MARVEL analyses of experimental data for the principal and the minor isotopologues [73,81–88] that will be considered for future updates of isotopologues.

2.2.2. Line intensities

For HITRAN2024, the intensities have generally remained unchanged from HITRAN2020, especially below 8000 cm^{-1}, with some notable exceptions described below.

The updated intensities in the NIR address the 0.3% accuracy target for retrieved CO_2 columns proposed by remote-sensing missions. These intensity requirements are particularly challenging for both experimental measurements and theoretical calculations. Nevertheless, a plethora of high-accuracy experimental measurements and high-level *ab initio* calculations have been carried out. In recent years, special attention has been paid to the 3001r'-00001 and 2001r'-00001 band regions (where r' is a ranking index as defined in [89]) because they are relatively strong while being in the water absorption windows. Many remote-sensing missions target these bands, including OCO-2 [90], OCO-3 [91], GOSAT [92], GOSAT-2 [93], MicroCarb [94] and CO2M [95]. In general, the best variational intensities [71,96] agree on a sub-percent level with highly-accurate measurements from DLR [97–100] and NIST [101–103]. It should be noted that while high-quality experimental measurements agree, they can still exhibit differences up to 0.2–0.3%. The HITRAN2020 intensity data for these bands are based on the *ab initio* calculations by Zak et al. [96] with the exception of transitions between the 20013, 30014, 30013, 30012 states and the ground state that were scaled to agree with measurements from Refs. [101,102]. More recent experiments from DLR [98–100] suggested that the corresponding data in the HITRAN2020 edition in general is very good, although some systematic discrepancies still exist, in addition to a slight disagreement in rotational dependence. These intensities were also compared with those from the recent update of the HITEMP database [72], which are based on the variational AI-3000K [71] values (except for the 30011–00001 band that was scaled by a factor of 0.99314). Fig. 4 demonstrates that, in general, the rotational dependence in HITEMP agrees with DLR experimental values marginally better than HITRAN2020 for these bands, but also has some systematic shifts on a level below 0.5%. For HITRAN2024, we therefore scaled the HITEMP values for these bands to better agree with the DLR measurements.

With discrepancies in recent experimental and computational results for the near-infrared (NIR) bands of CO_2 now at the sub-percent level, a careful treatment of parameter correlations and biases is essential for modeling atmospheric spectra. A recent evaluation with the TCCON spectra by Thiemann et al. [104] has reported that HITRAN2020 data (with non-Voigt effects included) improves the fits when compared to previous editions and alternative sources, but the improvement is even better when using DLR parameters used to benchmark HITRAN2024. At the same time, recent high-precision atmospheric measurements of the 30012–00001 and 30013–00001 bands by dual-comb spectroscopy reported Malarich et al. [105] appear to agree slightly better with HITRAN2020 than with the DLR measurements. This finding, however, may not be conclusive because of potentially significant unaccounted-for biases that would require further refinement in the spectral analyses. Ongoing work to resolve these subtle discrepancies for these bands necessitates close collaboration between laboratory spectroscopists and atmospheric scientists.

Similarly, the 00031-00001 intensities in HITRAN2024 are provided by scaling the AI-3000K intensities by a factor of 0.99314, which retains consistency with HITEMP [72]. The scaled AI-3000K/HITEMP intensities for the bands described above have also been applied to all other isotopologues for HITRAN2024.

As mentioned above, many "new" bands were added in HITRAN2020 above 8000 cm^{-1} using the intensities provided by the high-temperature UCL-4000 line list [106]. However, it has since been determined that the intensity of many of these bands was overestimated. Huang et al. [107] have highlighted the $v_1'110r'$-00001 sequences (where $v_1' = 7$ to 14 and denotes the number of ν_1 quanta for the upper state) that appear too strong when compared to the intensities of AI-3000K [71]. It was also demonstrated during the CO_2 update for HITEMP that these particular bands do not follow the normal intensity drop-off expected for overtones [108]. An experimental validation performed using a cavity ring-down spectrometer [70] was unable to detect any transitions of the 101108-00001 (here $v_1' = 10$, and $r' = 8$) band at 14370 cm^{-1}. Similarly, they were also unable to observe nearby weaker bands predicted by AI-3000K that are below the 10^{-30} cm/molecule threshold used for CO_2 in this region in HITRAN. For HITRAN2024, these bands with intensities from Yurchenko et al. [106] have been replaced by intensities provided in AI-3000K [96] and are consistent with HITEMP. As a result, many of these bands that were "new" in HITRAN2020 now do not contain lines above the 10^{-30} cm/molecule threshold and do not feature in the HITRAN2024 line list, but are provided in the updated HITEMP line list.

2.2.3. Air-broadened line-shape parameters

In HITRAN2020, the air-broadening parameters for Voigt and speed-dependent Voigt parametrizations were based on semi-empirical data from Hashemi et al. [26], where Padé approximants were fit to experimental and, in some cases, theoretical data. In the course of the preparation of the HITEMP database for carbon dioxide [72], it was noted that in the case of Voigt parametrization, the parameters for higher J values could be determined better by restricting the approximant at the very high rotational levels to semi-classically calculated values from [109]. In HITRAN2024, the Voigt air-broadening half-widths

[1] See also https://hitran.org/quanta/.

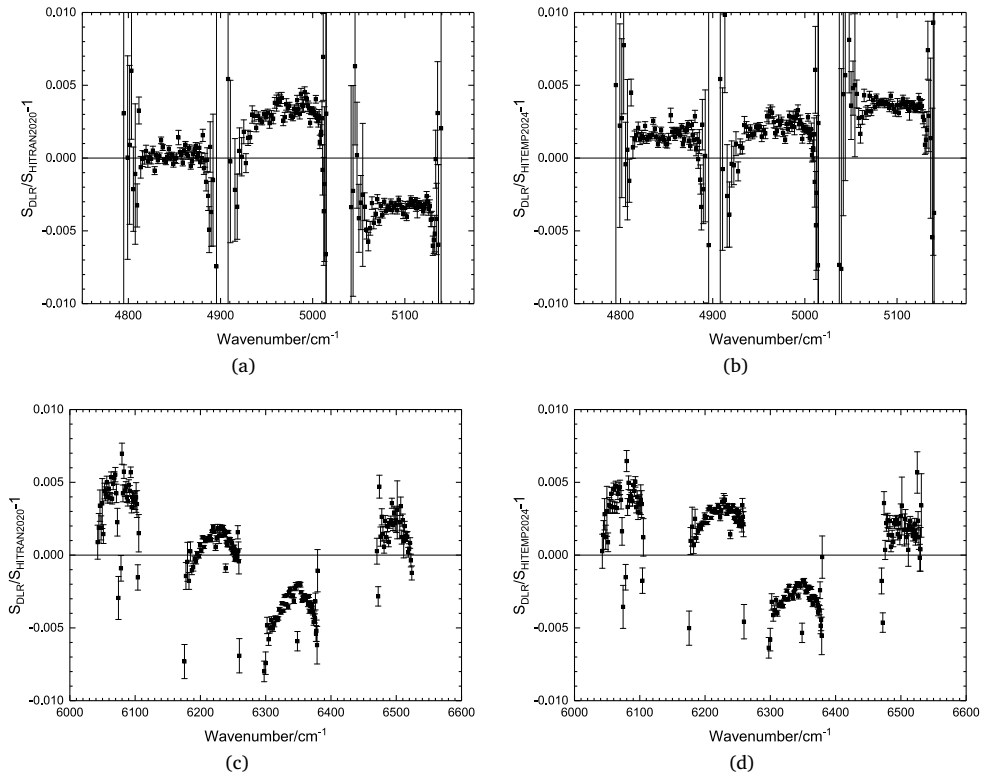

Fig. 4. Comparing measurements of intensities of the bands involving $2001r'$ (at 2 μm) and $3001r'$ (at 1.6 μm) upper states from DLR [97,98] with HITRAN 2020 [17] and recent update of HITEMP in 2024 [72]. Relative intensity differences are plotted on Y-axis.

and their temperature dependencies have been updated to the values from Gamache and Lamouroux [109]. Recent highly-accurate experimental measurements that employed speed-dependent Voigt (SDV) fits in different bands [99,100,110,111] have shown that the parameters calculated in Hashemi et al. [26] are accurate to within 1%. However, the unprecedented accuracy of the new experiments has shown that there were minor but systematic deviations of the γ_0 parameters from the HITRAN2020 values that depend on the rotational branch. We have now used the new data to fit the Padé approximants separately for P and R branches using data from Refs. [99,100,110,111]. A more substantial change has been introduced to the γ_2 parameters as they are more complicated to measure accurately, as it is hard to decorrelate without measuring a wide range of pressures. Many experimental studies fix that parameter to the HITRAN2020 values (see, for instance, Ref. [112]). Thanks to the new experimental data from DLR and new theoretical calculations by Tran et al. [113], a new function was fit to obtain the reliable values of γ_2. The experimental data were used for low and intermediate rotational levels, while for higher levels the Padé function was restricted using data from Tran et al. [113]. The highest levels in the fit were constrained by a constant a_w ($\gamma_2/\gamma 0$) ratio of 0.08. Fig. 5 illustrates this new function and the data used to fit it.

In addition, experiments on the ^{13}C-enriched isotopologue [115] have shown that while the choice made in HITRAN2020 to ignore isotopic dependence is reasonable, some small deviations have been observed. Experimental values for γ_0 parameters for the principal isotopologue are about 0.4% larger than those for ^{13}C-enriched isotopologues. We therefore have scaled these isotopologue values accordingly.

2.2.4. Other line-shape parameters

The self-broadening parameters have not been updated.

Based on a comprehensive analysis of the available data in Tan et al. [30], broadening parameters of CO_2 by He and H_2 were added to the database. For CO_2 spectral lines broadened by hydrogen, due to limited experimental data from Padmanabhan et al. [116] and Hanson & Whitty [117], the study implemented a scaling approach using the air broadening coefficient for $|m| < 35$, applying a scaling factor of 1.577 and ignoring difference in rotational dependence between colliders. The temperature dependence was set as a constant $n = 0.58$, obtained from a single line measurement by Hanson & Whitty [117]. Consequently, the data limitations are primarily due to a lack of experimental results for higher-J values ($|m| \geq 35$), necessitating extrapolation, which results in potential errors and very limited temperature dependence information.

It is worth noting that the recent *ab initio* calculations by Wiesenfeld et al. [118] show excellent agreement with measurements of Hanson & Whitty [117]. Once these calculations are expanded to more transitions, they will provide valuable data for H_2-broadened values. For helium broadening, benefiting from more extensive data, a Padé approximation was employed for fitting, resulting in a standard deviation of 2%. The initial temperature dependence in the original HITRAN2020 release was based on $n_{He} = 0.3$, originating from Nakamichi et al. [119]. This value was found to be too low. The revised method used in the update utilizes linear fitting for $J \leq 20$ and constant fitting beyond $J > 20$, as informed by experimental data from Deng et al. [120]. Recent measurements by Hendaoui et al. [121] showed generally good agreement with HITRAN; however, some deviations can be seen for transitions involving higher rotational levels. These values will be updated in the future.

The broadening of the lines of CO_2 by water vapor was introduced to HITRAN by Tan et al. [28] based on semi-empirical values. Recent semi-classical calculations by Vispoel and Gamache [122] agree well with the values from Tan et al. [28], but start to deviate with the increase of rotational quanta, which is not surprising since the values in Ref. [28] were extrapolated from experiments well beyond the observed values. The values from Vispoel and Gamache [122] will be considered for future updates.

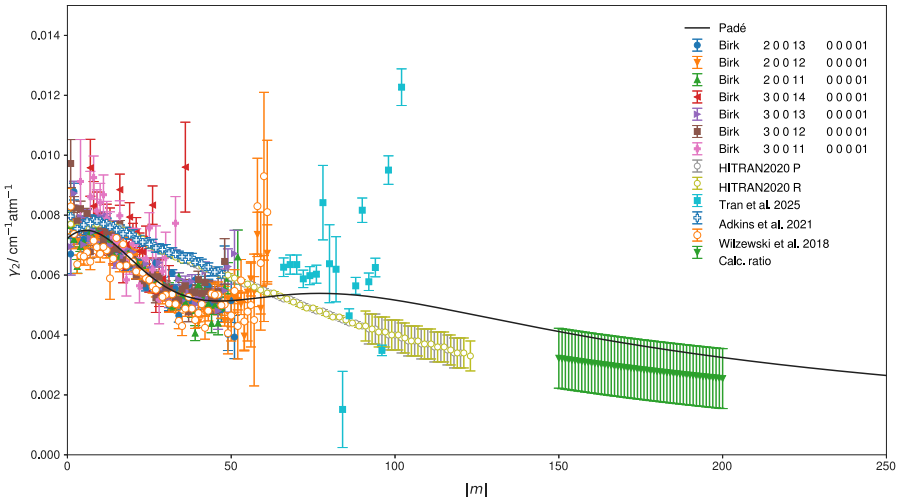

Fig. 5. Speed dependence of the air-pressure broadening (γ_2-air) from the new data [99,100] (denoted as "Birk"), Padé function fit to the data, values from HITRAN2020, Tran et al. [113], Adkins et al. [112], Wilzewski et al. [114]. All the colored-center points were used in the fit.

DLR has derived air- and water-broadening line parameter databases in the 1.6-μm and 2.0-μm regions with sub-permille accuracy within the project ISOGG (Improved Spectroscopy for satellite measurements Of Greenhouse Gases) dedicated to the upcoming CO2M mission [95]. These databases include intensity depletion of CO_2/air as well as the CO_2/air continuum, both with temperature dependence [99,100]. Remote-sensing applications, which need accuracy that exceeds 0.1%, should consider employing these data sets since the intensity depletion is not yet parametrized in HITRAN. The line model contains special temperature dependence of line mixing as well as depletion and continua. When using these data, the user is faced with the problem of implementation and validation, which can be rather time-consuming and error-prone. Therefore, the data were converted to absorption cross sections given in an ABSCO-type database [123] and uploaded to ZENODO [124]. Data are given in the wavenumber ranges 4750–5175 cm^{-1} and 5970–6575 cm^{-1} on a pressure, temperature, and humidity grid as defined in ABSCO.

2.2.5. *HITEMP line list for CO_2 updated*

As already mentioned, the carbon dioxide line list in HITEMP has been updated [72] from the version provided in HITEMP2010 [125]. This update to HITEMP was primarily built around the AI-3000K line list [71] for the four most abundant isotopologues, but also included additional minor isotopologues from Huang et al. [107], and a number of band-by-band substitutions and scalings to HITRAN2020 based on evaluations. The HITEMP line list is suitable for modeling the spectrum of CO_2 up to 3000 K. Due to high-temperature requirements, the HITEMP line list features significantly more transitions than HITRAN (about 320 million versus 0.5 million, respectively). In addition, a novel "effective line" methodology was implemented to reduce the number of lines provided by the ab initio work by two orders of magnitude. These effective lines were generated by binning the weakest transitions according to their position and lower-state energy, with their effective parameters weighted by the lines within each bin. The requirements of a high-temperature line list favor consistency and completeness to avoid intensity steps within bands, which can become apparent when intensities are converted to higher temperatures. Therefore, while the carbon dioxide line list in HITEMP is in good agreement with HITRAN2024, there will remain some differences, such as those described above. It is anticipated that updates to the carbon dioxide line list for HITRAN2024 will be carried over to HITEMP.

2.3. *O_3: Ozone (molecule 3)*

Ozone is one of the most important gases in the terrestrial atmosphere, playing an essential role in its chemistry [126,127], with stratospheric ozone being a protector of life by blocking harmful UV radiation, while the tropospheric ozone is a pollutant harmful to human health [127,128]. Due to the importance of ozone, its concentrations are being monitored [129–131] and its correlation with other gases is being studied extensively. Moreover, ozone is considered as a potential biosignature on exoplanets (see, for instance, [132]). In the previous edition (HITRAN2020), thanks to dedicated experimental and theoretical international efforts [133–138], the ozone data were substantially overhauled in all spectral regions from the MW to the UV, achieving much better consistency in intensities between the strongest bands as well as reduced RMS. These improvements substantially reduced existing biases in ozone retrievals (see, for instance, [139]).

The update in HITRAN2024 was carried out in the 0.02–273.2 cm^{-1} region (0.6 GHz–8.2 THz), thanks to the $^{16}O_3$ line list from Tyuterev et al. [140]. It is based on the analyses of high-resolution absorption spectra of ozone recorded using the Fourier transform spectrometer of the AILES beamline at Synchrotron SOLEIL [141]. Many ozone lines have been observed for the first time in the longwave ranges 0.96–6 THz thanks to the exceptional brightness of the Synchrotron radiation, the sensitivity of measurements, and the high SNR. These measurements were carried out for four ozone pressures from 1.023 to 10.66 mbar and three optical paths from 2.8 to 19.04 m. Line positions were calibrated to an absolute accuracy of about 0.00003–0.00005 cm^{-1} for the best lines using precise MW data of the ozone transitions [142,143] as well as relatively sparse water and CO_2 lines. The observed line positions showed deviations from the HITRAN2020 values for higher rotational quanta, where the previous values were extrapolations.

A new combined line list for the rotational band in the vibrational ground state (GS) and for the ν_2-ν_2 hot band of $^{16}O_3$, which contains empirically fitted line positions and *ab initio* line intensities, has been reported by Tyuterev et al. [140]. In total, 13 466 observed line positions, including transitions assigned in SOLEIL spectra and previously published MW and FIR experimental data, were simultaneously fitted with the weighted standard deviations of 0.707 and 0.64, correspondingly. The resulting extended effective Hamiltonian parameters (given in the supplementary materials of Ref. [140]) were used to calculate the new line positions. The HITRAN2024 $^{16}O_3$ data below 273.2 cm^{-1} is essentially based on the line list of Tyuterev et al. [140] with the following minor modifications. For a further refinement, we have replaced 56 calculated line positions with very accurate observed MW

values. This concerns less than 0.5% of the HITRAN2024 linelist for these bands. The intensity cut-off $S_{min} = 5 \times 10^{-29}$ cm/molecule was applied in the region 0.02–10 cm^{-1} and $S_{min} = 10^{-28}$ cm/molecule in the region above 10 cm^{-1}.

Line intensities for these bands in Ref. [140] were produced by variational calculations using the *ab initio* dipole moment surface of [136, 144] with the partition function of Gamache et al. [145]. Prior works showed that the intensities calculated from these dipole surfaces agree well with Stark measurements [146], and experimental intensities as well as the line intensities in HITRAN2020 and JPL database were found consistent with measurements by Birk et al. [138] at a 1% level. Nevertheless, to make the intensities consistent, we have scaled the variational intensities to agree with the experimental data from Birk et al. by a factor of 1.0073.

In the future, the self-broadening parameters, which in the present list are held fixed to the same values as in HITRAN2020, must be revised. As mentioned in Tyuterev et al. [140], the lines involving $K_a = J$, $K_a = J - 1, \ldots$, for $K_a > 20$ appear significantly narrower in observations, whereas the lines with big $J - K_a$ differences in quantum numbers show larger experimental widths. Improved rotational levels of (000) and (010) states will require line position corrections for other bands, particularly for large J, K_a values. Further improvements of the spectroscopy databases will concern empirical corrections in other energy levels as well. Recent work by Tashkun et al. [147] on 28 572 rovibrational levels up to $J = 80, K_a = 29$ confirms most HITRAN2020 line positions, with future updates (where positions can be improved) expected. Ongoing studies are also extending data for the heavy isotopologues $^{16}O^{18}O^{18}O$ and $^{18}O^{16}O^{18}O$ [148]. This improvement would be particularly helpful for interpreting data from the Microwave Limb Sounder (MLS), and the upcoming mission FORUM [149], which is planned to be launched in 2027 by ESA to carry spectrally resolved observations of Earth's outgoing long-wave radiation that could contain signatures of key climate forcing and feedback processes [150].

In addition, it was found that in the process of combining different line lists of ozone for HITRAN2020, the lines of the principal isotopologues of ozone in the 850–980 cm^{-1}spectral region that were supposed to be retained from the HITRAN2016 edition were accidentally omitted. These lines have been restored shortly after the official release of HITRAN2020 and are in the HITRAN2024 database.

2.4. N_2O: Nitrous oxide (molecule 4)

The presence of nitrous oxide (N_2O), a greenhouse gas, in the terrestrial atmosphere provides prominent spectral features used for remote sensing of N_2O concentrations. These bands also impact retrievals of other species that absorb in the same spectral windows (e.g., H_2O, CO_2, O_3, CO, CH_4). Thus, N_2O has been the focus of numerous spectroscopic investigations, especially in recent years.

The HITRAN2020 line list of N_2O [17] was primarily based on a line list by Toth [151], which did not contain lines of the principal isotopologue above 8000 cm^{-1} and had a 2×10^{-25} cm/molecule intensity threshold (at 296 K) based on experimental sensitivity. This lack of coverage in spectral and dynamic ranges has been highlighted (e.g., Ref. [152]), particularly since the $^{14}N_2{}^{18}O$ isotopologue contained transitions up to 10 363 cm^{-1} in HITRAN2020 with a much lower intensity cut-off. There have been a number of recent experimental works that have measured bands in the NIR region with increased sensitivity, e.g., CRDS measurements for the 5696–5910 cm^{-1} [153], 7250–7653 cm^{-1} [154], 7647–7918 cm^{-1} [155], 8321–8622 cm^{-1} [156], 11 937–12 223 cm^{-1} [157] ranges, and FTS measurements for the 9750–12 050 cm^{-1} range [158,159]. Line positions and intensities of numerous studies have been used to update the global effective Hamiltonian model used for the Nitrous Oxide Spectral Line list (NOSL-296) list for $^{14}N_2{}^{16}O$ [160, and references therein]. In addition, a MARVEL energy level analysis has been carried out using 91 published sources for $^{14}N_2{}^{16}O$ [161, and references therein]. It is worth noting that some of the N_2O line positions have been measured with really low uncertainties, employing techniques such as frequency combs (see, for instance, Refs. [162–168]).

Recently, Huang et al. [169] have published a comprehensive N_2O line list, denoted ABG-IMRHT, that incorporated a major upgrade of the PES over the Ames-1 PES [170], and was enhanced by empirical levels determined from a variety of experiment-based data sources that include Toth [151], NOSL-296 EH model [160], MARVEL level set [161], RITZ level sets and EH models from IAO [169]. This upgraded PES has been combined with the most up-to-date Ames dipole moment surface to provide a line list for the 12 stable isotopologues of N_2O. This work [169] forms the basis of the N_2O update for HITRAN2024 and is described below.

2.4.1. NOSL and ABG-IMRHT line list for nitrous oxide

In 2022, Tashkun and Campargue [160] published the NOSL-296 room temperature line list for $^{14}N_2{}^{16}O$ using a global non-polyad effective Hamiltonian (EH) model [171] and effective dipole moment (EDM) models, in which 199 EH parameters were fitted from 71 045 experimental line positions, and 152 EDM parameters were fitted from 27 639 measured and 24 337 calculated line intensities. The NOSL-296 line list includes nearly 900 000 lines in the range of 0.02–13 378 cm^{-1} with intensities $S_{296K} \geq 10^{-30}$ cm/molecule. Most published high-resolution experimental data have been incorporated into the global fitting of the NOSL-296 list. Subsequently, Karlovets et al. [154] revisited the spectral range of 7250–7653 cm^{-1}(or 1.34 μm), refined related EH/EDM parameters, and made comparisons to NOSL-296 and a preliminary release of Ames-296K.

The ABG-IMRHT line list contains 2.1 million transitions of all 12 stable isotopologues with $S_{296K} > 5 \times 10^{-31}$ cm/molecule in the 0.02–14 025 cm^{-1} range. It utilized a new PES (B1b) refined from a refit of Schröder's Comp I PES [172] with $\sigma_{rms} = 0.006$ cm^{-1} for reliable $^{14}N_2{}^{16}O$ levels in HITRAN2020 [17], and a new dipole moment surface (G10K) with fitting $\sigma_{rms} = 6.1 \times 10^{-7}$ a.u, for CCSD(T)/CBS dipoles up to 10 000 cm^{-1}. While comparison of the calculated line positions with the reliable lines in the JPL(Toth) [151] list showed good agreement, further improvements were introduced. The $^{14}N_2{}^{16}O$ line positions were first enhanced by the energy levels computed from the experiment-based EH model [171] of NOSL-296 [160], including more than 100 000 $J = 0$–125 levels up to 11 500 cm^{-1}, and selected higher energy levels up to 15 000 cm^{-1} if they were associated with observable IR intensities. More empirical corrections to line positions were incorporated using additional EH models and RITZ experimental data collections (IAO) for the six most abundant isotopologues, MARVEL level set for $^{14}N_2{}^{16}O$ (ExoMol) [173], as well as the reliable transitions in the HITRAN and JPL(Toth) [151] line lists. For example, simple 0th–2nd order correction formula were applied on the $E_{NOSL-296}$ of about 20 vibrational states above 10 000 cm^{-1}, based on band-by-band comparison between $E_{NOSL-296}$, E_{RITZ}, and E_{MARVEL}.

The PES and DMS upgrades have significantly strengthened the accuracy and reliability of IR intensity predictions. For example, the new IR line intensities computed for the 42^00-00^00 and 50^00-00^00 bands are 1.1% and 1.8% higher than the high-accuracy measurements that Adkins et al. [174] reported with uncertainty close to 1%. This is a notable improvement over previous Ames-296K (2%–5%) [170] or ExoMol TYM (4%–5%) [173]. Compared to HITRAN2020, the most significant intensity upgrades occurred in four hot bands of the ν_1 series and five hot bands of the $3\nu_2$ and $4\nu_2$ series. For these bands, the NOSL-296 and Ames intensities are derived from fundamentally different methodologies, yet they show excellent agreement. For example, both S_{Ames} and $S_{NOSL-296}$ are three times as large as $S_{HITRAN2020}$ and $S_{JPL(Toth)}$. An exception is that the S_{Ames} of the 10^00-01^10 band are 40% higher than corresponding $S_{HITRAN2020}$ and $S_{NOSL-296}$, so in better agreement with PNNL spectra [175]. The overall prediction accuracy of S_{Ames} was comparable to that of $S_{NOSL-296}$, as shown by an analysis of $R(16)e$ transitions. Compared to NOSL-296, the upgraded line list does not have

extra large deviations (e.g., > ±200%) against the IR line intensities that Karlovets et al. [154] measured in the 7250–7653 cm^{-1} range. However, theoretically-computed intensities for some ν_3 overtones and related hot bands are still systematically lower than the measurements, $S_{NOSL-296}$, and $S_{HITRAN2020}$, by −17% to −11% at least [169]. Examples include the 00^02-00^00 band near 4400 cm^{-1} and the 02^03-00^00 band near 7650 cm^{-1}. This discrepancy between theory and experiment calls for future investigation and upgrades. Compared to the 78 934 line intensities measured experimentally for six N_2O isotopologues, S_{Ames} has the majority of relative differences within ±15%. Compared to 47 561 transitions in the JPL(Toth) list (with outliers excluded), the relative differences have a mean of −1% with a standard deviation of 17%. More intensity data of ABG-IMRHT line list Huang et al. [169] of other minor isotopologues can be found on ZENODO [176].

2.4.2. Validations against experimental spectra and band scalings for HITRAN2024

For pure rotational bands, including the 00^00-$00^00, 10^00$-$10^00, 01^10$-01^10, and 00^01-00^01 bands, the Huang et al. [169] intensities have been scaled to agree with the lower J values in the JPL catalogue [177] as they are based on the precise value of the permanent dipole moment.

Validation of the ABG-IMRHT [169] line intensities in the infrared has been carried out by comparing absorption cross sections calculated from the ABG-IMRHT line list and HITRAN2020 against the measurements from PNNL [178]. The ν_2 fundamental band at 590 cm^{-1} of ABG-IMRHT is approximately 8% stronger than in HITRAN2020, but this change has improved the residual for this region. Similarly, the increased intensity for the 10^00-01^10 band (near 695 cm^{-1}) and ν_1 fundamental band near 1280 cm^{-1} demonstrates an improved agreement with PNNL. While the 10^00-01^10 band is relatively weak compared to the fundamental bands, the PNNL measurements have sufficient signal-to-noise ratio to demonstrate these improvements. There are a number of weak bands in HITRAN2020 with intensities provided by Toth [151], which differ from the ABG-IMRHT intensities by approximately a factor of two (see Section 3.3.8 of Huang et al. [169]). The updated intensities have been used for HITRAN2024, but they are below (or close to) the experimental detection limit in PNNL (and Toth [151]) and would benefit from further analyses to confirm the updated intensities provided for HITRAN2024.

For some N_2O bands, the line intensities in HITRAN2020 agree better with the PNNL measurements than the ABG-IMRHT intensities. Therefore, the ABG-IMRHT intensities have been scaled accordingly to retain the rotational structure. Most notably, the intensity of the ν_3 fundamental (the strongest band) needed to be scaled down by 2% to match HITRAN2020, and the $2\nu_3$ and $3\nu_3$ bands required a scaling up by 10%.

The 42^00-00^00 and 50^00-00^00 bands near 1.6 μm are below the PNNL noise limit, but were measured by Adkins et al. [174] using cavity ring-down spectroscopy [174] with measurement uncertainties of approximately 1%. The line positions and intensities from Adkins et al. [174] were included in HITRAN2020. For HITRAN2024, the ABG-IMRHT intensities included a scaling of the theoretical intensities by 1/1.011 and 1/1.018, for the 42^00-00^00 and 50^00-00^00 bands respectively, and replace the intensities from Adkins et al. [174].

Line intensities from Huang et al. [169] agree favorably when compared to experimental measurements in the 9800–12 000 cm^{-1} region covering the 10^04-$00^00, 30^03$-$00^00, 14^03$-$00^00, 10^05$-00^00, and 60^02-00^00 bands [157–159,179]. However, experimental measurements of band intensities beyond 10 000 cm^{-1} are still limited, with the strongest band in this region ($5\nu_3$ near 10 815 cm^{-1}) not included in recent works. As a consequence, the related effective dipole models (EDM) have caused a rapid decline and disappearance of intensity above 10 000 cm^{-1} and less reliable prediction for some bands above 9000 cm^{-1} [170,173]. Daumont et al. [179] provide an overview of the N_2O spectrum covering the 8800–11 000 cm^{-1} region, with a number of bands identified. The intensities provided by ABG-IMRHT appear in approximate agreement with those observed bands, whereas the NOSL-296 line list suggests additional bands should be observed within this region. For example, the 06^03-00^00 band at 9955 cm^{-1} has a similar intensity to the 10^04-00^00 band at 9888 cm^{-1} in NOSL-296, but is not apparent in the spectrum of Daumont et al. [179]. In ABG-IMRHT, the 06^03-00^00 band is significantly weaker than the 10^04-00^00 band, which was shown to have good agreement with experiment. Further intensity measurements of N_2O bands in this region and beyond 10 000 cm^{-1} are desirable to provide additional insight into the accuracy of the calculated intensities, and to upgrade the effective dipole models for the NIR region.

Note that the vibrational assignments for N_2O bands may vary between ABG-IMRHT and other line lists or EH models due to the strong polyad resonances and the complicated state mixing at high energies. This is well known and has been verified in the NOSL-296 [160] EH model and MARVEL analysis [161] (for the primary isotopologue $^{14}N_2{}^{16}O$), other datasets and EH models from IAO, and variational program calculations for all isotopologues. Band comparison across isotopologues or against future studies should use caution on the consistency of vibrational assignments, and use IR intensity as a guide in addition to strict matches on lower-state energy, J, and symmetries. For most ABG-IMRHT bands in HITRAN2024 that are also present in HITRAN2020, their vibrational assignments have been synchronized to HITRAN2020, e.g., 42^00 and 50^00 states of $^{14}N_2{}^{16}O$.

Note that we have also carried out comparisons with the recent TYM line list (Yurchenko et al. [173]) line list for the principal isotopologue. The residuals in the PNNL comparisons with TYM were larger than those with ABG-IMRHT. Therefore, the TYM line list was not used for HITRAN2024.

2.4.3. Isotopologues

For HITRAN2024, only the most abundant isotopologues (e.g. $^{14}N_2{}^{16}O$, $^{14}N^{15}N^{16}O$, $^{15}N^{14}N^{16}O$, $^{14}N_2{}^{18}O$, and $^{14}N_2{}^{17}O$) from Huang et al. [169] have been used to update the line parameters for the five existing isotopologues in HITRAN. In HITRAN2020 [17], the $^{14}N_2{}^{18}O$ line list presented a more extensive spectral and intensity coverage than other isotopologues (including $^{14}N_2{}^{16}O$). This rather unusual feature has been adjusted for HITRAN2024, so that transitions of all isotopologues are provided with an intensity threshold of 1×10^{-28} cm/molecule. A comparison of the HITRAN2024 to HITRAN2020 is presented in Fig. 6.

Additional minor isotopologues of N_2O have not been included in HITRAN at this time.

2.4.4. Line shapes

The broadening parameters for the Voigt and SDV line shapes for air- and self-broadening from Hashemi et al. [27] have been applied to all additional lines of N_2O. In addition, the H_2O-broadening parameters from Tan et al. [28] and the He- and CO_2-broadening from Tan et al. [30] have been included for newly added lines of N_2O for HITRAN2024.

2.4.5. Future work

Four isotopologues of N_2O, including $^{15}N_2{}^{16}O$ (not currently in HITRAN), have recently been compared to frequency comb measurements in the 3300–3550 cm^{-1} region [180]. This spectral range contains the $\nu_1 + \nu_3$ band of $^{15}N_2{}^{16}O$, where line positions from previous Ames-296K line list [170] were shown to exhibit 740 MHz (or −0.025 cm^{-1}) deviations from experiment. The updated B1b PES reduced the deviations to 0.002 cm^{-1}. The ABG-IMRHT line list adopted experiment/IAO-based line positions for $^{15}N_2{}^{16}O$, among all other minor isotopologues, and provides an improved accuracy, $6(\pm 4) \times 10^{-4}$ cm^{-1} for this band. It is comparable to the effective Hamiltonian model of Tashkun et al. [181], which was also included in the comparisons of Hjältén et al. [180]. Further validations on minor isotopologues are recommended for both line positions and line intensities, so that the $^{15}N_2{}^{16}O$ and other less

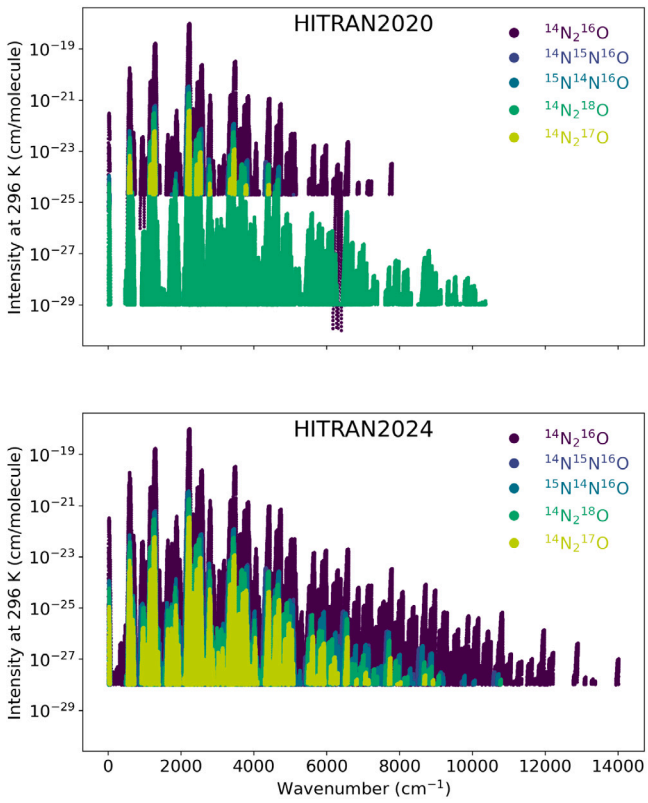

Fig. 6. Spectral coverage of isotopologues of N_2O included in the HITRAN2024 line list compared to HITRAN2020.

abundant isotopologues can be considered for addition to HITRAN in future updates.

N_2O was added to HITEMP in Hargreaves et al. [182] based primarily on the Nitrous Oxide Spectroscopic Databank at 1000 K (NOSD-1000) line list [183] in combination with the HITRAN2016 edition [16]. A number of bands are absent in the HITEMP line list in the NIR because they were not present in HITRAN2016 or NOSL-1000. In addition, there were also some small inconsistencies due to merging the two line lists. There are now sufficient new works to revisit the N_2O HITEMP line list and update with suitable high-temperature line lists such as the Ames-2000K [169] and possibly TYM line list [173].

2.5. CO: Carbon monoxide (molecule 5)

Gaseous carbon monoxide (CO) is a prominent pollutant in the troposphere of Earth. It is produced by natural (including vegetation emissions and biomass burning) and anthropogenic (e.g., automobile exhausts and waste burning) sources [184]. It is routinely monitored using different spectrometers onboard remote-sensing satellites, including ACE [185], IASI [186], TROPOMI [187], and GOSAT-2 [188]. Transitions of CO have been observed in the atmospheres of Mars [189] and Venus [190] and are now identified in exoplanets using the cross-correlation method from on-ground telescopes (see, for instance [191]) or JWST spectra, which even allow identification of isotopologues [192].

Before describing the updates in this edition, it is important to recap what is included for this molecule in the HITRAN2020 edition. The line positions and intensities for all six stable and three radioactive isotopologues were based on the line list calculated by Li et al. [193]. In that work, the semi-empirical dipole moment function (DMF) was derived based on *ab initio* calculations and all validated experimental works available at the time. This DMF was used together with the empirical potential energy function from Coxon and Hajigeorgiou [194] to calculate the line list. In HITRAN2016, this line list was supplemented with new line position measurements where available, while in HITRAN2020, an additional change was implemented for the intensities of the bands with $\Delta v = 1$ which were scaled down by 2% to agree better with the measurements of the lines of the principal isotopologue of CO in the fundamental band reported by Devi et al. [195]. In addition, intensities in the bands with $\Delta v = 3$ were increased by 2.6% to agree with accurate measurements [196] in the second overtone (3–0) band.

Since the release of the Li et al. [193] line list, many new high-quality experiments and new *ab initio* calculations have been carried out. Moreover, better physical representations (with correct asymptotic behavior) of the potential energy function (PEF) [197] and DMF have been derived [198–200] and used to carry out new semi-empirical fits. From an experimental view, there was a recent high-precision (0.6% relative uncertainty) cavity ring-down measurement of the R(17) transition in the fundamental band [201], and coordinated, international efforts targeting accurate intensity measurements in the second overtone band [202,203]. The latter study involves several independent techniques, including Fourier-transform, cavity ring-down, cavity mode-dispersion, and tunable diode laser spectroscopy. The experiments employ metrology-grade measurements of optical frequency, path length, absorption coefficient, temperature, pressure, absorber concentration, and isotopologue composition, combined with advanced line-shape analysis methods to yield integrated spectral areas and line intensities with relative combined uncertainties at the permille level or below. The semi-empirical fitted DMFs of Meshkov et al. (2022,2024) [198,200] and Medvedev and Ushakov (2022) [199] were obtained with the regular and irregular (i.e. containing branch points in the complex plane of the internuclear distance) dipole-moment functions having correct behavior in the $r \to 0$ and $r \to \infty$ asymptotic limits; the calculated intensities differ very slightly in the ranges covered by experimental data. Recognizing the advantages and limitations of the new experimental, theoretical, and semi-empirical data, the following improvements have been introduced to the HITRAN2024 edition.

1. The line positions for all bands of all isotopologues were calculated using the Meshkov et al. [197] PEF, which was fit using all new and best experimental data and a physical functional form. The results agree well with the original experimental data. The recent MARVEL study on $^{12}C^{16}O$ [204] also found that the line positions of Meshkov et al. [198] (used for HITRAN2024) agreed better with the MARVEL values than those in HITRAN2020 which originated from Coxon and Hajigeorgiou [194].
2. The intensities of all $\Delta v = 1$ lines for all isotopologues have been reverted to those from Li et al. [193]. This was prompted by two independent, high-quality experiments from NIST [201] and PTB in the fundamental (1–0) band [205]. These experiments are in good agreement (relative standard deviation of 0.4%) with Li et al. [193], therefore casting doubt on the scaling carried out for HITRAN2020 based on measurements reported in Devi et al. [195]. The new line lists from Meshkov et al. [198] and Medvedev and Ushakov [199] employ values from Ref. [195] in the fit and therefore have similar issues as HITRAN2020. Therefore, the values from Li et al. [193] have been restored in the database based on new experimental results by Bailey et al. [201] and Li et al. [205].
3. The first overtone band causes the least number of intensity controversies, as all best experiments and *ab initio* calculations agree with each other within 0.5%. The $\Delta v = 2$ intensities for all isotopologues in HITRAN2024 are taken from Meshkov et al. [198], which anchors to DLR the high-quality experimental data from [206]. The resultant intensities are only slightly different from HITRAN2020, but agree marginally better with the experiment.

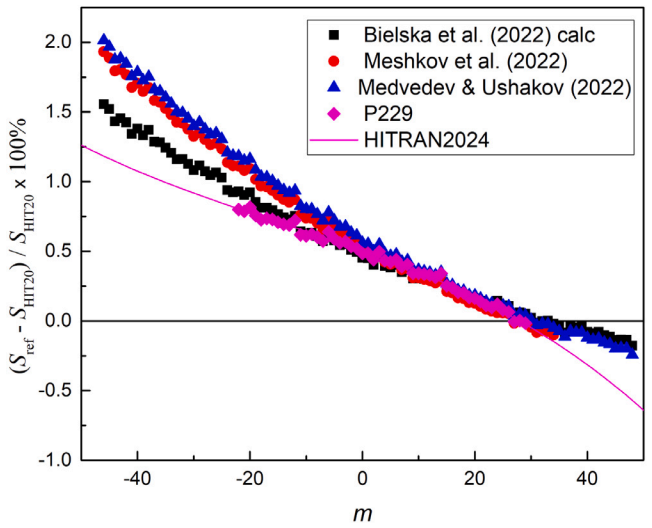

Fig. 7. Differences between the calculated intensities in the 3–0 band reported by Meshkov et al. [198], Medvedev and Ushakov [199], Bielska et al. [202], measured (P229) in Hodges et al. [203], and those from HITRAN2020. The values in HITRAN2024 are fitted to the differences between measurements from Ref. [203] and HITRAN2020.

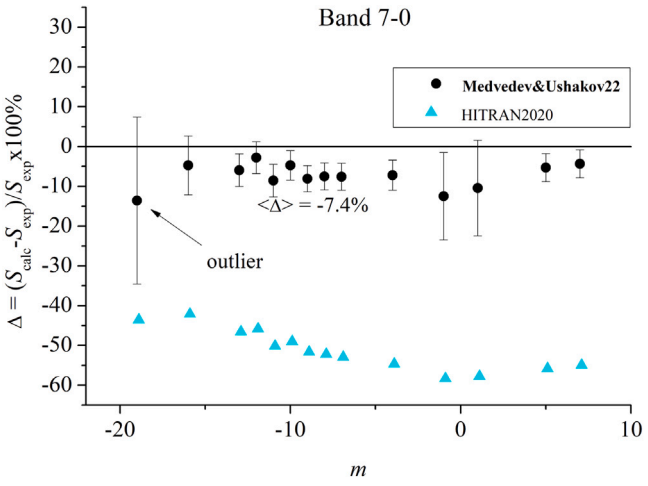

Fig. 8. Differences between the intensities measured by Balashov et al. [212], those calculated by Medvedev and Ushakov [199] (circles) and those from HITRAN2020 (triangles). $\langle\Delta\rangle$ is the average relative difference (in %) between the calculated and experimental intensities. It is calculated without accounting for the outlier at $m = -19$.

4. As already mentioned, in HITRAN2020 the Li et al. [193] intensities of the $\Delta v = 3$ transitions were scaled to agree better with recent experiments, but no fit to the new data was carried out. As a result, the intensities did not improve uniformly throughout the band as Li et al. [193] intensities relied heavily on values of relatively high-J transitions from Ref. [207], which turned out to be less accurate than originally reported. Fortunately, there is enough theoretical and experimental data to remedy the situation. The second overtone (3–0 band) has received a lot of scrutiny in the last few years, with a coordinated [202, 203] international campaign of accurate and complementary measurements in six different laboratories around the globe. These experiments, spearheaded by NIST, have been effectively summarized by Hodges et al. [203] where a recommended set of intensity values was presented based on weighted combined uncertainty analyses of the data. Fig. 7 shows recent semi-empirical works [198,199], *ab initio* calculations presented in Ref. [202] and experimentally-derived values from Hodges et al. [203]. For HITRAN2024, the fitted third-order polynomial function was applied to HITRAN2020 intensities in this band to match the values reported in Ref. [203].
5. The $\Delta v = 4$ band intensities for all isotopologues were adapted from Ref. [198], which had the best experimental data as input (notably recent experiments by Bordet et al. [208]).
6. The $\Delta v = 5$ bands exhibit the so-called vibrational anomaly[2] having "abnormally" low intensity and, as a consequence, being highly sensitive to the dipole-moment function [199], with different *ab initio* calculations producing very different results. The only experimental measurements that have been carried out in the 5-0 band are at very high pressure (about 5 bar) and with a relatively low signal-to-noise ratio [210]. These experimental data were used in the fit of Meshkov et al. [198], and the intensities calculated there are used for all $\Delta v = 5$ bands. As emphasized in Meshkov et al. [198], it would be important to carry out new measurements in this band.
7. The $\Delta v = 6$ band intensities for all isotopologues come from Ref. [198], which used the accurate experimental data from Tan et al. [211] in the fit.
8. The $\Delta v = 7$ band intensities from Li et al. [193] (and so are those in Medvedev and Ushakov [199]) are largely based on the *ab initio* calculations as no experimental data existed at the time. Very recently, Balashov et al. [212] were able to measure the intensities in the sixth overtone using a sensitive cavity-ring down spectroscopy technique. Fig. 8 shows the difference between the measurements from Ref. [212] and predictions from both Ref. [199] and HITRAN2020. Based on this comparison, the intensities from Ref. [199] for all $\Delta v = 7$ bands of all isotopologues were increased by 7.4% and included in HITRAN2024.
9. In HITRAN2020, the line-shape parameters from Hashemi et al. [27] were used for air- and self-broadening parameters and their temperature dependencies for both Voigt and SDV profiles. In HITRAN2024 these parameters have been retained, but in the near future the shifts will be updated based on the new fit carried out in Ref. [213]. Just as in HITRAN2020, the broadening of lines by the pressure of H_2, He, and CO_2 is based on values calculated from the functions obtained in Tan et al. [30].

From the description of the changes above, one can note that the intensities of pure rotational bands have not been changed, as they agree very well with recent measurements by Tretyakov et al. [214].

Meshkov et al. [198] have addressed in detail the issue regarding the isotopologue intensities, which was brought up in some of the experimental studies and summarized in Ref. [215]. These studies reported potential inconsistencies between experimental intensities of isotopologues and their values calculated based on the DMF fitted to the principal isotopologue data. Meshkov et al. [198] have shown that these inconsistencies arise from the isotopic abundance in experimental spectra being different from the abundances assumed in HITRAN.

The work on additional measurements and new *ab initio* calculations is ongoing. In the near future, a semi-empirical dipole moment fit will be carried out. It will be similar to those carried out in Refs. [193,198, 200] but with all the latest experimental data.

Recently, Ushakov and Medvedev [216] have performed such a fit with irregular DMF [199]. They found that this fitted function together with the PEF of Meshkov et al. [197] provided excellent agreement

[2] This anomaly in the 5–0 band was predicted by Medvedev in 1985 [209] and observed by Chung et al. [210] in 2005.

Table 4
Methane line lists used for the HITRAN2024 update.

Linelist	Range (cm^{-1})	Linelist	Range (cm^{-1})
Nikitin *et al.*, 2025 [217]	900–1050	Starikova *et al.*, 2024 [222]	4970–5300
ExoMol [228]	0–12 000	Birk *et al.* [229], Reed *et al.* [230], Yin *et al.*[231] 2025	5970–6250
MeCaSDa [219]	3–6620	Ben Fathallah *et al.*, 2024 [223]	6204–6394
Sung *et al.*, 2024 [232]	4000–4700	Malarich *et al.*, 2021 [224]	6770–7570
Nikitin *et al.*, 2013 [220]	4300–4550	Nikitin *et al.*, 2024 [225]	7606–7919
Rodina *et al.*, 2021 [221]	4100–4300	Campargue *et al.*, 2023 [226]	10 802–13 922
atm.161 [233]	0–11 320		

with the recent measurements, sometimes even those not included in the fitting. These results, along with other new data, will be considered for future updates.

2.6. CH_4: Methane (molecule 6)

The importance of accuracy and completeness of methane spectroscopy is challenged by its notorious complexity. Every edition of HITRAN features major updates; however, the challenge to reach sub-percent uncertainties on modeled cross-sections across many spectral regions remains. For HITRAN2024, more than 58 000 new lines of $^{12}CH_4$,$^{13}CH_4$,$^{12}CH_3D$, and $^{13}CH_3D$ were added to the database from 14 different experimental, theoretical and semi-empirical sources [217–226] (Table 4). This increases the maximum transition wavenumber from 12 000 cm^{-1} to 14 000 cm^{-1}. The extension of the spectral region is especially important for planetary applications, where researchers still use the so-called Karkoshka spectrum [227] based on planetary measurements rather than laboratory or theoretical spectra. In addition, for 40 000 transitions from HITRAN2020, spectral parameters and/or quantum assignments were updated using these line lists.

The most notable updates from the perspective of atmospheric retrievals are those in the pentad (around 3.3 μm), octad (~4.3 μm), and tetradecad (~1.66 μm) regions. These bands are important not only for methane retrievals but also to be able to detect trace species "hiding" underneath strong CH_4 bands. It is important to mention that speed-dependent Voigt parameters for air broadening are now provided for many lines in the tetradecad region. In this context, it is important to address some of the existing controversies regarding the tetradecad region. Many remote sensing experiments have concluded that using HITRAN2008 in that region was better than subsequent versions of HITRAN. It is important to stress that the reason for that is that the HITRAN2008 parameters were provided to compensate for non-Voigt effects and line mixing at higher pressures. Fig. 9 compares a high-quality laboratory spectrum at very low pressure with spectra generated using HITRAN2008, HITRAN2020, and HITRAN2024 under the same thermodynamic conditions. It is clear that at low pressure, the HITRAN2008 produces the worst residuals, and HITRAN2024 parameters result in the lowest residuals by far. It is interesting to see the differences between databases at higher pressures. Fig. 10 shows a comparison with experiments carried out at the higher pressures, zooming on the R(6) manifold, which is of particular interest for atmospheric missions. At higher pressures, non-Voigt effects incorporated in HITRAN2024 become important. One can see that at 198 Torr, HITRAN2008 produces residuals similar to HITRAN2020, but worse in comparison with speed-dependent Voigt calculations with HITRAN2024. At 399 Torr, HITRAN2008 appears to produce much better results than HITRAN2020, confirming the controversy of parameters in 2008 editions absorbing correlations of different line-shape parameters. Importantly, the non-Voigt effects parametrized in HITRAN2024 result in the smallest residuals and should be used in remote sensing.

The pressure-induced parameters were updated separately when new data were not provided with the lists. Using air- and N_2-pressure measurements and calculations [234–237], Padé-approximant functions were fit for each symmetry, replacing the Voigt broadening parameter of the newly added lines, and those that were found to be outside their physical boundaries. The air-induced shifts were replaced with the same function used in HITRAN2012 [238]. For CH_3D, the broadenings and shifts use the values calculated from Ref. [239], with the shift rescaled to account for vibrational dependence.

The details of the updates are provided in the overview article [240].

2.7. O_2: Molecular oxygen (molecule 7)

Molecular oxygen (O_2) is the second most abundant molecular species in our atmosphere. Because it is well-mixed and has a uniform (on a dry gas basis) fractional amount of approximately 21%, O_2 plays an important role in various remote sensing and satellite spectroscopic measurement applications. HITRAN includes O_2 magnetic dipole and electric quadrupole transitions involving the $X^3\Sigma_g^-$ (X) ground state and the $a^1\Delta_g$ (a), $b^1\Sigma_g^+$ (b), $B^3\Sigma_u^-$ (B), $A^3\Delta_u^+$ (A), $c^1\Sigma_u^-$ (c) and $A'\ ^3\Delta_u$ (A') excited electronic states. The addition of 1148 electric quadrupole lines in HITRAN2024 for wavenumbers less than 6300 cm^{-1} increased the number of transitions within the ground-state by about 50% [241]. In the wavenumber region from 5000 cm^{-1} to 18 000 cm^{-1}, HITRAN2024 includes twelve visible and near-infrared atmospheric bands of O_2. These data include four bands involving $a(v') - X(v'')$ $(v' = 0,1; v'' = 0,1)$, seven bands $b(v) - X(v)$ with $(v' = 0,1,2,3; v'' = 0,1)$, and the so-called Noxon band $(b(0) \rightarrow a(0))$, which is included for the first time in HITRAN 2024. Note that only electric quadrupole transitions are allowed in the Noxon band, and under terrestrial conditions, they can only be observed in emission due to photodissociation of ozone in the stratosphere that produces molecular oxygen in the b electronic states. Subsequent emission from b to the a states is then observed. Since thermal population of the a state on Earth is not possible, the HITRAN intensities (that assume local thermal equilibrium) of the corresponding lines are orders of magnitude weaker than the rest of the line list for molecular oxygen. Updates to line positions and line shape parameters are provided for the 1.27 μm $(a(0) - X(0))$ and B- $(b(1) - X(0))$ bands, while the primary update to the A-band $(b(0) - X(0))$ is for the line intensities. Finally, in the region above 33 000 cm^{-1}, HITRAN includes the Schumann-Runge bands $B(v)-X(v)$ for $(v' = 0,1..19; v'' = 0,1,2)$ and three Herzberg bands in the 240 nm to 300 nm region corresponding to [Herzberg I] $A(v')-X(0)$ for $(v' = 0..12)$, [Herzberg III] $A(v) - X(0)$ both $(v' = 2..12)$, and [Herzberg II] $c(v') - X(0)$ for $(v' = 2..19)$ [242]. HITRAN2024 includes updates to the Schumann-Runge bands to correct self broadened half-widths and treatment of the predissociative transitions.

The substantial updates to the HITRAN2024 O_2 line list are summarized in Table 5 and described in detail in Ref. [243].

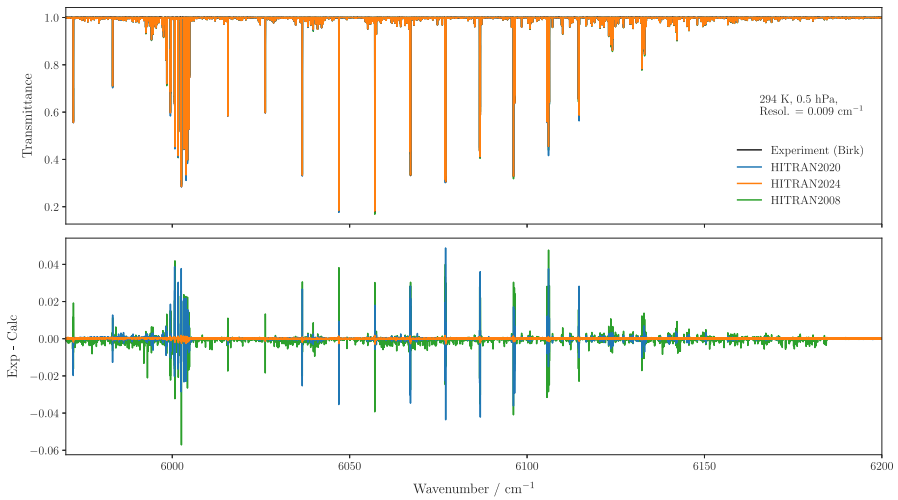

Fig. 9. Residuals obtained at 294 K and 0.5 hPa (low pressure) between the experiment from Ref. [229] and Voigt calculations from different versions of HITRAN.

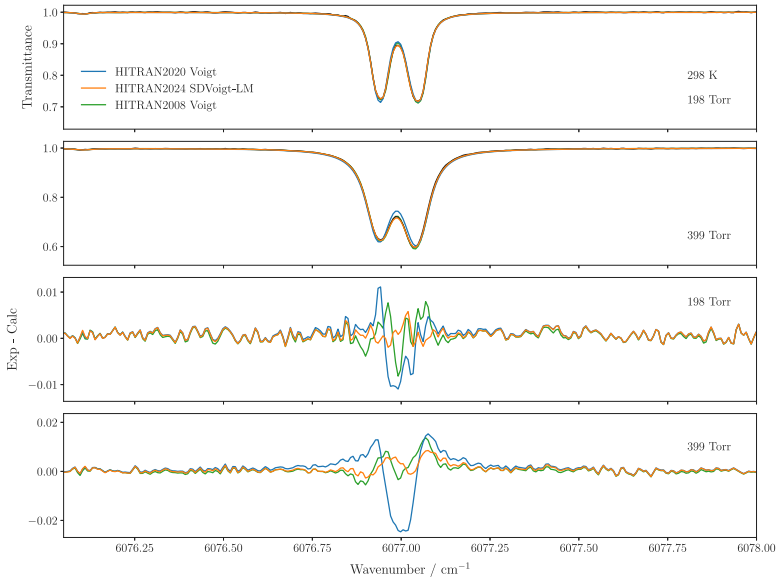

Fig. 10. Calculations using different versions of HITRAN compared to the FTS transmission spectrum of CH_4 in the R(6) manifold in tetradecad region at P = 198 and 399 Torr, T = 297.9 K, and X_{CH_4} = 0.01 (for a CH_4-air mixture) measured at Kitt Peak National Solar Observatory (NSO).

Although the parameters for the pure rotational magnetic dipole lines were not updated in this edition, the uncertainties for the intensities of these transitions were reduced based on recommendations from Refs. [253,254].

2.8. NO: Nitric oxide (molecule 8)

Unchanged.

2.9. SO_2: Sulfur dioxide (molecule 9)

Unchanged.

2.10. NO_2: Nitrogen dioxide (molecule 10)

Tropospheric NO_2 (a product of primarily biomass burning and soil emissions) is a major air pollutant detrimental to human health [255]; therefore, concentrations are routinely monitored [128]. The nitrogen dioxide line list ($^{14}N^{16}O_2$, $^{15}N^{16}O_2$ and $^{16}O^{14}N^{18}O$, the latter isotopologue added for the first time) present in the HITRAN2024 database covers the 0–7978 cm^{-1} spectral region and its description is provided below.

2.10.1. The $^{14}N^{16}O_2$ isotopic species

For the $^{14}NO_2$ line list in HITRAN2020 [17], several $^{14}NO_2$ bands were added to the previous edition [16] covering the 1934–7878 cm^{-1} spectral range. This was possible through simultaneous work on the introduction of NO_2 to the HITEMP database [182], which was largely based on Ref. [256]. However, one has to keep in mind that the overall set of NO_2 parameters was generated during numerous studies, carried out at different times and with differing accuracies [257]. One consequence of the complex and long history of NO_2 studies contributing to HITRAN is that the quality of these parameters is not uniform across the bands. As a result, some inconsistencies exist for line positions and line intensities. For example, in HITRAN2020 or HITEMP, the energies of the same rovibrational levels are not always consistent from one given band to another, as they originate from different sources. This is most apparent for NO_2 levels involving the (0,1,0) vibrational state.

Here we describe the HITRAN2024 line list for $^{14}NO_2$, which includes the addition and update for a number of bands in the 1153–4776

Table 5
Summary of O_2 Updates included in HITRAN2024 and summarized in Ref. [243].

Band Name	Transitions	HITRAN 2024 Updates[a]
pure-rotational fundamental overtones hot bands	$X(0)-X(0)$ $X(1)-X(0)$ $X(2,3,4)-X(0)$ $X(2,3)-X(1)$	addition of 1148 electric quadrupole transitions [241]
Noxon Band	$b(0) \rightarrow a(0)$[b]	Addition of band [243]
1.27 μm band	$a(0)-X(0)$	Line positions [244] $\Phi_{air}^{HTP}(x,T)$ [245,246]
A-band	$b(0)-X(0)$	Line intensities [247] correction to $\Phi_{air}^{VP}(x,T)$ and $\Phi_{air}^{HTP}(x,T)$ [123,243]
B-band	$b(1)-X(0)$	Line positions [248] $\Phi_{self}^{HTP}(x)$ [248–250] $\Phi_{air}^{HTP}(x,T)$ [251] and $\Phi_{air}^{VP}(x,T)$ [243,251]
Schumann-Runge bands	$B(0-19)-X(0,1,2)$	Correction to $\gamma_{0,self}$ [252] Supplementary code to treat predissociative transitions

[a] $\Phi_{air}^{HTP}(x,n)$ and $\Phi_{self}^{HTP}(x,n)$ indicate the air- and self- broadening parameters (x) and temperature dependencies (n) for Hartmann-Tran limiting case profiles beyond the Voigt profile, where $\Phi_{air}^{VP}(x,n)$ and $\Phi_{self}^{VP}(x,n)$ indicate the Voigt profile parameters and temperature dependencies.

[b] The right arrow highlights that under terrestrial conditions, this band can only be observed in emission.

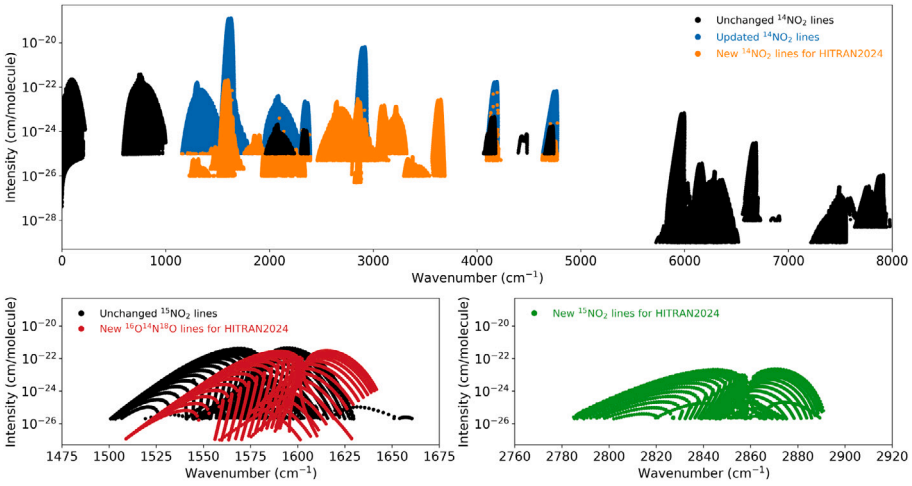

Fig. 11. Overview of the HITRAN2024 line list of NO_2 at 296 K. The upper panel presents the $^{14}NO_2$ lines, highlighting those bands that were unchanged or updated from HITRAN2020 along with the new additions for HITRAN2024. The lower panels show the minor isotopologues, with the lower left panel displaying the unchanged ν_3 band of $^{15}NO_2$ alongside the newly added ν_3 band of $^{16}O^{14}N^{18}O$. The lower right panel shows the newly added bands of $^{15}NO_2$ near 3.4 μm.

cm^{-1} spectral region. In the absence of recent spectroscopic studies in the microwave to far infrared region, the NO_2 lines in the low frequency range (ν < 1153 cm^{-1}) remain unchanged in HITRAN2024, while the high frequency range (ν > 4775.31 cm^{-1}) was also unchanged for HITRAN2024.

The bands included for this update are described in Table 4 of Perrin et al. [258], and the parameters were generated using existing literature data [259–262] or from empirical data extracted from high resolution Fourier transform spectra recorded at SOLEIL [258,263] for the purpose of this study.

For the $^{14}N^{16}O_2$ main isotopic species, the 6.2 μm and 3.4 μm spectral regions correspond to the strongest absorption bands. The most significant updates concern the improvement of the hot bands, $\nu_2+\nu_3-\nu_2$ and $\nu_1+\nu_2+\nu_3-\nu_2$, together with the inclusion, whenever possible, of higher-order hot bands (involving the (1,0,0), (0,2,0) and (0,0,1), (1,1,0), (2,0,0) or (0,0,2) states as lower states). Also, the $\nu_1+\nu_3$ line list was improved at high rotational quantum numbers. In addition, several weak cold bands in the 2.2 to 4.9 μm region were added for the first time. An overview of the $^{14}N^{16}O_2$ line list for HITRAN2024 is provided in the upper panel of Fig. 11.

2.10.2. The $^{15}N^{16}O_2$ isotopic species

For the $^{15}NO_2$ isotopologue, the $\nu_1+\nu_3$ and $\nu_1+2\nu_2$ bands near 3.4 μm [264] have been included for HITRAN2024. This is in addition to the previously existing ν_3 band at 6.2 μm [17,265], as shown in Fig. 11.

2.10.3. Addition of $^{16}O^{14}N^{18}O$

In the HITRAN2020 edition of the database, the $^{15}NO_2$ isotopologue was added for the first time. This was made possible thanks to the line list and the first interpretation of atmospheric results reported by Perrin et al. [265]. Although in HITRAN2020 the $^{15}NO_2$ isotopologue was given a local isotopologue ID, iso = 2, it was out of the common HITRAN convention where isotopologues are ordered in the order of descending abundance within the molecule. In fact, the $^{16}O^{14}N^{18}O$ isotopologue is slightly more abundant (0.00397 vs 0.00365 for $^{15}NO_2$). Nevertheless, since many codes already treat the $^{15}NO_2$ as the second isotopologue, it will be kept that way, and the $^{16}O^{14}N^{18}O$ will be added with local ID iso = 3.

As is the case for the other isotopologues of nitrogen dioxide, the ν_3 band of $^{16}O^{14}N^{18}O$ is the strongest and it is centered at 1603 cm^{-1}. Naturally, this band becomes the first band of this isotopologue to be

included in HITRAN and is shown in the lower left panel of Fig. 11. As explained in Ref. [266] the line positions and intensities were generated from the analysis of laboratory Fourier transform spectroscopy spectra of the mixture of gases originating from the oxidation and isotope exchange reactions of the two gases $^{18}O_2/^{14}N^{16}O$ (1:2). The $^{16}O^{14}N^{18}O$ data included for HITRAN2024 contain 9623 transitions between 1508.92 and 1641.69 cm^{-1}. These transitions have a maximum intensity of 3.13×10^{-22} cm/molecule at 296 K, with $N_{max} = 61$ and K_a between 0 and 15.

2.10.4. Lineshapes for NO_2

For inclusion to HITRAN, the γ_{air} parameters are based on the polynomial expressions developed in Benner et al. [267]. To avoid over-extrapolation of these functions, lines with $m > 40$ have γ_{air} equal to the value at $m = 40$ for each K_a. The n_{air} and δ_{self} parameters are determined by matching rotation quanta to broadening parameters calculated for NO_2 during the update of HITEMP [182]; if no match in quantum number was found, then the parameters added in Perrin et al. [258] were used (based on Benner et al. [267]). The air-pressure shifts (δ_{air}) are based on measurements of the ν_3 band of $^{14}NO_2$ [267], which have been applied to all other bands following the method described in [182] for NO_2.

2.10.5. Comparisons to PNNL

The validation of this updated NO_2 line list in the 1153–4776 cm^{-1} spectral region was achieved by detailed comparison at 296 K between computed and observed high-resolution Fourier transform laboratory spectra. This database was used to compute cross sections that were compared, as another validation process, with the PNNL data [178]. Also, the consistency of the upper- and lower-state energy level calculations was carefully checked, from one vibrational-rotational band to another.

Similar intercomparisons between high- and medium-resolution experimental spectra, as well as critical checks of the internal consistency of energy levels, were performed using the HITRAN2020 and HITEMP databases.

Fig. 12 provides an overview, in terms of computed cross sections of the NO_2 line list. In addition, a comparison with the HITRAN2020 [17] and HITEMP [182] databases and with the PNNL cross sections [178] is also provided for the region that has been updated for HITRAN2024. At a temperature of 296 K, this HITRAN2024 list provides a significant improvement when compared to HITRAN2020 or HITEMP in the 1153–4776 cm^{-1} spectral region.

2.11. NH_3: Ammonia (molecule 11)

In the terrestrial atmosphere, ammonia is considered a pollutant, mostly arising from agricultural and industrial practices. It is typically monitored through ground-based *in situ* measurements [268] or satellite-based remote sensing retrievals [269,270]. In addition, ammonia is a trace constituent of gas giant planets and is used as a tracer to interpret the atmospheric structure of Jupiter [271]. It has also been observed in brown dwarf spectra [272], and is considered detectable in exoplanet atmospheres [273,274].

The ammonia line list in HITRAN2020 [17] contained a series of improvements compared to HITRAN2016. However, there was a lack of completeness for some regions of the mid-IR due to missing hot bands (particularly in the 3750–5500 cm^{-1} range). In addition, the $^{15}NH_3$ list of HITRAN2020 contained only 126 transitions above 3100 cm^{-1} related to the $\nu_3 + \nu_4$ band centered near 5041 cm^{-1} [275]. For HITRAN2024, these issues have been addressed, and the line list has been extended further into the NIR.

2.11.1. The 3900–6350 cm^{-1} region

In Fig. 13, the overview of the update of the ammonia list in the 3900–6350 cm^{-1} region is compared to the previous HITRAN2020 list [17]. Below 5300 cm^{-1}, the HITRAN2020 list included the data of the preceding HITRAN2016 list (black circles on the lower panel, from Urban et al. [276] and Brown and Margolis [275]) together with calculated $^{14}NH_3$ transitions added when both their upper- and lower-state energies were known from experiment. This approach led to an unusual appearance of the line list below 5300 cm^{-1} with the inclusion of many hot band transitions with intensities as low as 10^{-25} cm/molecule, while the intensity threshold of the cold bands observed in this region is more than two orders of magnitude higher. Above 5300 cm^{-1}, the HITRAN2020 list relied on analysis of a Kitt Peak spectrum [277]. A significant number of these transitions were provided with rovibrational assignments obtained by the joint use of a variational line list and Lower State Combination Difference (LSCD) relations.

All ammonia transitions in the 3900–6350 cm^{-1} interval have been updated for HITRAN2024, based on a series of spectra recorded at the Université Libre de Bruxelles (ULB). Analysis of $^{14}NH_3$ spectra was reported in three successive studies, covering the ranges 3900–4700 cm^{-1} [278], 4700–5650 cm^{-1} [279] and 5650–6350 cm^{-1} [280]. As illustrated in Fig. 13, the present update provides a substantial increase in $^{14}NH_3$ coverage compared to HITRAN2020. The rovibrational assignments have been considerably extended using position and intensity agreement with the C2018 theoretical line list [281], secured by systematic validations with LSCD relations.

Regarding the $^{15}NH_3$ species, using FTS spectra of ammonia highly enriched in $^{15}NH_3$ recorded at Kitt Peak and at ULB, a global empirical line list was built for the $^{15}NH_3$ species for the entire 3900–6350 cm^{-1} region [282]. By comparison with the BYTe *ab initio* line list [283] and systematically validating the assignments with LSCD relations, a large number of transitions could be assigned.

In Cacciani et al. [282], the $^{14}NH_3$ results of Refs. [278–280] were combined with the $^{15}NH_3$ data to provide a recommended line list for ammonia in natural abundance, which was adopted for the HITRAN2024 update. Overall, the line list includes 21 580 $^{14}NH_3$ transitions and 8813 $^{15}NH_3$ transitions (to be compared to 7521 and 126 in HITRAN2020) and the assigned transitions represent more than 99% of the total absorption in the region at room temperature. Note that compared to the line list provided in Cacciani et al. [282], minor corrections have been implemented: *(i)* the $^{15}NH_3$ assignments are now based on the very recent CoYuTe-15 list [284] rather than the BYTe2015 used in the original paper [283] and, *(ii)* some inaccuracies concerning $^{15}NH_3$ lower-state energies and intensities of neighboring $^{14}NH_3/^{15}NH_3$ transitions were updated using the same source [284].

Room-temperature FTS spectra have previously been recorded for ammonia that encompass the 2400–5500 cm^{-1} [285] and 4800–9000 cm^{-1} [286] regions. These measurements have been used to validate the line list from Cacciani et al. [282] between 3800–5400 cm^{-1} using Beale et al. [285] and 5650–6350 cm^{-1} using Beale et al. [286].

2.11.2. The 0.793 μm region

The $^{14}NH_3$ line list for HITRAN2024 has been extended further into the NIR region by incorporating the empirical list of Zobov et al. [287]. This list spans the 0.793 μm (12 491–12 810 cm^{-1}) region and was obtained by analysis of a series of Fourier transform spectra recorded at Brussels and Prague. In total, 1481 lines of ammonia were measured and have been added to HITRAN. Transitions have been attributed to vibrational states containing 4 stretching quanta (such that $\nu_1 + \nu_3 = 4$) and tentative assignments have been applied to 278 of these transitions. For unassigned lines, a constant $E'' = 333$ cm^{-1} has been applied for addition to HITRAN.

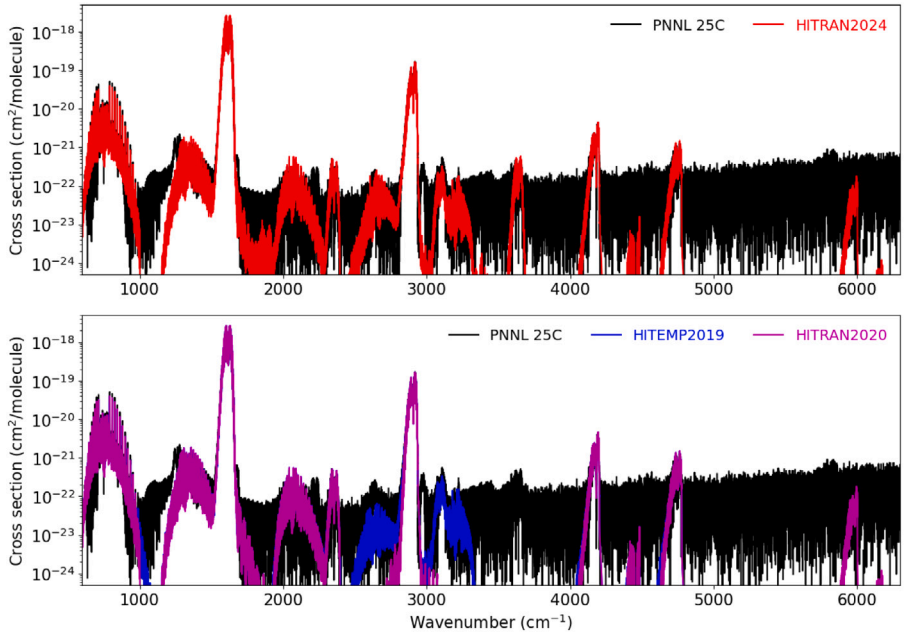

Fig. 12. Overview of cross sections computed for NO_2 using HITRAN2024, HITRAN2020 [17] and HITEMP2019 [182] line lists, compared with the PNNL experimental measurements [178]. The logarithmic intensity scale highlights the improved fit with HITRAN2024 for weak bands in the MIR. The broad black band shows the noise floor of the experimental measurement and appears large due to the many orders of magnitude covered by the intensity scale.

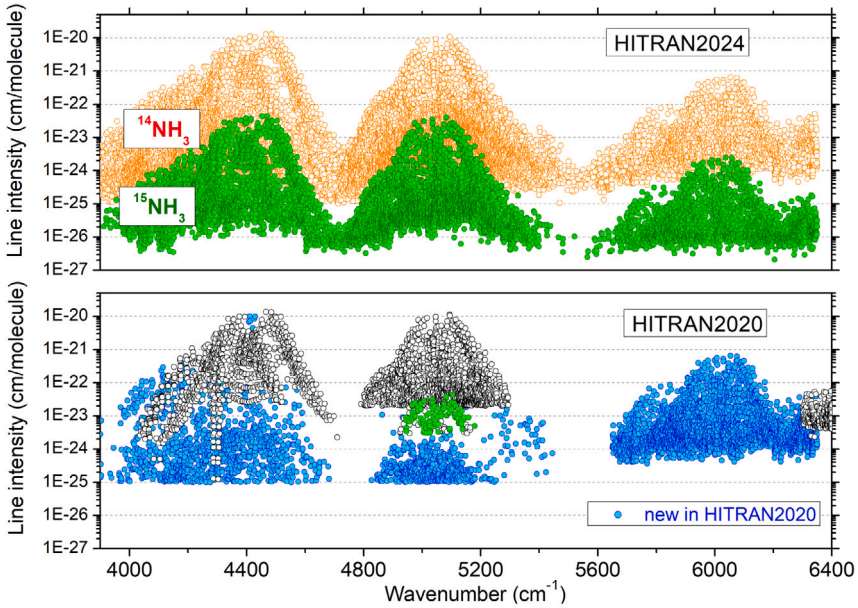

Fig. 13. Overview comparison of the HITRAN2024 and HITRAN2020 [17] line lists of ammonia between 3900 and 6350 cm^{-1}. For both panels, the green symbols correspond to the $^{15}NH_3$ isotopologue. In the upper panel, the $^{14}NH_3$ lines are shaded orange. In the lower panel, the $^{14}NH_3$ transitions that were newly added for HITRAN2020 are highlighted blue, while those from HITRAN2016 [16] - black. These include *(i) ab initio* transitions with empirically-adjusted positions below 5300 cm^{-1}, and *(ii)* lines above 5300 cm^{-1} from the analysis of a Kitt Peak spectrum [277].

2.11.3. $^{15}NH_3$ isotopologue

In addition to the $^{15}NH_3$ lines added to HITRAN for the 3900–6350 cm^{-1} region (described above), the MARVELized CoTuTe-15 line list for $^{15}NH_3$ [284] has been used to extend the $^{15}NH_3$ coverage in HITRAN by including transitions between 3100–3700 cm^{-1} and 6350–6900 cm^{-1} with intensities stronger than 10^{-26} cm/molecule.

2.11.4. Quantum number format, broadening, and future work

The quantum number format for $^{14}NH_3$ transitions was updated in HITRAN2012 (see Table 7 of Ref. [15]) following the recommendation of Down et al. [288] to allow a consistent set of unique assignments. This format was not adopted for $^{15}NH_3$ as analyses of transitions followed the previous format. Thus, both isotopologues used different quantum number notation in HITRAN2020 [17]. This has been addressed for HITRAN2024, with all $^{15}NH_3$ transitions from HITRAN2020 being updated to the assignments provided by Yurchenko et al. [284]. The newly added lines of $^{15}NH_3$ also follow this quantum number format.

In HITRAN, the lower-state energies refer to the lowest allowed lower-state energy level; thus, the lower-state energies of sources added above have been reduced by 0.7934 cm^{-1} for $^{14}NH_3$ and 0.7577 cm^{-1} for $^{15}NH_3$ when added to HITRAN. This correction accounts for the

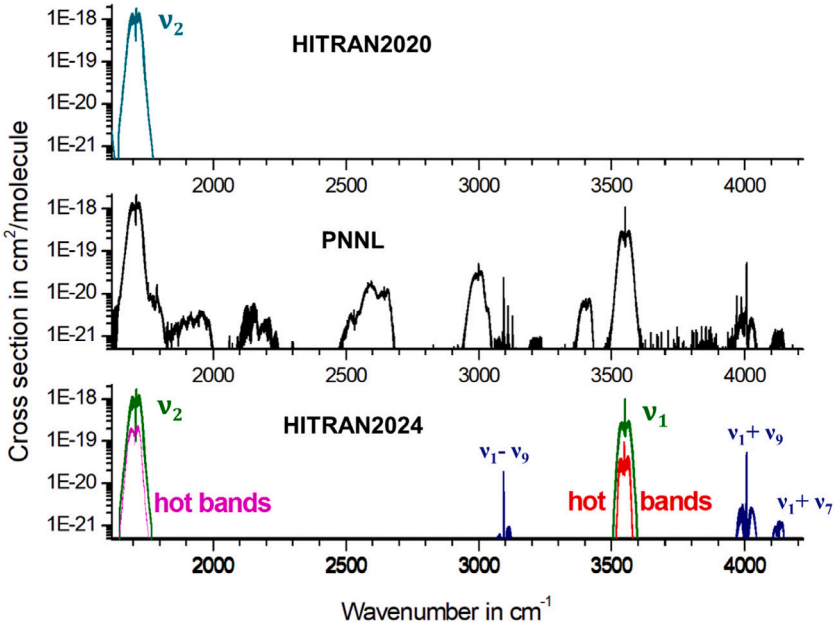

Fig. 14. Overview of the HNO_3 line list above 1600 cm^{-1} in HITRAN2020 and in HITRAN2024 in terms of computed cross-sections. Comparison with the PNNL [178,294] cross section data.

energy difference between the symmetric and anti-symmetric $J'' = K'' = 0$ levels of the ground vibrational state.

In addition, H_2-, He- and CO_2-broadening parameters (already available for existing lines in HITRAN) have been added to all the new transitions of ammonia based on the algorithms described in Wilzewski et al. [29].

Currently, HITRAN only includes the two most abundant isotopologues of ammonia. In the framework of the ExoMol project, a MARVELised line list for $^{14}NH_2D$ has been produced that covers the 0–3650 cm^{-1} spectral region. This work will be evaluated and considered for future updates to HITRAN.

2.12. HNO_3: Nitric acid (molecule 12)

In HITRAN2016 [16] and HITRAN2020 [17] the HNO_3 line list did not include parameters for wavenumbers above 1770 cm^{-1}. However, nitric acid possesses a strong infrared signature at 2.8 μm which corresponds to the ν_1 fundamental band. This band possesses a narrow Q-branch located at 3551.770 cm^{-1} which leads to a narrow signature reaching 50% depth in the solar infrared spectra recorded in the lower stratosphere by the balloon-borne MkIV instrument [57,289]. Furthermore, the HNO_3 list present in HITRAN2020 at 5.8 μm, which corresponds to the ν_2 fundamental band, cannot correctly reproduce the HNO_3 infrared signature in stratospheric spectra.

The present updates in HITRAN for the $H^{14}N^{16}O_3$ main isotopic species of nitric acid, are described in Refs. [290–293]. The goal of these works was (i) to improve the quality of the existing parameters for the ν_2 band in the 5.8 μm region, and (ii) to generate a line list at 2.8 μm. In HITRAN2024, these 5.8 μm and 2.8 μm lists also include contributions from the first associated hot bands, $\nu_2+\nu_i-\nu_i$ (with $i = 6$, 7, and 9) and $\nu_1+\nu_i-\nu_i$ (with $i = 7$ and 9), respectively. Finally, we have generated line lists for the weaker $\nu_1-\nu_9$ difference band, centered at 3093.545 cm^{-1} and for the $\nu_1+\nu_9$ and $\nu_1+\nu_7$ combination bands located at 4006.977 and 4137.782 cm^{-1}, respectively. An overview of this update in the 5.8 μm to 2.8 μm region is given on Fig. 14. The detailed descriptions of this line list are provided in Table 5 of Perrin et al. [291] and in Table 1 of Perrin et al. [293], for the 5.8 μm and 2.8 μm regions, respectively.

The line positions and intensities quoted in this list result from the analysis of a large set of high-resolution Fourier transform spectra recorded on the SOLEIL synchrotron facilities. The theoretical models used to compute the line position parameters account, as usual, for vibrational rotation resonances. However, for the 11 fundamental bands and 2191 combination vibrational states, this calculation also had to account for unexpected perturbations due to the large-amplitude character of the ν_9 torsional mode.

The parameters used to calculate the line intensities at 5.8 μm were obtained from a least squares fit computation performed on individual ν_2 experimental line intensities. This calculation takes into account, for the first time, the hybrid character of the ν_2 band: together with its main B-type character, the ν_2 band also possesses a weaker A-type character that was not considered by earlier studies or during the generation of the previous HITRAN line list.

For the ν_1 band, and for the weaker $\nu_1-\nu_9$, $\nu_1+\nu_9$, and $\nu_1+\nu_7$ bands in the 2.4 μm to 3.3 μm regions, the large values of the Doppler line widths at ~296 K prevent the measurements of individual line intensities in laboratory spectra. Therefore, the line intensities were estimated by comparisons between (i) calculated and observed high-resolution spectra and (ii) computed and measured cross section data [178,294]. It appears that the ν_1 band is a hybrid band (mostly of A-type with a weaker B-type character), while the $\nu_1-\nu_9$ and $\nu_1+\nu_9$ bands are C-type bands (as expected) and $\nu_1+\nu_7$ an A-type band. It is worth mentioning that the intensity computation for the ν_1 band was also complicated because of perturbations due to the large-amplitude behavior of the OH torsion. The users should be aware that for many lines, K_a and K_c quanta could not be determined, and a default flag '99' was used in these cases. This would not affect the radiative transfer calculations.

Line-shape parameters were set at the values that are provided in HITRAN2020 [17] for transitions of HNO_3 in the 11 μm region that involve the same rotational quantum numbers. More explicitly, the values $\gamma_{self} = 0.8070$ cm^{-1}/atm, and $n_{air} = 0.75$ were provided for the self-pressure broadening half-width coefficient at 296 K, and air-broadening temperature dependence. When the corresponding rotational transition was not identified, the default value $\gamma_{air} = 0.098$ cm^{-1}/atm was used for the air-broadening parameter. However, in the central part of the narrow Q-branch of the ν_1 band, the value $\gamma_{air} = 0.062$ cm^{-1}/atm has been implemented to account, empirically, for line mixing effects.

These new HNO_3 line lists were extensively validated using solar occultation spectra recorded in the stratosphere from the balloon-borne

MkIV spectrometer. Also, these lists were used to compute cross sections that were compared to experimental cross sections of Chackerian et al. [294].

The main conclusions of this validation process are as follows:

- In the 5.8 μm region, the "W-type" signal error observed during the retrieval process of the MkIV spectra was significantly reduced when using this new list rather than the previous HITRAN2020 database. This is obvious in Fig. (4) of Perrin et al. [291].
- In both the 5.8 μm and 2.8 μm regions, the retrievals of the MkIV spectra are of better quality when using this new line-by-line list rather than the empirical "HNO3 pseudo line list" generated previously by the JPL study [57].
- The intensities in this new line list for HNO_3 at 5.8 μm (ν_2 and $\nu_2 + \nu_i - \nu_i$ hot bands with $i = 7$ and 9) are, on average, about 8% weaker than in HITRAN2020. In HITRAN2020, the HNO_3 line intensities for the ν_2 band were scaled relative to the PNNL cross sections.
- On the other hand, the line intensities for the ν_1 band are consistent in our high-resolution spectra with those for the ν_2 band. These ν_1 intensities are also in reasonable agreement with its prediction from PNNL cross sections at 2.8 μm.
- The inclusion of new HNO_3 parameters for the ν_1 band (and associated hot bands) and of $\nu_1 + \nu_9$, $\nu_1 - \nu_9$ and $\nu_1 + \nu_7$ in the 3000–4200 cm^{-1} range will improve the quality of the retrievals for this spectral region. However, line parameters corresponding to several weak HNO_3 absorption bands (e.g., near 2500 cm^{-1} and 3000 cm^{-1}) are still missing in the updated HITRAN line list.
- Large discrepancies are found in the 2.8-μm region between the University College of London (UCL) calculations for nitric acid [295,296] and the PNNL cross section data.

2.12.1. Future studies

More precise "absolute" intensities for the 22 μm, 15 μm, 11 μm, 7.6 μm, 5.8 μm and 2.8 μm absorption bands of HNO_3 are planned. These measurements will be carried out at medium resolution using the Bruker[3] FTS spectrometer located at the SOLEIL synchrotron facilities. We note that the future FORUM [149] satellite instrument will cover both the 22 μm and 11 μm absorbing bands of HNO_3.

2.13. OH: Hydroxyl radical (molecule 13)

The OH radical is one of the main drivers of atmospheric chemistry. In the troposphere of Earth, OH is the most important oxidizing agent for organic molecules, and in the upper atmosphere produces prominent airglow emission. Atmospheric OH is measured spectroscopically in many spectral regions. Different missions target pure rotational transitions [297,298], vibration–rotation transitions (Meinel bands) [299], and the $A^2\Sigma^+$–$X^2\Pi$ electronic transitions [300]. OH is also prominent in many astronomical objects, including stellar atmospheres [301], ISM [302], atmospheres of Mars [303], Venus [304], and hot-Jupiter exoplanets [305,306]. The hydroxyl radical emits intensively in combustion environments, including flames [307].

The HITRAN2020 [17] line list of ^{16}OH was based on the line list calculated by Brooke et al. [308] with additional corrections to the line positions that took into account the airglow data from Noll et al. [299] (see the HITRAN2020 paper for details). While the line positions represent the current state-of-the-art, the quality of intensities leaves room for improvement. In particular, the airglow intensities of the X-X transitions observed by Noll et al. [299] showed discrepancies with HITRAN in the Q branch, and also the components of the observed Λ doublets often differed significantly, whereas the theory by Brooke et al. (2016) [308] predicted their intensities to be identical at the sub-percent level. The reasons for these discrepancies include: 1) the RKR potential and the *ab initio* dipole moment in Ref. [308] were interpolated by non-analytic functions (see Ref. [309] for explanations); 2) the coupling between the ground (X) and excited (A and higher) electronic states was ignored, whereas the coupling between the multiplet components of the X state was treated by the perturbation theory (see Ushakov et al. [310,311] for explanations).

The work of Ushakov et al. [310], in which the new intensities of the X-X transitions in ^{16}OH were calculated, partially resolved these issues. *Ab initio* calculations were performed in the extended range of r = 0.4–8.0 Bohr, and, as explained in Medvedev et al. [309], the repulsive branch of the OH potential was now correctly interpolated in the repulsive region, which is important for calculations of the intensities of the high-overtone transitions (although not as crucial for calculating the energy levels, see Sec. 8.2 in Ref. [199]).

Fully analytic molecular functions were constructed and fitted to the *ab initio* data and to all available experimental data on frequencies, intensities, and permanent dipole moments. The system of three coupled electronic Schrödinger equations, including two multiplet components of the X state and the A state, was solved precisely. The results showed that the approach employed by Brooke et al. [308] did not work well at high v and J where the X-A interaction increased; see Fig. 5 in Ref. [310].

The new set of the Einstein-A coefficients (and intensities calculated from them) included in the HITRAN2024 edition permitted us (1) to decrease the scatter of the logarithmic populations of the rovibrational levels derived from the observed radiation fluxes, (2) to achieve better agreement with the measured relative intensities, (3) and to obtain significant (up to 50% difference) improvement in the distribution of the intensities within the Λ doublets for large v and J in better accord with the observations by Noll et al. [299]. Yet, the agreement with the observed differences in the intensities of the Λ-doublet components was still far from perfect, presumably due to neglect of higher excited states.

The HITRAN2024 line list for ^{16}OH is composed of the transition wavenumbers included in HITRAN2020 and the intensities calculated by Ushakov et al. [310]. The final Einstein-A coefficients used for the HITRAN2024 OH line list were published in an erratum [311].

In the recent publication of Mitev et al. (2024) [313], the X-X line list was calculated in the framework of a broader ExoMol [218] project on the predissociation dynamics [314]. The focus of this study was on the transitions to the higher excited states, whereas the intensities of the X-X transitions were not optimized by fitting the model to the measured intensity ratios and permanent dipole moments, and therefore do not reproduce the experimental data within the experimental errors. Consequently, the results by Ushakov et al. have been selected for updating the HITRAN database. Fig. 15 demonstrates that it provides the best agreement with the intensity ratios from Brooke et al. and Noll et al.

It should be noted that the absolute values of the intensities of low-J P lines have changed by about 2% with respect to HITRAN2020. Interestingly, Chang et al. (2023) [315] reported measurements of intensities in the P lines of the fundamental band by simultaneous determination of hydrogen peroxide (H_2O_2) and OH upon laser photolysis of H_2O_2, and suggested that HITRAN2020 intensities are off by 40%. This contradicts all the previous experimental and high-level *ab initio* values that have been reviewed by the HITRAN community in the last few decades. While there are disagreements on the rotational distribution of intensities, the values in the fundamental band have all been well within 10%. For instance, the data from HITRAN2020 are just 5% different from [313, Table 10] (and 2% from HITRAN2024 as mentioned above).

[3] Identification of certain commercial equipment, instruments, software, or materials does not imply recommendation or endorsement by the organizations involved in this paper, nor does it imply that the products identified are necessarily the best available for the purpose.

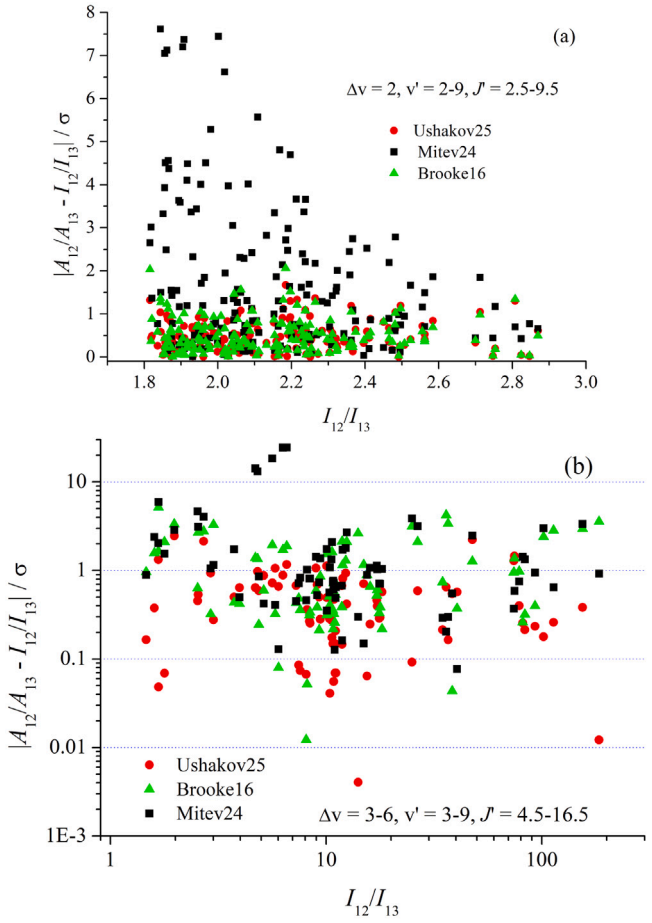

Fig. 15. Calculated-minus-observed ratios of the Einstein-*A* coefficients for ^{16}OH lines 1 → 2 and 1 → 3 emitted from a common upper level 1 divided by the experimental uncertainty, σ. I_{12}/I_{13} are ratios of the observed fluxes in Rayleigh emitted from the same level 1. (a), Experimental data of Brooke et al. (2016) recalculated from the laboratory spectra of Abrams et al. [312]. (b), Observational data of Noll et al. (2020). Theoretical data: circles, Ushakov et al. (2025) [310] (used for HITRAN2024); triangles, Brooke et al. [308] (used in HITRAN2016 [16] and HITRAN2020 [17]); squares, Mitev et al. (2024) [313] (used for ExoMol [218]).

2.14. HF: Hydrogen fluoride (molecule 14)

Unchanged.

2.15. HCl: Hydrogen chloride (molecule 15)

Hydrogen chloride (HCl) was added to HITRAN as one of the first trace gases [6]. As the main stratospheric chlorine reservoir, this gas plays a crucial role in the ozone chemistry in the terrestrial atmosphere and is being monitored by different remote sensing missions [316]. It is also present in planetary atmospheres [317,318] and the interstellar medium (ISM) [319].

The intensities of all spectral bands of all isotopologues of hydrogen chloride in HITRAN (starting from HITRAN2012 [15] through HITRAN2020 [17]) are based on the calculation that employed a semi-empirical dipole moment function by Li et al. [320,321]. For the overtone bands ($4 \le \Delta v \le 7$) the intensities were largely driven by the measurements reported in Gelfand et al. [322]. It was not clear if the values reported in that work included isotopic abundance or not, and in the end, it was erroneously assumed that they did not. Considering that the abundances of ^{35}Cl and ^{37}Cl are about 75% and 25%, respectively, the HCl intensities were thus underestimated by about 25%. This became apparent when Vasilchenko et al. [323] measured several P-branch transitions in the fourth overtone of HCl using the CRDS technique. The deviation from the intensity pattern for these bands was also noticed by Špirko [324] in their semi-empirical estimations. HITRAN2024 intensities and Einstein-*A* coefficients of the bands with $4 \le \Delta v \le 7$ for all isotopologues of hydrochloric acid were multiplied by a factor of 1.3 based on the measurements reported by Vasilchenko et al. [323]. In the future, a more appropriate approach would be to refit of the semi-empirical dipole moment function using the experimental and theoretical intensities as was done in Li et al. [320,321] but using corrected and new experimental values. Similarly, the line positions in the higher overtones will need to be revised as Vasilchenko et al. [323] report deviations of the 5–0 band line positions by up to 0.003 cm^{-1}.

2.16. HBr: Hydrogen bromide (molecule 16)

Unchanged.

2.17. HI: Hydrogen iodide (molecule 17)

Unchanged.

2.18. ClO: Chlorine monoxide (molecule 18)

Unchanged.

2.19. OCS: Carbonyl sulfide (molecule 19)

Carbonyl sulfide, or OCS, is the most abundant sulfur-containing gas in the atmosphere of Earth, being a product of biogenic activity [325]. It has also been detected in a variety of environments beyond Earth, including the atmospheres of Venus [326] and comets [327]. The HITRAN2024 OCS line list utilizes the transitions published in the Ames-296K IR line list [328] recently developed through the algorithm "Best Theory + Reliable High-resolution Experiment" [329]. A CCSD(T)/aug-cc-pV5Z potential energy surface (PES) was empirically refined using 1486 reliable rovibrational energy levels in HITRAN2020 for six isotopologues with *ierr* > 3 (see Table 2), and 29 experimental vibrational band origins of ^{16}O^{12}C^{32}S above 10 000 cm^{-1}. The refined PES reached an accuracy of 0.007 cm^{-1} for the related levels of the primary isotopologue in HITRAN2020, and an accuracy of 0.01–0.02 cm^{-1}for band origins above 10 000 cm^{-1}. The rovibrational energy levels and line positions were computed variationally on the refined PES. Infrared line intensities were calculated using CCSD(T)/aug-cc-pV(5+d)Z and extrapolated (to CBS) dipole moment surfaces (DMS) with fitting $\sigma_{rms} = 1.3 \times 10^{-7}$ a.u. in the 0 – 15 000 cm^{-1} range. For each of the 12 most abundant OCS isotopologues, the Ames-296K line list covers the range of 0 – 15 000 cm^{-1}and $S_{296K} > 10^{-31}$ cm^{-1}/molecule cm^{-2}, with $J_{max} = 240$. They are merged into a composite line list consisting of more than 9 million transitions with line intensity scaled by HITRAN "natural" abundances of corresponding isotopologues [328]. Near 4000 cm^{-1}, both the statistical mean and 1σ of the relative intensity differences between Ames-296K and the empirical line list from Ref. [330] are less than 10% for eight out of ten isotopologues.

To further improve the accuracy of the Ames-296K line positions, the computed energy levels of the OCS isotopologues were enhanced by consistent empirical corrections determined from comparison with the reliable energy levels in the CDMS [331] and HITRAN2020 [17] databases. These levels are based on effective Hamiltonian models that were fitted to the experimental data. After correction, most residuals $\delta_{\text{Ames-CDMS}}$ were within the uncertainty of the CDMS transitions, and most residuals $\delta_{\text{Ames-HITRAN}}$ were below 0.0001 cm^{-1} except for some over-extrapolations. The ^{16}O^{12}C^{32}S energy levels computed on the

refined Ames-1 PES could match the most accurate subset of MARVEL levels [332] up to 14 000 cm^{-1} with σ_{rms} less than 0.01 cm^{-1} [328]. For the $^{16}O^{12}C^{32}S$ bands experimentally measured but not present in HITRAN2020, 0th–2nd order correction formulas were determined by plotting the $\delta_{\text{Ames-MARVEL}}$ residuals with respect to J. Such empirical corrections effectively preserve the strength of the theoretical calculation to maintain consistent accuracy across a band. After these energy levels had been corrected, the Ames-296K composite line list was validated against the PNNL cross-sections and low-pressure high-resolution measurements from Brussels [333]. It has illustrated clear improvements over the HITRAN2020 [17] and ExoMol OYT8 line list [334], with better intensity agreement and less absorption residuals resulting from the line position deviations, for example, the $\nu_1+\nu_3$ band at 2900 $cm^{-1}$and the $2\nu_2+\nu_3$ band at 3100 cm^{-1}. More details of the line list can be found in Huang et al. [328], while the composite line list is publicly available at https://doi.org/10.5281/zenodo.13906149.

The line list of the six most abundant isotopologues of OCS from Huang et al. [328] was adapted for HITRAN2024 with the following adjustments.

- The intensity cut-off 1×10^{-28} cm/molecule was applied to all the bands. This allowed for substantial expansion of the spectral and dynamic range in HITRAN (see Fig. 16 that compares the 2020 and 2024 editions), while preserving sufficient accuracy at the temperatures up to those encountered on Venus.
- The line-shape parameters follow those used in the HITRAN database [17]. The air-broadening parameters were calculated using Padé approximants reported in Koshelev and Tretyakov [335] based on their experimental studies. Self-broadening parameters and temperature dependencies (used for air as well) were taken from Bouanich et al. [336]. For all the new transitions of OCS, H_2-, CO_2- and He-broadening parameters have been added using the Padé approximants reported in Ref. [30].
- During the update, the computed intensities of pure rotational transitions within the vibrational ground state were scaled to match the experiment-based R0/R1 intensities in HITRAN and CDMS, with scaling factors 1.02921 for isotopologues $^{16}O^{12}C^{32}S$ and $^{16}O^{12}C^{34}S$, and 1.01634 for the remaining minor isotopologues. The scaling factor difference results from the two DMS adopted in the calculation: 5Z level (for 622 and 624) vs. CBS extrapolation. The intensity of the ν_2 band is a particularly interesting case, where the intensities from both variational calculations [328,334] are over 40% larger than the values in HITRAN2020 that are based on the work of Kagann [337] (see HITRAN2000 paper [12] for details). Unfortunately, the PNNL spectra are obscured by a filter in the middle of the Q-branch so it is not possible to unambiguously evaluate this band. However, from observing higher J R-branch values, it appears that the best values should be between HITRAN and variational intensities. This is consistent with the scaling that was applied in HITRAN2004 to the ν_3 band, which was also based on Ref. [337] at the time. Considering that, based on the PNNL comparison, the HITRAN2020 data have some of the lines sticking out of the pattern in this band, we have adapted the line list from Huang et al. [328] and scaled down the computed intensities by 20% for all isotopologues in the ν_2 band.

In the near future, we expect to add the $^{17}O^{12}C^{32}S$ and $^{16}O^{12}C^{36}S$ isotopologues, which have respective abundances of 3.495×10^{-4} and 1.974×10^{-4}. They are only slightly less abundant than $^{16}O^{13}C^{34}S$ (abundance 4.672×10^{-4}), which is the sixth isotopologue of OCS in HITRAN. The corresponding TIPS have already been calculated [338].

As already mentioned, we use the air-broadening values proposed by Koshelev and Tretyakov [335] and self-broadening values from Bouanich et al. [336] for all the bands, ignoring vibrational dependence, as is a common approach for linear molecules (see Ref. [30], for instance). However, if one compares experimental results in different bands [335,339,340], discrepancies up to a few percent can be observed. This may be attributed to a large dipole moment of the OCS molecule and will be investigated in the future. As pointed out in Ref. [328], comparisons with PNNL revealed that the bands at higher wavenumbers need line-shift parameters, especially in the NIR. At the moment, only a limited number of lines of OCS in HITRAN have these parameters. Finally, no measurements or calculations of temperature dependencies of air-broadened values exist, and we had to use the self-broadening temperature exponents instead. Future measurements and calculations of these parameters would be beneficial.

2.20. H_2CO: Formaldehyde (molecule 20)

Formaldehyde (H_2CO) is a key reactive trace species in the terrestrial atmosphere [341] and an important intermediate in the formation of ozone and other secondary pollutants [342]. It is produced in significant quantities from biomass burning, fossil fuel combustion, and the photooxidation of volatile organic compounds (VOCs), as well as from the atmospheric breakdown of methane and other hydrocarbons [343]. Since its detection as the first polyatomic organic molecule in the interstellar medium [344], H_2CO has been observed in a range of astronomical environments such as comets [345] and protoplanetary disks [346]. It is expected to be present on Mars; however, its tentative detection [347] has been later attributed to instrumental noise [348].

The HITRAN2020 edition [17] contained notable gaps in its coverage of H_2CO, for example infrared absorption at wavelengths from about 6 to 20 μm (510 to 1620 cm^{-1}) and the bands above 3000 cm^{-1}. Coverage has now been significantly increased by utilizing an updated, MARVELised version of the ExoMol "AYTY" line list [349].

The original *ab initio* ExoMol AYTY line list [349] of $H_2{}^{12}C^{16}O$ contained around 10 billion transitions between rovibrational states up to $J \leq 70$ in the 0–10 000 cm^{-1} window. The first major update to the AYTY line list was performed by Al-Derzi et al. [350], who carried out an extensive MARVEL study of the H_2CO spectroscopic literature. A total of 16 403 transitions were validated from 43 sources, leading to the replacement of 367 779 transitions below 5887 cm^{-1}, determined with experimental accuracy. A second MARVEL update to the AYTY line list was performed by Germann et al. [351] based on optical frequency comb Fourier transform spectroscopic measurements of the ν_3, ν_4 and ν_6 fundamental bands and four hot bands in the 1250–1390 cm^{-1} range. The resulting extended MARVEL analysis further improved the accuracy of the AYTY line list and led to an additional 5382 transitions being replaced with experimental-quality values.

After populating it with broadening parameters using the same approach as in HITRAN (based on Ref. [352]), we carried out an extensive validation of the MARVELised AYTY linelist against the PNNL spectra [178]. In the overlapping spectral regions, the HITRAN data produce smaller residuals except for the edges of bands, where the AYTY linelist is more extensive. In some cases, scaling factors were applied to the ExoMol line list in these regions when adapting to HITRAN2024. Fig. 17 provides a sample comparison of PNNL cross-sections measured at 5 °C with those calculated from the ExoMol/AYTY, HITRAN2020 and HITRAN2024 line lists, showing that HITRAN2024 produces the smallest residuals in this 2700–3200 cm^{-1}region.

In the region of ν_3, ν_4, and ν_6 where HITRAN2020 data were absent, the ab initio line list works fairly well; nevertheless, it required some empirical scalings of the intensities, where measurements reported in Germann et al. [351] and PNNL comparisons were used as a guide. Many lines that were apparently missing from the new line list were taken from the semi-empirical list of Nadler et al. [353], which required intensity scaling to match PNNL as well. Fig. 18 provides a sample comparison of PNNL cross-sections measured in this region at 5 °C with those calculated from ExoMol/AYTY, and HITRAN2024 line lists.

In the region of the $2\nu_2$ overtone (centered at 3470 cm^{-1}), where there were no HITRAN data, the AYTY line list reproduces the PNNL

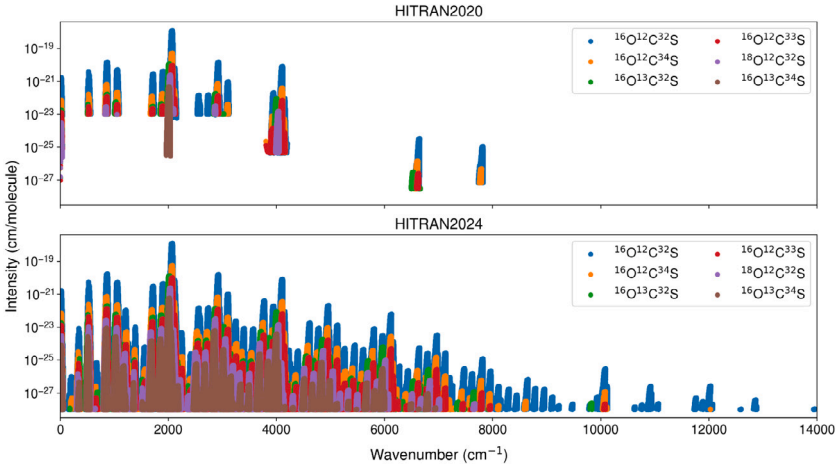

Fig. 16. The HITRAN2020 line list for the six isotopologues of OCS is shown in the upper panel, which can be compared to the spectral coverage of the new HITRAN2024 OCS line list shown in the lower panel. The intensities have been scaled to their "natural" abundance (see Table 1) per the HITRAN convention.

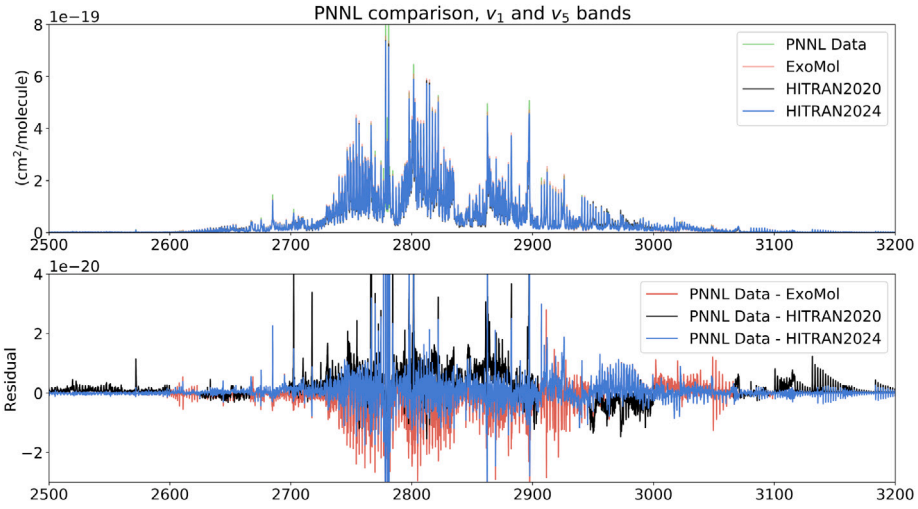

Fig. 17. Sample comparison of the cross-sections calculated using the updated ExoMol/AYTY, HITRAN2020 and HITRAN2024 line lists with PNNL cross-sections [178] recorded at 5 °C.

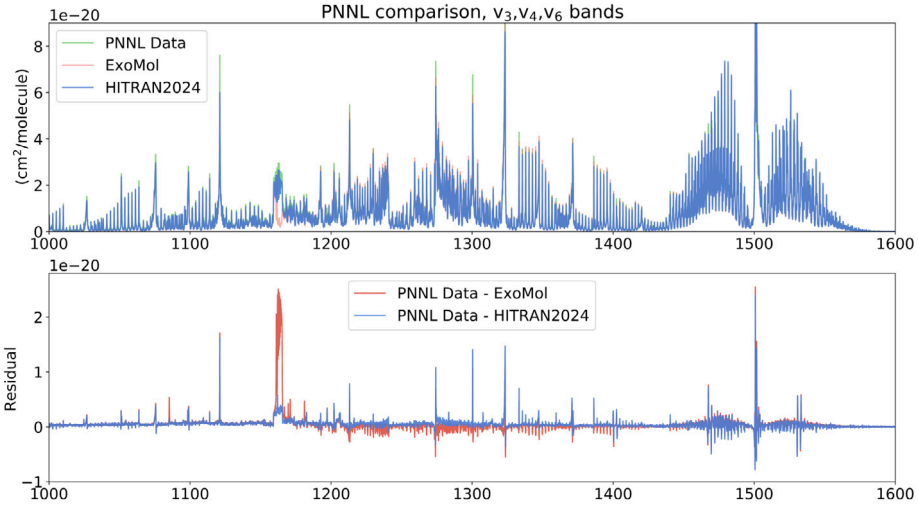

Fig. 18. Sample comparison of the H_2CO cross-sections calculated using the updated ExoMol/AYTY, and HITRAN2024 line lists with PNNL cross-sections [178] recorded at 5 °C. This region of formaldehyde was not covered in the previous HITRAN editions.

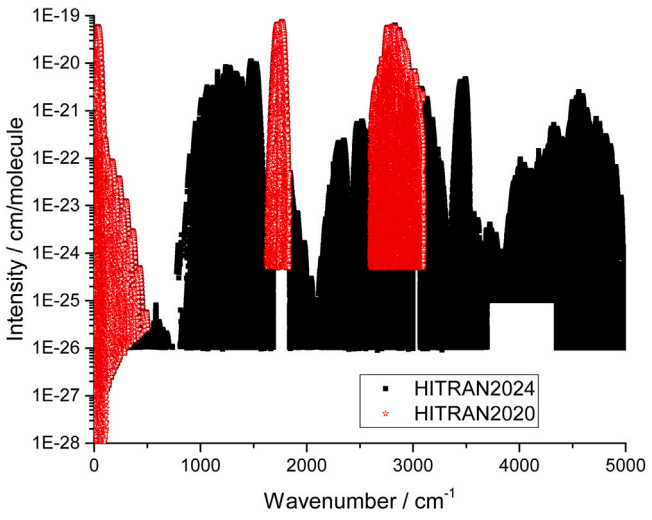

Fig. 19. T = 296 K spectra of $H_2^{12}C^{16}O$ from HITRAN 2020 [17] and HITRAN2024, showing substantial expansion in spectral and dynamic range. The major source for expansion is the AYTY line list [357] (which included MAREVLised transitions [350,351]). Note that based on the comparison with PNNL a large amount of HITRAN2020 transitions have been retained, while in the 3700–4450 cm^{-1} region the line list from Ref. [354] was adapted. This explains uneven intensity cut-offs in different spectral regions in HITRAN2024.

measurements well. In the 3700–4450 cm^{-1} region, the line list from Nikitin et al. [354] was evaluated against PNNL and proved to be a better fit than the AYTY line list (see discussion in Ref. [354] for details). The line list is based on the analyses of four formaldehyde spectra in natural isotopic abundance in the 3700–5200 cm^{-1} region recorded at low temperature 160–166 K, at Synchrotron SOLEIL for various pressures. Line positions and intensities were retrieved by non-linear least-squares curve-fitting procedures. Quantum assignments were made for 6177 transitions, which represent more than 95% of the integrated line intensity at 160 K and >70% at 296 K in this region. Contact transformation effective Hamiltonian [355] parameters based on the PES [356] were fitted to all assigned line positions with RMS deviations of 0.001 cm^{-1}. The initial values of line intensities were computed from the ab initio dipole moment determined in this work, transformed to the effective one following [355]. Using a sample of measured intensities allowed preliminary empirical optimization of a few parameters of the effective dipole transition moments, which led to the values being included in the line list. The assigned line list includes empirically fitted line positions and line intensities computed from ab initio DMS obtained in Nikitin et al. [354]. The original line list from the supplementary materials of Nikitin et al. [354] contained a large number of erroneous quantum assignments. These have been fixed during incorporation into HITRAN2024.

In the 4450–5000 cm^{-1} region, another concentration of strong bands is reproduced fairly well by the MARVELised AYTY list, although not as well as the region of $2\nu_2$ overtone. Above 5000 cm^{-1}, the line list cannot reproduce the PNNL measurements reasonably well, and therefore these lines were not taken for HITRAN. In addition, the intensity cut-off of 10^{-26} cm/molecule was introduced to keep the line list to a practical file size, but without losing accuracy for atmospheric retrievals. This is illustrated in Fig. 19 by shading out the portions of the AYTY line list that were not taken for HITRAN2024.

Approximately half of the transitions in the experimental line list from Germann et al. [351], belonging to hot bands and other H_2CO isotopologues, remained unassigned. Currently, H_2CO measurements are being performed using optical frequency comb Fourier transform spectroscopy in the 1170–1280 cm^{-1} range. The extended experimental line list covering the range of ν_3, ν_4 and ν_6 bands will be assigned using predictions based on the effective Hamiltonian [355], which also contains hot-band transitions and transitions of the isotopologues $H_2{}^{13}C^{16}O$ and $H_2{}^{12}C^{18}O$. The new data will be included in future MARVEL, and subsequently in HITRAN, updates.

For all the newly added transitions of H_2CO, broadening parameters for H_2, CO_2 and He have been added using the algorithms described in Tan et al. [30].

2.21. HOCl: Hypochlorous acid (molecule 21)

Unchanged.

2.22. N_2: Molecular nitrogen (molecule 22)

Unchanged.

2.23. HCN: Hydrogen cyanide (molecule 23)

Hydrogen cyanide is an atmospheric trace species that is released mainly during biomass burning and could play a non-negligible role in the nitrogen cycle [358]. Modern buildings and household items contain many synthetic materials that burn hotter than natural materials and release large amounts of HCN, which is toxic [359].

In addition, HCN is an important astrophysical species: it is an important component of the atmosphere of cool stars [360] and circumstellar disks. HCN has been detected in a number of exoplanets [361–363]. Many of these studies require simulations of the spectral signatures of the HCN gas at a variety of thermodynamic conditions, which is a strong motivation for updating the HCN line list in the HITRAN database.

The HITRAN2024 HCN dataset is based on MOMeNT-90 originating from the work of Mellau et al. [364]. The MOMeNT-90 linelist replaced the previous ExoMol data in HITRAN [365], which was based on a series of computational works [366,367] in the range from 3500 to 10 642 cm^{-1}. The HITRAN2020 lines originating from empirical works have been kept unchanged. Here we give a short description of the new line list as follows.

The complete set of eigenenergies allows the construction of a unique fitted pseudo-PES potential [364,368]. The rotational and vibrational energies calculated with this potential are orders of magnitude more accurate than those calculated in the past based on a first-principles PES. The accurate energies correlate with accurate wavefunctions, so the calculated intensities should be reliable. In addition, a new *ab initio* dipole moment surface was calculated at a high level of quantum chemical theory [364].

To create an accurate line list, it is necessary to replace the *ab initio* energies with the experimental eigenenergies. Based on high-temperature emission spectra, the J_{max}=60-90 rotational levels for almost all vibrational states up to 10 300 cm^{-1} above the ground state have been determined by Mellau [369–374] with an accuracy of better than 10^{-3} cm^{-1}. The data set for vibrational states above 10 300 cm^{-1} is not complete, but the majority of the HITRAN-relevant vibrational states have been determined. The data set allows the calculation of experimentally-accurate line positions for almost all transitions with intensities above the HITRAN cutoff. Such a mapping based only on the eigenenergies is straightforward at low J-values, but becomes a complicated task at higher J-values. The mapping algorithm was developed to map the experimental HCN eigenenergies, which have an accuracy better than 10^{-3} cm^{-1}, to an *ab initio* eigenenergy list with an accuracy several orders of magnitude worse. The current version of the mapping program can map the rotational levels up to J=90 for all vibrational states up to 10 300 cm^{-1}.

This new line list has been used to update the HITRAN database. In addition to the bands reported in [364], some additional bands have been compiled for the final HITRAN2024 version of the HCN linelist, especially many $\Delta l > 1$ transitions.

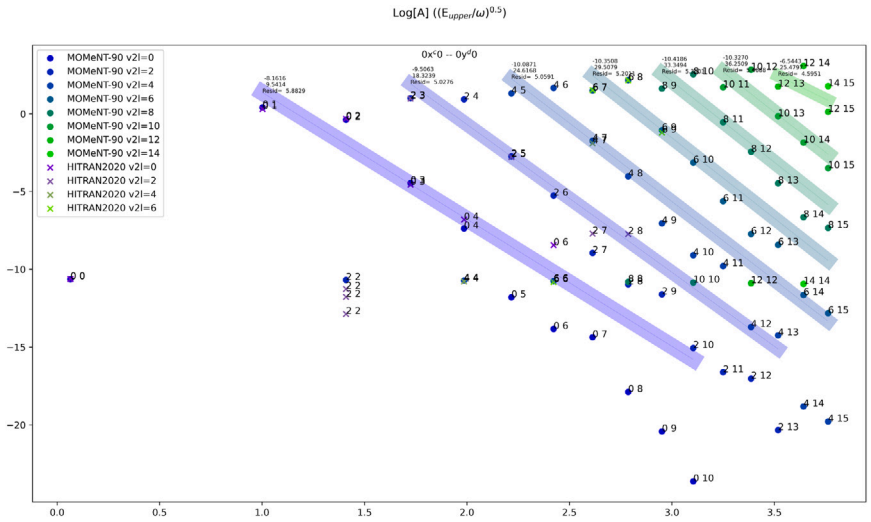

Fig. 20. Demonstration of the NID on the $0x^c0 - 0y^d0$ series of transitions of HCN with HITRAN2020 and HITRAN2024 (MOMENT-90) line lists.

To improve the behavior of the computed line intensities of high overtone bands, we used the Medvedev et al. [108] approach which suggests that the intensities should follow the so-called Normal Intensity Distribution (NID). The method was applied to the MOMeNT-90 line list to exclude the vibrational bands with intensities falling far from the suggested distribution. These were mostly bands with high ν_2 values. In Fig. 20, the logarithm of the Einstein A-coefficient as a function of $(E_{upper}/\omega)^{0.5}$ is presented for the different series of $0x^c0 - 0y^d0$ transitions (with trend line for each of them) and the labels of data points are v_2^{upper} and v_2^{lower} (E_{upper} is the upper state of the transition, ω is the harmonic frequency of the transition type).

Finally, for all HCN transitions, H_2- and He-broadening parameters have been added based on an algorithm described in Tan et al. [30].

2.24. CH_3Cl: Methyl chloride (molecule 24)

Unchanged.

Recently, high-resolution far-infrared spectra of the ν_3 and ν_6 bands of chloromethane (CH_3Cl) were recorded at the AILES beamline of the SOLEIL synchrotron facility. Using the tensorial formalism developed in Dijon, Hardy et al. [375] analyzed both chlorine-substituted isotopologues ($CH_3{}^{35}Cl$ and $CH_3{}^{37}Cl$), with a total of 6753 lines assigned. They derived 23 tensorial parameters for line positions (4 for the ground state, 6 for ν_3, and 13 for ν_6), and 7 for line intensities (4 for ν_3, 3 for ν_6). These parameters, combined with self-broadening coefficients from the literature, allowed us to create a new database of calculated chloromethane spectral lines (ChMeCaSDa, see Ref. [219]), accessible at http://vamdc.icb.cnrs.fr/PHP/CH3Cl.php. The database shows excellent agreement with HITRAN, but with improved line position accuracy (standard deviation of 0.303 for $CH_3^{35}Cl$ and 0.193 for $CH_3^{37}Cl$). Additionally, unlike the present HITRAN list, which contains empirically adjusted line intensities, these new data were calculated using the tensorial formalism, providing more precise parameters than those previously available in the literature. These positions and intensities will be included in the next HITRAN update.

2.25. H_2O_2: Hydrogen peroxide (molecule 25)

Unchanged.

2.26. C_2H_2: Acetylene (molecule 26)

Acetylene (C_2H_2) is a minor trace gas in the terrestrial atmosphere, primarily originating from combustion sources, and therefore its concentration is highly correlated with carbon monoxide [376]. It is present in the atmospheres of solar system gas giants and their satellites [377–379]. It has also been detected on exoplanets (see, for instance, Giacobbe et al. [191]). Recent JWST observations revealed strong C_2H_2 emission in some of the protoplanetary disks [380]. In addition, C_2H_2 is a prototype system for molecular dynamics with very rich IR spectra due to strong couplings between vibrational modes.

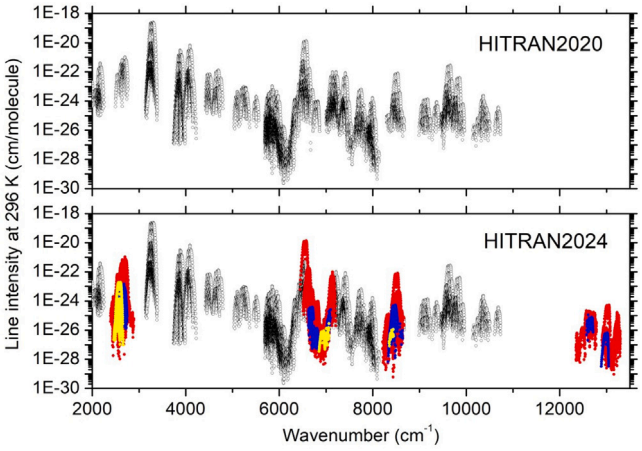

Fig. 21. Overview comparison of HITRAN2020 and HITRAN2024 lists of IR bands of acetylene. New data highlighted: $^{12}C_2H_2$ (red), $^{13}C^{12}CH_2$ (blue), C_2HD (yellow).

As illustrated in Fig. 21, the acetylene line list has been updated in four regions near 3.8, 1.45, 1.2, and 0.8 μm, the latter being included for the first time in the HITRAN database.

2.26.1. The 2389–2890 cm^{-1} region

This region near 3.8 μm is important for atmospheric and astrophysical applications due to strong Q branches used to retrieve acetylene concentrations. HITRAN2020 contained 421 lines of the five most intense vibrational bands in this region. New FTS experiments with optical paths of about 1 km [381–383] enabled more detailed information. The spectrum assignment was performed using the IAO-Tomsk line list [384]. This line list was generated using the results of the global modeling of the line positions and the line intensities within the framework of the method of effective operators [384,385]. The experimental line positions were used for the correction of the calculated values.

The derived spectroscopic constants were used for the calculation of the line positions for several bands. These calculated line positions were also included in the HITRAN2024 line list. The line intensities included in HITRAN2024 were calculated with the improved set of the effective dipole moment parameters. The new measured line intensities were used for the improvement. The line list generated for this region and included in HITRAN2024 contains 7515 transitions belonging to 71 bands of $^{12}C_2H_2$, 944 transitions of 11 bands of $^{13}C^{12}CH_2$ and 692 transitions of 6 bands of $^{12}C_2HD$.

2.26.2. The 6627–7065 cm^{-1} region

Acetylene's transparency window here was investigated by CRDS in Grenoble [386]. In this region, HITRAN2020 contains 397 acetylene transitions. The line list included in the HITRAN2024 in this region contains 4573 lines of $^{12}C_2H_2$, 591 lines of $^{12}C^{13}CH_2$ and 114 lines of $^{12}C_2HD$. Spectroscopic constants, vibrational transition dipole moment squared and Herman–Wallis coefficients were used for the rotational modeling, interpolations and limited extrapolation. This modeling was performed by merging new measurements with the empirical acetylene line list [387] and HITRAN2016 data for the strongest bands. The measured values of the line positions and intensities of the perturbed bands were used in the final line list. The new line list corrects some inaccurately extrapolated line parameters presented in the previous HITRAN list.

2.26.3. The 8200–8700 cm^{-1} region

The high sensitivity CRDS measurements of Ref. [388] allowed for a significant extension of the acetylene line list in the 8200–8700 cm^{-1} region. The HITRAN2020 edition in this region contains 760 transitions of 15 bands of $^{12}C_2H_2$, and 114 transitions of three bands of $^{12}C^{13}CH_2$. The new generated line list contains 2707 $^{12}C_2H_2$ transitions (44 bands), 404 $^{12}C^{13}CH_2$ transitions (7 bands) and 28 $^{12}C_2HD$ transitions (one band). As in the previous case, spectroscopic constants, vibrational transition dipole moments squared, and Herman-Wallis coefficients were used for the line position and line intensity calculation. The measured values of the line positions and intensities of the perturbed bands were kept in the line list.

2.26.4. The 12 350–12 790 cm^{-1} and 12 933–13 300 cm^{-1} regions

The prediction of line positions and line intensities with the global IAO-Tomsk models of the effective Hamiltonian and the effective dipole moment operator [384,385] and with the published spectroscopic constants [389–393] allowed for the partial assignment of the CRDS spectra recorded in Tomsk in the 12 350–12 790 cm^{-1} range [394] and in the 12 933–13 300 cm^{-1} [395] region. The spectrum analysis in these regions revealed numerous strong resonance interactions perturbing a rotational band structure. Many resonance interactions in the case of the highly-excited bending modes are not included in the global IAO-Tomsk model of the effective Hamiltonian, leading to large deviations between the observed and the calculated line positions and intensities. This prevents the complete assignment of the spectra. The parameters of the assigned lines were included in the HITRAN2024 database. In total, 677 lines belonging to 18 bands of $^{12}C_2H_2$ and 68 lines of two bands of $^{12}C^{13}CH_2$ from the 12 350–12 790 cm^{-1} regions are included in the database. The line list for the 12 933–13 300 cm^{-1} region has 1204 transitions of 16 bands of $^{12}C_2H_2$ and 1 band of $^{12}C^{13}CH_2$.

In addition, H_2-, He- and CO_2-broadening parameters have been added to the new transitions for C_2H_2 based on the algorithm described in Wilzewski et al. [29].

2.27. C_2H_6: Ethane (molecule 27)

The air- and self-broadening parameters for the torsional bands of C_2H_6 in the FIR (with $\nu < 350$ cm^{-1}) were previously updated for HITRAN2016 [16]. The γ_{air}, n_{air}, and γ_{self} values included in HITRAN for these lines exhibited a number of differences to the underlying dataset [396], and also deviated from the same parameters for lines with $\nu > 350$ cm^{-1}. The source of these differences has been identified to be arising from the computer codes that applied the air- and self-broadening parameters for the torsional bands in HITRAN2016. This code has been corrected for HITRAN2024 and the γ_{air}, n_{air}, and γ_{self} values for the torsional bands have been made consistent with Malathy Devi et al. [396] and with parameters for other bands of ethane.

2.28. PH_3: Phosphine (molecule 28)

Since the 1980s, a number of FTS spectra of phosphine were recorded in the range 1579–5700 cm^{-1} with a McMath Pierce FT-IR at the Kitt Peak National Observatory (see Table 1 of Butler et al. [397] and Table 1 of Nikitin et al. [398]). For HITRAN2024, the line list [399] based on the analysis of these spectra in the NIR region has been added, extending the line list of phosphine in the database to 4763 cm^{-1}. Transitions for all 26 sublevels of the tetradecad (3769—4763 cm^{-1}) were identified in Nikitin et al. [399]. Noticeably fewer transitions were identified for fourfold excited bands because of their weaker intensity. The CT effective Hamiltonian (H^{eff}) was built from the PES of Nikitin et al. [400]. First, the full nuclear motion Hamiltonian of phosphine was built using the procedure described in Rey et al. [401,402]. Second, this Hamiltonian was reduced to an effective Hamiltonian using the high-order CT method [403,404] that included resonance coupling intra-polyad terms predicted from the ab initio PES. Third, empirical optimization of H^{eff} parameters was performed with the MIRS code [405]. Effective dipole transition moments (EDTM) of the tetradecad bands were determined from *ab initio* line intensities computed using a variational method [355,406,407]. The final line list for the tetradecad transitions was constructed using experimental or empirical positions [399] and calculated intensities.

Malathy Devi et al. [408] reported that no significant vibrational dependence of the self-widths was observed between the pentad ($2\nu_4$, ν_1, ν_3) and dyad (ν_2, ν_4) regions for the transitions having identical rotational quantum numbers. Thus, we have introduced self- and N_2-broadened half-widths in the tetradecad region following the same procedure as in the octad region [409]. Briefly, for self-widths we have borrowed the self-width values measured for the ν_3 band [408] by matching their quantum identifiers (J, K, ΔJ, and ΔK). For the transitions having no match in their quantum assignments, their median values over K were adopted for the given J. For N_2-broadening, we have adopted the measurements of Bouanich et al. [410] in the dyad region. In either case, for the transitions with $J \geq 18$, a default value of 0.05 and 0.08 cm^{-1}/atm was assumed, respectively. For the temperature dependence exponents of the N_2-broadening coefficients, we have assumed a $(0.72 - 0.01 \times J)$ rotational dependence based on the work of Salem et al. [411] as was suggested by Butler et al. [397]. For inclusion into HITRAN, the N_2-broadening coefficients have been multiplied by 0.9 to convert to air-broadening values as done in earlier editions of HITRAN to convert the values of Butler et al. [397].

Finally, H_2- and He-broadening parameters have been added to the new transitions for PH_3 based on an algorithm described in Tan et al. [30].

To demonstrate the effectiveness of the resulting line list, an experimental PNNL cross section [175,178] of PH_3 in 1.0 atm of N_2 at 25 °C was compared with a spectrum generated using the HITRAN2024 update. As presented in Fig. 22, the residuals are at the noise level of the measurement across the spectral region, showing the good quality of the line list from the present work.

2.29. COF_2: Carbonyl fluoride (molecule 29)

Unchanged.

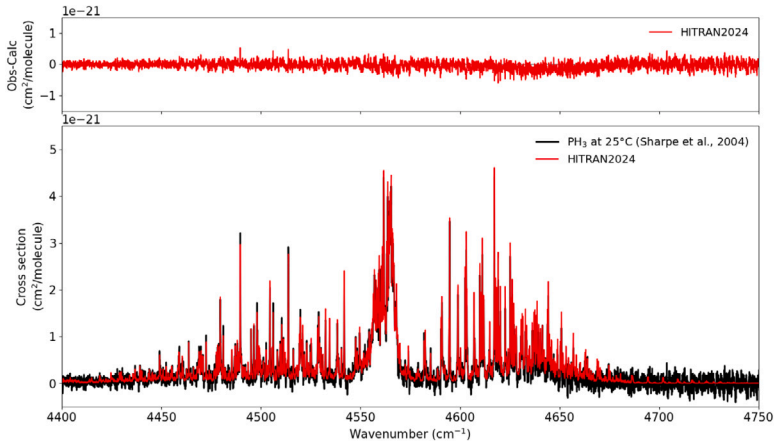

Fig. 22. Line list of phosphine in the NIR region in HITRAN compared to the PNNL spectrum at 25 °C [175,178]. The residuals (Obs−Calc) are presented in the upper panel.

2.30. SF_6: Sulfur hexafluoride (molecule 30)

In the work by Guest et al. [412], a simple machine learning model was trained on all of the air-broadening data in the HITRAN2020 database. It was designed to predict air-broadening values for new molecules based on the properties of said molecules, such as their mass and dipole moment (quadrupole moment contribution ignored for now). The results of this work can therefore be used as new estimates for the HITRAN database where other data are lacking and quadrupole-quadrupole interactions are not expected to play a considerable role.

The air broadening values for SF_6 in the previous versions of HITRAN were based on the 1987 calculations by Tejwani and Fox [413]. Later calculations by Gamache et al. [414] and very recent measurements by Dridi et al. [415] have indicated that the HITRAN2020 values may be too small by almost a factor of two. Interestingly, the machine learned prediction from Guest et al. [412] is in line with Refs. [414, 415]. Considering that the latter two references only provide averaged values, the parameters from Ref. [412] were used for HITRAN2024.

2.31. H_2S: Hydrogen sulfide (molecule 31)

Hydrogen sulfide (H_2S) is a vital component of the global sulfur cycle, occurring in natural environments including wetlands [416] and volcanoes [417], as well as being a byproduct of human activity such as wastewater treatment [418]. H_2S is also measured in natural gas and petrochemical industries (often with tunable diode laser absorption spectroscopy) in order to identify impurities [419]. H_2S is commonly observed in astronomical environments, where it has long been detected in galactic sources [420] and more recently identified in the atmosphere of the hot Jupiter exoplanet HD 189733b [421].

For $H_2{}^{32}S$, portions of an updated, MARVELised version of the ExoMol "AYT2" line list [357] has been used to improve the coverage in HITRAN2024. The original *ab initio* ExoMol AYT2 line list [357] contained over 115 million transitions between rovibrational states up to $J \leq 40$ in the 0–20 000 cm^{-1} range. The first major update to the AYT2 line list was performed by Chubb et al. [422], who carried out a comprehensive MARVEL study of the H_2S spectroscopic literature and validated 25 293 *ortho*- and 18 778 *para*- H_2S transitions from 33 sources.

A second update to the AYT2 line list, used here, added five additional sources to the MARVEL $H_2{}^{32}S$ dataset. Transitions were analyzed from studies in the region of the bending fundamental band between 700 – 1800 cm^{-1} [423], the second hexad between 5650–6660 cm^{-1} containing the $5\nu_2$ band [424] and six interacting bands ($2\nu_1+\nu_2, \nu_1+\nu_2+\nu_3, \nu_1+3\nu_2, 3\nu_2+\nu_3, 5\nu_2, \nu_2+2\nu_3$) [425], a reanalysis in the region containing highly-excited states of the first decad of H_2S [426], and the assignment of Fourier transform absorption spectra in the 9995 to 10 310 cm^{-1} region [427]. Overall, the final MARVELised ExoMol AYT2 line list replaced 294 916 transitions (with intensity above 10^{-32} cm^{-1}/(molecule cm^{-2}) at T = 296 K) up to 16 546 cm^{-1} with experimental-accuracy values.

For HITRAN2024, only data below 9000 cm^{-1} (with intensity above 10^{-28} cm^{-1}/(molecule cm^{-2}) were used to fill in the gaps in HITRAN, as at higher wavenumbers the reliability of *ab initio* intensities declines for such a complex molecule as hydrogen sulfide. Effectively, existing bands have been extended to the higher rotational levels while many hot bands were added. Fig. 23 shows the new and updated lines now available in HITRAN compared to those in HITRAN2020, as well as the lines that remain unchanged. Note that only lines outside of the PNNL region that had MARVEL energy levels were added, as *ab initio* line positions lack accuracy. Therefore, some weak lines are still missing, but are not expected to contribute to absorption noticeably. The new line list was tested against laboratory measurements from PNNL [178].

It is important to specifically address the lines that were updated, which are all related to the overtones of the bending vibration.

Upon comparison with the PNNL data [178], it was determined that the ExoMol intensities for the $3\nu_2$ band are an improvement over the HITRAN2020 values. Therefore, for the main isotopologue of the $3\nu_2$ band, all intensities were changed to those from the ExoMol line list.

Recent experiments by Ulenikov et al. [424,428] in the $4\nu_2$ and $5\nu_2$ bands have shown that there is substantial room for improvement in both HITRAN2020 and ExoMol databases. Most ExoMol intensities for the $4\nu_2$ band exhibited (for most lines) a systematic 12% offset compared to experimental values, see panel (a) in Fig. 24. Therefore, scaled ExoMol intensities were used for this band, with experimental values used when appropriate.

Similarly, for the $5\nu_2$ band, the ExoMol intensities appear to be systematically 39.4% higher than the experimental values (see panel (b) in Fig. 24). Scaled ExoMol transitions were used for HITRAN2024, with experimental values used in many cases.

All new H_2S lines added to HITRAN have had H_2 and He broadening parameters added using the formalism of Tan et al. [30] to allow for calculations relevant to planetary atmospheres.

2.32. HCOOH: Formic acid (molecule 32)

Formic acid, which plays a major role in acid rain formation, is produced in the atmosphere primarily via the oxidation of isoprene and other VOCs via reactions with hydroxyl radicals and ozone [429]. Despite its relevance, only the normal isotopologue has been included in HITRAN since the 1996 edition [11]. So far, the second most abundant isotopologue, $H^{13}COOH$, has only been indirectly identified

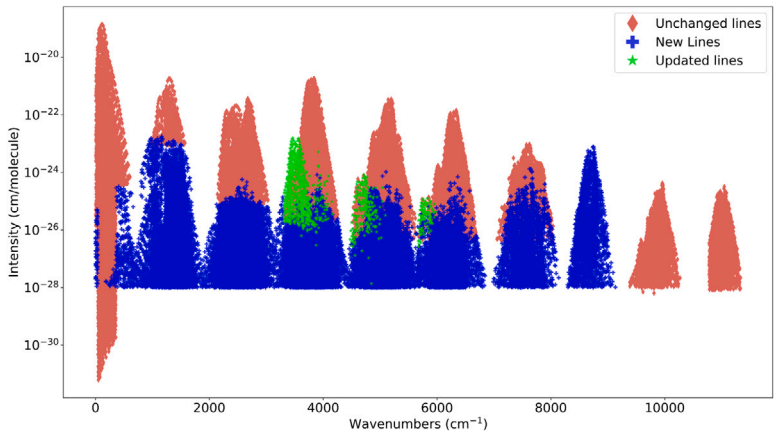

Fig. 23. Overview of the HITRAN2024 line list for H_2S, showing the lines that were unchanged from HITRAN2020 lines (red diamonds), updated lines (green stars), and newly added lines (blue crosses). Note that all isotopologues are shown; however, only the $H_2^{32}S$ lines were added or updated.

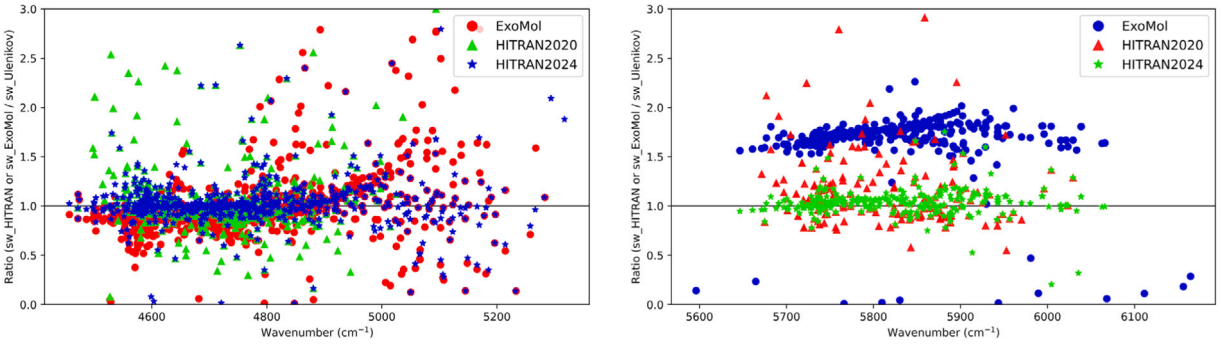

Fig. 24. Assessing the quality of the intensities for the (a) $4\nu_2$ and (b) $5\nu_2$ vibrational bands of H_2S from HITRAN2020, HITRAN2024 and ExoMol with the experimental data from Refs. [424,428]. 10 $4\nu_2$ ExoMol data points, 13 $4\nu_2$ HITRAN2020 data points and one $4\nu_2$ HITRAN2024 data point are outside of the y axis limits. One $5\nu_2$ HITRAN2020 data point is outside of the y axis limits.

in the atmosphere [430]. For these reasons, the $H^{13}COOH$ isotopologue of formic acid was added to HITRAN for the first time. Here, we take the first step toward developing a comprehensive line list by providing a pure rotational dataset in the MW-FIR. Line positions were computed with PGOPHER [431] using the spectroscopic constants (19 parameters included) recently reported for the ground vibrational state [432]. To our knowledge, absolute intensities have not been measured for pure rotational transitions of formic acid. We therefore calculated the Einstein-A coefficients (in PGOPHER) using the very precisely determined experimental dipole moment components of the principal isotopologue; 1.4071 D (a-axis) and 0.227 D (b-axis) [433]. This is similar to what was done when generating the HITRAN line list for the principal isotopologue of formic acid [434]. The intensities included in the line list of this isotopologue in HITRAN cover four orders of magnitude [1.26×10^{-27} to 1.26×10^{-23} cm^{-1}/(molecule cm^{-2})].

Fig. 25 provides a comparison of experimental and simulated spectra in somewhat randomly chosen regions, showing an excellent agreement.

2.33. HO_2: Hydroperoxyl radical (molecule 33)

Unchanged.

In a recent experiment, Chang et al. [435] carried out line strength measurements of the hydroperoxyl radical in the OO-stretching (ν_3) fundamental band using mid-infrared time-resolved dual-comb spectroscopy. They have reported intensities that are almost three-fold stronger than the corresponding values in HITRAN. This claim will have to be thoroughly investigated and, if confirmed, the intensities will need to be adjusted.

2.34. O: Atomic oxygen ("molecule" 34)

The 68 cm^{-1} $^3P_1$-$^3P_0$ and the 158.3 cm^{-1} $^3P_2$-$^3P_1$ lines of oxygen have been measured by Tunable Far-Infrared spectroscopy (Zink et al. [436] and De Natale et al. [437]). Comparison of the results is favorable for the $^3P_2$-$^3P_1$ transition, with essentially identical results achieving 150 kHz (30 ppb) uncertainty. Drouin et al. [438] performed a pressure-shift study of the 68 cm^{-1} transition with a heterodyne system to resolve the 460 kHz discrepancy in the $^3P_1$-$^3P_0$ TuFIR measurements and has reported an improved rest frequency with an accuracy of 17 kHz.

Pressure broadening was not reported in the literature, but the $^3P_1$-$^3P_0$ study of Drouin et al. indicates the HITRAN value for air broadening, 0.05 cm^{-1}atm^{-1}, is consistent with under-sampled N_2 and O_2 broadening in their data. Pressure induced O_2/N_2 shifting for $^3P_1$-$^3P_0$ is reported in Drouin et al. to be $-2.0(3) \times 10^{-5}$ cm^{-1}atm^{-1} and for He to be $-3(1) \times 10^{-6}$ cm^{-1}atm^{-1}. The new values have been included in HITRAN2024.

2.35. $ClONO_2$: Chlorine nitrate (molecule 35)

Unchanged.

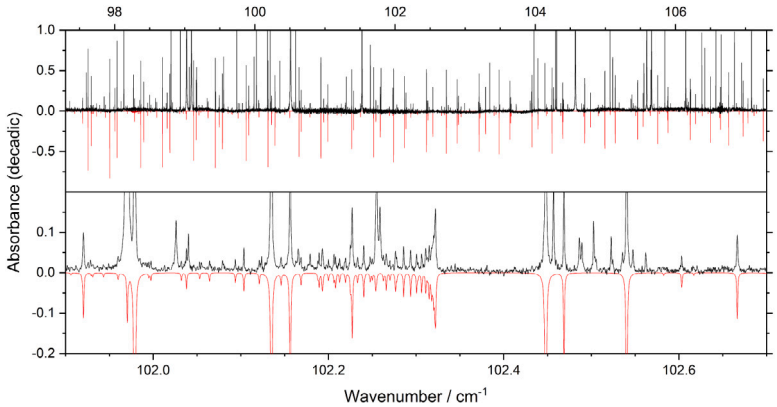

Fig. 25. Top panel: Experimental (upward; 0.25 Torr) and simulated (downward) spectra of $H^{13}COOH$ using a Gaussian FWHM of 0.0006 cm^{-1}. Bottom panel: Experimental (upward; 1.5 Torr) and simulated (downward) spectra using a Lorentzian FWHM of 0.0012 cm^{-1}.

2.36. NO^+: Nitric oxide cation (molecule 36)

Unchanged.

2.37. HOBr: Hypobromous acid (molecule 37)

Unchanged.

2.38. C_2H_4: Ethylene (molecule 38)

The line list of ethylene was not updated for HITRAN2024; however, it has been the subject of many recent experimental and theoretical works. Here, we review and provide preliminary evaluations of some of the new sources and their perspectives for future updates.

The ethylene line list in the 3.3 μm region has been incorporated in the HITRAN database since its 2000 edition [12]. The HITRAN2020 line list in this region still contains many unassigned transitions. In addition, it includes 281 transitions of $^{12}C^{13}CH_4$. Very recently, two studies have revisited the highly-congested room temperature ethylene spectrum in the 3.3-μm region, both using spectra recorded at ULB by Fourier transform spectroscopy: (i) In Ref. [439], more than 3300 transitions of four bands (ν_9, ν_{11}, $\nu_2+\nu_{12}$ and $2\nu_{10}+\nu_{12}$) were assigned and modeled using the tensorial formalism elaborated in Dijon. A polyad scheme was developed, taking into account some fundamental bands previously analyzed thanks to the tensorial formalism, but the polyad corresponding to the region of interest was limited to the upper states of the four assigned bands. As a result, 88 parameters of the effective Hamiltonian were adjusted, leading to a root mean square (RMS) of the (Exp.-Calc.) position differences significantly larger than the experimental position accuracy. The developed model led to the elaboration of the ECaSDa calculated line list accessible at https://vamdc.icb.cnrs.fr/PHP/ecasda.php. (ii) In Ref. [440], about 6870 lines have been retrieved from a single FTS spectrum between 2912 and 3270 cm^{-1}. Relying on the position and intensity agreements with a line list of transitions for the principal isotopologue calculated by the variational method [441], a total of 4287 lines were assigned to 5797 transitions of eight cold bands, four of them being newly reported. In addition, about 200 transitions were assigned to four hot bands. Overall, the assigned lines represent 94% of the total experimental intensity in the region. The detailed comparison to the HITRAN2020 list included in Ref. [440] shows an excellent agreement for both positions and intensities. The comparison of the ECaSDa list to both Ref. [440] and to the HITRAN list indicates that the model underlying the ECaSDa list is not sufficient to reproduce the observations. In a number of regions, large discrepancies are noted for the ECaSDa list, both for line positions and for line intensities, while a good agreement is noted between the HITRAN simulation and the FTS spectrum. Some minor deficiencies of the HITRAN list were evidenced and discussed in Ref. [440], in particular, some components are missing from the HITRAN list in the case of overlapping multiplets. One should note that the HITRAN assignments are limited to four cold bands and one hot band, while those of Ref. [440] belong to eight cold bands and four hot bands. Ideally, an improved recommended list based on HITRAN and Ref. [440] could be elaborated, but as there is no unique correspondence between the HITRAN and TheoReTS assignments, the merging of the two sets of assignments in a consistent way is not straightforward and remains to be done.

At the moment, the HITRAN list of ethylene does not provide data above 3242 cm^{-1}. In recent years, empirical line lists have become available in the 5800–8050 cm^{-1} region using a series of ethylene FTS spectra recorded at room temperature [442,443] and laser spectroscopy of jet-cooled spectra [444]. This region includes the strong $\nu_5+\nu_9$ band centered near 6150 cm^{-1} which is particularly suitable for quantitative detection in the 1.6 μm transparency window in the atmosphere. The complexity and the congestion of the ethylene spectrum in this range are such that traditional methods are hardly operative to assign the spectrum. The recent achievements of high-level extensive variational calculations based on accurate ab initio potential and dipole moment surfaces [441] made it possible to rovibrationally assign most of the strong or intermediate lines by position and intensity comparison between experiment and ab initio theory. While some preliminary lists are already available, more work is ongoing in this region to be included in the next edition of HITRAN.

2.39. CH_3OH: Methanol (molecule 39)

After methane, methanol (CH_3OH) is the most abundant volatile organic compound (VOC) in the terrestrial atmosphere, as it is released by plants during cell growth. It is routinely monitored by satellite instruments [445]. It is present in the ISM [446], protoplanetary disks [447], and comets [448]. Spectroscopy of methanol exhibits rovibrational structure complicated by the internal motion of the methyl (CH_3) rotor with respect to the hydroxyl (OH) frame, inducing multiple torsional bands and combinations. Because of its complexity, the line-by-line portion of the database for CH_3OH contains only the pure rotational region as well as the region of ν_7 and ν_8 fundamentals at 10 μm. Therefore, atmospheric scientists are forced to retrieve other regions with the help of experimental cross-sections, rather than the line list. In this edition, we add the torsional band of methanol.

Line positions and intensities of methanol ($^{12}CH_3OH$) in the torsional bands across the 300–500 cm^{-1} region were first measured by Brauer et al. [449], using high-resolution FT-IR spectra on a Bruker IFS 125 HR at JPL. In total, 1316 observed features were characterized, including torsional fundamental (υ_{12} – gs), overtones ($n\upsilon_{12}$ – gs, $n = 2,3,4$), and torsional hot bands.

Each K level is split into rotational symmetry species labeled A, E_1, or E_2. Levels with E_1 symmetry use positive K, those with E_2 negative. The A-state non-zero K transitions split into asymmetry doublets, labeled A^+ and A^- [450,451]. Most A species were observed as single lines in FT-IR spectra. Rotational weights consist of:

$$g(\text{rot}) = g(J) \times g(i) \times g(s)$$

where $g(J) = (2J + 1)$, $g(i) = 2$, and $g(s)$ from CH_3 symmetry follows [452,453]:

$$\epsilon(A^+) = \epsilon(A^-) = \epsilon(E_1) = \epsilon(E_2) = 4$$

or $\epsilon(A) = 8$ if A^+/A^- is not resolved. This work adopts $g(s) = 4$ for consistency with partition function calculations [448,454].

Note: HITRAN's 10-μm line list drops $g(s)$, which cancels out for Einstein-A coefficients as transitions between A and E species are forbidden.

Recently, J. Pearson (JPL) reviewed and extended models [451,453,455], noting the ground state is best described by rotation perturbed by hindered internal rotation, while the second excited torsional state resembles a free rotor. E'' values are referenced to the $J = K = 0A$ $v_t = 0$ level at 127.97549 cm^{-1} above the barrier (slightly above the zero-point energy from Ref. [453] at 127.683156 cm^{-1}).

For SOFIA/EXES analysis, Nickerson et al. [456] extended Brauer et al. [449] work by adding E'' values using Pearson's levels, combining [455] (low J), [453] (intermediate J), and new models (high J). Line positions and intensities from Brauer et al. [449] were unchanged. Air- and self-broadening widths were assumed to be 0.1 and 0.45 cm^{-1}/atm.

The new linelist in the 300–500 cm^{-1} region includes:

- 395 A–A transitions (unsplit),
- 86 A–A (split),
- 109 A–A (split in only one state),
- 724 E–E (all split).

It enabled the first astrophysical detection of CH_3OH near 25 μm toward a massive protostar [456].

2.40. CH_3Br: Methyl bromide (molecule 40)

Unchanged.

2.41. CH_3CN: Methyl cyanide (molecule 41)

Methyl cyanide, also known as acrylonitrile or cyanomethane, is a trace species in the terrestrial atmosphere where it is detected by high-resolution spectroscopy employing microwave limb-sounding [457] or balloon-borne IR spectroscopy [458]. Most of CH_3CN is produced by biomass burning [459,460]. Methyl Cyanide was one of the first molecules to be detected by radio astronomy [461]. Besides high-mass star-forming regions, it was found toward low-mass protostars [462], cold, dark molecular clouds [463], carbon-rich late-type stars [464], in the disks around young protostars [465], and toward external galaxies [466]. CH_3CN was identified in the atmosphere of Titan [467] and was also found in comets [467].

CH_3CN was first introduced in HITRAN2008 [14] by adding the ν_4 band, with additional unassigned lines probably due to its $\nu_4 + \nu_8 - \nu_8$ hot band. The data were based on a multispectrum analysis of this band and preliminary modeling of positions and intensities [468] as well as additional unpublished data. The HITRAN2024 data is based on Müller et al. [469], comprising rotational and rovibrational data up to $v_4 = 1$ with consideration of spectroscopic parameters of $v_7 = 1$ and $v_8 = 3$, mostly from a previous study [470], along with data pertaining to $v_4 = v_8 = 1$ and the $\nu_4 + \nu_8 - \nu_8$ hot band. The rotational data are new in HITRAN, as are the ν_8, $2\nu_8 - \nu_8$, and $2\nu_8$ bands.

The line positions of the present dataset were derived by Müller et al. [469] mostly in a combined fit of rotational and rovibrational data employing Pickett's spfit and spcat programs [471–474]. Most of the $v = 0$ data are based on Ref. [475]. Higher frequency submillimeter data are from that work, most of the millimeter to mid-submillimeter data are from Ref. [476], and $\Delta K = 3$ ground state combination loops [477] are the basis for the purely K-dependent parameters. The treatment of the high-K resonant interaction between $v = 0$ and $v_8 = 1$ was carried out later [478] with some additional measurements of perturbed transitions from Ref. [469]. Ref. [478] also contributed additional high-frequency submillimeter data.

The emphases of Ref. [478] were the analyses of $v_8 = 1$ and 2 and their high-K interactions pertaining to the selection rules $\Delta v_8 = \pm 1$, $\Delta K = 0$, $\Delta l = \pm 3$ on one hand and $\Delta v_8 = \pm 1$, $\Delta K = \mp 2$, $\Delta l = \pm 1$ on the other hand. The latter selection rule describes the interaction between $v = 0$ and $v_8 = 1$. Spectroscopic parameters of $v_4 = 1$, $v_7 = 1$, and $v_8 = 3$ from a previous study [470] were used to account for the interaction of $v_8 = 2$ with these states, which manifest themselves in particular in the pure rotational data. The $v_8 = 1$ and 2 rotational data were predominantly from Ref. [478], the $2\nu_8$ rovibrational data were entirely from that work, whereas the ν_8 data were taken from an earlier study [479]. Additional measurements of perturbed transitions in $v_8 = 1$ and 2 are from Ref. [469]; the perturbations involve mostly those differing in v_8 by one, but also an l-type resonance within $v_8 = 2$. Furthermore, some $2\nu_8$ assignments were corrected because of the use of a different calibration in the early stages of the investigation [469,478], and a few more new assignments were also added.

The latest account on the lower-lying vibrational states of methyl cyanide [469] added in particular an extensive analysis of $v_4 = 1$ and its associated ν_4 rovibrational band to the picture. The rotational data were again predominantly, and the rovibrational data entirely, from that study. One of the difficulties in modeling the data satisfactorily in the early days was the fact that $K = 7$ of $v_4 = 1$ interacts with all four l-substates of $v_8 = 3$, while only the $\Delta K = 0$ interaction at $K = 7$ and 8 was mentioned previously [470]. Fig. 2 of Ref. [469] indicates further resonances.

Even though the $v_4 = v_8 = 1$ spectroscopic parameters were defined as an extension to the existing fit and could have been added to the combined fit, the fit of the rotational data pertaining to this state as well as the $\nu_4 + \nu_8 - \nu_8$ rovibrational data were treated in a separate fit to avoid affecting the lower-state parameters through perturbations in $v_4 = v_8 = 1$. While this state is heavily perturbed by states such as $v_8 = 3$ and 4, among others, [469,480], the lower K levels, between −5 and +6 are only slightly perturbed at most, except possibly for high J, above ~50.

The accuracy and precision of the ν_4 band is 1×10^{-4} cm^{-1} except possibly at the highest K level and the highest about 5 in J. The accuracy and precision of the $2\nu_8$ band and the $\nu_4 + \nu_8 - \nu_8$ hot band are 2×10^{-4} cm^{-1}, possibly slightly better, and with some deterioration to the highest values of K and J. The precision of the ν_8 band is about 2×10^{-4} cm^{-1}, that of the $2\nu_8 - \nu_8$ hot band probably 3×10^{-4} cm^{-1}. The precision and accuracy of the rotational data is usually much better than 3×10^{-6} cm^{-1} for J up to about 60 and K up to 15 with the exception of $v_8 = 2$,, where caution is advised above $K = 12$ (when $l = 0$) and 10 (when $l = -2$).

The intensities of the rotational transitions of CH_3CN are well described by the permanent dipole moment in the respective vibrational state. The ground state value was determined in Ref. [481], while the small changes upon vibrational excitation were derived from laser-Stark IR spectroscopic studies of $CH_3C^{15}N$ [482,483]. The ν_8 and the $2\nu_8$ intensities are each well modeled by a single transition dipole moment, which was determined in Ref. [478]. The ν_8 value is also appropriate for the $2\nu_8 - \nu_8$ hot band components. A preliminary analysis of the $3\nu_8 - \nu_8$ hot band and $\nu_7 - \nu_8$ difference band system suggests that their intensities are also well modeled by the $2\nu_8$ transition dipole moment. In contrast, the ν_4 intensities required a Herman-Wallis correction to

account quite well for the stronger *P*-branch compared to the *R*-branch [469]. Small systematic deviations, up to the 1 or 2% level, suggested the need for a higher order Herman-Wallis correction, but this appeared to be unavailable in the spcat program. Therefore, the Herman-Wallis correction was chosen to best account for medium to high values of J and K.

The broadening and shift parameters were also refined. Müller et al. [478] provided self- and N_2-broadening coefficients, initially modeled as polynomial functions of quantum numbers J and K derived from the ν_4 investigation [468]. While the N_2-broadening was well reproduced, the self-broadening coefficients required refitting, yielding significantly different values from the original publication. Additional corrections were made using semi-classical broadening coefficients from Dudaryonok et al. [484,485]. A fixed value of $\gamma_{N_2} = 0.12$ was applied for transitions with $J > 50$ or $K > 17$. In order to obtain γ_{air} for consistency with the rest of the molecules in HITRAN, a scaling factor of 0.93 was applied to the values of γ_{N_2} based on a recommendation from Ma and Boulet [486]. Pressure-induced frequency shifts were estimated using scaling relations [478], ensuring that all bands, including ν_8, and $2\nu_8$, and ν_4 were supplemented with reliable parameters.

Since the $3\nu_8-\nu_8$ hot band and $\nu_7-\nu_8$ difference band system are not yet available in HITRAN, the $2\nu_8$ band is not as appropriate for low to modest resolution investigations because the Q-branch of $3\nu_8-\nu_8$ shows up near 713 cm^{-1}, as can be derived from Ref. [469]. In addition, the hot band affects intensities around the Q-branch of the cold band and also in the P-branch. The analysis of the strongly interacting $\nu_7/3\nu_8$ system is intended for the not-too-distant future. This will result in calculations of the respective cold bands as well as the main hot bands in the $2\nu_8$ region.

Note that the line list described above corresponds to the update to the HITRAN2020 database issued in October 2024.

2.42. CF_4: Carbon tetrafluoride (molecule 42)

Very high-resolution THz spectra of $\nu_3 - \nu_3$ lines in the 0–110 cm^{-1} region of CF_4 have recently been recorded thanks to a new high finesse cavity coupled to the CRDS technique [487]. This has enabled the measurement of 54 line positions with unrivaled accuracy, as well as absolute intensities of 52 of these transitions. As for line positions, although this is a small number of data points, compared to the known CF_4 transitions, their extreme precision has a significant influence when introduced in global effective Hamiltonian fits. This is also the first time that THz line intensities have been measured for this molecule. The results compare very well to *ab initio* calculations. The transitions in question have thus been introduced in the present HITRAN edition.

In the HITRAN2020 paper, there was already a discussion of potentially using the *ab initio* calculated line lists in the future. Construction of the *ab initio* line list for $^{12}CF_4$, as originally presented in Ref. [488] and validated in [489], has been revisited using the methodology recently proposed [355] to construct effective Hamiltonians and dipole moment operators from ab initio surfaces. It is a numerical procedure accounting for full symmetry properties that brings the nuclear-motion Hamiltonian into a block-diagonal form up to a polyad P (here $P = 15$). For the first time, an *ab initio* effective dipole moment is derived automatically for line intensity calculations while the parameters of the Hamiltonian can be easily refined on experimental data. The final line list contains around 86 million transitions in the range 0–3641 cm^{-1} up to $J_{max} = 80$. It is composed of 87 cold bands and 593 hot bands whose the sum of intensities is 1.29×10^{-16} and 0.66×10^{-16} cm/molecule, respectively. This will be used for future updates of CF_4 in HITRAN.

2.43. C_4H_2: Diacetylene (molecule 43)

Diacetylene (HC_4H) is the simplest member of the polyacetylene family ($HC_{2n}H$ with $n = 1, 2, 3, \ldots$) and is a well-known interstellar molecule. It has been detected in Titan's atmosphere in the early 1980's as well as in the atmosphere of all four giant planets of the Solar system between 1997 and 2008. Within our galaxy, diacetylene has been observed in protoplanetary nebulae; outside the Milky Way, HC_4H has been detected only in the Large Magellanic Cloud (see Ref. [490] for a brief review of the astronomical bibliography). Since diacetylene has no permanent dipole moment, all these detections were based on the observation of its infrared spectrum and in particular through the very strong ν_8 band, located around 628 cm^{-1} ($\Pi_u - \Sigma_g^+$, absolute intensity $I = 563$ $cm^{-2}\,atm^{-1}$); only in a few cases, the υ_9 ($\Pi_u - \Sigma_g^+$, 220 cm^{-1}, $I = 60$ $cm^{-2}\,atm^{-1}$) and $\nu_6 + \nu_8$ bands ($\Sigma_u^+ - \Sigma_g^+$, 1241 cm^{-1}, $I = 169$ cm^{-2} atm^{-1}) were also observed. In the 3 μm region, diacetylene possesses the second most intense feature of its infrared spectrum, i.e. the ν_4 fundamental band ($\Sigma_u^+ - \Sigma_g^+$, $I = 476$ $cm^{-2}\,atm^{-1}$) centered at 3333 cm^{-1}. However, due to the presence of several perturbations, the analysis of the ν_4 band was so far preliminary and limited to low J levels [491].

In the HITRAN2024 edition, we included a reliable line list for the ν_4 band of diacetylene, which extends between 3297 cm^{-1} and 3365 cm^{-1} and includes rotational levels up to $J = 115$ analyzed at experimental accuracy. The new analysis is based on newly recorded infrared spectra obtained at high resolution (0.005 cm^{-1}) at the AILES beamline of the SOLEIL synchrotron facility and will be presented in a dedicated paper [492].

To achieve a good modeling of the rotational manifold in the $\upsilon_4 = 1$ state, it has been necessary to include the interactions with four different Σ-like dark states, which also give rise to perturbation-enhanced ro-vibrational transitions. The line strengths have been calculated starting from the absolute intensities determined by Jolly et al. in Ref. [490] and following the procedure described in the Appendix of Ref. [493].

2.44. HC_3N: Cyanoacetylene (molecule 44)

HC_3N is ubiquitous in a large variety of extraterrestrial environments such as star-forming cores, interstellar and circumstellar medium, comet comas, and planetary atmospheres (see Ref. [494] for an extensive bibliography account). The infrared spectrum of HC_3N has been targeted by a number of investigations in recent years [493,494] and a linelist up to 3360 cm^{-1} has been already included in the HITRAN 2020 paper [17]. Despite the breadth of such studies, one of the most prominent spectral features of HC_3N, the $2\nu_5$ overtone located at $\sim$ 1300 cm^{-1}, lacks a satisfactory analysis. In fact, the upper $\upsilon_5 = 2$ level is involved in a complex network of anharmonic resonances and the spectrum shows anomalies in the retrieved spectroscopic constants and evidence of local perturbations. These issues had already been reported in an earlier study [495], but the lack of reliable energy values for the interacting ($\upsilon_4 = 1, \upsilon_7 = 2$) levels and the neglect of other minor resonances prevented an accurate modeling of the full resonance system. We carried out a comprehensive analysis of a five-state polyad including $\upsilon_5 = 2$, ($\upsilon_4 = 1, \upsilon_7 = 2$), ($\upsilon_6 = 2, \upsilon_7 = 2$), ($\upsilon_5 = 1, \upsilon_7 = 3$), and $\upsilon_7 = 6$ states. The detailed description of the analysis and an account of the experimental data used will be presented in a dedicated paper [492]. In the HITRAN2024 issue, we include a new linelist for $2\nu_5$ in the 1270–1360 cm^{-1} wavenumber range characterized by a precision as good as 1×10^{-4} cm^{-1}. The line strengths for the $2\nu_5$ band have been calculated by deriving the Θ_{55} intensity factor from the absolute intensities determined in Ref. [496] and following the procedure described in the Appendix of Ref. [493]. In addition, we further explored the 3–5 μm stretching region. The HC_3N stretching fundamentals are located at 2079 cm^{-1} (ν_3), 2274 cm^{-1} (ν_2), and 3327 cm^{-1} (ν_1). This spectral interval was studied by Jiang et al. [497] and a linelist for the fundamentals and the ν_7-associated hot bands was

included in the HITRAN2020 edition [17]. In that list, some lines for the ν_1 and $\nu_1+\nu_7-\nu_7$ bands showed evidence of local perturbations, and were excluded from the analysis. With the goal of providing reliable data for the present HITRAN2024 issue, we performed a detailed treatment of these accidental resonances generating an updated linelist in the 2030–3360 cm^{-1} range, including also the $\nu_2+2\nu_7-2\nu_7$, and $\nu_3+2\nu_7-2\nu_7$ hot bands. The precision of this latter data compilation is better than 5×10^{-4} cm^{-1}.

2.45. H_2: Molecular hydrogen (molecule 45)

Molecular hydrogen, the most abundant molecule in the universe, plays a crucial role in the chemistry and thermal balance of a wide range of environments, including the interstellar medium [498–500], the atmospheres of giant planets in the Solar System [501–503], and hot Neptune- and Jupiter-type exoplanets [118,504]. Although the deuterated isotopologue of hydrogen, HD, is significantly less abundant, its small electric dipole moment gives rise to observable rovibrational transitions, which are notably stronger than those of H_2 [505]. These electric dipole transitions are particularly important for determining the D/H ratio in giant planets within the Solar System, a key parameter in planetary evolution models [501–503]. Accurate collisional line-shape parameters for both H_2 and HD lines, perturbed by both H_2 and often considerably abundant He atoms, are therefore essential for reliable modeling of these astrophysical environments [501,503].

2.45.1. Line positions and intensities

The 2024 edition of HITRAN features datasets for the two most important isotopologues of molecular hydrogen: H_2 and HD. In this edition, we update the electric dipole and quadrupole line lists, as well as add magnetic dipole transition data [506], which were previously absent, see Fig. 26.

For the intensities of electric transitions (both dipole and quadrupole), we used the results of calculations performed in Ref. [507] for H_2 and Refs. [508,509] for HD. Compared to the HITRAN2020 edition, the line intensities are corrected, on average, by approximately 1%, but for some weak lines the improvement is much larger, see Ref. [506] for details. We also removed inconsistencies between line intensities and corresponding Einstein coefficients that were present in HITRAN2020 for some lines (mainly for some quadrupole lines in HD). For the intensities of the magnetic dipole lines of the H_2 isotopologue, we relied on the results of Ref. [507], and for HD we used the calculations from Ref. [506].

The 2024 edition of HITRAN uses the line positions for the electric dipole and quadrupole lines from Ref. [507] for H_2 and Ref. [510, 511] for HD. These values are very similar to those present in the HITRAN2020 database, but the uncertainties were overoptimistic and are corrected in the 2024 edition [506]. The positions of the newly-added magnetic dipole lines are taken from Refs. [507,510,511] for H_2 and HD.

2.45.2. Line-shape parameters

In HITRAN2024, a comprehensive dataset of the beyond-Voigt line-shape parameters for the four systems (He- and H_2-perturbed H_2 and HD lines) was added. We used the recently adopted modified Hartmann-Tran (mHT) [512] parametrization together with the double power-law temperature dependencies [513]. We used data from Ref. [506] which provides a compilation of the recent accurate *ab initio* calculations for He-perturbed lines of H_2 [514–516] and HD [517–519], as well as for the H_2-perturbed HD [520] and H_2 [513,521] lines. These results have been validated against accurate experimental spectra [520, 522–524], leading to sub-percent agreement between theoretical and measured spectral line shapes.

For the He-perturbed H_2 and HD lines, we used the recently published comprehensive sets of accurate *ab initio* line-shape parameters [516,518]. The *ab initio* calculations cover not only the strongest bands but also weak overtones and hot bands. For very weak lines, the datasets were populated based on *ab initio* data extrapolations. For every line we provide the six mHT line-shape parameters: broadening and shift (γ_0 and δ_0), speed dependence of the broadening and shift (γ_2 and δ_2), and the real and imaginary parts of the complex Dicke parameter ($\tilde{\nu}^r_{opt}$, $\tilde{\nu}^i_{opt}$), see Ref. [512] for details.

For the H_2-perturbed H_2 and HD lines, the accurate *ab initio* line-shape parameters recently became available but only for several transitions [506,513,520,521]. We used the rotational and vibrational quantum number dependencies from He-perturbed lines to extrapolate the H_2-perturbed line-shape parameters. For some lines, we also included the available experimental data. The details of this procedure are described in Ref. [506].

In HITRAN2024, for the first time, we provide the six mHT line-shape parameters for magnetic dipole transitions in H_2 and HD. For the He-perturbed case, we took the recently published accurate *ab initio* data [506]. For the H_2-perturbed case, we used the extrapolation based on the line-shape datasets for the He- and H_2-perturbed H_2 electric quadrupole lines and He-perturbed magnetic lines, see Ref. [506].

In addition to the sophisticated dataset of the beyond-Voigt line-shape parameters (the mHT profile parameters) described in the previous paragraphs, HITRAN2024 also provides standard Voigt profile parameters that are consistent with the HITRAN 160-character ".par" file format. The broadening and shift parameters are taken from the mHT dataset with corrections due to the speed-dependent effects, see Refs. [506,525,526] for details. Since for most astrophysical applications the main perturber is H_2, we took H_2-perturbed parameters for both self- and air-broadened cases in the 160-character ".par" file format.

2.45.3. Future perspective

One should note that the H_2-perturbed cases are much more challenging from a computational perspective (than the He-perturbed cases) due to the increased dimensionality of the interaction potential (six dimensions for diatom-diatom systems compared to three for diatom-atom) and the need to account for the internal rotational structure of both collision partners in quantum scattering calculations. Additionally, the perturbing H_2 molecule occupies a range of rotational states at a given temperature, requiring thermal averaging over the results obtained from separate scattering calculations performed for each populated rotational level. Nevertheless, it was recently shown that such accurate *ab initio* calculations are feasible for the H_2-perturbed cases [513,520,521]. In the case of self-perturbed H_2 lines, quantum indistinguishability presents an additional challenge: standard calculations of the line-shape parameters make a clear distinction between the spectroscopically active molecule and the perturber [527]. When the two molecules are identical, additional symmetry considerations must be incorporated into quantum scattering calculations [528]. Although theoretical extensions of line-shape theory have been developed to include such symmetry effects [529]—as well as for the resonant exchange of excitation between indistinguishable molecules [530]—they have not yet been applied in actual quantum scattering calculations and validated against experimental spectra. The ongoing work on this problem (in the group of authors of Ref. [520]) allows one to anticipate that the comprehensive dataset of accurate H_2-perturbed H_2 and HD line-shape parameters should appear in the next HITRAN editions.

2.46. CS: Carbon monosulfide (molecule 46)

Unchanged.

2.47. SO_3: Sulfur trioxide (molecule 47)

The quantum number format for the SO_3 line list has been updated for consistency with other D_{3h} planar molecules (e.g., CH_3). For a complete description of quantum number identifications of the energy levels, users are referred to https://hitran.org/quanta/ where the global and local quanta are described. The Einstein A values for SO_3 bands in the IR have been updated.

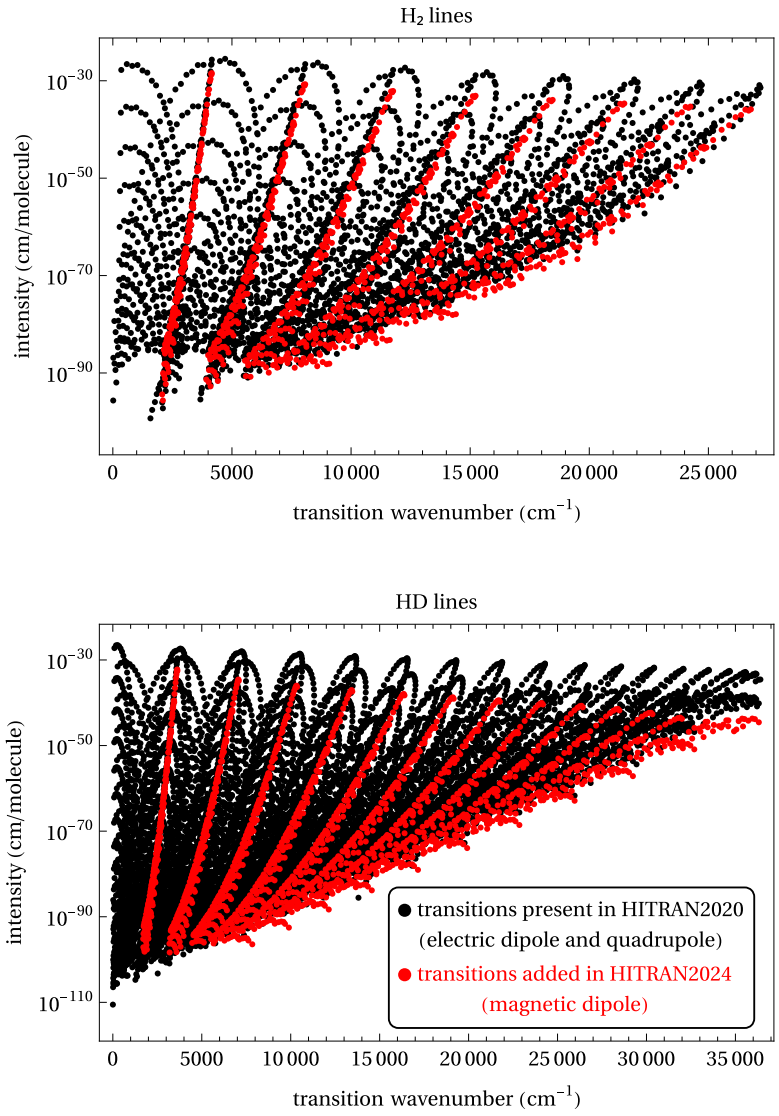

Fig. 26. H_2 and HD lines present in HITRAN2024. The black points are the electric quadrupole and dipole (for HD) lines. The red points are the magnetic dipole lines. Besides adding new lines, HITRAN2024 updates positions, intensities, and line-shape parameters for all the lines (including the ones available in the previous editions of HITRAN).

2.48. C_2N_2: Cyanogen (molecule 48)

Unchanged.

2.49. $COCl_2$: Phosgene (molecule 49)

Unchanged.

2.50. SO: Sulfur monoxide (molecule 50)

Sulfur monoxide is found in several astronomical sources, including star-forming regions, the upper atmosphere of Venus [531], and in the volcanic plumes on Io, a moon of Jupiter [532]. As summarized by Calmonte et al. [533], SO was detected in the atmospheres of different comets.

Vibration–rotation bands for the ground $X^3\Sigma^-$ state have been added for the principal isotopologue $^{32}S^{16}O$. Line positions and lower-state energies were calculated with PGOPHER [534] from the spectroscopic constants obtained previously for v = 0 to v = 6 for the $X^3\Sigma^-$ state and v = 0–5 for the metastable $a^1\Delta$ state [535,536]. Line strengths were based on *ab initio* dipole moment functions. RKR potential energy curves were calculated with the equilibrium spectroscopic constants and input to Le Roy's LEVEL program [537] along with the calculated dipole moment points [535].

The Herman–Wallis effect [538] for the vibration–rotation bands was taken into account by calculating N- and v-dependent dipole matrix elements with LEVEL. These matrix elements were transformed to J-dependent dipole matrix elements as needed for PGOPHER to calculate line lists. PGOPHER provides Einstein A values, line positions, and lower-state energies.

For inclusion in HITRAN, the supplemental PGOPHER file from Bernath et al. [535] was used to recalculate the line list up to $J = 75$, as some transitions were excluded in the supplemental line list of Bernath et al. [535] due to an intensity threshold limit in PGOPHER. Lines assigned as $R(J'' = 7)$, $T(N'' = 73)$ contained anomalous intensities and were omitted. The PGOPHER file was converted to the HITRAN format [17], which includes a shift of the energy levels by 5.5913 cm^{-1} to account for the lowest occupied energy level. At this time, only the vibrational transitions for the ground electronic state ($X - X$) are new additions to HITRAN. The entries for the pure rotational transitions and the forbidden $a^1\Delta - X^3\Sigma^-$ and $b^1\Sigma^+ - X^3\Sigma^-$ transitions of SO are unchanged from HITRAN2020. Fig. 27 summarizes the SO line list for HITRAN2024.

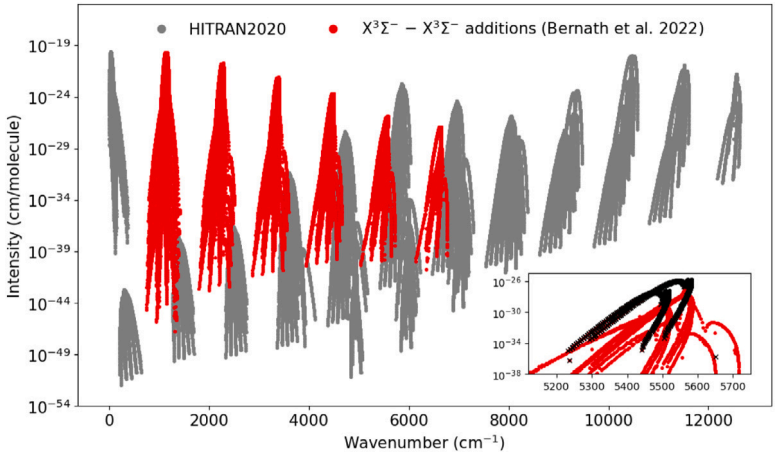

Fig. 27. Overview of the SO line list in HITRAN. The red points highlight the $X^3\Sigma^-$ ground state transitions from Bernath et al. [535] that have been included for HITRAN2024. The inset displays the 5 – 0 band, with black crosses indicating lines that were included in the supplementary material of Bernath et al. [535] and demonstrates the expanded coverage in HITRAN.

The broadening parameters for SO are estimated from those of the iso-electronic oxygen molecule, as was done for HITRAN2020. The air- and self-broadening functions used for the oxygen A-band [539] have been used for SO lines, with a default value for temperature dependence. However, we note that the machine learning model of Guest et al. [412] predict that the air-broadening of SO is larger than that for O_2 by a factor of up 3.5. This issue will be investigated in future.

A more recent and comprehensive semi-empirical line list for $^{32}S^{16}O$ has been calculated as part of the ExoMol project [540], which extends into the UV region and includes MARVELized energy levels. Line positions and intensities have been compared to those in HITRAN and a number of differences between the line lists was observed. This includes a differing structure for the intensity ratio of *P*- and *R*-branches in the $b - X$ (0 – 0) band, which appears to shift the band center when compared to HITRAN (from [536]). An update to Brady et al. [540] is being undertaken and will be considered for future updates of the SO line list.

2.51. CH_3F: Methyl fluoride (molecule 51)

Methyl fluoride (CH_3F) is present in trace amounts in the atmosphere, playing a role in the depletion of the ozone layer (through CH_3 and F radicals) and also in the greenhouse effect (global warming potential = 97, lifetime = 2.6 years) [541]. Up to now, atmospheric detection of this gas by spectroscopic methods could only be performed using absorption cross-sections since only the weak ν_6 band was present in HITRAN2020 [17] around 8.3 μm. The HITRAN2024 edition now contains the strong ν_3 band around 9.5 μm, ten times more intense than the ν_6 band. Based on recent measurements and calculations from Khan et al. [542] and calculated line positions from Papoušek et al. [543], Papoušek et al. [544], a line list has been generated between 945 and 1103 cm^{-1} for a total of 8907 transitions belonging to the ν_3, $2\nu_3$–ν_3, ν_3+ ν_6–ν_6 bands of $^{12}CH_3F$ and to the ν_3 band of $^{13}CH_3F$ (see Ref. [542] for details). The $^{13}CH_3F$ isotopologue is included for the first time in HITRAN. For the ν_6 band included in HITRAN2020, the air-broadening was roughly estimated to be equal to the N_2-broadening coefficients modeled in Ref. [545] multiplied by 0.9. However, by comparing the O_2- and N_2-broadening coefficients obtained at room temperature for the ν_2 and ν_5 bands from Refs. [546–548], the average γ_{O2}/γ_{N2} ratio was found to be equal to 0.787(20) leading to a ratio γ_{air}/γ_{N2} around 0.955. Assuming no vibrational (or isotopologue) dependence of CH_3F broadening coefficients, the ratio 0.955 (instead of 0.9 used in HITRAN2020) has been used to calculate the air-broadening coefficients from the N_2-broadening coefficients modeled in Ref. [545] for all bands present in HITRAN.

2.52. GeH_4: Germane (molecule 52)

Unchanged.

2.53. CS_2: Carbon disulfide (molecule 53)

CS_2 is a volatile and highly toxic gas, present in small but detectable amounts in the Earth's atmosphere due to volcanic and industrial processes [549]. It has also been identified in planets [550] and comets [533]. In fact, the addition of the four most abundant CS_2 isotopologues to HITRAN2020 [551] in the range of 0 - 6470 cm^{-1} and J up to 150 has enabled its first detection in the atmosphere of Venus [326] and a sub-Neptune exoplanet TOI-270 d [552]. It is expected to contribute to the sulfur chemistry and photochemistry of exoplanets, and is considered to be a potential biomarker [553].

In 2022, Tashkun [554] published a new global non-polyad effective Hamiltonian model for the primary isotopologue, $^{12}C^{32}S_2$. The model was fitted from more than 13 000 measured line positions in the range of 240–12 000 cm^{-1}. The empirical energy levels derived from the EH model up to 9000 cm^{-1} with polyad number $P_{max} = 40$, $l_2^{max} = 40$, and $J_{max} = 200$ were adopted to replace their counterpart $^{12}C^{32}S_2$ (222 in AFGL notation) levels in the Ames-296K line lists [555]. The line lists were computed on a semi-empirically refined PES (Ames-1) and an *ab initio* DMS determined from CBS extrapolation of CCSD(T)/aug-cc-pV(X+d)Z (X = T, Q, 5) dipoles with fitting $\sigma_{rms} = 1.4 \times 10^{-6}$ a.u. under 10 000 cm^{-1}. The enhanced Ames line list for the primary isotopologue is denoted A+I.296 K. The PES refinement included 319 rovibrational energy levels of $^{12}C^{32}S_2$ (222) in the vibrational quanta and J range of the experimental transition set of Karlovets et al. [551], plus 30 levels of $^{13}C^{32}S_2$ (232) and 14 levels of $^{32}S^{12}C^{34}S$ (224) to maintain similar accuracy for minor isotopologues at low J and to prevent large deviations at high J. The reliable levels of isotopologues 224, 223, and 232 in HITRAN2020 were also incorporated to improve the accuracy of the computed line positions. With line intensity scaled by their terrestrial abundances, the merged "natural" CS_2 line list includes about 10 million transitions of the 20 most abundant isotopologues, from $^{12}C^{32}S_2$ to $^{36}S^{13}C^{36}S$, in the range of 0–10 000 $cm^{-1}$and $S_{296K} > 10^{-31}$ cm^{-1}/molecule.cm^{-2}. More details of the CS_2 line list can be found in Huang et al. [555]. This line list was used as a base for the HITRAN2024 update with the following modifications. The update was limited to the four most abundant isotopologues, while the intensity cutoff of 10^{-28} cm^{-1}/molecule cm^{-2} was introduced after intensities were scaled by their isotopic abundance. The HITRAN2020 line list had a lower intensity cut-off, but uncertainty on the spectral parameters of weak lines was high, while many higher intensity bands were missing.

Compared to HITRAN2020, despite the new cut-off being two orders of magnitude higher, significantly more lines are present in HITRAN2024. The HITRAN2024 line list should be reliable up to the temperatures that exist in the Venusian atmosphere.

Air-broadening parameters and their temperature dependencies and self-broadening parameters are calculated for CS_2 transitions using the Padé approximants reported in Karlovets et al. [551]. These approximants are based on fits to experimental data from Misago et al. [556,557] and Kongolo Tshikala et al. [558,559]. No measurements of the line shifts are available in the literature, and, therefore, a default value of zero was adopted.

The absorption cross-sections computed from the line list (with HITRAN isotopic abundances applied) were evaluated against the PNNL spectra [178]. General improvements were found for the strongest band ν_3, strong hot band $\nu_3 - \nu_1$, and the combination bands $\nu_1 + \nu_3$, $2\nu_2 + \nu_3$, and $2\nu_1 + \nu_3$. During the update, relatively large deviations in line positions (that existed for some lines) and an issue of a small number of bands forbidden by nuclear spin statistics in HITRAN2020 were effectively fixed. Very large differences in the intensities have been observed for the bending ν_2 fundamental, which unfortunately lie outside of the PNNL spectral range and therefore could not be validated. Considering that the intensities for this band in HITRAN [551] were measured in the 1960s [560] at low resolution and high uncertainty and excellent agreement of the *ab initio* intensities [555] in other bands with PNNL, we have decided to use the *ab initio* intensities for this band as well. However, experimental confirmation would be beneficial in the future.

In the future, we will add more isotopologues based on Huang et al. [555].

2.54. CH_3I: Methyl iodide (molecule 54)

Unchanged.

2.55. NF_3: Nitrogen trifluoride (molecule 55)

Unchanged.

2.56. H_3^+: Trihydrogen cation (molecule 56)

H_3^+ is rapidly formed in cold hydrogen plasma by the collision of H_2 and H_2^+, so is important in a variety of astronomical environments. In our solar system, H_3^+ has been observed to emit brightly in gas giants Jupiter [561], Saturn [562], Uranus [563], and very recently in Neptune [564]. The H_3^+ ion is a major driver of interstellar chemistry, where it is monitored via infrared absorption against a suitable star. Miller et al. [565] provide a comprehensive review of the astrophysics of H_3^+.

The spectroscopy of H_3^+ is somewhat unusual. It forms an equilateral triangle in its equilibrium geometry and therefore does not have a permanent dipole. Although theory suggests that there should be a weak rotational spectrum [566], this has yet to be observed. The electronic spectrum of H_3^+ has also yet to be observed. This leaves the infrared: H_3^+ has two vibrational modes: a dipole forbidden symmetric stretch and a degenerate bending mode. It is the bending fundamental and overtone bands which therefore provide the means by which H_3^+ is observed.

H_3^+ is a relatively simple physical system comprising three protons and only two electrons. It is therefore amenable to high-accuracy first-principles calculations. The H_3^+ line list provided by HITRAN is relatively unique in that it is substantially based on ab initio calculations. The first comprehensive H_3^+ line list was provided by Neale et al. [567]; this was replaced by the MiZATeP line list of Mizus et al. [568], which was constructed as part of the ExoMol project [218]. The MiZATeP line list is based on a very accurate potential energy surface [569] and associated dipole moment surfaces [570]. It is important to note that while there have been laboratory studies of relative transition intensities for H_3^+ [569,571], all absolute intensities including those provided by HITRAN come from *ab initio* calculations. Furtenbacher et al. [572] performed an H_3^+ MARVEL study which was updated by Bowesman et al. [573] who presented an updated version of the MiZATeP line list. It is this line list that the HITRAN entry is based on. Bowesman et al. [573] also presented similar line lists for the H_2D^+, D_2H^+ and D_3^+ isotopologues of H_3^+; at present these isotopologues are not included in HITRAN.

The H_3^+ line list comprises all transitions from the updated MiZATeP line list of Bowesman et al. [573] between 0–25 000 cm^{-1} with intensities above the cutoff (10^{-30} cm molecule^{-1}), totaling 108 428 transitions. The levels of H_3^+ are identified by the global quantum numbers: total symmetry, the ν_1 symmetric stretching and ν_2 bending modes, and the L_2 vibrational angular momentum quantum number. The total rotational angular momentum quantum number J, rotationless parity e/f, Coriolis quantum number G of Hougen [574], U notation of Watson [575], and the projection of the angular momentum, K, are used for the local quanta. The subset of transitions taken from the MiZATeP line list involves levels with $J = 0$–18. Vibrational quantum number assignments are available for states up to $\nu_1 = 4$ and $\nu_2 = 8$, although transitions arising from more highly-excited states without vibrational assignment are also provided.

The intensities provided in the HITRAN line lists were calculated using the partition sums from Bowesman et al. [573]. These partition sums exhibit a difference of ~25% when compared to the values of Gamache et al. [338]. This discrepancy will be investigated for future updates to the database.

2.57. CH_3: Methyl radical (molecule 57)

CH_3 is a highly reactive intermediate species associated with the photodissociation of methane [576] and it is involved in the ion-molecular reactions of the formation of organic molecules at low temperatures and densities, which are typical for interstellar clouds [577]. CH_3 has zero permanent electric dipole moment due to a planar configuration of the nuclei at equilibrium. However, the out-of-plane bending $\nu_2(A_2'')$ mode produces an extensive absorption in the infrared spectral range around 16.5 μm (≈606 cm^{-1}). This makes the observation of CH_3 relevant by infrared telescopes, in particular, by JWST. Currently, CH_3 has been detected in the atmospheres of Saturn [578,579] and Neptune [580], and in the interstellar medium toward the Galactic center Sagittarius A* [581]. The CH_3 radicals play an important role in combustion science as it is a primary decomposition product of all hydrocarbon fuels [582].

The short lifetime of CH_3 complicates laboratory measurements of its spectra, especially in the gas phase. Therefore, high quality theoretical calculations serve as an important alternative. The nearest electronic transitions in CH_3 (first studied by Herzberg [583]) fall into the ultraviolet range at 216 nm, allowing the electronic structure problem to be solved with high accuracy for the ground electronic state ($\tilde{X}^2A_2''$) of CH_3 using the single-reference *ab initio* approach. Among the recent theoretical studies, the variational line lists of $^{12}CH_3(\tilde{X}^2A_2'')$ were constructed by Adam et al. [584] and Egorov et al. [585] from the *ab initio* developed PES and DMS within the ro-vibrational approximation (*i.e.*, the spin-rotational splitting was not considered). The *ab initio* PES of Ref. [585] included the high-level contributions, namely, Douglas-Kroll-Hess scalar relativistic Hamiltonian, diagonal Born–Oppenheimer correction, and high-order electronic correlations. As a result, all infrared empirical band origins were reproduced with an RMS error of 0.18 cm^{-1} without any empirical corrections of the PES.

The current infrared line list of $^{12}CH_3$ corresponds to the combination of the effective and variational data. The variational line list was computed up to 8000 cm^{-1} using the *ab initio* PES of Ref. [585] and the *ab initio* DMS newly-developed (at the CCSD(T) / aug-cc-pCVQZ level of the theory) for the Eckart-Sayvetz frame (for further details see Rey et al. [586]). In parallel, a novel approach proposed by Rey [355] was applied to construct the effective models of the Hamiltonian and dipole

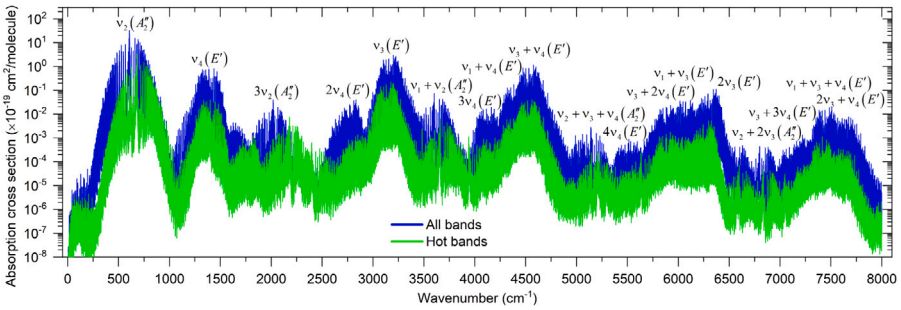

Fig. 28. Absorption cross section of $^{12}CH_3(\tilde{X}^2A_2'')$ at $T = 296$ K simulated with the step of 0.01 cm^{-1} using a Lorentzian profile function with HWHM = 0.07 cm^{-1}. The vibrational assignment of the strongest cold bands (within a certain spectral region) is displayed.

moment numerically from the *ab initio* PES and DMS up to polyad $P = 8$ (~6300 cm^{-1}), where $P = 4v_1+v_2+4v_3+2v_4$.

The transformation of the variational eigenfunctions to an effective Hamiltonian offers two key advantages: (1) it ensures a fast computation of the ro-vibrational levels, even for high-J values, with any convergence issues due to the small dimensionality, (2) the Hamiltonian parameters can be refined in a straightforward manner to reproduce high-resolution data, unlike to a fit of the PES.

At present, the construction of the global effective models directly from the *ab initio* PES has become popular for rigid polyatomic molecules because it considerably simplifies the assignment of the dense spectra. In terms of vibrations, the out-of-plane bending mode of CH_3 has a large amplitude behavior, although there is no quantum tunneling in CH_3, unlike NH_3. As demonstrated empirically by Hirota and Yamada [587], and theoretically in Ref. [585], the shape of the CH_3 PES is not totally quadratic near the equilibrium geometry, leading to large contributions by the anharmonic terms. Here, we propose a first global effective model for CH_3, as an alternative to the standard perturbation treatment, which may fail.

The final infrared line list of $^{12}CH_3$ consists of more than 340 000 transitions with a cut-off value in line intensity of 10^{-28} cm^{-1}/(molecule·cm^{-2}) and up to $J = 24$ (here $J \equiv N$, because the fine structure was not included). The partition function at 296 K was 715.96 with the statistical weights of 8, 0, 4, 8, 0, and 4 for the A_1', A_2', E', A_1'', A_2'', and E'' irreducible representations in the D_{3h} point group. Each spectral line has both vibrational and rotational quantum assignments of the upper and lower states and their symmetries.

For the 0–6500 cm^{-1} spectral range, the strongest transitions correspond to the effective line list, supplemented by some missing hot bands computed variationally. Some parameters of the global effective Hamiltonian were refined using the empirical data on the $\nu_2(A_2'')$, $2\nu_2(A_1')-\nu_2(A_2'')$, and $3\nu_2(A_2'')-2\nu_2(A_1')$ bands obtained by Yamada et al. [588]. The variational part mainly contributes to the 6500–8000 cm^{-1} spectral range. As shown in Fig. 28, all the strongest cold bands are those involving the upper vibrational level of the A_2'' or E' symmetries, which are consistent with the symmetries of the z and x components of the DMS of CH_3. The hot bands make a considerable contribution to the $^{12}CH_3$ spectrum even at room temperature. Thanks to the completeness provided by the *ab initio* calculations, all the bands of $^{12}CH_3$ required for reliable modeling are present in the developed line list, although most of them have never been studied empirically.

Only one measurement of air-broadening parameters of methyl radical exists in the literature [589]. The reported value is very different from the values predicted using the machine learning procedure described by Guest et al. [412]. We therefore used the rotational distribution of air-broadening values predicted in Ref. [412] scaled to the value measured in Ref. [589]. The temperature-dependence exponent n_{air} was fixed to 0.75.

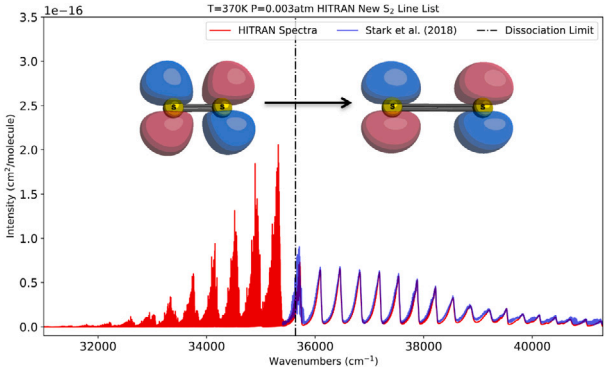

Fig. 29. Experimental S_2 absorption cross section at 370 K from Stark et al. [596] compared to a calculated spectrum (red) that uses the line list from Gomez et al. [595]. Predissociated bands with $v' \geq 10$ have been calculated using the Lorentz HWHM values given in Gomez et al. [595]. S_2 lowest unoccupied molecular orbitals (LUMO) at ground state are shown before the arrow and S_2 LUMO orbitals near dissociation are shown after the arrow.

2.58. S_2: Sulfur dimer (molecule 58)

S_2 is a key molecular species in cometary and planetary environments, particularly in sulfur-rich atmospheres. It has been observed in cometary spectra, such as those of comet IRAS-Araki-Alcock 1983d [590] and comet Hyakutake [591], as well as in the volcanic plumes of Jupiter's moon Io [592]. The presence of S_2 is significant because it acts as an intermediary in sulfur chemistry, influencing the formation of larger sulfur allotropes like S_8 [593,594].

The work presented in Gomez et al. [595] summarizes a new HITRAN-formatted ultraviolet (UV) line list for the sulfur dimer (S_2), which covers the electronic transitions $B\,^3\Sigma_u^- - X\,^3\Sigma_g^-$ and $B''\,^3\Pi_u - X\,^3\Sigma_g^-$. The line list spans 21 700–41 300 cm^{-1} (242–461 nm), covering $B - X$ vibrational bands with $v' = 0$–27 and $v'' = 0$–10, ensuring a detailed dataset. The line list was constructed by utilizing deperturbed spectroscopic parameters from literature sources with the computational modeling program PGOPHER [431]. The line list was validated against laboratory spectra [596] and provides a more accurate dataset for astrophysical and atmospheric modeling.

A significant aspect of this work is the incorporation of predissociation effects and perturbations, which add complexity to the S_2 spectrum in the UV. These spectral effects arise from spin–orbit interactions with crossing ungerade electronic states [597], as well as the B state exceeding the dissociation limit for vibrational levels $v \geq 10$ [598]. The predissociation therefore causes individual rovibronic lines of S_2 to have lifetime broadening (HWHM) of up to 25 cm^{-1} [597,599]. This broadening of spectral UV lines can be seen distinctly after the dissociation limit plotted in Fig. 29. Capturing this pre-dissociation effect

accurately is essential for producing reliable absorption spectra of S_2. To address this need, a Python program was developed that works with HAPI (HITRAN Application Programming Interface) to allow users to include pre-dissociation half-width at half-maximum (HWHM) values into cross-section calculations. The widths used are based on values calculated by Lewis et al. [597] and are provided in the supplementary material of Gomez et al. [595]. This new tool is necessary because HAPI previously lacked built-in support for pre-dissociation line widths. By enabling their inclusion, spectra calculated with HAPI will match experimental observations more closely. Moreover, this tool has potential applications beyond S_2, such as modeling pre-dissociation effects in other molecules, like the Schumann–Runge bands of O_2.

The intensities in this work were derived from literature oscillator strengths and fits to experimental data from Stark et al. [596]. These fits assume that the measured spectra primarily correspond to the $B-X$ transition of $^{32}S_2$, though about 8% of the intensity likely comes from the minor isotopologue $^{32}S^{34}S$, which is omitted due to limited spectroscopic data [600]. Additionally, Stark et al. [596] and Lewis et al. [597] reported a spectral continuum ($\sim 3 \times 10^{-18}$ cm^2) contributing to residuals at higher wavenumbers; this continuum is not included in this work. Finally, resolved transitions near 40 000 cm^{-1} and 40 800 cm^{-1} at 370 K, attributed to the $f\,^1\Delta_u - a\,^1\Delta_g$ transition, are also absent from the line list.

The detection and accurate modeling of S_2 spectral features are essential for interpreting data from telescopes like the upcoming Habitable Worlds Observatory (HWO) [601]. Furthermore, sulfur species have already been identified outside the UV with JWST in exoplanetary atmospheres [602]. The S_2 line list is also expected to help refine atmospheric composition and evolution models, particularly for planets where sulfur chemistry influences cloud formation, radiative properties, and potential biomarkers. Thus, S_2 is a vital molecule for studying planetary atmospheres, exoplanetary photochemistry, and the broader sulfur cycle in diverse environments. Overall, this work provides a critical advancement by delivering a validated S_2 line list formatted for direct integration into the HITRAN database. By bridging gaps in previous datasets and improving accuracy in spectral modeling, this work supports future studies of sulfur chemistry in a range of astrophysical and planetary environments.

2.59. COFCl: Carbonyl chlorofluoride (molecule 59)

Carbonyl chlorofluoride (COFCl) is one of the oxidation products of the chlorofluorocarbons (CFCs) which gives rise to a significant infrared signature in Earth's stratospheric spectra [603]. For this reason, HITRAN2024 includes, for the first time, line parameters for the strongest bands of the $^{12}C^{16}OF^{35}Cl$ and $^{12}C^{16}OF^{37}Cl$ isotopologues. These are the ν_1, ν_2, and ν_3 fundamental bands, located at 5.3 μm, 9.1 μm, and 13.1 μm, respectively. In addition, for the most abundant isotopologue ($^{12}C^{16}OF^{35}Cl$), this list includes lines from the first two associated hot bands, $\nu_x + \nu_4 - \nu_4$ and $\nu_x + \nu_5 - \nu_5$ (with x = 1, 2, and 3). The line-position parameters were obtained during a detailed investigation of high-resolution Fourier transform spectra recorded in Wuppertal, followed by a theoretical analysis [604,605]. The intensity parameters were calibrated in absolute terms with respect to the results of ab initio computations [606]. Validation of these line lists against atmospheric retrievals was carried out in Ref. [605]. Analyses of atmospheric solar occultation spectra measured by the JPL MkIV interferometer show that this COFCl list not only leads to high-quality retrievals of COFCl but also improves the accuracy of remote sensing of several other gases whose absorptions overlap with those of COFCl. This is the case, for example, for formic acid (HCOOH) in the 1105 cm^{-1}region (9.1 μm). A band-by-band overview of the COFCl line list in HITRAN is presented in Fig. 30.

No measurements of the line-shape parameters exist for this molecule; therefore, the values based on machine learning predictions of Guest et al. [412] were used for the air-broadening parameters, with their temperature dependencies fixed to 0.75.

2.60. HONO: Nitrous acid (molecule 60)

Nitrous acid (HONO) has been known for a long time as an important player in the chemistry of the troposphere [607,608]. In addition, HONO proved recently to be of astrophysical interest [609]. The HONO line list, that is now present for the far infrared region in HITRAN2024, is described in Table 5 of Betnga et al. [610], and an overview of this line list is shown in Fig. 31.

The HONO molecule exists in two conformer forms, trans-HONO and cis-HONO, with the vibrational ground-state energy levels of cis-form located with an energy difference $\Delta E_{\text{cis-trans}}$ above those from the trans form. For this parameter, we used $\Delta E_{\text{Cis-Trans}} = 95.8 \pm 9$ cm^{-1} as this value was obtained in Betnga et al. [610] by the investigation of line intensities in several high-resolution FTS spectra recorded at the SOLEIL synchrotron facilities. In this HONO line list, the line positions for trans-HONO and cis-HONO were computed using the rotational constants available in Dehayem-Kamadjeu et al. [611].

The pure rotation spectra of trans-HONO and cis-HONO are hybrid bands, with both A-type and B-type components. For the calculation of the line intensity, the transition moment operators of these pure rotation bands involve, at its zeroth order, the trans-HONO and cis-HONO permanent dipole moments, $^{\text{trans}}\mu_0$ and $^{\text{cis}}\mu_0$, respectively. These $^{\text{trans}}\mu_0$ and $^{\text{cis}}\mu_0$, are already well known from Stark measurements [612]. Additionally, the intensities account for centrifugal distortion corrections that are associated to the B-type components of the trans-HONO and cis-HONO permanent dipole moments. It is worth mentioning that A-type transitions do not consider (possible) centrifugal distortion corrections, as such information is still missing.

In the absence of existing line-shape parameters for HONO in the literature, it was decided to use "a priori" values for the HONO line-shape parameters similar to those of water.

In Betnga et al. [610], this HONO line list was found to be more robust for improved HONO detection in astrophysical objects using ALMA-PILS survey compared to the previous one [609], for which the JPL catalog list was used [177].

For HONO, the 16 μm (ν_5 and ν_6 bands), 11 μm (ν_4 bands of cis-HONO and trans-HONO), 8 μm (ν_3 band of Trans-HONO) and 5.8 μm (ν_2 bands of cis-HONO and trans-HONO) correspond to the strongest infrared bands of this species. The Infrared Atmospheric Sounding Interferometer (IASI) instrument on the METOP satellite [186] could detect HONO in the 11-μm region during the (rather) exceptional conditions of the large Australian bush fires [186]. The future IASI-NG [613] and Far-infrared Outgoing Radiation Understanding and Monitoring (FORUM) [149] satellite instruments will cover simultaneously the 11 μm to 8 μm, and the 16 μm to 11 μm spectral regions, respectively.

For remote sensing by satellite instruments, the HONO line lists must have consistent intensities from one infrared band to another. Obtaining absolute intensities is a complex task because of the chemical instability of nitrous acid. Of the infrared bands mentioned, only the 11-μm region has been extensively studied [614]. The preliminary investigation of the 16-μm region requires updating [615], and HONO line lists are still missing in the 8-μm and 5.8-μm regions. Therefore, future spectroscopic studies should address these issues.

Only a single experimental study is available for air-broadening measurements of HONO [616], reporting an average value of 0.098 cm^{-1}/atm. Prediction based on machine learning from Ref. [412] is in good agreement with this value but provides an approximated rotational distribution. Therefore, the values from Ref. [412] were used. The default values: $\gamma_{\text{self}} = 0.4$ cm^{-1}/atm, and $n_{\text{air}} = 0.7$ were implemented for the self-broadened half width, and for the air temperature-dependent coefficient, respectively.

2.61. $ClNO_2$: Nitryl chloride (molecule 61)

Nitryl chloride ($ClNO_2$) is a new molecule for HITRAN and is included due to its environmental importance. This gas forms in the

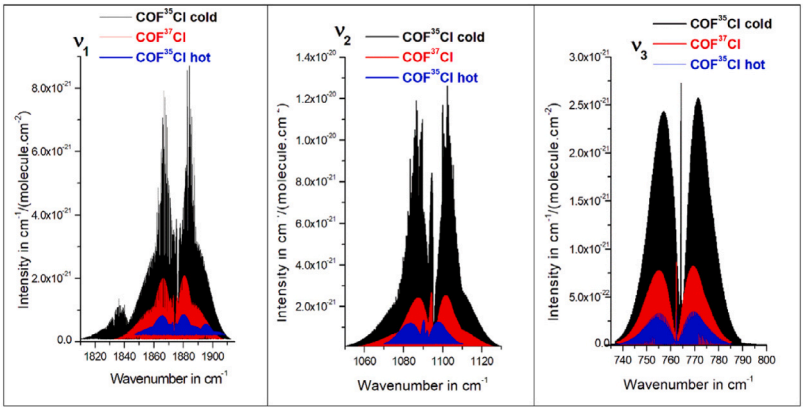

Fig. 30. Band-by-band overview of the line list present for COFCl in HITRAN2024. This list includes hot band contributions only for the $COF^{35}Cl$ (main) isotopologue.

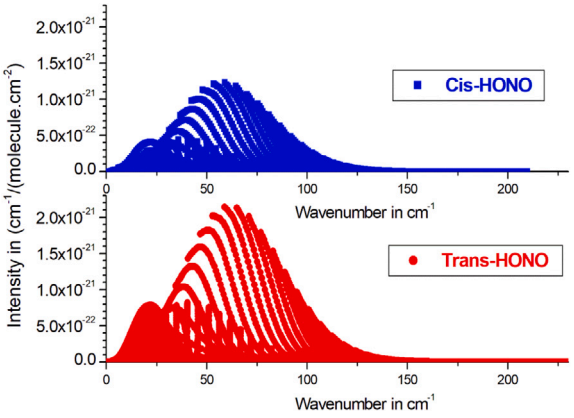

Fig. 31. Overview of the HONO line list in HITRAN2024 and in the far-infrared region.

polluted marine troposphere [617,618] as well as in polar stratospheric clouds [619,620]. Gaseous nitryl chloride is a relatively stable compound (lifetime > 30 hours [621]) and therefore is not reactive at night and is a Cl and NOx reservoir. When exposed to sunlight in the early morning, $ClNO_2$ undergoes rapid photolysis and breaks into chlorine (Cl) radicals and nitrogen dioxide (NO_2) molecules [621]. The further oxidation of volatile organic compounds by Cl radicals negatively impacts the air quality and the atmospheric oxidation capacity, with harmful consequences, such as tropospheric ozone and secondary aerosol formation. Consequently, there are efforts to monitor the concentrations of these species in the atmosphere through various in situ ground-based and aircraft observations using chemical ionization mass spectrometry [621,622].

$ClNO_2$ has been identified as one of the bleach-related compounds observed in indoor air [623]. For instance, it was reported [624] that the indoor mixing ratio reaches up to 30 ppbv, which is ten thousand times higher than the outdoor mixing ratio measured during bleach cleaning events. Remote sensing using spectroscopic techniques is an attractive alternative to the in situ measurements of $ClNO_2$. However, there has been no infrared detection of this trace gas largely due to a lack of reference spectroscopic information. The $ClNO_2$ spectrum exhibits sharp Q branches, in particular that of the ν_2 band in the 12.6 μm region [625], which is an atmospheric "window" and could therefore be used for a possible atmospheric detection. In particular, the new space mission (IASI-NG [613], to be launched around 2026) with twice the resolution of IASI [186] and a noise level reduced by a factor of 2 to 4 (depending on the spectral range) should allow the observation of new key atmospheric species such as $ClNO_2$. The FIR spectrum of this molecule will be relevant to the upcoming mission FORUM (150–1400 cm^{-1}) [149]. which is expected to be launched in 2027. FORUM will fly in close formation with IASI-NG, allowing synergistic observations in the far and mid-IR regions [626]. However, this will only be possible if the necessary spectroscopic data exist. The 12.6 μm region contains not only the absorption of the ν_2 band, but also that of various hot bands ($\nu_2+\nu_3-\nu_3$, $\nu_2+\nu_4-\nu_4$ and $\nu_2+\nu_6-\nu_6$) involving low-energy vibrations (i.e. the ν_3 band at 370 cm^{-1}, ν_4 at 652 $cm^{-1}$and ν_6 at 408 cm^{-1}).

In order to provide an accurate line list for the remote sensing of nitryl chloride, a complete and detailed analysis of the low-energy vibrations is thus required. The ν_3 band of $ClNO_2$ has been previously studied in Ref. [627] but the spectrum was recorded at a resolution of 0.002 cm^{-1}, with a pressure of 3.06 hPa and at room temperature, resulting in a very dense rotational structure that was not fully resolved. The recent re-investigation of line positions of the ν_3 bands of $^{35}ClNO_2$ and $^{37}ClNO_2$ around 370 cm^{-1} was carried out by Anantharajah et al. [628]. In this work, Fourier transform spectrum (FTS) of nitryl chloride, was taken at 0.00102 cm^{-1} resolution using the SOLEIL synchrotron radiation, an optical path length of 8.16 m at a pressure of 0.025 hPa and a temperature of 221 K. These more favorable experimental conditions for the analyses resulted in a well-resolved spectrum (see Fig. 3 of Anantharajah et al. [628]), allowing a new and extensive line positions analysis of the ν_3 bands of $^{35}ClNO_2$ and $^{37}ClNO_2$. Thanks to the new experimental conditions, the line assignments were pursued up to higher rotational quanta, $J = 83$ and $K_a = 44$. For both isotopologues, a total of 6331 transitions were reproduced with a root-mean-square deviation of 2×10^{-4} cm^{-1} using a Watson-type A-reduced Hamiltonian. Improved rotational and centrifugal distortion constants for the ν_3 fundamental bands of $^{35}ClNO_2$ and $^{37}ClNO_2$ have been determined. The band centers are 370.1510773(92) cm^{-1} for the ν_3 fundamental band of $^{35}ClNO_2$ and 364.5218094(96) cm^{-1} for $^{37}ClNO_2$. It should be mentioned that in Ref. [628], no attempt was made to determine dipole moment operator parameters, and only relative line intensities can be compared between the experiment and simulation. The dipole moment was crudely estimated and used to calculate the synthetic spectra, which were simply scaled to match the observed spectra. The line list from Ref. [628] that contains 10 000 lines and covers the 336–387 cm^{-1} region is now included in HITRAN.

The values based on machine learning predictions from Ref. [412] were used for the air-broadening parameters.

2.62. Modified Hartmann-Tran profile

We introduce the quadratic speed-dependent hard-collision (qSDHC) profile with double-power-law (DPL) temperature dependencies

as a recommended beyond-Voigt line-shape profile in the HITRAN database, which replaces the previously recommended Hartmann-Tran (HT) profile [25] due to limitations that have since become apparent. This new profile is referred to as a *modified Hartmann-Tran* (mHT) profile [512]. Although other beyond-Voigt parameterizations are still available in HITRAN, we encourage users to use the mHT profile in cases where the beyond-Voigt effects are relevant.

Since the original formulation of the HT profile [629], it has been widely used for accurate spectral simulations and analysis (e.g. Refs. [630,631]). This has allowed the community to identify some limitations related to the parametrization of the velocity-changing collision part. The first problematic feature is the singular behavior of the temperature dependencies of the velocity-changing parameters when the shift parameter crosses zero. The second limitation is the difficulty in evaluating the velocity-changing parameters for mixtures. Wcisło et al. [512] and Stolarczyk et al. [513] discuss the other, more subtle, problematic features of the HT profile. These limitations are overcome in the mHT profile by explicitly expressing the complex rate of the velocity-changing collisions, $\tilde{\nu}_{\text{opt}}$, as a sum of its real and imaginary parts

$$\tilde{\nu}_{\text{opt}} = \tilde{\nu}^{r}_{\text{opt}} + i\tilde{\nu}^{i}_{\text{opt}}. \tag{1}$$

A detailed discussion on the mHT profile, its structure, properties, and its relationship to the earlier HT profile, is provided in Wcisło et al. [512]. This reference also presents an efficient algorithm for evaluating the mHT profile and includes implementation codes in several programming languages: Fortran, Python, MATLAB, Wolfram Mathematica, and LabVIEW.

For the cases in which the available line-shape parameters cover a wide temperature range (especially low temperatures), we recommend using the double-power law (DPL) [506,513] representation of the temperature dependencies of the mHT parameters, such that the generalized form is given as

$$\text{Param.(T)} = Coef.1\left(\frac{\text{T}_{\text{ref}}}{\text{T}}\right)^{Exp.1} + Coef.2\left(\frac{\text{T}_{\text{ref}}}{\text{T}}\right)^{Exp.2}. \tag{2}$$

where Param.(T) is a mHT parameter at temperature T, Exp.1 and Exp.2 are exponents of the temperature ratio (with $\text{T}_{\text{ref}} = 296$ K), and Coef.1 and Coef.2 are the respective coefficients. The generalized DPL temperature dependence applies to the mHT parameters of pressure broadening (γ_0), pressure shift (δ_0), speed dependence of the pressure broadening and shift (γ_2, δ_2), and the real and imaginary parts of the Dicke parameter ($\tilde{\nu}^{r}_{\text{opt}}$, $\tilde{\nu}^{i}_{\text{opt}}$). The full list of labeling for the DPL is provided in Table 1 of Stolarczyk et al. [513].

The mHT profile is now integrated with HAPI [23] to allow for automatic spectral simulations for given thermodynamic conditions and mixture composition, see Wcisło et al. [512] for a detailed explanation and an example of working with the mHT profile.

3. Absorption cross-sections

The HITRAN database includes a substantial number of absorption cross-sections for molecules where line-by-line parameters are insufficient (or absent) to accurately reproduce the molecular spectrum. Many, but not all, of these molecules are heavy polyatomic species with numerous low-lying vibrational modes and small spacing between rovibrational transitions, making their spectra complex and difficult to analyze at low spectral resolution. Yet these molecular species are often considered to be important species for remote sensing applications. Among many reasons, they can be tracers for biomass burning, have relatively large contributions toward radiative forcing, be products of pollution, or even be trace constituents in (exo-)planetary atmospheres. Some of the anthropogenic pollutants in the terrestrial atmosphere could be considered as indicators of intelligent life on these planets. In addition, some molecules could also be biomarkers in anoxic atmospheres. It is therefore necessary to have knowledge of the spectroscopy over an appropriate temperature, pressure, and gas mixture to enable accurate retrievals.

Absorption cross-sections have been included in HITRAN since 1986 [9]. In subsequent editions, the number of molecules with absorption cross-sections has typically increased, with many improvements and updates along the way. For HITRAN2016 [16], a comprehensive update to the absorption cross-sections was carried out [632], which greatly expanded the number of molecules represented. This was facilitated by a large number of contributions from the Pacific Northwest National Laboratory (PNNL) [178,633], Hodnebrog et al. [634] compilation, and a number of high-resolution laboratory observations. Although this update was substantial, there was still room for improvement. For instance, many molecules with absorption cross-sections from PNNL were unavailable to HITRAN at the time. Also, the coverage of environmental conditions was typically limited to standard temperatures and pressures. In HITRAN2020 [17], the first set of absorption cross-sections was included for elevated temperatures suitable for diverse planetary environments.

For HITRAN2024, a further expansion to the absorption cross-sections has been carried out and is described in detail in a supporting article [635]. Absorption cross-sections are now available for 644 molecules in HITRAN, marking an almost two-fold increase in the number compared to HITRAN2020. Fig. 32 presents an overview of this increase, which also includes a breakdown by molecular category. These broad categories are used to group molecules with similar structure on HITRAN*online* (www.hitran.org/xsc/). It can be seen that there has been a substantial increase in coverage across all types of molecules, with the largest increase realized for the *Alcohol, ethers, and oxygenated hydrocarbons* (i.e., molecules containing only H, C, and O) and the *Hydrocarbons* (i.e., molecules containing only H and C) categories.

Over 1400 individual absorption cross-section measurements have contributed to the increase for HITRAN2024, with coverage across both existing and new molecular species. A thorough description is provided in the corresponding supporting article [635], but key details are summarized here. Approximately 700 of these absorption cross-sections (for 260 new molecules) have been contributed by measurements performed at PNNL [178], with coverage for each measurement typically spanning 500–6500 cm^{-1} at a resolution of 0.112 cm^{-1}. These measurements were carried out in an atmosphere of N_2 at standard pressure (760 Torr) and typically include three temperatures: 278.15, 298.15, 323.15 K.

Absorption cross-sections for many molecules have been added to HITRAN for species that can directly or indirectly contribute to depletions of stratospheric ozone, or are potent greenhouse gases. These include expanded temperature and pressure coverage of infrared absorption cross-sections of hydrofluorocarbons [636–638], hydrofluoroethers [639,640], perfluoroalkane compounds [641–647], methoxyphenols [648], nitriles [649], and other chlorinated or fluorinated species [489,650–654].

High-resolution absorption cross-sections at pressures consistent with the upper atmosphere can provide detail of individual lines within dense bands that are often obscured at standard pressure. To this end, absorption cross-sections obtained from high-resolution dual-comb spectroscopic infrared studies of methanol, ethanol, dimethyl sulfide, and isoprene have been added [655–658] with a resolution as fine as 0.00023 cm^{-1} near 1000 cm^{-1}.

Many absorptions cross-sections of hydrocarbons that are important constituents of planetary atmospheres have been added, with measurements carried out in atmospheres of H_2, He, Ar, N_2, and air at terrestrial temperatures and below. These include measurements from laboratories at Old Dominion University [659–669], NASA's Jet Propulsion Laboratory [670], the University of Central Florida [657,658], and the University of Leicester [637].

High-temperature absorption cross-sections have been added to HITRAN2024 for a number of species that are found in combustion environments and expected to be present in (exo-)planetary atmospheres.

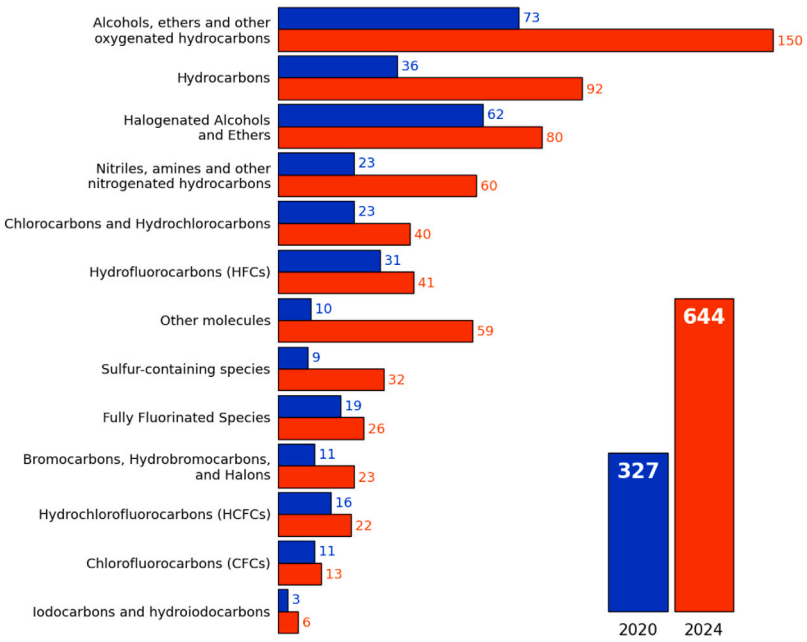

Fig. 32. Number of molecules with absorption cross-sections in HITRAN2024 compared to HITRAN2020. The bar chart on the right provides an indication of the increase in the total number of molecules represented with absorption cross-sections in HITRAN2024 (red) compared to HITRAN2020 (blue). This total is broken down into molecular categories on the left to demonstrate that molecules have been added to all categories represented in the HITRAN database. These categories are used on HITRAN*online* (www.hitran.org/xsc/) to collect together similar molecules.

These have been carried out using Fourier-transform spectrometers combined with heated cells [671–675] and broadband rapidly-tuned laser measurements of shock tube environments [676–684].

In addition, absorption cross-sections for the UV region have also been included for HITRAN2024 for ozone [685,686], glyoxal [687], and 1-butene [672].

During preparation of the update to the cross-sections for HITRAN2024, the data for a number of new measurements of potent greenhouse gases have become available. These include FIR measurements of HCFC-132b [688], which will be considered for inclusion to HITRAN in future updates to the database.

4. Collision-induced absorption

Collision-induced absorption (CIA) is a process in which light is absorbed by pairs of molecules due to the dipole moment that is induced by their interaction. A brief introduction to CIA can be read in Karman et al. [689], which was the first update of the CIA section of HITRAN in 2019, after the first release in 2012 [690]. CIA-related mechanisms, nomenclature, and general definitions are presented in [689], and the second update [691] for HITRAN2024 follows the same framework.

4.1. Relevance of CIA and the 2024 update

The study of planetary atmospheres is the field in which this absorption mechanism has the biggest impact: from the terrestrial atmosphere, to planets and moons inside and outside the Solar System, CIA plays an important role in the heat balance of planetary atmospheres. For example, the warming effect of N_2-N_2 and CH_4-N_2 CIAs prevent the condensation of Titan's atmosphere, preserving its thick nitrogen atmosphere [692]. CO_2-H_2 and CO_2-CH_4 CIAs are key quantities in understanding the atmosphere of early Mars and predicting its surface temperature [693,694], while CO_2-CO_2 collisional pairs present multiple CIA bands that determine the amount of solar radiation that is absorbed at the different layers of the hot, dense, and CO_2-rich atmosphere of Venus [695]. These are just a few examples that demonstrate the relevance of CIA when studying planetary atmospheres. Nonetheless, highlighting the importance of CIAs in planetary science just in connection with the atmospheric energy balance would be an underestimation. In fact, CIAs in which O_2 is part of the collisional pair (O_2–X) may be the most detectable O_2 feature for transit observations of exoplanets, and can be interpreted as a possible biosignature [696]. Specifically, it could be the only O_2 signature detectable with JWST for a modern Earth-like cloudy atmosphere with biological quantities of O_2 [697]. Going even beyond the field of planetary sciences, these continuous absorption processes have also proven to be interesting from a technological point of view, particularly in the development of sensors for industrial applications [698]. H_2-H_2 and H_2-N_2 CIAs can be at the core of fast-response, accurate, compact, and cost-effective sensors to monitor and control hydrogen concentrations during its production, storage, and transportation [699]. The examples reported above, in addition to illustrating the wide range of research fields in which CIA processes are relevant, directly refer to molecular pairs whose binary absorption coefficients have been added and/or updated in the HITRAN CIA section. The entire list of the available data in the updated CIA section is reported in Table 6, grouped for different collisional pairs.

Looking in more detail at the new features introduced in this second update of the HITRAN CIA section, there are two collisional pairs being added to the database for the first time. The first one is N_2-Ar, where the rototranslational and vibrational data are taken from the computational work by Serov et al. [728]. These data are particularly useful for modeling nitrogen-rich atmospheres, such as those of Earth or Titan. The second one is CO_2-H_2O, which has been investigated in the work by Fleurbaey et al. [713], a study combining Cavity Ring-Down Spectroscopy and molecular dynamics simulations, providing data potentially highly relevant for the study of the atmosphere of early Mars.

This second update also includes data for collisional pairs already present in the database. New data extending both spectral and temperature range are available for N_2–H_2 [698], CO_2–CO_2 [711], CO_2–H_2 [706], CO_2–CH_4 [704], O_2–O_2 [738,739], and O_2–CO_2 [745], while interesting new experimental data about H_2–H_2 and H_2–He [719] have been included alongside the respective theoretical calculations. Details about

Table 6
Summary of all collisional pairs available in the HITRAN CIA database, both *Main* and *Alternate* folders. A more complete table is available in Terragni et al. [691], which includes a description of the spectral coverage of each data source for each collisional pair.

System	Folder	ν range (cm^{-1})	T range (K)	# of sets	References
CH_4-Ar	Alternate	1–697	70–296	5	[700]
CH_4-CH_4	Alternate	0–990	20–400	10	[701]
CH_4-He	Main	1–1000	40–350	10	[702]
CO_2-Ar	Main	0–300	200–400	21	[703]
CO_2-CH_4	Main	0–720	100–600	6[a]	[704]
	Alternate	0–2000	100–600	10[a]	[705,706]
CO_2-CO_2	Main	1–4500	192–800	37[a]	[707–712]
	Alternate	1–250	200–800	7	[707]
CO_2-H_2	Main	5–1500	100–600	6[a]	[706]
	Alternate	0–2000	200–350	4[a]	[705]
CO_2-H_2O	Main	5700–6300	296	1[a]	[713]
CO_2-He	Main	0–1000	300	1	[714]
H_2-CH_4	Main	0–1946	40–400	20[b]	[715]
H_2-H	Main	100–10 000	1000–2500	4	[716]
H_2-H_2	Main	20–10 000	200–3000	113	[717]
	Alternate	0–8650	40–501	128[a,b]	[718–720]
H_2-He	Main	20–20 000	200–9900	334	[721]
	Alternate	0–6000	40–504	27[a,b]	[719,722]
He-H	Main	50–11 000	1500–10 000	10	[723]
N_2-Air	Main	1850–5000	228–363	24	[724–727]
N_2-Ar	Main	0–2600	70–500	45[a]	[728]
	Alternate	2131–2559	300	1[a]	[729]
N_2-CH_4	Main	0–800	70–400	34[a]	[730]
	Alternate	0–1379	40–400	10	[731]
N_2-H_2	Main	0–5100	40–400	11[a]	[698,732]
N_2-H_2O	Main	1930–2830	250–350	11	[733]
N_2-He	Main	1–1000	300	1	[714]
N_2-N_2	Main	0–5000	70–400	58	[724,726,727,734]
	Alternate	30–300	78–129	4	[735]
O_2-Air	Main	1300–13 839	193–356	25[a]	[736–743]
	Alternate	7583–14 806	206–346	76	[741,744]
O_2-CO_2	Main	9105–13 839	293–296	2[a]	[745,746]
O_2-N_2	Main	1300–13 840	193–363	33[a]	[724–726,736–740,743]
	Alternate	7583–13 402	206–346	30	[741]
O_2-O_2	Main	1150–29 800	193–353	46[a]	[724,738–743,747–749]
	Alternate	1300–14 806	193–356	82	[736,737,741]

[a] CIA sets that have been newly added, updated, or have changed folder for HITRAN2024.
[b] Count includes CIA sets for multiple ratios of ortho:para H_2.

these new data, comparison among different data sources, and selection criteria, are discussed in detail in a paper entirely dedicated to the second update [691].

The CIA section of the HITRAN database can be accessed at www.hitran.org/cia, where instructions about the data format can be found at www.hitran.org/data/CIA/CIA_Readme_2024.pdf. In this document, the distinction between *Main* and *Alternate* folder (see Table 6, Column 2) is presented. The general idea behind this subdivision is that the Main folder contains the recommended CIA data, while the Supplementary folder contains data that, while not generally recommended, offer specific advantages over the ones in "Main" folder, such as an extended temperature range, incorporation of spin statistics, or consistency with monomer line lists.

4.2. Outlook for the future

Between the first update in 2019 and the current release of the HITRAN CIA section, a major event has fundamentally reshaped the scientific perspective in both astrophysics and planetary science: the successful launch of the James Webb Space Telescope (JWST) has made it possible to observe astrophysical phenomena and celestial bodies with unprecedented detail. As JWST is now the primary instrument for studying exoplanet atmospheres, the new CIA data that would be most valuable to the scientific community are strongly guided by the spectral coverage of JWST. In particular, when these atmospheres are studied in transmission spectroscopy with NIRISS/NIRSpec, the typical observational range extends from 0.6 to 5.3 μm [750], with the possibility of extending this range to approximately 10–12 μm using MIRI/LRS slitless mode for planets with a high signal-to-noise (S/N) ratio, such as Hot Jupiters. Going beyond this limit is very challenging because of the increasing noise from the source that leads to a poor S/N ratio and detectability [751]. Having identified this as the wavelength range of interest, the new data should try to expand the temperature range, covering the large variety of atmospheres that can be found outside our Solar System. Regarding hot atmospheres, our knowledge of magma oceans would benefit from CIA data at high temperatures of collisional pairs that can be found in reducing atmospheres (*e.g.*, X-H_2) [752], while our modeling of Venus and the atmosphere of early Earth would benefit from CO_2-X CIA data above 350 K [753,754]. Moving to even higher temperatures (stellar temperatures), new CIA data for N_2-X collisional pairs would improve for M and brown dwarf stellar characterization [755]. This, in turn, would help in the characterization

of exoplanet atmospheres since stellar contamination has long been recognized as a major bottleneck in transmission spectroscopy, which could lead to the wrong interpretation of key atmospheric molecular features [756].

5. Aerosol refractive indices

The aerosol folder of HITRAN2024 contains the real and imaginary refractive indices of many materials that make up the composition of water and ice clouds and liquid and solid aerosols in the Earth's atmosphere, other solar system atmospheres, and exoplanets. Knowing the real and imaginary indices, and the size distribution of particles at a specific altitude, one can calculate the optical properties (extinction, scattering, absorption, single scattering albedo, and asymmetry parameter) as a function of wavelength [757]. For a path length ds, the aerosol optical depth contribution in this path length is the product of the extinction (in length^{-1} units) times the path length. The addition of gas and aerosol optical depth contributions determine the total optical depth, as a function of altitude, in a planetary atmosphere. The accuracy to which gas mixing ratios can be retrieved from remote sensing experiments is frequently related to how well one can determine the aerosol contributions to the sensed radiation. Aerosol particles are also important in atmospheric chemistry in their own right, with ozone hole heterogeneous chemistry on liquid and solid Polar Stratospheric Clouds (PSCs) being an important example [758].

HITRAN2024 main and supplementary refractive indices are listed in Table 7. Supplementary datasets include older laboratory measurements or datasets with just the imaginary indices. Table 7 starts with the indices compiled at the Air Force Cambridge Research Laboratory in 1987 [759], including water, ice, sodium chloride, sea salt, water soluble aerosol, ammonium sulfate, carbonaceous aerosol, volcanic dust, sulfuric acid, meteoric dust, quartz, hematite, and sand. Table 7 then continues with indices of supercooled water, ice at various temperatures, materials which comprise PSC particles, desert dust, volcanic ash, secondary organic aerosol (SOA), combustion related indices, surface minerals, Titan and Pluto aerosol indices, and materials that likely are present in exoplanet atmospheres.

New additions to the HITRAN2024 refractive indices include Di Biagio [771] desert dust indices from nineteen globe-wide locations, Reed [774] volcanic ash indices (for eight sample locations), He [777] SOA and Fang [778] SOA indices, Hashemi vanillic acid indices [779], Shepherd [783] wood smoke and humic indices, Chehab [789] kaolinite and Herbin [790] quartz, and Jovanovic [794] Pluto aerosol analogue indices. The Chehab kaolinite indices are noteworthy since they were determined from an experimental setup which determines the indices from the UV to the far-IR and simultaneously determines in-suspension aerosol particle size distributions for fine and coarse particles. The Herbin quartz indices are based upon a similar experimental methodology. Both groups apply optimal estimation and Kramers–Kronig relations in their analyses.

An example of new SOA indices, and the complexity of aerosol optical properties is illustrated in Fig. 33. In addition to particle size distributions which change with time, the chemical composition of aerosols is also time-dependent. The real and imaginary SOA indices in Fig. 33 in the visible are a function of the OH exposure time (in days). The SOA refractive indices evolve temporally as the SOA is subjected to OH-oxidation over 0.7, 5.5, and 10.6 days in the ambient conditions.

In Fig. 33, both the real and imaginary indices vary in a time dependent manner over several days. These variations are of interest since the absorption of light is dependent upon the imaginary component. As discussed by Bohren and Huffman [818], the complex refractive index m is a function of wavelength, with real m_{real} and imaginary m_{imag} components.

$$m = m_{\text{real}} + i m_{\text{imag}} \tag{3}$$

A plane light wave of wavelength is attenuated along the propagation x axis according to

$$E = E_0 \exp(-2\pi m_{\text{imag}} x/\lambda) \exp[i2\pi(m_{\text{real}} x - ct)/\lambda] \tag{4}$$

with speed of light c and time t. Light intensity ($\propto E^2$) is attenuated by $\exp(-4\pi m_{\text{imag}} x/\lambda)$ along a distance x.

The investigation of Exoplanet atmospheres is a recent research frontier. Exoplanet atmosphere particles likely exist for a range of temperatures much wider than those encountered in our Solar system. HITRAN2024 includes many of the materials tabulated by Wakeford and Sing [819], who discussed hot Jupiter exoplanet atmospheres. H. Mutschke of the Friedrich Schiller University Jena kindly provided exoplanet indices to HITRAN. Additional exoplanet material indices not listed in Table 7 can be downloaded from the comprehensive Jena web site (http://www2.astro.uni-jena.de/Laboratory/OCDB/index.html).

The HITRAN-RI program (an extension of [820]), can be downloaded from the HITRAN website, and includes programming written in IDL (Interactive Design Language), Fortran 90, and Python. All three versions apply the Bohren-Huffman [818] Mie code. Both ASCII and netCDF data file versions of the indices are included in the HITRAN-RI distribution (in a single tar file). A README file instructs the user how to apply the HITRAN-RI progam. The user only needs to specify input and output subdirectories in the "directory.dat" ascii file, and specify the work to be carried out in the "work.dat" ascii file (which includes user-specified particle size distribution parameters). The user does not need to access the source code; it is accessible from the HITRAN-RI distribution and can be modified. The Fortran 90 version reads in ASCII refractive index files and just calculates the wavelength-dependent extinction, absorption, scattering, single scattering albedo, and asymmetry parameters (which are sent to an output ASCII file). The IDL version of HITRAN-RI produces output graphics postscript graphics and netCDF files of the input indices, particle size distribution, and wavelength-dependent optical properties. The Python version of the program creates an output ASCII file with the optical properties and a graphics PNG file of the extinction spectrum.

6. Water-vapor continuum

Since the release of the 2020 version of HITRAN, a major gap in the database compilation of key absorption parameters has now been filled with the inclusion of the MT_CKD water-vapor continuum model (Mlawer-Tobin_Clough-Kneizys-Davies; Mlawer et al. [821]). The MT_CKD model provides a representation of smoothly varying water-vapor absorption and its temperature dependence that, once added to the absorption due to water-vapor lines, best agrees with high-quality observations and theoretical calculations of the total water-vapor absorption. As is the case for other HITRAN components, observations from different studies and calculations may provide conflicting information on the strength of the water-vapor continuum in certain spectral regions, and a judgment must be made as to which source provides the best foundation for the continuum coefficients in MT_CKD. The first version of the MT_CKD water-vapor continuum released as part of HITRAN was v4.0 (December 2022) and is detailed in Mlawer et al. [22].

The MT_CKD water-vapor continuum data consists of continuum coefficients (cm^2/molecule/cm^{-1}) every 10 cm^{-1} from -20 cm^{-1} to 20 000 cm^{-1} at a reference density (corresponding to 1013 mb and 296 K). Self continuum coefficients are provided for two temperatures, 296 K and 260 K. The accompanying MT_CKD code performs a linear scaling in density, spectral interpolation, and applies the temperature dependence (for the self continuum) to these coefficients to compute the continuum coefficient (or absorption coefficient in cm^2/molecule) at the desired pressure and temperature.

Shortly after the release of MT_CKD_4.0, a modification to the MT_CKD foreign continuum in the far-infrared was released as v4.1

Table 7
Refractive indices included in HITRAN2024.

Compound	Measurement specifics	Ref.
Water, ice, sodium chloride, sea salt, water soluble aerosol, ammonium sulfate, carbonaceous aerosol, volcanic dust, sulfuric acid, meteoric dust, quartz, hematite, sand	Room temperature, 0.2–40 μm	[759]
Water	300 K, 10–5000 cm^{-1}	[760]
Supercooled water	238–269 K, 1100–4500 cm^{-1}	[761]
Ice	266 K, 0.04 μm–2 m	[762]
Ice	130–210 K, 800–4000 cm^{-1}	[763]
Sulfuric acid (H_2SO_4/H_2O)	215 K, 499–6996 cm^{-1}	[764]
Sulfuric acid (H_2SO_4/H_2O)	273–298 K, 400–7500 cm^{-1}	[765]
Nitric acid (HNO_3)	223–293 K, 450–6500 cm^{-1}	[766]
Ternary Solution ($H_2SO_4/H_2O/HNO_3$)	203–293 K, 450–6500 cm^{-1}	[766]
NAD (nitric acid dihydrate)	160–190 K, 700–4700 cm^{-1}	[767]
NAT (nitric acid trihydrate)	160 K, 711–4004 cm^{-1}	[768]
Amorphous nitric acid (aNAM, aNAD, aNAT)	153 K, 482–7000 cm^{-1}	[769]
NAM (nitric acid monohydrate)	179 K, 482–6002 cm^{-1}	[769]
NAD	184 K, 482–6981 cm^{-1}	[769]
αNAT	181 K, 482–6989 cm^{-1}	[769]
βNAT	196 K, 482–6364 cm^{-1}	[769]
Saharan dust	0.30–0.95 μm	[770]
Desert dust	3.0–15.0 μm	[771]
Volcanic ash	0.45–25 μm	[772]
Volcanic ash	690–32500 cm^{-1}	[773]
Volcanic ash	0.4–18.9 μm	[774]
SOA	0.23–1.2 μm	[775]
SOA	0.23–1.2 μm	[776]
SOA	0.31–0.65 μm	[777]
SOA	0.31–0.53 μm	[778]
Vanillic acid	0.27–0.60 μm	[779]
Organic acids (Oxalic, malonic, succinic, pinonic, pyruvic, phthalic)	0.25–1.1 μm	[780]
Brown carbon	0.2–1.2 μm	[781]
Burning vegetation	525–5000 cm^{-1}	[782]
Wood smoke	0.48–0.70 μm	[783]
Humic acid	0.48–0.70 μm	[783]
Burning vegetation	0.35–1.5 μm	[784]
Carbon flame	0.4–0.7 μm, 296–773 K	[785]
Flame soot	0.2–38 μm	[786]
Minerals (clay, illite, kaolin, montmorillonite)	2.5–200 μm	[787]
Minerals (granite, montmorillonite)	5–40 μm	[788]
Kaolinite	0.25–46 μm	[789]
Quartz	0.25–15 μm	[790]
Titan tholins	0.02–920 μm	[791]
Titan tholins	0.2–1 μm	[792]
Titan tholins	2.5–25 μm	[793]
Pluto aerosol	0.27–2 μm	[794]
KCl	0.22–166 μm	[787]
ZnS	0.22–166 μm	[787]
SiO_2 (amorphous)	6.6–487 μm, 10–300 K	[795]
SiO_2 (crystalline)	6.25–10 μm, 300–928 K	[796]
Al_2O_3	7.8–200 μm	[797]
FeO	0.2–500 μm	[798]
$CaTiO_3$ (Perovskite)	2.0–500 μm	[799]
Fe_2O_3	0.1–1000 μm	[800]
Fe_2SiO_4 (Fayalite)	0.4–10 μm	[801]
Fe_2SiO_4 (Fayalite)	2–10000 μm	[802]
$MgAl_2O_4$ (annealed)	1.6–6825 μm	[803]
$MgAl_2O_4$ (natural)	2.0–10000 μm	[803]
Mg_2SiO_4	0.19–948 μm	[804]
$MgSiO_3$	0.2–500 μm	[804]
TiO_2 (Rutile)	0.47–36.2 μm	[805]
TiO_2 (Anastase)	2.0–5843 μm	[805]
TiO_2 (Brookite)	2.0–5843 μm	[806]
Supplementary		
Water and Ice	0.67–2.5 μm, imaginary	[807]
Saharan Dust	0.35–0.65 μm	[808]
SOA	0.375 and 0.632 μm, various radical sources	[809]
SOA	0.532 μm, various cases	[810]
Diesel Soot	0.45–10 μm	[787]
Sulfuric acid (H_2SO_4/H_2O)	200–300 K, 825–4700 cm^{-1}	[811]
Sulfuric acid (H_2SO_4/H_2O)	183–293 K, 2–23 μm	[812]
Nitric acid (H_2SO_4/HNO_3)	213–293 K, 2–23 μm	[812]
Sulfuric acid (H_2SO_4/H_2O)	Room temperature, 75 and 90% H_2SO_4	[813]
Nitric acid (H_2SO_4/HNO_3)	220 K, 754–4700 cm^{-1}	[814]
Nitric acid (H_2SO_4/HNO_3)	Room temperature, 2–40 μm	[815]
Sulfuric and Nitric acids	Room temperature, 6–11 μm	[816]
Titan organic haze	0.532 μm (single wavelength)	[817]

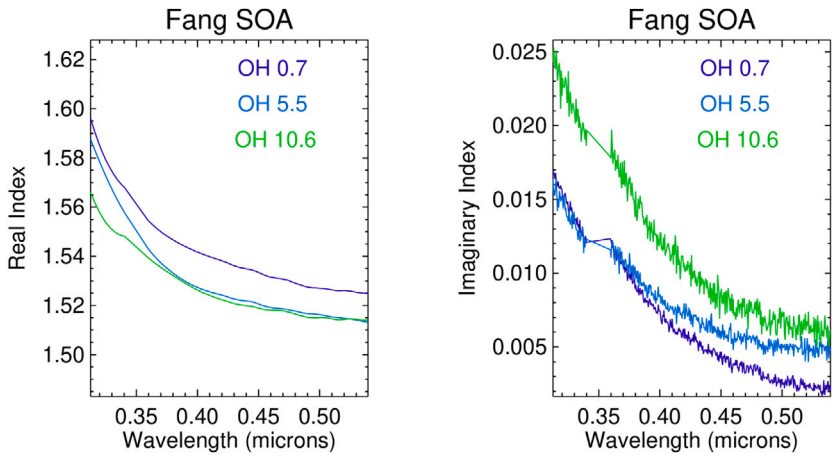

Fig. 33. Variations in the real and imaginary indices of SOA as a function of OH exposure time (in days) [778].

(with technical revisions released in v4.1.1 a month later). The modifications in v4.1, which were detailed in Mlawer et al. [22], were motivated by previous changes to the far-infrared self continuum that were previously implemented in MT_CKD_3.5.

In 2024, a major modification was made to MT_CKD in the infrared window region (780–1250 cm^{-1}, 12.8 to 8.0 μm) based on an analysis of ground-based radiometric observations taken over several years at two sites of the Atmospheric Radiation Measurement (ARM) program. This analysis, detailed in Mlawer et al. [822], indicated that the self continuum in the infrared window was too strong in the previous version of MT_CKD, while the foreign continuum was significantly too weak. Since the self continuum is the dominant absorption source in this region, the overall result of the continuum modification was an overall reduction in the transparency of the atmosphere, especially for highly moist atmospheres. The greater transparency increases the overall fraction of surface-leaving radiation that escapes to space, resulting in a notable increase in climate feedback (i.e. less warming in climate simulations than had previously been thought).

The final MT_CKD revision to date was v4.3, released in February 2024, which implemented modifications to the foreign continuum in window regions for wavenumbers greater than 4000 cm^{-1}. Several recent laboratory studies of the foreign continuum in windows between water-vapor bands in the near-infrared region had made it clear that the existing MT_CKD foreign continuum was too weak [823–827]. These studies were performed at the University of Grenoble using the highly-accurate cavity ring-down and optical feedback cavity enhanced absorption spectroscopy techniques. Fig. 34 shows the previous version of the MT_CKD continuum (green, v4.2) and the observations from these studies (black circles). Analysis of the observed foreign continuum coefficients in the windows shown in this figure, as well as in windows at lower wavenumbers that had been measured in other studies (not shown), determined that the rate of decrease of the coefficients transitioning from band wings into the windows differed for different spectral regions. Prior to these recent studies, the limited number of foreign continuum observations in wing-to-window transition regions permitted the use of a single parameter in the MT_CKD line-shape formulation to successfully model the decrease in continuum coefficients in all such transition regions. However, after these recent experimental studies, this simple approach was no longer able to provide consistency with all observations. For the revised MT_CKD_4.3 (red in Fig. 34), distinct decay parameters were used in the line-shape formulation depending on the dominant vibrational transition for a specific line. (For example, if $\Delta\nu_1$ is greater than both $\Delta\nu_2$ and $\Delta\nu_3$, a different parameter is used than if $\Delta\nu_2$ is the greatest, where 1, 2, 3 are the different vibrational modes of water vapor.) Clearly, MT_CKD_4.3 agrees better with the laboratory measurements than its predecessor. Importantly, the significantly greater foreign continuum values in windows that were measured in these studies propagate to windows at higher wavenumber values due to modified parameters in the MT_CKD line-shape formulation.

Fig. 35 shows the MT_CKD_4.3 self and foreign continuum coefficients from 0–20 000 cm^{-1}. For definitions of the continuum coefficients and further context, including the temperature dependence of the self continuum (the MT_CKD foreign continuum coefficients have no temperature dependence), see Section 2 of Mlawer et al. [22].

Ongoing analyses are expected to lead to improvements in the MT_CKD model in the next year. First, an analysis of a decade of ground-based radiometric observations in the far-infrared by an instrument deployed in Antarctica is underway – preliminary results from this study indicate that the foreign continuum absorption in this region is slightly greater than is needed for agreement with these observations. A reduction of the strength of the far-infrared foreign continuum would be consistent with a previous analysis of two years of measurements from this instrument [828]. Second, Simonova et al. [829] have developed a comprehensive model for the contribution of bound dimer absorption to the self continuum. As a result, the MT_CKD self continuum will soon include the bound dimer model of Simonova et al. [829]). To maintain the accuracy of total self continuum absorption, the existing MT_CKD self continuum coefficients are being modified to exclude the contributions from the bound dimer.

Associated code and data are available through the HITRAN website at https://hitran.org/mtckd and at the AER GitHub site at https://github.com/AER-RC/MT_CKD_H2O.

7. Global data and software

7.1. Database structure and interface

Since HITRAN2020, a number of incremental updates and minor improvements have been applied to HITRAN*online*, the website that provides online access to the HITRAN database at https://hirtan.org, and supporting infrastructure. These updates include a new staging server for hosting and testing database updates before pushing to the live website, along with maintenance upgrades to the software stack and security certificates in accordance with recommended best practices.

In addition, users should be aware that the storage location of supplemental data at HITRAN*online* now requires users to log in before downloading data. This change was instigated by the large addition of absorption cross-section files that are described in Section 3 and to encourage citation of the original data sources, as advised in the HITRAN Citation Policy (https://hitran.org/citepolicy/). Furthermore, a generous but finite limit on the maximum number of API requests permitted each day has been applied to deter excessive use of the fetch commands in HAPI [23].

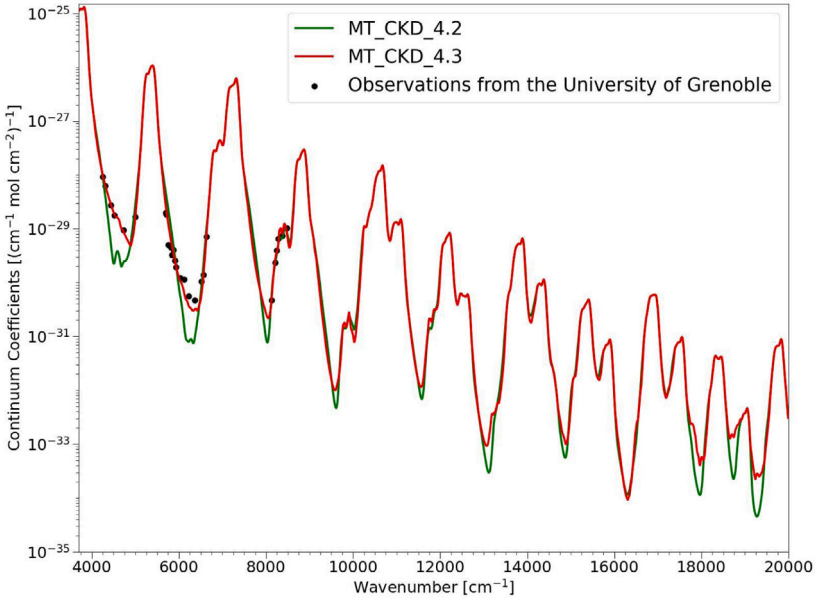

Fig. 34. Recent observations of water vapor foreign continuum coefficients from high quality experimental studies (black points), coefficients from the previous MT_CKD release (v4.2, green curve), and the current release (v4.3, red curve).

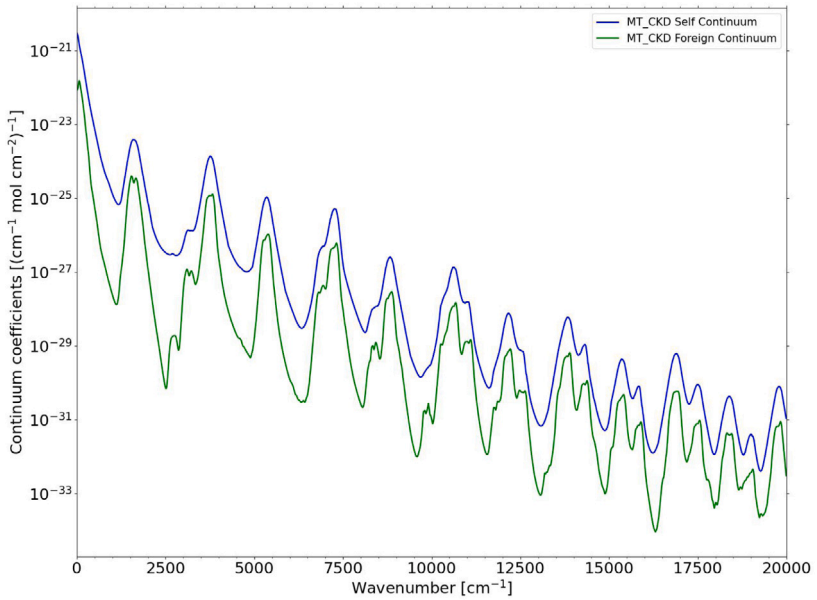

Fig. 35. Self (blue) and foreign (green) continuum coefficients from v4.3 of the MT_CKD water-vapor continuum model. Both sets of coefficients scale linearly with the density of the respective colliding gaseous molecules interacting with water vapor that results in each continuum component – water vapor for the self continuum or all gaseous molecules except for water vapor for the foreign continuum. In all spectral regions, the self continuum is stronger for the same number of colliding molecules. Since water-vapor molecules are a small fraction of the total atmospheric density, the foreign continuum is typically stronger than the self within water-vapor bands, while the self is typically stronger in between bands.

7.2. HITRAN application programming interface

The HITRAN Application Programming Interface (HAPI) [23], is a set of routines in Python that provides remote access to functionality and data provided by HITRAN. Since its release in 2016, it has been an indispensable tool for scientists and engineers. For instance, in the HITRAN group, it is used for the validation of data. Figs. 9,10,17,18,22,29 provide visual examples where validations were carried out using HAPI.

In the previous release of the HITRAN database [17], the second generation of the HAPI library was introduced. In this section, we present the updates that have been applied to HAPI2.

Since the latest HITRAN release, the HAPI2 library code was refactored for more flexible support of database backends, LBL code backends, and data format backends. Now, all three back-end types are implemented in HAPI through the plugin system.

For example, we have added support for the ClickHouse database engine [830] as a separate plugin. This engine allows data analysis on very large high-temperature linelists, including CDSD-4000 [831],

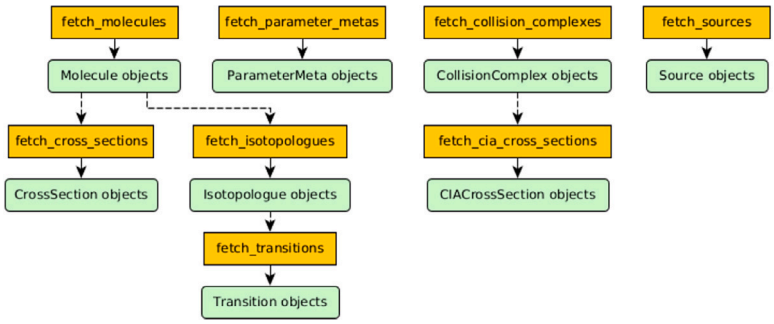

Fig. 36. Fetch functions hierarchy in HAPI2.

ExoMoL [218], HITEMP [72,125,182,832], and AI-3000K [71], and allows performing aggregate SQL queries on these linelists at reasonable speed. Note that HAPI2 uses SQLAlchemy to access the database backends, so the upper-level abstractions used in the library are database-agnostic. The ClickHouse plugin is available for download at the HITRAN*online* github page [833].

The other plugin, which is currently available, is a fast LBL code that implements the Direct Integral Transform method [834]. This method is based on the discrete Fourier transform, and its algorithmic complexity grows much slower with the number of lines compared to the "naive" LBL method, so it is preferable in the high-temperature cases when this number is large. For details of this method, we refer the reader to the original paper by Van den Bekerom and Pannier [834].

The Total Internal Partition Sum packages, TIPS-2021 [145] and TIPS-2024 [338], were incorporated into both HAPI and HAPI2. In HAPI2, previous versions of TIPS [145,454,835] are available as SQLAlchemy object-relational mapping instances of the PartitionFunction class. TIPS-2024 is expected to be available in this parametrization in the near future.

To facilitate the search for items in the local database, the alias-based lookup has been added for each searchable object. For example, the water molecule has a number of names, or aliases, which all can be used in a search. Using InChIKey or the molecule name will invoke the same object, as shown in the following code snippet:

```
Input: Molecule("XLYOFNOQVPJJNP-UHFFFAOYSA-N")
is Molecule("water")
Output: True
```

HAPI2 allows one to fetch objects from the HITRAN*online* server and store them in the local database for further work. All downloadable objects form the type hierarchy, which is similar to the relational database schema given in Hill et al. [24]. To download lower-level objects, such as spectroscopic transitions or cross-sections, one must download higher-level objects, as shown in Fig. 36. For instance, to download the transitions of carbon dioxide, the user must first download the corresponding Molecule object using the fetch_molecules function. Then, one should download isotopologues of this molecule using fetch_isotopologues, which will make it possible to run the fetch_transitions function. The orange blocks in Fig. 36 correspond to the HAPI2 functions, while the green blocks show the outputs of these functions.

Besides using the HAPI2 functions for fetching the data, the user can retrieve them directly from the HITRAN*online* site using the REST API GET requests. Such requests use the URLs with the following structure:

```
https://hitran.org/api/v2/<api_key>/<endpoint>
[?parameters]
```

Here, the user must provide an API key and API endpoint, as well as the list of parameters. The response of the server is given in JSON format. The example of such API request is given in Fig. 37 for the cross-section case. The request parameters are optional and can narrow down the database search.


```
{
  "status": "OK",
  "message": "Fetched 1 instance(s) of APICrossSection",
  "content": {
    "class": "CrossSection",
    "format": "json",
    "data": [
      {
        "id": 2371,
        "molecule_id": 200,
        "source_id": 1164,
        "numin": 599.994293,
        "numax": 6499.953174,
        "npnts": 97902,
        "sigma_max": 5.40769325456542e-19,
        "temperature": 298.15,
        "pressure": 760.0,
        "resolution": 0.112,
        "resolution_units": "cm-1",
        "broadener": "N2",
        "filename": "C3H4Cl2_298.1K-760.0K_600.0-6500.0_0.11_N2_396_43.xsc",
        "valid_to": "3000-01-01",
        "valid_from": "2017-06-08",
        "__class__": "CrossSection",
        "__identity__": "id",
        "molecule_alias": "1,3-Dichloropropene (cis)",
        "source_alias": "Ref. [1164]",
        "format": "xsc",
        "status": "main",
        "description": "",
        "apodization": "",
        "json": ""
      }
    ]
  },
  "timestamp": "2025-06-04 05:42:38.326874",
  "query": "id=2371",
  "source": "HITRANonline"
}
```


Fig. 37. HITRAN*online* REST API raw JSON response from the cross-sections endpoint with the specified item id.

The connection of the HAPI2 fetch functions with the REST API is shown in Table 8.

The HAPI2 package, its plugins, and documentation are available on the HITRAN*online* Github account (https://github.com/hitranonline) and on the Python Package Index. The installation can be done via pip:

```
pip install hitran-api2
```

An alternative way would be installing directly from the Github repository:

```
git clone https://github.com/hitranonline/hapi2.git
cd hapi2
pip install .
```

7.2.1. *Pre-dissociation widths*

To account for the necessary inclusion of pre-dissociation half-width at half-maximum (HWHM) values for the HITRAN line list of S_2 (see Section 2.58), a Python code was provided with the supplementary material of the published S_2 line list [595] that worked as a plugin application for HAPI. The code applies the pre-dissociation line widths,

Table 8
Summary on the HAPI REST API endpoints.

HAPI2 Class	REST API endpoint	HAPI2 Function	Sample request parameters
Source	sources	fetch_sources	id,title,authors
Molecule	molecules	fetch_molecules	id,inchi,common_name
Isotopologue	isotopologues	fetch_isotopologues	id,inchi,afgl_code
ParameterMeta	parameter-metas	fetch_parameter_metas	id,name
CrossSection	cross-sections	fetch_cross_sections	id,molecule_id,source_id
CollisionComplex	collision-complexes	fetch_collision_complexes	id,chemical_symbol
CIACrossSection	cia-cross-sections	fetch_cia_cross_sections	id,collision_complex_id,source_id

in addition to the pressure- and temperature broadening of the lines, to enable accurate reproduction of the experimental spectrum. While this code can be used to simulate the S_2 spectrum using the HITRAN line list and HAPI, a complete incorporation into the HAPI code is planned for a future update. This is to enable more flexibility for other molecules that demonstrate pre-dissociation effects, such as the Schumann–Runge bands of O_2 in the UV.

7.2.2. Expanded parameter lists

The mHT line profile [512] and double-power-law (DPL) temperature dependencies, as introduced in Section 2.62, require a substantial expansion in the number of parameters accessible to HAPI. Ref. [512] provides an overview of the seven mHT lineshape parameters, alongside their additional parameters for the DPL temperature-dependence (i.e., 35 parameters in total). While these parameters are initially only available for the hydrogen molecule, they can be retrieved from the HITRAN website with HAPI by following the instructions provided in Wcisło et al. [512].

7.3. Total Internal Partition Sums (TIPS)

For the 2024 edition of HITRAN, Total Internal Partition Sums (TIPS), Q(T), were calculated [338] for: four new isotopologues of molecules present on HITRAN2020: $^{16}O^{14}N^{18}O$, $^{14}NH_2D$, $H^{13}COOH$, $^{13}CH_3F$; and for six new molecules added to HITRAN2024: CH_3, S_2, COFCl (two isotopologues, $^{12}C^{16}OF^{35}Cl$ and $^{12}C^{16}OF^{37}Cl$), HONO, $ClNO_2$ (two isotopologues, $^{35}ClNO_2$ and $^{37}ClNO_2$), and H_3^+ (only the main isotopologue is added to HITRAN but TIPS were also calculated for H_2D^+, HD_2^+, and D_3^+). New calculations were also carried out for the five most abundant isotopologues of N_2O; for the two most abundant isotopologues of NO_2; for the two most abundant isotopologues of NH_3; the seven most abundant isotopologues of OCS; and the four most abundant isotopologues of CS_2. The TIPS calculations for N_2 [836] and NO [837] were also added to TIPS2024, replacing the previous data. Furthermore, all partition sums in TIPS2021 [145] calculated prior to 2020 were recalculated using the most recent CODATA constants [838]; while the differences are very small, TIPS2024 provides a consistent set of partition sums for all molecules/isotopologues on HITRAN2024. TIPS2024 also contains a number of isotopologues that are not yet provided in the HITRAN database. In total, TIPS2024 provides data for 196 isotopologues of 62 molecules. The calculations range from $T = 1$ K to T_{max} in 1 K steps, where the maximum temperatures (T_{max}) were determined based on the available energy states for the isotopologue in question, and to ensure convergence of Q(T). The dissociation energies were also a factor in determining T_{max}. In the codes, a simple linear interpolation routine calculates values with less than 0.001 absolute average percent difference compared to the direct calculation at the same temperature. The FORTRAN and Python codes are available at Zenodo (v1.2 https://doi.org/10.5281/zenodo.17191976), and in the supplementary section on the HITRAN website (https://hitran.org/files/TIPS/). The TIPS2024 data will also be made available for use with HAPI.

8. Conclusions

This article summarizes extensive updates and expansion of the HITRAN molecular spectroscopic database that culminated in the release of the HITRAN2024 quadrennial edition. The improvements follow the PACT philosophy (explained in the Introduction) by providing the most accurate (often sub-percent uncertainty) spectroscopic parameters for the most prominent absorbers of light in the terrestrial and planetary atmospheres, while also substantially increasing spectral and dynamic ranges, adding new molecular species and their isotopologues, as well as addressing additional spectroscopic phenomena. For all newly-added molecules/isotopologues, new TIPS and other auxiliary parameters have been calculated.

HITRAN continues to take pride in being practical for a very wide area of applications, thanks to the use of standardized parametrizations, while the new parametrizations have been adopted in consultation with a broad community of spectroscopists and atmospheric and planetary scientists. Most of the parameters in the database are traceable to their original sources as explained in Ref. [839]. The number of molecules in the line-by-line portion of the database has increased from 55 to 61, while the number of molecules represented with experimental cross-sections has increased twofold and now boasts over 600 molecules with many temperature-pressure sets. Substantial improvements and expansions were also carried out in the collision-induced absorption and aerosol sections of the database. A much-anticipated addition to the database, the water-vapor continuum model, has finally been added.

Altogether, HITRAN2024 makes a very substantial step toward our ability to account for different molecular phenomena when modeling or interpreting radiative transfer in the terrestrial atmosphere, while also substantially increasing our capability to model planetary and exoplanetary atmospheres.

9. Future work

Many molecules still have limited spectral coverage in the line-by-line section. Indeed, historically, some measurements that were included in HITRAN were carried out for specific bands in the window region of water-vapor absorptions, so they can be targeted by certain terrestrial remote-sensing missions. Other factors that often limit the expansion of the spectral range include the difficulty of experimental analyses and the complexity of theoretical calculations. Considering that there have been major advances in instrumentation and speed of the calculations, one can expect a substantial expansion of the spectral line lists in HITRAN. Even more intriguing is the potential impact of the emergence of Artificial Intelligence (AI), which is expected to accelerate the calculations and aid in experimental spectra assignments.

More molecules/isotopologues need to be added to HITRAN to fill in the gaps in our knowledge of spectroscopy of molecules needed for terrestrial and planetary applications. For instance, SiF_4 [840] and SiH_4 [841] are important for studies of volcanic plumes and of the interstellar medium, as well as for industrial measurement applications.

The database will continue to expand with the addition of the parameters associated with non-Voigt line shapes, including line mixing. Simultaneous parametrization of speed-dependent Voigt and full line mixing has been challenging so far, but new methods have been

proposed [842], and it is likely that the future editions of HITRAN will be able to tackle this issue.

The accounting for different collisional effects near the line centers has been addressed through the introduction of the modified Hartmann-Tran profile [512]. Away from the center of the line, a more rigorous characterization of the line shape adds an extra degree of complexity and involves taking into account the breakdown of the impact approximation (BIA). The BIA effect, which causes intensity to be transferred from line centers to line wings [843–845], was recognized (see, for instance, Refs. [97,845]) to be appreciable (considering sub-percent requirements on the accuracy of the parameters) when working at atmospheric pressure. The current suggested solution is to introduce experimentally-determined (and in some cases theoretically constrained) "intensity depletion" coefficients and their temperature dependencies that can be provided for each transition in the database and used as additional multiplicative factors on intensities when calculating absorption cross-sections. This parametrization is being actively discussed in the community [243], and future editions of HITRAN will likely include it.

In general, the far-wing parametrization will be the next challenge for the HITRAN community, as the Voigt or even mHT profiles cannot properly model absorption beyond a few $cm^{-1}$from the line center under terrestrial atmospheric conditions. At the moment, only empirical parametrizations exist per molecule, which include the MT_CKD water-vapor continuum, where the far-wing effect is being treated together with CIA and the water dimer, although, as discussed in the corresponding Section 6, the latter effect will be separated within the model. The need for far-wing representation is even more pronounced in the exoplanetary and brown dwarf communities, as highlighted in Refs. [846,847].

As already mentioned, this edition has overseen a massive update and expansion of the dataset of IR cross-sections; however, only a few have been added in the UV. For the next edition of the database, we plan to substantially enhance the database of the UV cross-sections and even line lists (where possible). This will aid the interpretation of the results for past, current, and future Earth (including TEMPO [128] and GEMS [848]) and (exo)planetary (including EnVision [849] and HWO [850]) remote-sensing missions operating in this spectral range.

CRediT authorship contribution statement

I.E. Gordon: Writing – review & editing, Writing – original draft, Visualization, Validation, Supervision, Resources, Project administration, Methodology, Investigation, Funding acquisition, Formal analysis, Data curation, Conceptualization. **L.S. Rothman:** Writing – review & editing, Writing – original draft, Methodology, Conceptualization. **R.J. Hargreaves:** Writing – review & editing, Writing – original draft, Visualization, Validation, Software, Methodology, Investigation, Funding acquisition, Formal analysis, Data curation. **F.M. Gomez:** Writing – review & editing, Writing – original draft, Visualization, Validation, Investigation, Formal analysis, Data curation. **T. Bertin:** Writing – review & editing, Writing – original draft, Visualization, Validation, Investigation, Formal analysis, Data curation. **C. Hill:** Software, Resources. **R.V. Kochanov:** Writing – original draft, Visualization, Software, Conceptualization. **Y. Tan:** Writing – original draft, Visualization, Investigation, Formal analysis. **P. Wcisło:** Writing – review & editing, Writing – original draft, Visualization, Software, Investigation, Formal analysis. **V. Yu. Makhnev:** Writing – original draft, Visualization, Validation, Investigation, Formal analysis, Data curation. **P.F. Bernath:** Formal analysis. **M. Birk:** Writing – review & editing, Writing – original draft, Visualization, Investigation, Formal analysis, Conceptualization. **V. Boudon:** Writing – original draft, Investigation, Formal analysis. **A. Campargue:** Writing – review & editing, Writing – original draft, Visualization, Validation, Investigation, Data curation. **A. Coustenis:** Conceptualization. **B.J. Drouin:** Writing – original draft, Investigation, Formal analysis. **R.R. Gamache:** Writing – review & editing, Writing – original draft, Investigation, Formal analysis, Data curation. **J.T. Hodges:** Writing – review & editing, Writing – original draft, Investigation, Formal analysis. **D. Jacquemart:** Writing – review & editing, Writing – original draft, Visualization, Investigation, Formal analysis. **E.J. Mlawer:** Writing – review & editing, Writing – original draft, Visualization, Investigation, Formal analysis. **A.V. Nikitin:** Writing – review & editing, Writing – original draft, Validation, Investigation, Formal analysis. **V.I. Perevalov:** Writing – review & editing, Writing – original draft, Validation, Investigation, Formal analysis. **M. Rotger:** Investigation, Formal analysis. **S. Robert:** Investigation, Conceptualization. **J. Tennyson:** Writing – review & editing, Writing – original draft, Investigation, Formal analysis. **G.C. Toon:** Validation. **H. Tran:** Writing – original draft, Investigation, Formal analysis. **V.G. Tyuterev:** Writing – review & editing, Writing – original draft, Investigation, Formal analysis. **E.M. Adkins:** Writing – review & editing, Writing – original draft, Investigation, Formal analysis, Data curation. **A. Barbe:** Investigation, Formal analysis. **D.M. Bailey:** Formal analysis. **K. Bielska:** Investigation, Formal analysis. **L. Bizzocchi:** Investigation, Formal analysis. **T.A. Blake:** Investigation, Formal analysis. **C.A. Bowesman:** Formal analysis. **P. Cacciani:** Formal analysis. **P. Čermák:** Writing – original draft, Investigation, Formal analysis. **A.G. Császár:** Methodology, Investigation, Formal analysis. **L. Denis:** Writing – original draft, Visualization, Methodology, Investigation, Formal analysis, Data curation. **S.C. Egbert:** Formal analysis. **O. Egorov:** Visualization, Formal analysis. **A. Yu. Ermilov:** Formal analysis. **A.J. Fleisher:** Investigation, Formal analysis. **H. Fleurbaey:** Investigation, Formal analysis. **A. Foltynowicz:** Writing – original draft, Investigation, Formal analysis. **T. Furtenbacher:** Investigation, Data curation. **M. Germann:** Formal analysis. **E.R. Guest:** Writing – original draft, Investigation. **J.J. Harrison:** Investigation. **J.-M. Hartmann:** Investigation. **A. Hjältén:** Formal analysis. **S.-M. Hu:** Investigation, Formal analysis. **X. Huang:** Writing – review & editing, Writing – original draft, Investigation, Formal analysis, Data curation. **T.J. Johnson:** Methodology, Investigation, Formal analysis, Data curation. **H. Jóźwiak:** Visualization, Formal analysis. **S. Kassi:** Formal analysis. **M.V. Khan:** Formal analysis. **F. Kwabia-Tchana:** Writing – original draft, Visualization, Investigation, Formal analysis. **D. Lisak:** Investigation, Formal analysis. **A.-W. Liu:** Formal analysis. **O.M. Lyulin:** Writing – original draft, Investigation, Formal analysis. **N.A. Malarich:** Investigation, Formal analysis. **L. Manceron:** Investigation, Formal analysis. **A.A. Marinina:** Investigation, Formal analysis. **S.T. Massie:** Writing – review & editing, Writing – original draft, Visualization, Methodology, Investigation, Formal analysis, Data curation. **J. Mascio:** Investigation, Formal analysis. **E.S. Medvedev:** Writing – review & editing, Writing – original draft, Visualization, Investigation, Formal analysis. **V.V. Meshkov:** Formal analysis. **G. Ch. Mellau:** Writing – original draft, Formal analysis. **M. Melosso:** Writing – review & editing, Writing – original draft, Investigation, Formal analysis. **S.N. Mikhailenko:** Investigation, Formal analysis. **D. Mondelain:** Investigation, Formal analysis. **H.S.P. Müller:** Writing – original draft, Investigation, Formal analysis. **M. O'Donnell:** Visualization, Investigation, Formal analysis. **A. Owens:** Writing – original draft, Investigation, Formal analysis. **A. Perrin:** Writing – original draft, Visualization, Methodology, Investigation, Formal analysis. **O.L. Polyansky:** Investigation, Formal analysis. **P.L. Raston:** Writing – original draft, Visualization, Investigation, Formal analysis. **Z.D. Reed:** Investigation, Formal analysis. **M. Rey:** Writing – original draft, Visualization, Methodology, Investigation, Formal analysis. **C. Richard:** Investigation, Formal analysis. **G.B. Rieker:** Investigation, Formal analysis. **C. Röske:** Investigation, Formal analysis. **S.W. Sharpe:** Methodology, Investigation, Formal analysis, Data curation. **E. Starikova:** Investigation, Formal analysis. **N. Stolarczyk:** Writing – original draft, Investigation, Formal analysis. **A.V. Stolyarov:** Investigation, Formal analysis. **K. Sung:** Writing – original draft, Investigation, Formal analysis. **F. Tamassia:** Writing – original draft, Investigation, Formal analysis. **J. Terragni:** Writing – review & editing, Writing –

original draft, Visualization, Validation, Investigation, Formal analysis, Data curation. **V.G. Ushakov:** Investigation, Formal analysis. **S. Vasilchenko:** Investigation, Formal analysis. **B. Vispoel:** Investigation, Formal analysis. **K.L. Vodopyanov:** Investigation. **G. Wagner:** Visualization, Investigation, Formal analysis. **S. Wójtewicz:** Formal analysis. **S.N. Yurchenko:** Investigation, Formal analysis. **N.F. Zobov:** Investigation, Formal analysis.

Declaration of competing interest

The authors declare that they have no known competing financial interests or personal relationships that could have appeared to influence the work reported in this paper.

Acknowledgments

The development of the HITRAN2024 database and associated tools was supported by NASA grants 80NSSC20K0962, 80NSSC20K1059, 80NSSC23K1596, and 80NSSC24K0080. Portions of the research described in this paper were performed at the Jet Propulsion Laboratory, California Institute of Technology, under contract with NASA. We thank many scientists who carried out research that resulted in some of the data adapted in the HITRAN2024 edition: Ons Ben Fathallah, Kirill Berezkin, Jeanna Buldyreva, Arnaud Cuisset, Alexandra Domanskaya, Aamir Farooq, Artem Finenko, Paul Godin, Ronald Hanson, Osama Ishtiak, Elena Jiménez, Isabelle Kleiner, Karine Le Bris, Gang Li, Jeong Sik Lim, David Long, Harrald Mutschke, Olga Naumenko, Ole John Nielsen, Vivienne Payne, John Pearson, Tatiana Petrova, Laurence Regalia, David Schwenke, Christopher Strand, Kimberly Strong, Mads P. Sulbaek Andersen, Mohamed Sy, Sergey Tashkun, Jean Vander Auwera, Andrey Vigasin, Rainer Volkamer.

We thank many colleagues who provided independent validations of the HITRAN data and reported their findings and constructive feedback: Andrea Banzatti, Chris Boone, Julien De Wit, Norbert Glatthor, Richard Larsson, Prajwal Niraula, Erwan Pannier, Dirk Van den Bekerom, and Laurent Wiesenfeld.

Appendix. Abbreviations

When describing the inclusion of data into HITRAN, the following abbreviations and acronyms have been used at various points throughout the article:

- ABSCO – Absorption coefficient [123]
- ACE – Atmospheric Chemistry Experiment [185]
- AER – Atmospheric and Environmental Research
- API – Application programming interface
- ASCII – American standard code for information interchange
- CCSD(T) – Coupled-cluster singles, doubles, and perturbative triples
- CDMS – Cologne Database for Molecular Spectroscopy
- CDSD – Carbon Dioxide Spectroscopic Database
- CFC – Chlorofluorocarbon
- ChMeCaSDa – Chloromethane Calculated Spectroscopic Database
- CIA – Collision-induced absorption
- CRDS – Cavity ring-down spectroscopy
- DLR – Deutsches Zentrum für Luft und Raumfahrt (German Aerospace Center)
- DMS – Dipole moment surface
- DPL – Double-power law
- ECaSDa – Ethylene Calculated Spectroscopic Database
- EDTM – Effective dipole transition moment
- EH – Effective Hamiltonian
- ESA – European Space Agency
- FIR – Far-infrared
- FORUM – Far-infrared Outgoing Radiation Understanding and Monitoring [149]
- FT – Fourier transform
- FTS – Fourier transform spectrometer
- GEMS – Geostationary Environment Monitoring Spectrometer [848]
- GOSAT – Greenhouse Gases Observing Satellite [92]
- HAPI – HITRAN Application Programming Interface [23]
- HCFC – Hydrochlorofluorocarbon
- HITRAN – High-resolution transmission molecular absorption database [1]
- HITEMP – High-temperature molecular spectroscopic database [125]
- HR – High-resolution
- HT – Hartmann–Tran
- IAO – Institute of Atmospheric Optics
- IASI – Infrared Atmospheric Sounding Interferometer [186]
- ICB – Laboratoire de l'Université de Bourgogne
- IDL – Interactive Design Language
- IR – Infrared
- ISOGG – Improved Spectroscopy for satellite measurements Of Greenhouse Gases
- JPL – Jet Propulsion Laboratory
- JSON – JavaScript Object Notation
- JWST – James Webb Space Telescope [19]
- LBL – Line-by-line
- LISA – Laboratoire Interuniversitaire des Systèmes Atmosphériques
- MARVEL – Measured Active Rotational-Vibrational Energy Levels
- MeCaSDa – Methane Calculated Spectroscopic
- MIR – Mid-infrared
- MT_CKD – Mlawer-Tobin Clough-Kneizys-Davies [821]
- MW – Microwave
- NASA – National Aeronautics and Space Administration
- NOSL – Nitrous Oxide Spectral Line list
- netCDF – Network common data form
- NIR – Near-infrared
- NIST – National Institute of Standards and Technology
- NOSD-1000 – Nitrous Oxide Spectroscopic Data Bank at 1000 K [183]
- NSO – National Solar Observatory
- OCO – Orbiting Carbon Observatory [90,91]
- ODU – Old Dominion University
- PACT – Practicality, Accuracy, Completeness, and Traceability
- PES – Potential energy surface
- PNNL – Pacific Northwest National Laboratory
- PSC – Polar stratospheric cloud
- REST API – Representational state transfer application programming interface
- RFM – Reference Forward Model [851]
- RI – Refractive indices
- RKR – Rydberg–Klein–Rees
- RMS – Root mean square
- S&MPO – Spectroscopy and Molecular Properties of Ozone
- SDV – Speed-dependent Voigt
- SI – Système International
- SISAM – Spectromètre Interférentiel à Sélection par l'Amplitude de la Modulation (Interferential Spectrometer by Selection of Amplitude Modulation)
- SNR – Signal to noise ratio
- SOA – Secondary organic aerosol
- TCCON – Total Carbon Column Observing Network [32]
- TEMPO – Tropospheric Emissions: Monitoring of Pollution [128]
- TheoReTS – Theoretical Reims-Tomsk Spectral data [407]
- TIPS – Total Internal Partition Sums

- TROPOMI – Tropospheric Monitoring Instrument [187]
- UCL – University College London
- ULB – Université Libre de Bruxelles
- UV – Ultraviolet
- VP – Voigt profile

Data availability

This article describes public database.

References

[1] Rothman LS. History of the HITRAN database. Nat Rev Phys 2021;0123456789. http://dx.doi.org/10.1038/s42254-021-00309-2.

[2] McClatchey R, Benedict W, Clough S, Burch D, Calfee R, Fox K, et al. AFCRL atmospheric absorption line parameters compilation. Environ Res Pap 1973;434:1–86, URL https://lweb.cfa.harvard.edu/HITRAN/Download/AFCRL73.pdf.

[3] Rothman LS, McClatchey RA. Updating of the AFCRL atmospheric absorption line parameters compilation. Appl Opt 1976;15(11):2616–7. http://dx.doi.org/10.1364/AO.15.2616_1.

[4] Rothman LS. Update of the AFGL atmospheric absorption line parameters compilation. Appl Opt 1978;17(22):3517–8. http://dx.doi.org/10.1364/AO.17.003517.

[5] Rothman LS, Clough SA, McClatchey RA, Young LG, Snider DE, Goldman A. AFGL trace gas compilation. Appl Opt 1978;17(4):507. http://dx.doi.org/10.1364/AO.17.000507.

[6] Rothman LS, Goldman A, Gillis JR, Tipping RH, Brown LR, Margolis JS, et al. AFGL trace gas compilation: 1980 version. Appl Opt 1981;20(8):1323–8. http://dx.doi.org/10.1364/AO.20.001323.

[7] Rothman LS, Gamache RR, Barbe A, Goldman A, Gillis JR, Brown LR, et al. AFGL atmospheric absorption line parameters compilation: 1982 edition. Appl Opt 1983;22(15):2247–56. http://dx.doi.org/10.1364/ao.22.002247.

[8] Rothman LS, Goldman A, Gillis JR, Gamache RR, Pickett HM, Poynter RL, et al. AFGL trace gas compilation: 1982 version. Appl Opt 1983;22(11):1616–27. http://dx.doi.org/10.1364/ao.22.001616.

[9] Rothman LS, Gamache RR, Goldman A, Brown LR, Toth RA, Pickett HM, Poynter RL, et al. The HITRAN database: 1986 edition. Appl Opt 1987;26:4058–97. http://dx.doi.org/10.1364/AO.26.004058.

[10] Rothman L, Gamache R, Tipping R, Rinsland C, Smith M, Benner DC, et al. The HITRAN molecular database: Editions of 1991 and 1992. J Quant Spectrosc Radiat Transfer 1992;48(5–6):469–507. http://dx.doi.org/10.1016/0022-4073(92)90115-K.

[11] Rothman LS, Rinsland CP, Goldman A, Massie ST, Edwards DP, Flaud J-M, et al. The HITRAN molecular spectroscopic database and HAWKS (HITRAN atmospheric workstation): 1996 edition. J Quant Spectrosc Radiat Transfer 1998;60:665–710. http://dx.doi.org/10.1016/S0022-4073(98)00078-8.

[12] Rothman LS, Barbe A, Benner DC, Brown LR, Camy-Peyret C, Carleer MR, et al. The HITRAN molecular spectroscopic database: Edition of 2000 including updates through 2001. J Quant Spectrosc Radiat Transfer 2003;82:5–44. http://dx.doi.org/10.1016/S0022-4073(03)00146-8.

[13] Rothman LS, Jacquemart D, Barbe A, Chris Benner D, Birk M, Brown LR, et al. The HITRAN 2004 molecular spectroscopic database. J Quant Spectrosc Radiat Transfer 2005;96:139–204. http://dx.doi.org/10.1016/j.jqsrt.2004.10.008.

[14] Rothman LS, Gordon IE, Barbe A, Benner DC, Bernath PF, Birk M, et al. The HITRAN 2008 molecular spectroscopic database. J Quant Spectrosc Radiat Transfer 2009;110:533–72. http://dx.doi.org/10.1016/j.jqsrt.2009.02.013.

[15] Rothman L, Gordon I, Babikov Y, Barbe A, Chris Benner D, Bernath P, et al. The HITRAN2012 molecular spectroscopic database. J Quant Spectrosc Radiat Transfer 2013;130:4–50. http://dx.doi.org/10.1016/j.jqsrt.2013.07.002.

[16] Gordon IE, Rothman LS, Hill C, Kochanov RV, Tan Y, Bernath PF, et al. The HITRAN2016 molecular spectroscopic database. J Quant Spectrosc Radiat Transfer 2017;203:3–69. http://dx.doi.org/10.1016/j.jqsrt.2017.06.038.

[17] Gordon IE, Rothman LS, Hargreaves RJ, Hashemi R, Karlovets EV, Skinner FM, et al. The HITRAN2020 molecular spectroscopic database. J Quant Spectrosc Radiat Transfer 2022;277:107949. http://dx.doi.org/10.1016/j.jqsrt.2021.107949.

[18] MacDonald RJ, Batalha NE. A catalog of exoplanet atmospheric retrieval codes. Res Notes the AAS 2023;7:54. http://dx.doi.org/10.3847/2515-5172/ACC46A.

[19] Rigby J, Perrin M, McElwain M, Kimble R, Friedman S, Lallo M, et al. The science performance of JWST as characterized in commissioning. Publ Astron Soc Pac 2023;135(1046):048001. http://dx.doi.org/10.1088/1538-3873/acb293, arXiv:2207.05632.

[20] Colmenares MJ, Bergin EA, Salyk C, Pontoppidan KM, Arulanantham N, Calahan J, et al. JWST/MIRI detection of a carbon-rich chemistry in the disk of a solar nebula analog. Astrophys J 2024;977(2):173. http://dx.doi.org/10.3847/1538-4357/ad8b4f, arXiv:2410.18187.

[21] Salyk C, Pontoppidan KM, Banzatti A, Bergin E, Arulanantham N, Najita J, Blake GA, Carr J, Zhang K, Xie C. Emission from multiple molecular isotopologues in a high-inclination protoplanetary disk. Astron J 2025;169(3):184. http://dx.doi.org/10.3847/1538-3881/adb397, arXiv:2502.05061.

[22] Mlawer E, Cady-Pereira K, Mascio J, Gordon I. The inclusion of the MT_CKD water vapor continuum model in the HITRAN molecular spectroscopic database. J Quant Spectrosc Radiat Transfer 2023;306:108645. http://dx.doi.org/10.1016/j.jqsrt.2023.108645.

[23] Kochanov RV, Gordon IE, Rothman LS, Wcisło P, Hill C, Wilzewski JS. HITRAN Application Programming Interface (HAPI): A comprehensive approach to working with spectroscopic data. J Quant Spectrosc Radiat Transfer 2016;177:15–30. http://dx.doi.org/10.1016/j.jqsrt.2016.03.005.

[24] Hill C, Gordon IE, Kochanov RV, Barrett L, Wilzewski JS, Rothman LS. HITRAN*online*: An online interface and the flexible representation of spectroscopic data in the HITRAN database. J Quant Spectrosc Radiat Transfer 2016;177:4–14. http://dx.doi.org/10.1016/j.jqsrt.2015.12.012.

[25] Wcisło P, Gordon I, Tran H, Tan Y, Hu S-M, Campargue A, et al. The implementation of non-Voigt line profiles in the HITRAN database: H_2 case study. J Quant Spectrosc Radiat Transfer 2016;177:75–91. http://dx.doi.org/10.1016/j.jqsrt.2016.01.024.

[26] Hashemi R, Gordon IE, Tran H, Kochanov RV, Karlovets EV, Tan Y, et al. Revising the line-shape parameters for air- and self-broadened CO_2 lines toward a sub-percent accuracy level. J Quant Spectrosc Radiat Transfer 2020;256:107283. http://dx.doi.org/10.1016/j.jqsrt.2020.107283.

[27] Hashemi R, Gordon IE, Adkins EM, Hodges JT, Long DA, Birk M, et al. Improvement of the spectroscopic parameters of the air- and self-broadened N_2O and CO lines for the HITRAN2020 database applications. J Quant Spectrosc Radiat Transfer 2021;107735. http://dx.doi.org/10.1016/j.jqsrt.2021.107735.

[28] Tan Y, Kochanov RV, Rothman LS, Gordon IE. Introduction of water-vapor broadening parameters and their temperature-dependent exponents into the HITRAN database: Part I—CO_2, N_2O, CO, CH_4, O_2, NH_3, and H_2S. J Geophys Res (Atmospheres) 2019;124(21):11,580–94. http://dx.doi.org/10.1029/2019JD030929, arXiv:1906.01475.

[29] Wilzewski JS, Gordon IE, Kochanov RV, Hill C, Rothman LS. H_2, He, and CO_2 line-broadening coefficients, pressure shifts and temperature-dependence exponents for the HITRAN database. Part 1: SO_2, NH_3, HF, HCl, OCS and C_2H_2. J Quant Spectrosc Radiat Transfer 2016;168:193–206. http://dx.doi.org/10.1016/j.jqsrt.2015.09.003.

[30] Tan Y, Skinner FM, Samuels S, Hargreaves RJ, Hashemi R, Gordon IE. H_2, He, and CO_2 pressure-induced parameters for the HITRAN database. II. Line lists of CO_2, N_2O, CO, SO_2, OH, OCS, H_2CO, HCN, PH_3, H_2S, and GeH_4. Astrophys J Suppl Ser 2022;262(2):40. http://dx.doi.org/10.3847/1538-4365/ac83a6.

[31] De Biévre P, Gallet M, Holden NE, Barnes IL. Isotopic abundances and atomic weights of the elements. J Phys Chem Ref Data 1984;13(3):809–91. http://dx.doi.org/10.1063/1.555720.

[32] Wunch D, Toon GC, Blavier J-FL, Washenfelder RA, Notholt J, Connor BJ, et al. The total carbon column observing network. Philos Trans R Soc A: Math Phys Eng Sci 2011;369(1943):2087–112. http://dx.doi.org/10.1098/rsta.2010.0240.

[33] Vispoel B, Cavalcanti JH, Paige ET, Gamache RR. Vibrational dependence, temperature dependence, and prediction of line shape parameters for the H_2O-N_2 collision system. J Quant Spectrosc Radiat Transfer 2020;253:107030. http://dx.doi.org/10.1016/j.jqsrt.2020.107030.

[34] Cady-Pereira K, Alvarado M, Mlawer E, Iacono M, Delamere J, Pernak R. AER line file parameters (v3.8.1). 2020, http://dx.doi.org/10.5281/zenodo.5120012, Spectroscopic line parameter database; version 3.8.1..

[35] Campargue A, Mikhailenko SN, Kassi S, Vasilchenko S. Validation tests of the W2020 energy levels of water vapor. J Quant Spectrosc Radiat Transfer 2021;276:107914. http://dx.doi.org/10.1016/J.JQSRT.2021.107914.

[36] Furtenbacher T, Tóbiás R, Tennyson J, Polyansky OL, Kyuberis AA, Ovsyannikov RI, et al. The W2020 database of validated rovibrational experimental transitions and empirical energy levels of water isotopologues. II. $H_2{}^{17}O$ and $H_2{}^{18}O$ with an update to $H_2{}^{16}O$. J Phys Chem Ref Data 2020;49(4):043103. http://dx.doi.org/10.1063/5.0030680.

[37] Furtenbacher T, Tóbiás R, Tennyson J, Gamache RR, Császár AG. The W2024 database of the water isotopologue $H_2^{16}O$. Sci Data 2024;11:1–15. http://dx.doi.org/10.1038/s41597-024-03847-3.

[38] Tóbiás R, Furtenbacher T, Simkó I, Császár AG, Diouf ML, Cozijn FMJ, et al. Spectroscopic-network-assisted precision spectroscopy and its application to water. Nat Commun 2020;11:1708. http://dx.doi.org/10.1038/s41467-020-15430-6.

[39] Diouf ML, Tóbiás R, van der Schaaf TS, Cozijn FMJ, Salumbides EJ, Császár AG, et al. Ultraprecise relative energies in the (2 0 0) vibrational band of $H_2{}^{16}O$. Mol Phys 2022;120:e2050430. http://dx.doi.org/10.1080/00268976.2022.2050430.

[40] Tóbiás R, Diouf ML, Cozijn FM, Ubachs W, Császár AG. All paths lead to hubs in the spectroscopic networks of water isotopologues $H_2{}^{16}O$ and $H_2{}^{18}O$. Commun Chem 2024;7:34. http://dx.doi.org/10.1038/s42004-024-01103-8.

[41] Toureille M, Koroleva AO, Mikhailenko SN, Pirali O, Campargue A. Water vapor absorption spectroscopy and validation tests of databases in the far-infrared (50–720 cm^{-1}). Part 1: Natural water. J Quant Spectrosc Radiat Transfer 2022;291:108326. http://dx.doi.org/10.1016/J.JQSRT.2022.108326.

[42] Koroleva AO, Mikhailenko SN, Kassi S, Campargue A. Frequency comb-referenced cavity ring-down spectroscopy of natural water between 8041 and 8633 cm^{-1}. J Quant Spectrosc Radiat Transfer 2023;298:108489. http://dx.doi.org/10.1016/J.JQSRT.2023.108489.

[43] Yang Q-Y, Conway EK, Liang H, Gordon IE, Tan Y, Hu S-M. Cavity ring-down spectroscopy of water vapor in the deep-blue region. Atmos Meas Tech 2022;15:4463–72. http://dx.doi.org/10.5194/amt-15-4463-2022.

[44] Furtenbacher T, Egbert SC, Sung K, Coburn SC, Drouin BJ, Rieker GB, et al. Improved assessment of $H_2{}^{16}O$ transitions in the region 6600 – 7500 cm^{-1}. J Quant Spectrosc Radiat Transfer 2025;109513. http://dx.doi.org/10.1016/j.jqsrt.2025.109513.

[45] Conway EK, Gordon IE, Tennyson J, Polyansky OL, Yurchenko SN, Chance K. A semi-empirical potential energy surface and line list for $H_2{}^{16}O$ extending into the near-ultraviolet. Atmos Chem Phys 2020;20:10015–27. http://dx.doi.org/10.5194/acp-20-10015-2020.

[46] Solodov AM, Petrova TM, Solodov AA, Deichuli VM, Naumenko OV. FT spectroscopy of water vapor in the 0.9 μm transparency window. J Quant Spectrosc Radiat Transfer 2022;293:108389. http://dx.doi.org/10.1016/j.jqsrt.2022.108389.

[47] Birk M, Röske C, Wagner G. Measurement database and line parameter database for air- and self-broadened H_2O in the 5970–6575 cm^{-1} region. 2024, http://dx.doi.org/10.5281/zenodo.13866910, Dataset published under Creative Commons Attribution 4.0 International license. Funded by ESA ISOGG (Contract No. 4000132228/20/I-NS).

[48] Gordon IE, Rothman LS, Gamache RR, Jacquemart D, Boone C, Bernath PF, et al. Current updates of the water-vapor line list in HITRAN: A new "Diet" for air-broadened half-widths. J Quant Spectrosc Radiat Transfer 2007;108(3):389–402. http://dx.doi.org/10.1016/j.jqsrt.2007.06.009.

[49] Jacquemart D, Gamache R, Rothman LS. Semi-empirical calculation of air-broadened half-widths and air pressure-induced frequency shifts of water-vapor absorption lines. J Quant Spectrosc Radiat Transfer 2005;96:205–39. http://dx.doi.org/10.1016/j.jqsrt.2004.11.018.

[50] Podobedov VB, Plusquellic DF, Fraser GT. THz laser study of self-pressure and temperature broadening and shifts of water vapor lines for pressures up to 1.4kPa. J Quant Spectrosc Radiat Transfer 2004;87:377–85. http://dx.doi.org/10.1016/J.JQSRT.2004.03.001.

[51] Petrova TM, Solodov AM, Solodov AA, Deichuli VM, Starikov VI. Measurements and calculations of air-broadening and shift parameters of water vapour transitions in a wide spectral region. Mol Phys 2021;119. http://dx.doi.org/10.1080/00268976.2021.1906967.

[52] Petrova TM, Solodov AM, Solodov AA, Deichuli VM, Starikov VI. Measurements of air-broadening parameters of water vapour transitions in the 7520–8586 cm^{-1} spectral region. Mol Phys 2022;120. http://dx.doi.org/10.1080/00268976.2021.1988169.

[53] Deichuli VM, Petrova TM, Solodov AM, Solodov AA, Starikov VI. Measurements of air-broadening parameters of water vapour transitions in the 5090–7490 cm^{-1} spectral region. Mol Phys 2023;121. http://dx.doi.org/10.1080/00268976.2023.2216133.

[54] Egbert SC, Sung K, Coburn SC, Drouin BJ, Rieker GB. Water-vapor absorption database using Dual Comb Spectroscopy from 300 to 1300 K Part II: Air-Broadened H_2O, 6600 to 7650 cm^{-1}. J Quant Spectrosc Radiat Transfer 2024;328:109119. http://dx.doi.org/10.1016/J.JQSRT.2024.109119.

[55] Vasilchenko S, Tran H, Mondelain D, Kassi S, Campargue A. Accurate absorption spectroscopy of water vapor near 1.64 μm in support of the MEthane Remote LIdar missioN (MERLIN). J Quant Spectrosc Radiat Transfer 2019;235:332–42. http://dx.doi.org/10.1016/J.JQSRT.2019.06.027.

[56] Toon G. Spectroscopic evaluations and recommendations. Tech. Rep., Jet Propulsion Laboratory, California Institute of Technology; 2024, URL https://mark4sun.jpl.nasa.gov/report/H2O_spectroscopy_evaluation_700_12000-compressed.pdf, Includes evaluations of C_2H_6 and H_2O spectroscopy, and comparison of HITRAN and ATM linelists for NDACC windows. Government sponsorship acknowledged.

[57] Toon GC, Blavier J-F, Sung K, Rothman LS, E. Gordon I. HITRAN spectroscopy evaluation using solar occultation FTIR spectra. J Quant Spectrosc Radiat Transfer 2016;182:324–36. http://dx.doi.org/10.1016/j.jqsrt.2016.05.021.

[58] Egbert SC, Sung K, Coburn SC, Drouin BJ, Rieker GB. Water-vapor absorption database using dual comb spectroscopy from 300 to 1300 K part I: Pure H_2O, 6600 to 7650 cm^{-1}. J Quant Spectrosc Radiat Transfer 2024;318:108940. http://dx.doi.org/10.1016/J.JQSRT.2024.108940.

[59] Röske C, Birk M, Wagner G. Line parameter database H_2O self-broadened 700–2000 cm^{-1}. 2024, http://dx.doi.org/10.5281/zenodo.13861692, Dataset published under Creative Commons Attribution 4.0 International license. Measurements conducted using a Bruker 125HR Interferometer in the 700–2000 cm^{-1} spectral range.

[60] Coudert LH, Mikhailenko S, Campargue A, Mellau GC. Line position and line intensity modelings of $H_2{}^{18}O$ up to the first triad and $J = 20$. J Phys Chem Ref Data 2023;52. http://dx.doi.org/10.1063/5.0152187.

[61] Diouf ML, Tóbiás R, Simkó I, Cozijn FMJ, Salumbides EJ, Ubachs W, et al. Network-based design of near-infrared lamb-dip experiments and the determination of pure rotational energies of $H_2{}^{18}O$ at kHz accuracy. J Phys Chem Ref Data 2021;50. http://dx.doi.org/10.1063/5.0052744.

[62] Melosso M, Diouf ML, Bizzocchi L, Harding ME, Cozijn FMJ, Puzzarini C, et al. Hyperfine-resolved near-infrared spectra of $H_2{}^{17}O$. J Phys Chem A 2021;125:7884–90. http://dx.doi.org/10.1021/acs.jpca.1c05681.

[63] Kyuberis AA, Zobov NF, Naumenko OV, Voronin BA, Polyansky OL, Lodi L, et al. Room temperature line lists for deuterated water. J Quant Spectrosc Radiat Transfer 2017;203:175–85. http://dx.doi.org/10.1016/j.jqsrt.2017.06.026.

[64] Mikhailenko SN, Karlovets EV, Koroleva AO, Campargue A. The far-infrared absorption spectrum of $HD^{16}O$: Experimental line positions, accurate empirical energy levels, and a recommended line list. Molecules 2024;29:5508. http://dx.doi.org/10.3390/molecules29235508.

[65] Diouf ML, Tóbiás R, Cozijn FMJ, Salumbides EJ, Fábri C, Puzzarini C, et al. Parity-pair-mixing effects in nonlinear spectroscopy of HDO. Opt Express 2022;30:46040. http://dx.doi.org/10.1364/oe.474525.

[66] Mikhailenko SN, Karlovets EV, Koroleva AO, Campargue A. The far infrared absorption spectrum of $D_2{}^{16}O$, $D_2{}^{17}O$, and $D_2{}^{18}O$: Experimental line positions, empirical energy levels and recommended line lists. J Phys Chem Ref Data 2024;53:23102. http://dx.doi.org/10.1063/5.0202355.

[67] Wang J, Zhou M, Langerock B, Nan W, Wang T, Wang P. Optimizing the atmospheric CO_2 retrieval based on the NDACC-type FTIR mid-infrared spectra at Xianghe, China. Remote Sens 2024;16(5). http://dx.doi.org/10.3390/rs16050900.

[68] Liu L, Zhang H. Development and evaluation of a new correlated K-distribution scheme for BCC_RAD radiative transfer model. J Geophys Res (Atmos) 2025;130(1). http://dx.doi.org/10.1029/2024JD041257, e2024JD041257.

[69] Karlovets E, Gordon I, Rothman L, Hashemi R, Hargreaves R, Toon G, et al. The update of the line positions and intensities in the line list of carbon dioxide for the HITRAN2020 spectroscopic database. J Quant Spectrosc Radiat Transfer 2021;107896. http://dx.doi.org/10.1016/j.jqsrt.2021.107896.

[70] Balashov AA, Raj A, Wójtewicz S, Ciuryło R, Lisak D, Bielska K. Theoretically predicted CO_2 lines near 700 nm not observed. J Quant Spectrosc Radiat Transfer 2024;108978. http://dx.doi.org/10.1016/j.jqsrt.2024.108978.

[71] Huang X, Freedman RS, Tashkun S, Schwenke DW, Lee TJ. AI-3000K infrared line list for hot CO_2. J Mol Spectrosc 2023;392:111748. http://dx.doi.org/10.1016/j.jms.2023.111748.

[72] Hargreaves R, Gordon I, Huang X, Toon G, Rothman L. Updating the carbon dioxide line list in HITEMP. J Quant Spectrosc Radiat Transfer 2025;333:109324. http://dx.doi.org/10.1016/J.JQSRT.2024.109324.

[73] Kochanov RV, Perevalov VI. CDSD-2024-PI: The update of the CDSD databank for the principal isotopologue of carbon dioxide. J Quant Spectrosc Radiat Transfer 2025;341:109428. http://dx.doi.org/10.1016/J.JQSRT.2025.109428.

[74] Tashkun SA, Perevalov VI, Gamache RR, Lamouroux J. CDSD-296, high-resolution carbon dioxide spectroscopic databank: An update. J Quant Spectrosc Radiat Transfer 2019;228:124–31. http://dx.doi.org/10.1016/j.jqsrt.2019.03.001.

[75] Hu CL, Perevalov VI, Cheng CF, Hua TP, Liu AW, Sun YR, et al. Optical-optical double-resonance absorption spectroscopy of molecules with kilohertz accuracy. J Phys Chem Lett 2020;11:7843–8. http://dx.doi.org/10.1021/ACS.JPCLETT.0C02136.

[76] Wu H, Hu CL, Wang J, Sun YR, Tan Y, Liu AW, et al. A well-isolated vibrational state of CO_2 verified by near-infrared saturated spectroscopy with kHz accuracy. Phys Chem Chem Phys 2020;22:2841–8. http://dx.doi.org/10.1039/c9cp05121j.

[77] Reed ZD, Drouin BJ, Long DA, Hodges JT. Molecular transition frequencies of CO_2 near 1.6 μm with kHz-level uncertainties. J Quant Spectrosc Radiat Transfer 2021;271:107681. http://dx.doi.org/10.1016/J.JQSRT.2021.107681.

[78] Fleurbaey H, Čermák P, Campargue A, Kassi S, Romanini D, Votava O, et al. $^{12}CO_2$ transition frequencies with kHz-accuracy by saturation spectroscopy in the 1.99–2.09 μm region. Phys Chem Chem Phys 2023;25:16319–30. http://dx.doi.org/10.1039/D3CP01603J.

[79] Lyulin OM, Solodov AM, Solodov AA, Petrova TM, Perevalov VI. The absorption bands of $^{12}C^{16}O_2$ near 718 nm. J Quant Spectrosc Radiat Transfer 2023;303:108595. http://dx.doi.org/10.1016/J.JQSRT.2023.108595.

[80] Borkov YG, Solodov AM, Solodov AA, Petrova TM, Perevalov VI. The first observation of the $^{12}C^{16}O_2$ absorption bands near 660 nm. J Mol Spectrosc 2023;397:111843. http://dx.doi.org/10.1016/J.JMS.2023.111843.

[81] Alatoom D, Ibrahim MTI, Furtenbacher T, Császár AG, et al. MARVEL analysis of high-resolution rovibrational spectra of $^{16}O^{12}C^{18}O$. J Comput Chem 2024;45:2558–73. http://dx.doi.org/10.1002/JCC.27453.

[82] Azzam AAA, Tennyson J, Yurchenko SN, Furtenbacher T, Császár AG. MARVEL analysis of high-resolution rovibrational spectra of $^{16}O^{13}C^{18}O$. J Comput Chem 2025;46:e27541. http://dx.doi.org/10.1002/JCC.27541.

[83] Azzam AAA, Azzam SAA, Aburumman KAA, Tennyson J, Yurchenko SN, Császár AG, et al. MARVEL analysis of high-resolution rovibrational spectra of the $^{18}O^{12}C^{18}O$, $^{17}O^{12}C^{18}O$, and $^{18}O^{13}C^{18}O$ isotopologues of carbon dioxide. J Mol Spectrosc 2024;405:111947. http://dx.doi.org/10.1016/J.JMS.2024.111947.

[84] Ibrahim MTI, Alatoom D, Furtenbacher T, Császár AG, Yurchenko SN, Azzam AA, et al. MARVEL analysis of high-resolution rovibrational spectra of $^{13}C^{16}O_2$. J Comput Chem 2024;45:969–84. http://dx.doi.org/10.1002/JCC.27266.

[85] Obaidat SAM, Azzam AAA, Alatoom D, Ibrahim MTI, Tennyson J, Furtenbacher T, et al. MARVEL analysis of high-resolution rovibrational spectra of $^{16}O^{12}C^{17}O$. J Quant Spectrosc Radiat Transfer 2025;340:109444. http://dx.doi.org/10.1016/J.JQSRT.2025.109444.

[86] Azzam AAA, AlAlawin JMA, Tennyson J, Furtenbacher T, Császár AG. MARVEL analysis of high-resolution rovibrational spectra of $^{17}O^{13}C^{18}O$ and $^{17}O^{13}C^{17}O$. J Quant Spectrosc Radiat Transfer 2025;343:109485. http://dx.doi.org/10.1016/J.JQSRT.2025.109485.

[87] Mansour MHI, Azzam AAA, Tennyson J, Yurchenko SN, Furtenbacher T, Császár AG. MARVEL analysis of high-resolution rovibrational spectra of $^{16}O^{13}C^{17}O$ and $^{17}O^{12}C^{17}O$. Mol Phys 2025;e2550568. http://dx.doi.org/10.1080/00268976.2025.2550568.

[88] Azzam AAA, Alatoom D, Abou Doud BMJ, Shersheer MQA, Almasri BKM, Bader CNM, et al. The 626M24 dataset of validated transitions and empirical rovibrational energy levels of $^{16}O^{12}C^{16}O$. Sci Data 2025;12. http://dx.doi.org/10.1038/s41597-025-04755-w.

[89] Rothman LS, Young LD. Infrared energy levels and intensities of carbon dioxide-II. J Quant Spectrosc Radiat Transfer 1981;25:505–24. http://dx.doi.org/10.1016/0022-4073(81)90026-1.

[90] Crisp D, Atlas R, Breon F-M, Brown L, Burrows J, Ciais P, et al. The Orbiting Carbon Observatory (OCO) mission. Adv Space Res 2004;34(4):700–9. http://dx.doi.org/10.1016/j.asr.2003.08.062.

[91] Eldering A, Taylor TE, O'Dell CW, Pavlick R. The OCO-3 mission: measurement objectives and expected performance based on 1 year of simulated data. Atmos Meas Tech 2019;12(4):2341–70. http://dx.doi.org/10.5194/amt-12-2341-2019.

[92] Kuze A, Suto H, Nakajima M, Hamazaki T. Thermal and near infrared sensor for carbon observation Fourier-transform spectrometer on the Greenhouse Gases Observing Satellite for greenhouse gases monitoring. Appl Opt 2009;48(35):6716. http://dx.doi.org/10.1364/AO.48.006716.

[93] Imasu R, Matsunaga T, Nakajima M, Yoshida Y, Shiomi K, Morino I, et al. Greenhouse gases Observing SATellite 2 (GOSAT-2): mission overview. Prog Earth Planet Sci 2023;10(1):33. http://dx.doi.org/10.1186/s40645-023-00562-2.

[94] Pasternak F, Georges L, Pascal V, Bernard P. The Microcarb instrument. In: Karafolas N, Cugny B, Sodnik Z, editors. International conference on space optics — ICSO 2016. Vol. 10562, SPIE; 2017, p. 258. http://dx.doi.org/10.1117/12.2296225.

[95] Bazalgette Courrèges-Lacoste G, Pachot C, Ouslimani H, Durand Y, Pasquet A, Chanumolu A, et al. Progress on the development of the Copernicus CO2M mission. In: Babu SR, Hélière A, Kimura T, editors. Society of photo-optical instrumentation engineers (SPIE) conference series. Society of photo-optical instrumentation engineers (SPIE) conference series, Vol. 13192, 2024, p. 131920S. http://dx.doi.org/10.1117/12.3033794.

[96] Zak EJ, Polyansky OL, Lodi L, Zobov NF, Tashkun SA, Perevalov VI. A room temperature CO_2 line list with *ab initio* computed intensities. J Quant Spectrosc Radiat Transfer 2016;177:31–42. http://dx.doi.org/10.1016/j.jqsrt.2015.12.022.

[97] Birk M, Röske C, Wagner G. The pressure dependence of the experimentally-determined line intensity and continuum absorption of pure CO_2 in the 1.6μm region. J Quant Spectrosc Radiat Transfer 2024;324:109055. http://dx.doi.org/10.1016/j.jqsrt.2024.109055.

[98] Birk M, Wagner G, Röske C. Measurement and line parameter database for self-broadened CO_2 in the 4750–5175 cm^{-1} region (version 1). 2024, http://dx.doi.org/10.5281/zenodo.13838847, Measurements at 294 K and 200 K for pressures up to 40 mbar; part of ESA-ISOGG project. Published under CC-BY 4.0.

[99] Birk M, Röske C, Wagner G. Measurement database and line parameter database for air- and H_2O-broadened CO_2 in the 4750–5175 cm^{-1} region, including continuum (version 1). 2024, http://dx.doi.org/10.5281/zenodo.13847849.

[100] Birk M, Röske C, Wagner G. Measurement database and line parameter database for air- and H_2O-broadened CO_2 in the 5970–6575 cm^{-1} region, including continuum (version 1). 2024, http://dx.doi.org/10.5281/zenodo.13862461, Dataset published under CC-BY 4.0. Measurements cover 210–294 K and 100–1000 mbar; includes continuum data and uncertainty estimates.

[101] Fleurbaey H, Yi H, Adkins EM, Fleisher AJ, Hodges JT. Cavity ring-down spectroscopy of CO_2 near λ=2.06 μm: Accurate transition intensities for the Orbiting Carbon Observatory-2 (OCO-2) "strong band". J Quant Spectrosc Radiat Transfer 2020;252:107104. http://dx.doi.org/10.1016/j.jqsrt.2020.107104, arXiv:2002.09584.

[102] Long DA, Reed ZD, Fleisher AJ, Mendonca J, Roche S, Hodges JT. High-accuracy near-infrared carbon dioxide intensity measurements to support remote sensing. Geophys Res Lett 2020;47. http://dx.doi.org/10.1029/2019GL086344, e2019GL086344.

[103] Fleisher AJ, Yi H, Srivastava A, Polyansky OL, Zobov NF, Hodges JT. Absolute $^{13}C/^{12}C$ isotope amount ratio for vienna PeeDee belemnite from infrared absorption spectroscopy. Nat Phys 2021;17:889–93. http://dx.doi.org/10.1038/s41567-021-01226-y.

[104] Thiemann L, Schmitt T, Birk M, Röske C, Wagner G, Butz A. Investigating the impact of modern absorption cross-section databases on CO_2 retrievals. In: EGU general assembly 2025. Vienna, Austria & Online; 2025, http://dx.doi.org/10.5194/egusphere-egu25-10453, Abstract EGU25-10453, 27 April–2 May 2025.

[105] Malarich N, Giorgetta FR, Mead G, Baumann E, Genest J, Newbury NR, et al. Evaluating CO_2 and CH_4 absorption models with open-path dual-comb spectroscopy at the Mauna Loa Observatory. J Quant Spectrosc Radiat Transfer 2025;345:109567. http://dx.doi.org/10.1016/J.JQSRT.2025.109567.

[106] Yurchenko SN, Mellor TM, Freedman RS, Tennyson J. ExoMol line lists - XXXIX. Ro-vibrational molecular line list for CO_2. Mon Not R Astron Soc 2020;496(4):5282–91. http://dx.doi.org/10.1093/mnras/staa1874, arXiv:2007.02122.

[107] Huang X, Schwenke DW, Freedman RS, Lee TJ. Ames-2021 CO_2 dipole moment surface and IR line lists: Toward 0.1% uncertainty for CO_2 IR intensities. J Phys Chem A 2022;126(35):5940–64. http://dx.doi.org/10.1021/acs.jpca.2c01291.

[108] Medvedev ES, Ushakov VG, Conway EK, Upadhyay A, Gordon IE, Tennyson J. Empirical normal intensity distribution for overtone vibrational spectra of triatomic molecules. J Quant Spectrosc Radiat Transfer 2020;252:107084. http://dx.doi.org/10.1016/j.jqsrt.2020.107084.

[109] Gamache RR, Lamouroux J. Predicting accurate line shape parameters for CO_2 transitions. J Quant Spectrosc Radiat Transfer 2013;130:158–71. http://dx.doi.org/10.1016/j.jqsrt.2013.05.021.

[110] Mondelain D, Campargue A, Fleurbaey H, Kassi S, Vasilchenko S. CRDS measurements of air-broadened lines in the 1.6 μm band of $^{12}CO_2$: Line shape parameters with their temperature dependence. J Quant Spectrosc Radiat Transfer 2022;288:108267. http://dx.doi.org/10.1016/j.jqsrt.2022.108267.

[111] Mondelain D, Campargue A, Fleurbaey H, Kassi S, Vasilchenko S. Line shape parameters of air-broadened $^{12}CO_2$ transitions in the 2.0 μm region, with their temperature dependence. J Quant Spectrosc Radiat Transfer 2023;108485. http://dx.doi.org/10.1016/J.JQSRT.2023.108485.

[112] Adkins EM, Long DA, Hodges JT. Air-broadening in near-infrared carbon dioxide line shapes: quantifying contributions from O_2, N_2, and Ar. J Quant Spectrosc Radiat Transfer 2021;107669. http://dx.doi.org/10.1016/j.jqsrt.2021.107669.

[113] Tran H, Denis L, Lepère M, Vispoel B, Ngo NH. Complete set of broadening coefficients and high-order line-shape parameters for N_2-broadened CO_2 lines, for temperatures ranging from 100 K to 1000 K. J Quant Spectrosc Radiat Transfer 2025;342:109499. http://dx.doi.org/10.1016/j.jqsrt.2025.109499.

[114] Wilzewski JS, Birk M, Loos J, Wagner G. Temperature-dependence laws of absorption line shape parameters of the CO_2 ν_3 band. J Quant Spectrosc Radiat Transfer 2018;206:296–305. http://dx.doi.org/10.1016/j.jqsrt.2017.11.021.

[115] Mondelain D, Campargue A, Gamache RR, Hartmann J-M, Gibert F, Wagner G, et al. Isotopologue dependence of the CO_2-air broadening and shifting coefficients: Experimental evidence and comparison with theory for $^{13}CO_2$ and $^{12}CO_2$. J Quant Spectrosc Radiat Transfer 2025;333:109271. http://dx.doi.org/10.1016/j.jqsrt.2024.109271.

[116] Padmanabhan A, Tzanetakis T, Chanda A, Thomson M. Study of pressure broadening effects of h_2 on CO_2 and CO in the near infrared region between 6317 and 6335 cm^{-1} at room temperature. J Quant Spectrosc Radiat Transfer 2014;133:81–90. http://dx.doi.org/10.1016/j.jqsrt.2013.07.016.

[117] Hanson RK, Whitty KJ. Tunable diode laser sensors to monitor temperature and gas composition in high-temperature coal gasifiers DE-FE0001180 final scientific/technical report. Tech. Rep., Stanford University; 2014, p. 1–39. http://dx.doi.org/10.2172/1222583.

[118] Wiesenfeld L, Niraula P, de Wit J, Jaïdane N, Gordon IE, Hargreaves RJ. *Ab Initio* quantum dynamics as a scalable solution to the exoplanet opacity challenge: A case study of CO_2 in a hydrogen atmosphere. Astrophys J 2025;981(2):148. http://dx.doi.org/10.3847/1538-4357/adb02e.

[119] Nakamichi S, Kawaguchi Y, Fukuda H, Enami S, Hashimoto S, Kawasaki M, et al. Buffer-gas pressure broadening for the $(3\ 0^0\ 1)_{III} \leftarrow (0\ 0\ 0)$ band of CO_2 measured with continuous-wave cavity ring-down spectroscopy. Phys Chem Chem Phys 2006;8:364–8. http://dx.doi.org/10.1039/B511772K.

[120] Deng W, Mondelain D, Thibault F, Camy-Peyret C, Mantz AW. Experimental He-pressure broadening for the R(10) and P(2) lines in the ν_3 band of $^{13}CO_2$, and experimental pressure shifts for R(10) measured at several temperatures between 300K and 100K. J Mol Spectrosc 2009;256(1):102–8. http://dx.doi.org/10.1016/j.jms.2009.02.021, PRAHA2008, The 20th International Conference on High Resolution Molecular Spectroscopy.

[121] Hendaoui F, Jacquemart D, Hessani A, Tremblay B, Aroui H, Tran H. Measurements of He-collision-induced line-shape parameters of CO_2 lines in the ν_3 band. J Quant Spectrosc Radiat Transfer 2025;334:109361. http://dx.doi.org/10.1016/J.JQSRT.2025.109361.

[122] Vispoel B, Gamache RR. Modified Complex Robert-Bonamy calculations of line shape parameters for the CO_2-H_2O collision system. J Quant Spectrosc Radiat Transfer 2024;316:108896. http://dx.doi.org/10.1016/J.JQSRT.2024.108896.

[123] Payne VH, Drouin BJ, Oyafuso F, Kuai L, Fisher BM, Sung K, et al. Absorption coefficient (ABSCO) tables for the Orbiting Carbon Observatories: Version 5.1. J Quant Spectrosc Radiat Transfer 2020;255:107217. http://dx.doi.org/10.1016/j.jqsrt.2020.107217.

[124] Birk M, Wagner G, Röske C. Absorption cross sections for air- and h_2o-broadened CO_2 in the 1.6 μm and 2 μm regions (including continuum) and air- and self-broadened h_2o in the 1.6 μm region. 2025, http://dx.doi.org/10.5281/zenodo.16746357.

[125] Rothman LS, Gordon IE, Barber RJ, Dothe H, Gamache RR, Goldman A, et al. HITEMP, the high-temperature molecular spectroscopic database. J Quant Spectrosc Radiat Transfer 2010;111:2139–50. http://dx.doi.org/10.1016/j.jqsrt.2010.05.001.

[126] Bernhard G, Bais A, Aucamp P, et al. Stratospheric ozone, UV radiation, and climate interactions. Photochem Photobiol Sci 2023;22:937–89. http://dx.doi.org/10.1007/s43630-023-00371-y.

[127] De Marco A, Garcia-Gomez H, Collalti A, et al. Ozone modelling and mapping for risk assessment: An overview of different approaches for human and ecosystems health. Environ Res 2022;211:113048. http://dx.doi.org/10.1016/J.ENVRES.2022.113048.

[128] Zoogman P, Liu X, Suleiman R, Pennington W, Flittner D, Al-Saadi J, et al. Tropospheric emissions: Monitoring of pollution (TEMPO). J Quant Spectrosc Radiat Transfer 2017;186:17–39. http://dx.doi.org/10.1016/j.jqsrt.2016.05.008.

[129] Boynard A, Wespes C, Hadji-Lazaro J, Sinnathamby S, Hurtmans D, Coheur P-F, et al. Tropospheric Ozone Assessment Report (TOAR): 16-year ozone trends from the IASI Climate Data Record. EGUsphere 2025;2025:1–48. http://dx.doi.org/10.5194/egusphere-2025-1054.

[130] Zou J, Walker KA, Sheese PE, Boone CD, Stauffer RM, Thompson AM, et al. Validation of ACE-FTS version 5.2 ozone data with ozonesonde measurements. Atmos Meas Tech 2024;17(23):6983–7005. http://dx.doi.org/10.5194/amt-17-6983-2024.

[131] Keppens A, Di Pede S, Hubert D, Lambert J-C, Veefkind P, Sneep M, et al. 5 years of Sentinel-5P TROPOMI operational ozone profiling and geophysical validation using ozonesonde and lidar ground-based networks. Atmos Meas Tech 2024;17(13):3969–93. http://dx.doi.org/10.5194/amt-17-3969-2024.

[132] Kozakis T, Mendonça JM, Buchhave LA. Is ozone a reliable proxy for molecular oxygen?. I. The O_2-O_3 relationship for Earth-like atmospheres. Astron Astrophys 2022;665:A156. http://dx.doi.org/10.1051/0004-6361/202244164, arXiv:2208.09415.

[133] Mikhailenko S, Barbe A. High resolution infrared spectrum of $^{16}O_3$: The 3600–4300 cm^{-1} range reinvestigated. J Quant Spectrosc Radiat Transfer 2020;244:106823. http://dx.doi.org/10.1016/J.JQSRT.2019.106823.

[134] Barbe A, Mikhailenko S, Starikova E, Tyuterev V. Infrared spectra of $^{16}O_3$ in the 900 - 5600 cm^{-1} range revisited: empirical corrections to the S&MPO and HITRAN2020 line lists. J Quant Spectrosc Radiat Transfer 2021;107936. http://dx.doi.org/10.1016/J.JQSRT.2021.107936.

[135] Jacquemart D, Makhnev VY, Zobov NF, Tennyson J, Polyansky OL. Synthesis of *ab initio* and effective Hamiltonian line lists for ozone. J Quant Spectrosc Radiat Transfer 2021;269:107651. http://dx.doi.org/10.1016/j.jqsrt.2021.107651.

[136] Tyuterev VG, Barbe A, Jacquemart D, Janssen C, Mikhailenko SN, Starikova EN. *Ab initio* predictions and laboratory validation for consistent ozone intensities in the MW, 10 and 5 μm ranges. J Chem Phys 2019;150:184303. http://dx.doi.org/10.1063/1.5089134.

[137] Jacquemart D, Boursier C, Elandaloussi H, Jeseck P, Té Y, Janssen C. Multi-spectral investigation of ozone: Part II. Line intensity measurements at one percent accuracy around 5 μm and 10 μm. J Quant Spectrosc Radiat Transfer 2022;279:108050. http://dx.doi.org/10.1016/J.JQSRT.2021.108050.

[138] Birk M, Wagner G, Gordon I, Drouin B. Ozone intensities in the rotational bands. J Quant Spectrosc Radiat Transfer 2019;226:60–5. http://dx.doi.org/10.1016/j.jqsrt.2019.01.004.

[139] Björklund R, Vigouroux C, Effertz P, García OE, Geddes A, Hannigan J, et al. Intercomparison of long-term ground-based measurements of total, tropospheric, and stratospheric ozone at Lauder, New Zealand. Atmos Meas Tech 2024;17(23):6819–49. http://dx.doi.org/10.5194/amt-17-6819-2024.

[140] Tyuterev V, Barbe A, Manceron L, Grouiez B, Tashkun S, Burgalat J, et al. Ozone spectroscopy in the terahertz range from first high-resolution Synchrotron SOLEIL experiments combined with far-infrared measurements and *ab initio* intensity calculations. Spectrochim Acta Part A: Mol Biomol Spectrosc 2024;305:123456. http://dx.doi.org/10.1016/j.saa.2023.123456.

[141] Roy P, Brubach J, Rouzieres M, Pirali O, Kwabia Tchana F, Manceron L. AILES: the infrared and THz beamline on SOLEIL synchrotron radiation source. REE Rev de L'Electricite et de L'Electronique 2025;(3).

[142] de Natale P, Lorini L, Inguscio M, Nolt IG, Park JH, di Lonardo G, et al. Accurate frequency measurements for H_2O and $^{16}O_3$ in the 119 cm^{-1} OH atmospheric window. Appl Opt 1997;36(33):8526–32. http://dx.doi.org/10.1364/AO.36.008526.

[143] Colmont JM, Bakri B, Demaison J, Mäder H, Willaert F, Tyuterev VG, et al. Microwave Fourier transform, millimeterwave, and submillimeterwave spectra of ozone in its vibrational ground state. J Mol Spectrosc 2005;233(2):293–6. http://dx.doi.org/10.1016/j.jms.2005.06.017.

[144] Tyuterev VG, Kochanov RV, Tashkun SA. Accurate *ab initio* dipole moment surfaces of ozone: First principle intensity predictions for rotationally resolved spectra in a large range of overtone and combination bands. J Chem Phys 2017;146(6):064304. http://dx.doi.org/10.1063/1.4973977.

[145] Gamache RR, Vispoel B, Rey M, Nikitin A, Tyuterev V, Egorov O, et al. Total internal partition sums for the HITRAN2020 database. J Quant Spectrosc Radiat Transfer 2021;271:107713. http://dx.doi.org/10.1016/j.jqsrt.2021.107713.

[146] Mack KM, Muenter JS. Stark and Zeeman properties of ozone from molecular beam spectroscopy. J Chem Phys 1977;66(12):5278–83. http://dx.doi.org/10.1063/1.433909.

[147] Tashkun S, Barbe A, Mikhailenko S, Starikova E, Tyuterev V. Complete RITZ set of ro-vibrational energy levels of $^{16}O_3$ deduced from experimental spectra: Critical analysis of transition frequencies in spectroscopic databases. J Phys Chem Ref Data 2024;53(4):043101. http://dx.doi.org/10.1063/5.0232298.

[148] Starikova EN, Barbe A, Manceron L, Grouiez B, Burgalat J, Tyuterev VG. Analysis of New Measurements of ^{18}O-substituted Isotopic Species $^{16}O^{16}O^{18}O$ and $^{16}O^{18}O^{16}O$ of Ozone in the THz and Far-Infrared Ranges. Atmospheric and Oceanic Optics 2024;37:132–41. http://dx.doi.org/10.1134/S1024856024700167.

[149] Palchetti L, Brindley H, Bantges R, Buehler SA, Camy-Peyret C, Carli B, et al. FORUM: Unique far-infrared satellite observations to better understand how earth radiates energy to space. Bull Am Meteorol Soc 2020;101(12):E2030–46. http://dx.doi.org/10.1175/bams-d-19-0322.1.

[150] Bantges RJ, Brindley HE, Chen XH, Huang XL, Harries JE, Murray JE. On the detection of robust multidecadal changes in earth's outgoing longwave radiation spectrum. J Clim 2016;29(13):4939–47. http://dx.doi.org/10.1175/JCLI-D-15-0713.1.

[151] Toth RA. Linelist of N_2O parameters from 500 to 7500 cm^{-1}, URL http://mark4sun.jpl.nasa.gov/n2o.html.

[152] Karlovets EV, Kassi S, Tashkun SA, Campargue A. The absorption spectrum of nitrous oxide between 8325 and 8622 cm^{-1}. J Quant Spectrosc Radiat Transfer 2021;262:107508. http://dx.doi.org/10.1016/j.jqsrt.2021.107508.

[153] Bertin T, Mondelain D, Karlovets E, Kassi S, Perevalov V, Campargue A. High sensitivity cavity ring down spectroscopy of N_2O near 1.74 μm. J Quant Spectrosc Radiat Transfer 2019;229:40–9. http://dx.doi.org/10.1016/j.jqsrt.2019.02.011.

[154] Karlovets EV, Mondelain D, Tashkun SA, Campargue A. The absorption spectrum of nitrous oxide between 7250 and 7653 cm^{-1}. J Quant Spectrosc Radiat Transfer 2023;301:108511. http://dx.doi.org/10.1016/j.jqsrt.2023.108511.

[155] Karlovets EV, Kassi S, Tashkun SA, Campargue A. The absorption spectrum of nitrous oxide between 7647 and 7918 cm^{-1}. J Quant Spectrosc Radiat Transfer 2022;288:108199. http://dx.doi.org/10.1016/j.jqsrt.2022.108199.

[156] Karlovets EV, Tashkun SA, Kassi S, Campargue A. An improved analysis of the N_2O absorption spectrum in the 1.18 μm window. J Quant Spectrosc Radiat Transfer 2022;278:108003. http://dx.doi.org/10.1016/j.jqsrt.2021.108003.

[157] Sinitsa LN, Vasilchenko SS, Emelyanov NM, Marinina AA, Perevalov VI. Cavity ring-down spectroscopy of $^{14}N_2$ ^{16}O near 0.83 μm. J Quant Spectrosc Radiat Transfer 2024;329:109210. http://dx.doi.org/10.1016/j.jqsrt.2024.109210.

[158] Sinitsa LN, Serdyukov VI, Emelyanov NM, Marinina AA, Perevalov VI. LED-based Fourier transform spectroscopy of $^{14}N_2$ ^{16}O in the 9750-12050 cm^{-1} region. J Quant Spectrosc Radiat Transfer 2024;315:108888. http://dx.doi.org/10.1016/j.jqsrt.2023.108888.

[159] Sinitsa LN, Serdyukov VI, Emelyanov NM, Marinina AA, Perevalov VI. Erratum to the paper "LED-based Fourier transform spectroscopy of $^{14}N_2$ ^{16}O in the 9750-12,050 cm^{-1}" by L.N. Sinitsa, V.I. Serdyukov, N.M. Emelyanov, A.A. Marinina, and V.I. Perevalov [J. Quant. Spectrosc. Radiat. Transf. 315 (2024) 108,888]. J Quant Spectrosc Radiat Transfer 2024;323:109038. http://dx.doi.org/10.1016/j.jqsrt.2024.109038.

[160] Tashkun S, Campargue A. The NOSL-296 high resolution $^{14}N_2$ ^{16}O line list for atmospheric applications. J Quant Spectrosc Radiat Transfer 2023;295:108417. http://dx.doi.org/10.1016/j.jqsrt.2022.108417.

[161] Tennyson J, Furtenbacher T, Yurchenko SN, Császár AG. Empirical rovibrational energy levels for nitrous oxide. J Quant Spectrosc Radiat Transfer 2024;316:108902. http://dx.doi.org/10.1016/j.jqsrt.2024.108902.

[162] Lamperti M, Alsaif B, Gatti D, Fermann M, Laporta P, Farooq A, et al. Absolute spectroscopy near 7.8 μm with a comb-locked extended-cavity quantum-cascade-laser. Sci Rep 2018;8:1–7. http://dx.doi.org/10.1038/s41598-018-19188-2.

[163] AlSaif B, Lamperti M, Gatti D, Laporta P, Fermann M, Farooq A, et al. High accuracy line positions of the ν_1 fundamental band of $^{14}N_2$ ^{16}O. J Quant Spectrosc Radiat Transfer 2018;211:172–8. http://dx.doi.org/10.1016/J.JQSRT.2018.03.005.

[164] AlSaif B, Gatti D, Lamperti M, Laporta P, Farooq A, Marangoni M. Comb-calibrated sub-Doppler spectroscopy with an external-cavity quantum cascade laser at 7.7 μm. Opt Express 2019;27:23785. http://dx.doi.org/10.1364/oe.27.023785.

[165] Hjältén A, Germann M, Krzempek K, Hudzikowski A, Głuszek A, Tomaszewska D, et al. Optical frequency comb Fourier transform spectroscopy of $^{14}N_2$ ^{16}O at 7.8 μm. J Quant Spectrosc Radiat Transfer 2021;271:107734. http://dx.doi.org/10.1016/J.JQSRT.2021.107734.

[166] Komagata KN, Gianella M, Jouy P, Kapsalidis F, Shahmohammadi M, Beck M, et al. Absolute frequency referencing in the long wave infrared using a quantum cascade laser frequency comb. Opt Express 2022;30:12891–901. http://dx.doi.org/10.1364/OE.447650.

[167] Iwakuni K. Absolute frequency measurement of the $3\nu_1$ band of N_2O with comb-locked rapid scan spectroscopy using a multi-pass cell. J Mol Spectrosc 2022;384:111571. http://dx.doi.org/10.1016/J.JMS.2022.111571.

[168] Chevalier P, Piccardo M, Amirzhan A, Capasso F, Everitt HO. Accurately measuring molecular rotational spectra in excited vibrational modes. Appl Spectrosc 2022;76:1494–503. http://dx.doi.org/10.1177/00037028221111174.

[169] Huang X, Tashkun SA, Schwenke DW. Accurate N_2O IR line lists with consistent empirical line positions: ABG-IMRHT and Ames-2000K. J Quant Spectrosc Radiat Transfer 2025;343:109502. http://dx.doi.org/10.1016/j.jqsrt.2025.109502.

[170] Huang X, Schwenke DW, Lee TJ. Highly accurate potential energy surface and dipole moment surface for nitrous oxide and 296K infrared line lists for $^{14}N_2$ ^{16}O and minor isotopologues. Mol Phys 2024;122(7–8):e2232892. http://dx.doi.org/10.1080/00268976.2023.2232892.

[171] Tashkun SA. Global modeling of the $^{14}N_2$ ^{16}O line positions within the framework of the non-polyad model of effective Hamiltonian. J Quant Spectrosc Radiat Transfer 2019;231:88–101. http://dx.doi.org/10.1016/j.jqsrt.2019.04.023.

[172] Schröder B, Sebald P, Stein C, Weser O, Botschwina P. Challenging high-level *ab initio* rovibrational spectroscopy: The nitrous oxide molecule. Z Für Phys Chem 2015;229(10–12):1663–90. http://dx.doi.org/10.1515/zpch-2015-0622.

[173] Yurchenko SN, Mellor TM, Tennyson J. ExoMol line lists-LIX. High-temperature line list for N_2O. Mon Not R Astron Soc 2024;534(2):1364–75. http://dx.doi.org/10.1093/mnras/stae2201, arXiv:2409.19447.

[174] Adkins EM, Long DA, Fleisher AJ, Hodges JT. Near-infrared cavity ringdown spectroscopy measurements of nitrous oxide in the (4200)←(0000) and (5000)←(0000) bands. J Quant Spectrosc Radiat Transfer 2021;262:107527. http://dx.doi.org/10.1016/j.jqsrt.2021.107527.

[175] Johnson TJ, Sams RL, Sharpe SW. The PNNL quantitative infrared database for gas-phase sensing: a spectral library for environmental, hazmat, and public safety standoff detection. In: Sedlacek III AJ, Colton R, Vo-Dinh T, editors. Chemical and biological point sensors for homeland defense. Society of photo-optical instrumentation engineers (SPIE) conference series, 5269, 2004, p. 159–67. http://dx.doi.org/10.1117/12.515604.

[176] Huang X, Tashkun S, Schwenke D. ABG-IMRHT and Ames-2000K IR line lists for N_2O as reported in "accurate N_2O IR line lists with consistent empirical line positions: ABG-IMRHT and Ames-2000K". 2025, http://dx.doi.org/10.5281/zenodo.15687077.

[177] Pickett HM, Poynter RL, Cohen EA, Delitsky ML, Pearson JC, Müller HSP. Submillimeter, millimeter, and microwave spectral line catalog. J Quant Spectrosc Radiat Transfer 1998;60(5):883–90. http://dx.doi.org/10.1016/S0022-4073(98)00091-0.

[178] Sharpe SW, Johnson TJ, Sams RL, Chu PM, Rhoderick GC, Johnson PA. Gas-phase databases for quantitative infrared spectroscopy. Appl Spectrosc 2004;58(12):1452–61. http://dx.doi.org/10.1366/0003702042641281.

[179] Daumont L, Vander Auwera J, Teffo J-L, Perevalov VI, Tashkun SA. Line intensity measurements in $^{14}N_2$ ^{16}O and their treatment using the effective dipole moment approach.II. The 5400-11000 cm^1 region. J Quant Spectrosc Radiat Transfer 2007;104(3):342–56. http://dx.doi.org/10.1016/j.jqsrt.2006.09.004.

[180] Hjältén A, Sadiek I, Foltynowicz A. Precision frequency comb spectroscopy of the $^{14}N_2O$, $^{14}N^{15}NO$, $^{15}N^{14}NO$, and $^{15}N_2O$ isotopocules in the 3300 – 3550 cm^{-1} range. J Quant Spectrosc Radiat Transfer 2025;340:109452. http://dx.doi.org/10.1016/j.jqsrt.2025.109452, arXiv:2412.07311.

[181] Tashkun SA, Perevalov VI, Liu AW, Hu SM. Global modeling of the $^{15}N_2$ ^{16}O line positions within the framework of the polyad model of effective Hamiltonian and a room temperature $^{15}N_2$ ^{16}O line list. J Quant Spectrosc Radiat Transfer 2016;175:1–7. http://dx.doi.org/10.1016/j.jqsrt.2016.01.038.

[182] Hargreaves RJ, Gordon IE, Rothman LS, Tashkun SA, Perevalov VI, Lukashevskaya AA, et al. Spectroscopic line parameters of NO, NO_2, and N_2O for the HITEMP database. J Quant Spectrosc Radiat Transfer 2019;232:35–53. http://dx.doi.org/10.1016/j.jqsrt.2019.04.040, arXiv:1904.02636.

[183] Tashkun SA, Perevalov VI, Lavrentieva NN. NOSD-1000, the high-temperature nitrous oxide spectroscopic databank. J Quant Spectrosc Radiat Transfer 2016;177:43–8. http://dx.doi.org/10.1016/j.jqsrt.2015.11.014.

[184] Beale CA, Buzan EM, Boone CD, Bernath PF. Near-global distribution of CO isotopic fractionation in the Earth's atmosphere. J Mol Spectrosc 2016;323:59–66. http://dx.doi.org/10.1016/J.JMS.2015.12.005.

[185] Bernath PF. Atmospheric chemistry experiment (ACE): Mission overview. Geophys Res Lett 2005;32(15):L15S01. http://dx.doi.org/10.1029/2005GL022386.

[186] Clerbaux C, Boynard A, Clarisse L, George M, Hadji-Lazaro J, Herbin H, et al. Monitoring of atmospheric composition using the thermal infrared IASI/MetOp sounder. Atmos Chem Phys 2009;9(16):6041–54. http://dx.doi.org/10.5194/acp-9-6041-2009.

[187] Veefkind J, Aben I, McMullan K, Förster H, de Vries J, Otter G, et al. TROPOMI on the ESA Sentinel-5 Precursor: A GMES mission for global observations of the atmospheric composition for climate, air quality and ozone layer applications. Remote Sens Environ 2012;120:70–83. http://dx.doi.org/10.1016/j.rse.2011.09.027.

[188] Noël S, Reuter M, Buchwitz M, Borchardt J, Hilker M, Schneising O, et al. Retrieval of greenhouse gases from GOSAT and GOSAT-2 using the FOCAL algorithm. Atmos Meas Tech 2022;15(11):3401–37. http://dx.doi.org/10.5194/amt-15-3401-2022.

[189] Olsen KS, Lefèvre F, Montmessin F, Fedorova AA, Trokhimovskiy A, Baggio L, et al. The vertical structure of CO in the Martian atmosphere from the ExoMars Trace Gas Orbiter. Nat Geosci 2021;14:67–71. http://dx.doi.org/10.1038/s41561-020-00678-w.

[190] Vandaele AC, Mahieux A, Chamberlain S, Ristic B, Robert S, Thomas IR, et al. Carbon monoxide observed in Venus' atmosphere with SOIR/VEx. Icarus 2016;272:48–59. http://dx.doi.org/10.1016/J.ICARUS.2016.02.025.

[191] Giacobbe P, Brogi M, Gandhi S, Cubillos PE, Bonomo AS, Sozzetti A, et al. Five carbon- and nitrogen-bearing species in a hot giant planet's atmosphere. Nature 2021;592:205–8. http://dx.doi.org/10.1038/s41586-021-03381-x.

[192] Esparza-Borges E, López-Morales M, Adams Redai JI, Pallé E, Kirk J, Casasayas-Barris N, et al. Detection of carbon monoxide in the atmosphere of WASP-39b applying standard cross-correlation techniques to JWST NIRSpec G395H data. Astrophys J Lett 2023;955(1):L19. http://dx.doi.org/10.3847/2041-8213/acf27b.

[193] Li G, Gordon IE, Rothman LS, Tan Y, Hu S-M, Kassi S, et al. Rovibrational line lists for nine isotopologues of the CO molecule in the $X^1\Sigma^+$ ground electronic state. Astrophys J Suppl Ser 2015;216:15. http://dx.doi.org/10.1088/0067-0049/216/1/15.

[194] Coxon JA, Hajigeorgiou PG. Direct potential fit analysis of the $X^1\Sigma^+$ ground state of CO. J Chem Phys 2004;121:2992–3008. http://dx.doi.org/10.1063/1.1768167.

[195] Devi VM, Benner DC, Sung K, Crawford TJ, Li G, Gamache RR, et al. Positions, intensities and line shape parameters for the 1←0 bands of CO isotopologues. J Quant Spectrosc Radiat Transfer 2018;218:203–30. http://dx.doi.org/10.1016/j.jqsrt.2018.06.007.

[196] Cygan A, Wcisło P, Wójtewicz S, Kowzan G, Zaborowski M, Charczun D, et al. High-accuracy and wide dynamic range frequency-based dispersion spectroscopy in an optical cavity. Opt Express 2019;27:21810–21. http://dx.doi.org/10.1364/OE.27.021810.

[197] Meshkov VV, Stolyarov AV, Ermilov AY, Medvedev ES, Ushakov VG, Gordon IE. Semi-empirical ground-state potential of carbon monoxide with physical behavior in the limits of small and large inter-atomic separations. J Quant Spectrosc Radiat Transfer 2018;217:262–73. http://dx.doi.org/10.1016/j.jqsrt.2018.06.001.

[198] Meshkov VV, Ermilov AY, Stolyarov AV, Medvedev ES, Ushakov VG, Gordon IE. Semi-empirical dipole-moment function of carbon monoxide and line lists for all its isotopologues revisited. J Quant Spectrosc Radiat Transfer 2022;280:108090. http://dx.doi.org/10.1016/j.jqsrt.2022.108090.

[199] Medvedev ES, Ushakov VG. Irregular semi-empirical dipole-moment function for carbon monoxide and line lists for all its isotopologues verified for extremely high overtone transitions. J Quant Spectrosc Radiat Transfer 2022;288:108255. http://dx.doi.org/10.1016/j.jqsrt.2022.108255.

[200] Meshkov VV, Pazyuk EA, Stolyarov AV. A robust dipole moment of carbon monoxide (CO) is a permanent puzzle for both spectroscopic and *ab initio* studies. Mol Phys 2024;e2429740. http://dx.doi.org/10.1080/00268976.2024.2429740.

[201] Bailey DM, Truong G-W, Hall BD, Crotwell AM, Harris KJ, Carney J, et al. Mid-infrared line intensity for the fundamental (1–0) vibrational band of carbon monoxide (CO). J Quant Spectrosc Radiat Transfer 2025;347:109652. http://dx.doi.org/10.1016/j.jqsrt.2025.109652, URL https://www.sciencedirect.com/science/article/pii/S0022407325003140.

[202] Bielska K, Kyuberis AA, Reed ZD, Li G, Cygan A, Ciurylo R, et al. Subpromille measurements and calculations of CO (3-0) overtone line intensities. Phys Rev Lett 2022;129(4):043002. http://dx.doi.org/10.1103/PhysRevLett.129.043002.

[203] Hodges JT, Bielska K, Birk M, Guo R, Li G, Lim JS, et al. International comparison CCQM-P229 pilot study to measure line intensities of selected $^{12}C^{16}O$ transitions. Metrologia 2025;62(1A):08006. http://dx.doi.org/10.1088/0026-1394/62/1A/08006.

[204] Mahmoud S, El-Kork N, Abu Elkher N, Almehairbi M, Khalil MS, Furtenbacher T, et al. MARVEL analysis of the measured high-resolution spectra of $^{12}C^{16}O$. Astrophys J Suppl Ser 2025;276:66. http://dx.doi.org/10.3847/1538-4365/ada3c9.

[205] Li G, Rubin TM, Kussicke A, Bielska K, Zobov NF, Lisak D, et al. CO line intensities: Solution of the fundamental band problem by the Study of 5 Hot and Cold Bands Intensities. Phys Rev Lett 2025. in preparation.

[206] Loos J, Birk M, Wagner G, Mondelain D, Campargue A. Scientific exploitation of operational missions – improved atmospheric spectroscopy database ESA/AO/1-7566/13/I-BG. 2017, http://www.wdc.dlr.de/seom-ias/.

[207] Wójtewicz S, Stec K, Masłowski P, Cygan A, Lisak D, Trawiński RS, et al. Low pressure line-shape study of self-broadened CO transitions in the (3←0) band. J Quant Spectrosc Radiat Transfer 2013;130:191–200. http://dx.doi.org/10.1016/j.jqsrt.2013.06.005.

[208] Bordet B, Kassi S, Campargue A. Line parameters of the 4-0 band of carbon monoxide by high sensitivity cavity ring down spectroscopy near 1.2 μm. J Quant Spectrosc Radiat Transfer 2021;260:107453. http://dx.doi.org/10.1016/j.jqsrt.2020.107453.

[209] Medvedev ES. Determination of a new molecular constant from overtone vibrational spectra. J Mol Spectrosc 1985;114:1–12. http://dx.doi.org/10.1016/0022-2852(85)90330-3.

[210] Chung C-Y, Ogilvie JF, Lee Y-P. Detection of vibration-rotational band 5-0 of $^{12}C^{16}O$ $X^1\Sigma^+$ with cavity ringdown absorption near 0.96 μm. J Phys Chem A 2005;109:7854–8. http://dx.doi.org/10.1021/jp052035x.

[211] Tan Y, Wang J, Zhao X-Q, Liu A-W, Hu S-M. Cavity ring-down spectroscopy of the fifth overtone of CO. J Quant Spectrosc Radiat Transfer 2017;187:274–9. http://dx.doi.org/10.1016/j.jqsrt.2016.10.003.

[212] Balashov AA, Bielska K, Li G, Kyuberis AA, Wójtewicz S, Domysławska J, et al. Measurement and calculation of CO (7–0) overtone line intensities. J Chem Phys 2023;158(23):234306. http://dx.doi.org/10.1063/5.0152996.

[213] Balashov AA, Wójtewicz S, awska JD, o RC, Lisak D, Bielska K. CRDS line-shape study of the (7–0) band of CO. Spectrochim Acta Part A: Mol Biomol Spectrosc 2024;312:124041. http://dx.doi.org/10.1016/j.saa.2024.124041.

[214] Tretyakov MY, Serov EA, Makarov DS, Vilkov IN, Golubiatnikov GY, Galanina TA, et al. Pure rotational R(0) and R(1) lines of CO in Ar baths: experimental broadening, shifting and mixing parameters in a wide pressure range *versus ab initio* calculations. Phys Chem Chem Phys 2023;25:1310–30. http://dx.doi.org/10.1039/D2CP04917A.

[215] Perevalov VI, Karlovets EV. Line intensities of the radioactive isotopologues of carbon monoxide. J Mol Spectrosc 2019;364:111184. http://dx.doi.org/10.1016/j.jms.2019.111184.

[216] Ushakov VG, Medvedev ES. Updated line list for the principal isotopologue of carbon monoxide. J Mol Spectrosc 2025;413–414:112037. http://dx.doi.org/10.1016/j.jms.2025.112037.

[217] Nikitin AV, Solodov AA, Protasevich AE, Rey M, Solodov AM, Tyuterev VG. Improved line list of methane in the 900–1050 cm^{-1} region. J Quant Spectrosc Radiat Transfer 2025;331:109286. http://dx.doi.org/10.1016/j.jqsrt.2024.109286.

[218] Tennyson J, Yurchenko SN, Zhang J, Bowesman CA, Brady RP, Buldyreva J, et al. The 2024 release of the ExoMol database: Molecular line lists for exoplanet and other hot atmospheres. J Quant Spectrosc Radiat Transfer 2024;326:109083. http://dx.doi.org/10.1016/J.JQSRT.2024.109083.

[219] Richard C, Fathallah OB, Hardy P, Kamel R, Merkulova M, Rotger M, et al. CaSDa24: Latest updates to the Dijon calculated spectroscopic databases. J Quant Spectrosc Radiat Transfer 2024;327:109127. http://dx.doi.org/10.1016/j.jqsrt.2024.109127.

[220] Nikitin A, Brown L, Sung K, Rey M, Tyuterev VG, Smith M, et al. Preliminary modeling of CH_3D from 4000 to 4550 cm^{-1}. J Quant Spectrosc Radiat Transfer 2013;114:1–12. http://dx.doi.org/10.1016/j.jqsrt.2012.08.005.

[221] Rodina AA, Nikitin AV, Manceron L, Thomas X, Daumont L, Rey M, et al. Improved line list of $^{12}CH_4$ in the 4100–4300 cm^{-1} region. J Quant Spectrosc Radiat Transfer 2022;279:108021. http://dx.doi.org/10.1016/j.jqsrt.2021.108021.

[222] Starikova E, Sung K, Nikitin AV, Rey M, Tyuterev V. Assignment and modeling of $^{13}CH_4$ spectrum at 298 K in the lower part of the Tetradecad in the 4970–5300 cm^{-1} range. J Quant Spectrosc Radiat Transfer 2024;329:109196. http://dx.doi.org/10.1016/j.jqsrt.2024.109196.

[223] Ben Fathallah O, Lembei A, Rey M, Mondelain D, Campargue A. The CH_3D absorption spectrum near 1.58 μm: Extended line lists and rovibrational assignments. Molecules 2024;29(22):5276. http://dx.doi.org/10.3390/molecules29225276.

[224] Malarich NA, Yun D, Sung K, Egbert S, Coburn SC, Drouin BJ, et al. Dual frequency comb absorption spectroscopy of CH_4 up to 1000 Kelvin from 6770–7570 cm^{-1}. J Quant Spectrosc Radiat Transfer 2021;272:107812. http://dx.doi.org/10.1016/j.jqsrt.2021.107812.

[225] Nikitin AV, Rey M, Campargue A, Tyuterev VG. First assignments of the $6\nu_4$, $\nu_2+5\nu_4$, and $\nu_1+4\nu_4$ Triacontad band system of $^{12}CH_4$ in the 7606-7919 cm^{-1} region. J Quant Spectrosc Radiat Transfer 2024;325:109098. http://dx.doi.org/10.1016/j.jqsrt.2024.109098.

[226] Campargue A, Karlovets EV, Vasilchenko SS, Turbet M. The high resolution absorption spectrum of methane in the 10 800–14 000 cm^{-1} region: literature review, new results and perspectives. Phys Chem Chem Phys 2023;25(48):32778–99. http://dx.doi.org/10.1039/D3CP02385K.

[227] Karkoschka E. Spectrophotometry of the jovian planets and titan at 300- to 1000-nm wavelength: The methane spectrum. Icarus 1994;111(1):174–92. http://dx.doi.org/10.1006/icar.1994.1139.

[228] Yurchenko SN, Owens A, Kefala K, Tennyson J. ExoMol line lists – LVII. High accuracy ro-vibrational line list for methane (CH_4). Mon Not R Astron Soc 2024;528:3719–29. http://dx.doi.org/10.1093/mnras/stae148.

[229] Birk M, Wagner G, Röske C. Measurement database and line parameter database for pure CH_4 in the 5970–6250 cm^{-1} region. 2025, http://dx.doi.org/10.5281/zenodo.15118739.

[230] Reed ZD, Birk M, Tan Y, Cecelski CE, Röske C, Wagner Ga. Multi-laboratory measurements of $^{12}CH_4$ $2\nu_3$-band line parameters. Part I: Line intensities with relative combined standard uncertainties at the permille level. J Quant Spectrosc Radiat Transfer 2025;109571. http://dx.doi.org/10.1016/j.jqsrt.2025.109571.

[231] Yin RH, Li JK, Wang J, Liu AW, Reed ZD, Hodges JT, et al. Multi-laboratory measurements of$^{12}CH_4 2\nu_3$-band line parameters. Part II: Spectrum analysis based on the speed dependent Voigt profile with first-order line mixing. J Quant Spectrosc Radiat Transfer 2025;109588. http://dx.doi.org/10.1016/j.jqsrt.2025.109588.

[232] Sung K, Coy BP, Broussard AW, Nikitin AV, Rey M, Tyuterev VG, et al. A new$^{13}CH_4$ linelist in the Octad region updated with quantum assignments and lower state energies through a two temperature method. 2024.

[233] Toon GC, Roehl C. Atmospheric voigt line list for the TCCON 2020 data release. 2022, http://dx.doi.org/10.14291/TCCON.GGG2020.ATM.R0, Dataset, CaltechDATA, Version GGG2020.R0, URL https://data.caltech.edu/records/zrkbg-re307, Published January 13, 2022.

[234] Antony BK, Niles DL, Wroblewski SB, Humphrey CM, Gabard T, Gamache RR. N_2-, O_2- and air-broadened half-widths and line shifts for transitions in the ν_3 band of methane in the 2726- to 3200 cm^{-1} spectral region. J Mol Spectrosc 2008;251(1–2):268–81. http://dx.doi.org/10.1016/j.jms.2008.03.012.

[235] Farji A, Aroui H, Vander Auwera J. Air-induced collisional parameters in the ν_3 band of methane. J Quant Spectrosc Radiat Transfer 2021;107878. http://dx.doi.org/10.1016/j.jqsrt.2021.107878.

[236] Ghysels M, Gomez L, Cousin J, Tran H, Amarouche N, Engel A, et al. Temperature dependences of air-broadening, air-narrowing and line-mixing coefficients of the methane ν_3 $R(6)$ manifold lines—Application to *in-situ* measurements of atmospheric methane. J Quant Spectrosc Radiat Transfer 2014;133:206–16. http://dx.doi.org/10.1016/j.jqsrt.2013.08.003.

[237] Pine AS, Gabard T. Speed-dependent broadening and line mixing in CH_4 perturbed by Ar and N_2 from multispectrum fits. J Quant Spectrosc Radiat Transfer 2000;66(1):69–92. http://dx.doi.org/10.1016/S0022-4073(99)00222-8.

[238] Brown LR, Sung K, Benner DC, Devi VM, Boudon V, Gabard T, et al. Methane line parameters in the HITRAN2012 database. In: HITRAN2012 special issue, J Quant Spectrosc Radiat Transfer In: HITRAN2012 special issue, 2013;130:201–19.http://dx.doi.org/10.1016/j.jqsrt.2013.06.020,

[239] Dudaryonok AS, Lavrentieva NN, Buldyreva J. Semi-empirical calculations of line-shape parameters and their temperature dependences for the ν_6 band of CH_3D perturbed by N_2. J Quant Spectrosc Radiat Transfer 2018;212:75–87. http://dx.doi.org/10.1016/j.jqsrt.2018.03.006.

[240] Bertin T, Gordon IE, Hargreaves RJ, Tennyson J, Yurchenko SN, Kefala K, et al. The HITRAN2024 methane update. J Quant Spectrosc Radiat Transfer 2026;349:109736. http://dx.doi.org/10.1016/j.jqsrt.2025.109736.

[241] Gancewski M, Jóźwiak H, Cybulski H, Wcisło P. Intensities of all fine-structure resolved rovibrational electric quadrupole absorption lines in $^{16}O_2(X^3\Sigma_g^-)$ calculated with a new *ab initio* quadrupole moment curve. J Quant Spectrosc Radiat Transfer 2025;337:109395. http://dx.doi.org/10.1016/j.jqsrt.2025.109395.

[242] Mérienne M-F, Jenouvrier A, Coquart B, Carleer M, Fally S, Colin R, et al. Improved dataset for the Herzberg band system of $^{16}O_2$. J Mol Spectrosc 2001;207:120. http://dx.doi.org/10.1006/jmsp.2001.8314.

[243] Adkins EM, Hodges JT, Bielska K, Alain Camparguec RCo, Domyslawska J, Fernandezand RP, et al. Survey of the updated O_2 line list in the HITRAN2024 spectroscopic database. J Quant Spectrosc Radiat Transfer 2025;347:109629. http://dx.doi.org/10.1016/j.jqsrt.2025.109629.

[244] Gordon I, Mondelain D, Kassi S, Campargue A, Fleurbaey H, Long D, et al. Disentangling magnetic dipole and electric quadrupole intensity contributions in spectra of molecular oxygen at 1.27 μm. Updated line positions and intensities. J Quant Spectrosc Radiat Transfer 2025. in prep..

[245] Klemm J, Campargue A, Fleurbaey H, Kassi S, Romanini D, Mondelain D. Temperature dependence of the air-broadened line-shape parameters of the 1.27 μm O_2-band. J Quant Spectrosc Radiat Transfer 2025;342:109448. http://dx.doi.org/10.1016/j.jqsrt.2025.109448.

[246] Fleurbaey H, Reed ZD, Adkins EM, Long DA, Hodges JT. High accuracy spectroscopic parameters of the 1.27 μm band of O_2 measured with comb-referenced, cavity ring-down spectroscopy. J Quant Spectrosc Radiat Transfer 2021;270:107684. http://dx.doi.org/10.1016/j.jqsrt.2021.107684.

[247] Adkins E, Yurchenko S, Somogyi W, Hodges J. An accurate determination of O_2 A-band line intensities through experiment and theory. J Quant Spectrosc Radiat Transfer 2025;338:109412. http://dx.doi.org/10.1016/j.jqsrt.2025.109412.

[248] awska JD, Wójtewicz S, owski PM, Bielska K, Cygan A, owiński MS, et al. Line-shape analysis for high J R-branch transitions of the oxygen B band. J Quant Spectrosc Radiat Transfer 2020;242:106789. http://dx.doi.org/10.1016/j.jqsrt.2019.106789.

[249] awska JD, Wójtewicz S, Bielska K, Bilicki S, o RC, Lisak D. Line mixing in the oxygen B band head. J Chem Phys 2022;156:084301. http://dx.doi.org/10.1063/5.0079158.

[250] Bielska K, awska JD, Wójtewicz S, Balashov A, owiński MS, Piwiński M, et al. Simultaneous observation of speed dependence and Dicke narrowing for self-perturbed P-branch lines of O_2 B band. J Quant Spectrosc Radiat Transfer 2021;276:107927. http://dx.doi.org/10.1016/j.jqsrt.2021.107927.

[251] Bielska K, Tran D, Balashov A, awska JD, Wójtewicz S, Bober M, et al. Pressure and temperature dependencies of air-perturbed O_2 B-band line shapes. Spectrochim Acta Part A: Mol Biomol Spectrosc 2023;303:123185. http://dx.doi.org/10.1016/j.saa.2023.123185.

[252] Tomazzeli OG, Palancar GG, Minschwaner K, Ji A, Madronich S, Fernandez RP. Impact of the overlapping O_2 Schumann-Runge and Herzberg continua with Schumann-Runge bands on photolysis rate coefficients: comparing the Koppers & Murtagh parameterization with line-by-line cross section. Journal of Quantitative Spectroscopy and Radiative Transfer 2025;347:109678. http://dx.doi.org/10.1016/J.JQSRT.2025.109678.

[253] Toureille M, Béguier S, Odintsova T, Tretyakov M, Pirali O, Campargue A. The O_2 far-infrared absorption spectrum between 50 and 170 cm^{-1}. J Quant Spectrosc Radiat Transfer 2020;242:106709. http://dx.doi.org/10.1016/j.jqsrt.2019.106709, URL https://linkinghub.elsevier.com/retrieve/pii/S0022407319306739.

[254] Makarov DS, Serov EA, Galanina TA, Koroleva AO, Tretyakov MY. The molecular oxygen 118-GHz line intensity revision. J Mol Spectrosc 2023;395:111792. http://dx.doi.org/10.1016/j.jms.2023.111792.

[255] Anenberg SC, Henze DK, Tinney V, Kinney PL, Raich W, Fann N, et al. Estimates of the global burden of ambient $PM_{2.5}$, ozone, and NO_2 on asthma incidence and emergency room visits. Environ Health Perspect 2018;126(10):107004. http://dx.doi.org/10.1289/EHP3766.

[256] Lukashevskaya A, Lavrentieva N, Dudaryonok A, Perevalov V. NDSD-1000: High-resolution, high-temperature nitrogen dioxide spectroscopic databank. J Quant Spectrosc Radiat Transfer 2016;184:205–17. http://dx.doi.org/10.1016/J.JQSRT.2016.07.014.

[257] Perrin A, Flaud JM, Goldman A, Camy-Peyret C, Lafferty WJ, Arcas P, et al. NO_2 and SO_2 line parameters: 1996 HITRAN update and new results. J Quant Spectrosc Radiat Transfer 1998;60(5):839–50. http://dx.doi.org/10.1016/S0022-4073(98)00086-7.

[258] Perrin A, Manceron L, Flaud JM, Kwabia-Tchana F, Armante R, Roy P, et al. The new nitrogen dioxide (NO_2) linelist in the GEISA database and first identification of the $\nu_1+2\nu_3-\nu_3$ band of $^{14}N^{16}O_2$. J Mol Spectrosc 2021;376:111394. http://dx.doi.org/10.1016/j.jms.2020.111394.

[259] Perrin A, Ndao M, Manceron L. Comment on the paper "NDSD-1000: High-resolution, high-temperature nitrogen dioxide spectroscopic Databank; by A.A. Lukashevskaya, N.N. Lavrentieva, A.C. Dudaryonok, V.I. Perevalov, J Quant Spectrosc Radiat Transfer 2016;184:205-17. J Quant Spectrosc Radiat Transfer 2017;200:12–6. http://dx.doi.org/10.1016/j.jqsrt.2017.05.029.

[260] Stephen TM, Goldman A, Perrin A, Flaud JM, Keller F, Rinsland CP. New high-resolution analysis of the $3\nu_3$ and $2\nu_1+\nu_3$ bands of nitrogen dioxide (NO_2) by Fourier transform spectroscopy. J Mol Spectrosc 2000;201(1):134–42. http://dx.doi.org/10.1006/jmsp.2000.8064.

[261] Gueye F, Kwabia Tchana F, Landsheere X, Perrin A. New line positions analysis of the $\nu_1+\nu_2+\nu_3$ band of NO_2 at 3637.848 cm^{-1}. J Quant Spectrosc Radiat Transfer 2014;138:60–9. http://dx.doi.org/10.1016/j.jqsrt.2014.01.023.

[262] Perrin A, Flaud JM, Camypeyret C, Ngom A, Mbiake R, Gbaguidi H, et al. The $\nu_1 + \nu_2$ Band of $^{14}N\ ^{16}O_2$. J Mol Spectrosc 1995;171(2):354–7. http://dx.doi.org/10.1006/jmsp.1995.1124.

[263] Perrin A, Manceron L, Kwabia Tchana F. New line positions analysis of the $2\nu_1$ and $\nu_1+\nu_3$ bands of NO_2 at 3637.848 and 2906.070 cm^{-1}. Mol Phys 2020;118(11):e1711235. http://dx.doi.org/10.1080/00268976.2019.1711235.

[264] Miljanic S, Perrin A, Orphal J. New high-resolution analysis of the $\{\nu_1 + \nu_3\}$ band of the $^{15}N\ ^{16}O_2$ isotopomer of nitrogen dioxide: Line positions and intensities. J Mol Spectrosc 2007;242(2):176–81. http://dx.doi.org/10.1016/j.jms.2007.02.024.

[265] Perrin A, Toon G, Orphal J. Detection of atmospheric $^{15}NO_2$ in the ν_3 spectral region (6.3 μm). J Quant Spectrosc Radiat Transfer 2015;154:91–7. http://dx.doi.org/10.1016/j.jqsrt.2014.12.006.

[266] Marinina A, Jacquemart D, Krim L, Soulard P, Perevalov V. The ν_3 band of $^{16}O^{14}N^{18}O$: Line positions and intensities. J Quant Spectrosc Radiat Transfer 2022;290:108312. http://dx.doi.org/10.1016/J.JQSRT.2022.108312.

[267] Benner DC, Blake TA, Brown LR, Malathy Devi V, Smith MAH, Toth RA. Air-broadening parameters in the ν_3 band of $^{14}N^{16}O_2$ using a multispectrum fitting technique. J Mol Spectrosc 2004;228(2):593–619. http://dx.doi.org/10.1016/j.jms.2004.07.006.

[268] Lindaas J, Pollack IB, Calahorrano JJ, O'Dell K, Garofalo LA, Pothier MA, et al. Empirical insights into the fate of ammonia in western U.S. wildfire smoke plumes. J Geophys Res (Atmos) 2021;126(11). http://dx.doi.org/10.1029/2020JD033730, e2020JD033730.

[269] Abeed R, Viatte C, Porter WC, Evangeliou N, Clerbaux C, Clarisse L, et al. A roadmap to estimating agricultural ammonia volatilization over Europe using satellite observations and simulation data. Atmos Chem Phys 2023;23(19):12505–23. http://dx.doi.org/10.5194/acp-23-12505-2023.

[270] Zeng Z-C, Lee L, Qi C, Clarisse L, Van Damme M. Optimal estimation retrieval of tropospheric ammonia from the Geostationary Interferometric Infrared Sounder on board FengYun-4B. Atmos Meas Tech 2023;16(15):3693–713. http://dx.doi.org/10.5194/amt-16-3693-2023.

[271] Moeckel C, de Pater I, DeBoer D. Ammonia abundance derived from juno MWR and VLA observations of jupiter. Planet Sci J 2023;4(2):25. http://dx.doi.org/10.3847/PSJ/acaf6b, arXiv:2209.03513.

[272] Martín EL, Zhang JY, Esparza P, Gracia F, Rasilla JL, Masseron T, et al. Ammonia-methane ratios from H-band near-infrared spectra of late-T and Y dwarfs. Astron Astrophys 2021;655:L3. http://dx.doi.org/10.1051/0004-6361/202142470, arXiv:2111.07449.

[273] Fortney JJ, Visscher C, Marley MS, Hood CE, Line MR, Thorngren DP, et al. Beyond equilibrium temperature: How the atmosphere/interior connection affects the onset of methane, ammonia, and clouds in warm transiting giant planets. Astonomical J 2020;160(6):288. http://dx.doi.org/10.3847/1538-3881/abc5bd, arXiv:2010.00146.

[274] Yang J, Hammond M, Piette AAA, Blecic J, Bell TJ, Irwin PGJ, et al. Simultaneous retrieval of orbital phase resolved JWST/MIRI emission spectra of the hot Jupiter WASP-43b: evidence of water, ammonia, and carbon monoxide. Mon Not R Astron Soc 2024;532(1):460–75. http://dx.doi.org/10.1093/mnras/stae1427, arXiv:2406.03490.

[275] Brown L, Margolis J. Empirical line parameters of NH_3 from 4791 to 5294 cm^{-1}. J Quant Spectrosc Radiat Transfer 1996;56(2):283–94. http://dx.doi.org/10.1016/0022-4073(96)00041-6.

[276] Urban Š, Misra P, Narahari Rao K. The $\nu_1+\nu_2$ and $\nu_1+\nu_2-\nu_2$ bands of $^{14}NH_3$ and $^{15}NH_3$. J Mol Spectrosc 1985;114(2):377–94. http://dx.doi.org/10.1016/0022-2852(85)90233-4.

[277] Cacciani P, Čermák P, Béguier S, Campargue A. The absorption spectrum of ammonia between 5650 and 6350 cm^{-1}. J Quant Spectrosc Radiat Transfer 2021;258:107334. http://dx.doi.org/10.1016/j.jqsrt.2020.107334.

[278] Cacciani P, Čermák P, Vander Auwera J, Campargue A. The ammonia absorption spectrum between 3900 and 4700 cm^{-1}. J Quant Spectrosc Radiat Transfer 2022;277:107961. http://dx.doi.org/10.1016/j.jqsrt.2021.107961.

[279] Cacciani P, Čermák P, Vander Auwera J, Campargue A. The ammonia absorption spectrum between 4700 and 5650 cm^{-1}. J Quant Spectrosc Radiat Transfer 2022;292:108350. http://dx.doi.org/10.1016/j.jqsrt.2022.108350.

[280] Cacciani P, Čermák P, Votava O, Vander Auwera J, Campargue A. The ammonia absorption spectrum revisited between 5650 and 6350 cm^{-1}. Mol Phys 2023;122(7–8):e2256893. http://dx.doi.org/10.1080/00268976.2023.2256893.

[281] Coles P, Ovsyannikov R, Polyansky O, Yurchenko S, Tennyson J. Improved potential energy surface and spectral assignments for ammonia in the near-infrared region. J Quant Spectrosc Radiat Transfer 2018;219:199–212. http://dx.doi.org/10.1016/j.jqsrt.2018.07.022.

[282] Cacciani P, Čermák P, Auwera J, Campargue A. The ammonia absorption spectrum between 3900 and 6350 cm^{-1}: $^{15}NH_3$ contribution and a recommended list for natural ammonia. J Quant Spectrosc Radiat Transfer 2024;329:109148. http://dx.doi.org/10.1016/j.jqsrt.2024.109148.

[283] Yurchenko S. A theoretical room-temperature line list for $^{15}NH_3$. J Quant Spectrosc Radiat Transfer 2015;152:28–36. http://dx.doi.org/10.1016/j.jqsrt.2014.10.023.

[284] Yurchenko S, Bowesman C, Brady R, Guest E, Kefala K, Mitev G, et al. ExoMol line lists – LX. Molecular line list for the ammonia isotopologue $^{15}NH_3$. Mon Not R Astron Soc 2024;533(3):3442–56. http://dx.doi.org/10.1093/mnras/stae1849.

[285] Beale CA, Hargreaves RJ, Coles P, Tennyson J, Bernath PF. Infrared absorption spectra of hot ammonia. J Quant Spectrosc Radiat Transfer 2017;203:410–6. http://dx.doi.org/10.1016/j.jqsrt.2017.02.012.

[286] Beale CA, Wong A, Bernath P. Infrared transmission spectra of hot ammonia in the 4800-9000 cm^{-1} region. J Quant Spectrosc Radiat Transfer 2020;246:106911. http://dx.doi.org/10.1016/j.jqsrt.2020.106911.

[287] Zobov NF, Bertin T, Vander Auwera J, Civiš S, Knížek A, Ferus M, et al. The spectrum of ammonia near 0.793μm. J Quant Spectrosc Radiat Transfer 2021;273:107838. http://dx.doi.org/10.1016/j.jqsrt.2021.107838.

[288] Down MJ, Hill C, Yurchenko SN, Tennyson J, Brown LR, Kleiner I. Re-analysis of ammonia spectra: Updating the HITRAN $^{14}NH_3$ database. J Quant Spectrosc Radiat Transfer 2013;130:260–72. http://dx.doi.org/10.1016/j.jqsrt.2013.05.027.

[289] Toon GC. The JPL MkIV interferometer. Opt Photonics News 1991;2(10):19–21. http://dx.doi.org/10.1364/OPN.2.10.000019.

[290] Perrin A, Manceron L, Armante R, Kwabia-Tchana F, Roy P, Doizi D. First analysis of the $\nu_2+\nu_7$ and $\nu_2+\nu_9$ and $\nu_2+\nu_6$ combination bands of HNO_3: evidence of perturbations due to large amplitude OH torsion in the 2^19^1 excited state. Mol Phys 2022;120(15–16):e1987543. http://dx.doi.org/10.1080/00268976.2021.1987543.

[291] Perrin A, Manceron L, Armante R, Kwabia-Tchana F, Roy P, Doizi D, et al. The 5.8 μm absorption bands for nitric acid ($H^{14}N^{16}O_3$): line positions and intensities for the ν_2 band at 1709.567 cm^{-1} and for its first associated hot bands ($\nu_2+\nu_9-\nu_9$, $\nu_2+\nu_7-\nu_7$, $\nu_2+\nu_6-\nu_6$). Mol Phys 2022;120(15–16):e1998931. http://dx.doi.org/10.1080/00268976.2021.1998931.

[292] Perrin A, Manceron L, Armante R, Kwabia-Tchana F, Roy P, Toon GC. First investigation of the ν_1, $\nu_1-\nu_9$, $\nu_1+\nu_9$, and $\nu_1+\nu_7$ absorption bands of nitric acid ($^1H^{14}N^{16}O_3$) at 3551.766 cm^{-1}, 3092.708 cm^{-1}, 4006.974 cm^{-1}, and 4127.782 cm^{-1}, respectively. J Mol Spectrosc 2023;392:111741. http://dx.doi.org/10.1016/j.jms.2023.111741.

[293] Perrin A, Manceron L, Armante R, Kwabia-Tchana F, Roy P, Toon GC. Part 2:Validation for line lists generated for nitric acid ($H^{14}N^{16}O_3$) for the ν_1 band and its first two associated hot bands ($\nu_1+\nu_9-\nu_9$, $\nu_1+\nu_7-\nu_7$) in the 2.8 μm region, the $\nu_1-\nu_9$, $\nu_1+\nu_9$ and $\nu_1+\nu_7$ bands at 3.2 μm, 2.5 μm and 2.4 μm, respectively. J Mol Spectrosc 2023;392:111740. http://dx.doi.org/10.1016/j.jms.2023.111740.

[294] Chackerian C, Sharpe SW, Blake TA. Anhydrous nitric acid integrated absorption cross sections: 820-5300cm^{-1}. J Quant Spectrosc Radiat Transfer 2003;82:429–41. http://dx.doi.org/10.1016/S0022-4073(03)00168-7.

[295] Pavlyuchko AI, Yurchenko SN, Tennyson J. A hybrid variational-perturbation calculation of the ro-vibrational spectrum of nitric acid. J Chem Phys 2015;142(9):094309. http://dx.doi.org/10.1063/1.4913741, arXiv:1412.6744.

[296] Pavlyuchko AI, Yurchenko SN, Tennyson J. ExoMol molecular line lists - XI. The spectrum of nitric acid. Mon Not R Astron Soc 2015;452(2):1702–6. http://dx.doi.org/10.1093/mnras/stv1376, arXiv:1507.02276.

[297] Pickett HM, Drouin BJ, Canty T, Salawitch RJ, Fuller RA, Perun VS, et al. Validation of Aura Microwave Limb Sounder OH and HO_2 measurements. J Geophys Res: Atmos 2008;113(D16):D16S30. http://dx.doi.org/10.1029/2007JD008775.

[298] Carlotti M, Ade PAR, Carli B, Chipperfield M, Hamilton PA, Mencaraglia F, et al. Diurnal variability and night detection of stratospheric hydroxyl radical from far infrared emission measurements. J Atmos Sol-Terr Phys 2001;63(14):1509–18. http://dx.doi.org/10.1016/S1364-6826(01)00030-X.

[299] Noll S, Winkler H, Goussev O, Proxauf B. OH level populations and accuracies of Einstein-A coefficients from hundreds of measured lines. Atmos Chem Phys 2020;20(9):5269–92. http://dx.doi.org/10.5194/acp-20-5269-2020, arXiv:2005.06603.

[300] Cheung R, Fai Li K, Wang S, Pongetti TJ, Cageao RP, Sander SP, et al. Atmospheric hydroxyl radical (OH) abundances from ground-based ultraviolet solar spectra: an improved retrieval method. Appl Opt 2008;47(33):6277–84. http://dx.doi.org/10.1364/AO.47.006277.

[301] Asplund M, Grevesse N, Sauval AJ, Allende Prieto C, Kiselman D. Line formation in solar granulation. IV. [O I], O I and OH lines and the photospheric O abundance. Astron Astrophys 2004;417:751–68. http://dx.doi.org/10.1051/0004-6361:20034328, arXiv:astro-ph/0312290.

[302] Goicoechea JR, Joblin C, Contursi A, Berné O, Cernicharo J, Gerin M, et al. OH emission from warm and dense gas in the Orion Bar PDR. Astron Astrophys 2011;530:L16. http://dx.doi.org/10.1051/0004-6361/201116977, arXiv:1105.2623.

[303] Todd Clancy R, Sandor BJ, García-Muñoz A, Lefèvre F, Smith MD, Wolff MJ, et al. First detection of Mars atmospheric hydroxyl: CRISM Near-IR measurement versus LMD GCM simulation of OH Meinel band emission in the Mars polar winter atmosphere. Icarus 2013;226(1):272–81. http://dx.doi.org/10.1016/j.icarus.2013.05.035.

[304] Piccioni G, Drossart P, Zasova L, Migliorini A, Gérard JC, Mills FP, et al. First detection of hydroxyl in the atmosphere of Venus. Astron Astrophys 2008;483(3):L29–33. http://dx.doi.org/10.1051/0004-6361:200809761.

[305] Landman R, Sánchez-López A, Mollière P, Kesseli AY, Louca AJ, Snellen IAG. Detection of OH in the ultra-hot Jupiter WASP-76b. Astron Astrophys 2021;656:A119. http://dx.doi.org/10.1051/0004-6361/202141696, arXiv:2110.11946.

[306] Nugroho SK, Kawahara H, Gibson NP, de Mooij EJW, Hirano T, Kotani T, et al. First detection of hydroxyl radical emission from an exoplanet atmosphere: High-dispersion characterization of WASP-33b using subaru/IRD. Astrophys J Lett 2021;910(1):L9. http://dx.doi.org/10.3847/2041-8213/abec71, arXiv:2103.03094.

[307] Maillard JP, Chauville J, Mantz AW. High-resolution emission spectrum of OH in an oxyacetylene flame from 3.7 to 0.9 μm. J Mol Spectrosc 1976;63(1):120–41. http://dx.doi.org/10.1016/0022-2852(67)90139-7.

[308] Brooke JSA, Bernath PF, Western CM, Sneden C, Afşar M, Li G, et al. Line strengths of rovibrational and rotational transitions in the $X^2\Pi$ ground state of OH. J Quant Spectrosc Radiat Transfer 2016;168:142–57. http://dx.doi.org/10.1016/j.jqsrt.2015.07.021.

[309] Medvedev ES, Ermilov AY, Ushakov VG. Manifestation of the Normal Intensity Distribution Law (NIDL) in the rovibrational emission spectrum of hydroxyl radical. Mol Phys 2024;e2395439. http://dx.doi.org/10.1080/00268976.2024.2395439.

[310] Ushakov VG, Ermilov AY, Medvedev ES. Three-states model for calculating the *X-X* rovibrational transition intensities in hydroxyl radical. J Mol Spectrosc 2025;407:111977. http://dx.doi.org/10.1016/j.jms.2024.111977, URL http://ssrn.com/abstract=4995810, [Erratum: 2025;408:111996. http://dx.doi.org/10.1016/j.jms.2025.111996].

[311] Ushakov VG, Ermilov AY, Medvedev ES. Three-states model for calculating the X-X rovibrational transition intensities in hydroxyl radical (Erratum). J Mol Spectrosc 2025;408:111996. http://dx.doi.org/10.1016/J.JMS.2025.111996.

[312] Abrams MC, Davis SP, Rao MLP, Engleman Jr R, Brault JW. High-resolution Fourier transform spectroscopy of the Meinel system of OH. Astrophys J Suppl Ser 1994;93:351–95. http://dx.doi.org/10.1086/192058.

[313] Mitev GB, Bowesman CA, Zhang J, Yurchenko SN, Tennyson J. ExoMol line lists – LXI. A trihybrid line list for rovibronic transitions of the hydroxyl radical (OH). Mon Not R Astron Soc 2024;536(4):3401–20. http://dx.doi.org/10.1093/mnras/stae2803.

[314] Mitev GB, Tennyson J, Yurchenko SN. Predissociation dynamics of the hydroxyl radical (OH) based on a five-state spectroscopic model. J Chem Phys 2024;160(14):144110. http://dx.doi.org/10.1063/5.0198241.

[315] Chang C-W, Chen I-Y, Fittschen C, Luo P-L. Measurements of absolute line strength of the ν_1 fundamental transitions of OH radical and rate coefficient of the reaction OH + H_2O_2 with mid-infrared two-color time-resolved dual-comb spectroscopy. J Chem Phys 2023;159:184203. http://dx.doi.org/10.1063/5.0176311.

[316] Mahieu E, Chipperfield MP, Notholt J, Reddmann T, Anderson J, Bernath PF, et al. Recent Northern Hemisphere stratospheric HCl increase due to atmospheric circulation changes. Nature 2014;515:104–7. http://dx.doi.org/10.1038/nature13857.

[317] Krasnopolsky V, Belyaev D, Gordon I, Li G, Rothman L. Observations of D/H ratios in H_2O, HCl, and HF on Venus and new DCl and DF line strengths. Icarus 2013;224:57–65. http://dx.doi.org/10.1016/j.icarus.2013.02.010.

[318] Korablev O, Olsen KS, Trokhimovskiy A, Lefèvre F, Montmessin F, Fedorova AA, et al. Transient HCl in the atmosphere of Mars. Sci Adv 2021;7:eabe4386. http://dx.doi.org/10.1126/SCIADV.ABE4386.

[319] Lanza M, Kalugina Y, Wiesenfeld L, Faure A, Lique F. New insights on the HCl abundance in the interstellar medium. Mon Not R Astron Soc 2014;443(4):3351–8. http://dx.doi.org/10.1093/MNRAS/STU1371.

[320] Li G, Gordon I, Bernath P, Rothman L. Direct fit of experimental ro-vibrational intensities to the dipole moment function: Application to HCl. J Quant Spectrosc Radiat Transfer 2011;112(10):1543–50. http://dx.doi.org/10.1016/j.jqsrt.2011.03.014.

[321] Li G, Gordon IE, Hajigeorgiou PG, Coxon JA, Rothman LS. Reference spectroscopic data for hydrogen halides, Part II: The line lists. J Quant Spectrosc Radiat Transfer 2013;130:284–95. http://dx.doi.org/10.1016/j.jqsrt.2013.07.019.

[322] Gelfand J, Zughul M, Rabitz H, Han C. Absorption intensities for the 4–0 through 7–0 overtone bands of HCl. J Quant Spectrosc Radiat Transfer 1981;26(4):303–5. http://dx.doi.org/10.1016/0022-4073(81)90124-2.

[323] Vasilchenko SS, Lyulin OM, Perevalov VI. High sensitivity absorption spectroscopy of hydrogen chloride near 770 nm. J Quant Spectrosc Radiat Transfer 2023;296:108460. http://dx.doi.org/10.1016/j.jqsrt.2022.108460.

[324] Špirko V. Reduced radial curves of diatomic molecules. J Chem Theory Comput 2023;19:7324–32. http://dx.doi.org/10.1021/ACS.JCTC.3C00622.

[325] Yousefi M, Bernath PF, Boone CD, Toon GC. Global measurements of atmospheric carbonyl sulfide (OCS), $OC^{34}S$ and $O^{13}CS$. J Quant Spectrosc Radiat Transfer 2019;238:106554. http://dx.doi.org/10.1016/J.JQSRT.2019.06.033.

[326] Mahieux A, Robert S, Mills F, Jessup K, Trompet L, Aoki S, et al. Update on SO_2, detection of OCS, CS, CS_2, and SO_3, and upper limits of H_2S and HOCl in the Venus mesosphere using SOIR on board Venus Express. Icarus 2023;399:115556. http://dx.doi.org/10.1016/j.icarus.2023.115556.

[327] Saki M, Gibb EL, Bonev BP, Roth NX, DiSanti MA, Dello Russo N, et al. Carbonyl sulfide (OCS): Detections in comets C/2002 T7 (LINEAR), C/2015 ER61 (PanSTARRS), and 21P/giacobini-zinner and stringent upper limits in 46P/wirtanen. Astron J 2020;160(4):184. http://dx.doi.org/10.3847/1538-3881/aba522.

[328] Huang X, Gordon IE, Bertin T, Schwenke DW, Lee TJ. Accurate potential energy surface, dipole moment surface, and IR line lists for OCS isotopologues up to 2000 K. J Quant Spectrosc Radiat Transfer 2025;339:109425. http://dx.doi.org/10.1016/j.jqsrt.2025.109425.

[329] Huang X, Schwenke DW, Lee TJ. What it takes to compute highly accurate rovibrational line lists for use in astrochemistry. Acc Chem Res 2021;54(6):1311–21. http://dx.doi.org/10.1021/acs.accounts.0c00624.

[330] Toth RA, Sung K, Brown LR, Crawford TJ. Line positions and strengths of 41 bands including 10 OCS isotopologues in the 3850-4200cm^{-1}region. J Quant Spectrosc Radiat Transfer 2010;111(9):1193–208. http://dx.doi.org/10.1016/j.jqsrt.2009.10.014.

[331] Endres CP, Schlemmer S, Schilke P, Stutzki J, Müller HSP. The cologne database for molecular spectroscopy, CDMS, in the virtual atomic and molecular data centre, VAMDC. J Mol Spectrosc 2016;327:95–104. http://dx.doi.org/10.1016/j.jms.2016.03.005, arXiv:1603.03264.

[332] Xu E, Tennyson J. Empirical rovibrational energy levels for carbonyl sulphide. Mol Phys 2023;122(15–16):e2279694. http://dx.doi.org/10.1080/00268976.2023.2279694.

[333] Auwera JV, Fayt A. Absolute line intensities for carbonyl sulfide from 827 to 2939 cm^{-1}. J Mol Struct 2006;780–781:134–41. http://dx.doi.org/10.1016/j.molstruc.2005.04.052.

[334] Owens A, Yurchenko SN, Tennyson J. ExoMol line lists - LVIII. High-temperature molecular line list of carbonyl sulphide (OCS). Mon Not R Astron Soc 2024;530(4):4004–15. http://dx.doi.org/10.1093/mnras/stae1110.

[335] Koshelev MA, Tretyakov MY. Collisional broadening and shifting of OCS rotational spectrum lines. J Quant Spectrosc Radiat Transfer 2009;110(1–2):118–28. http://dx.doi.org/10.1016/j.jqsrt.2008.09.010.

[336] Bouanich J-P, Blanquet G, Walrand J, Courtoy C. Diode laser measurements of line strengths and collisional half-widths in the ν_1 band of OCS at 298 and 200K. J Quant Spectrosc Radiat Transfer 1986;36(4):295–306. http://dx.doi.org/10.1016/0022-4073(86)90053-1.

[337] Kagann RH. Infrared absorption intensities for OCS. J Mol Spectrosc 1982;94(1):192–8. http://dx.doi.org/10.1016/0022-2852(82)90303-4.

[338] Gamache RR, Vispoel B, Tennyson J, Yurchenko SN, Polyansky OL, Gordon IE, et al. Partition sums for molecules and their isotopologues for HITRAN2024. J Quant Spectrosc Radiat Transfer 2025;345:109568. http://dx.doi.org/10.1016/J.JQSRT.2025.109568.

[339] Jellali C, Galalou S, KwabiaTchana F, Aroui H. Line broadening, shifting and mixing parameters for the $\nu_1+\nu_3$ band of OCS perturbed by N_2 and O_2. Mol Phys 2014;112(8):1189–200. http://dx.doi.org/10.1080/00268976.2013.839062.

[340] Domenech J, Bermejo D, Bouanich J-P. Pressure lineshift and broadening coefficients in the $2\nu_3$ band of $^{16}O^{12}C^{32}S$. J Mol Spectrosc 2000;200(2):266–76. http://dx.doi.org/10.1006/jmsp.1999.8055.

[341] De Smedt I, Müller J-F, Stavrakou T, van der A R, Eskes H, Van Roozendael M. Twelve years of global observations of formaldehyde in the troposphere using GOME and SCIAMACHY sensors. Atmos Chem Phys 2008;8(16):4947–63. http://dx.doi.org/10.5194/acp-8-4947-2008.

[342] de Blas M, Ibáñez P, García JA, Gómez MC, Navazo M, Alonso L, et al. Summertime high resolution variability of atmospheric formaldehyde and non-methane volatile organic compounds in a rural background area. Sci Total Environ 2019;647:862–77. http://dx.doi.org/10.1016/j.scitotenv.2018.07.411.

[343] Duce RA, Mohnen VA, Zimmerman PR, Grosjean D, Cautreels W, Chatfield R, et al. Organic material in the global troposphere. Rev Geophys 1983;21(4):921–52. http://dx.doi.org/10.1029/rg021i004p00921.

[344] Snyder LE, Buhl D, Zuckerman B, Palmer P. Microwave detection of interstellar formaldehyde. Phys Rev Lett 1969;22:679–81. http://dx.doi.org/10.1103/physrevlett.22.679.

[345] Milam SN, Remijan AJ, Womack M, Abrell L, Ziurys LM, Wyckoff S, et al. Formaldehyde in comets C/1995 O1 (Hale-Bopp), C/2002 T7 (LINEAR), and C/2001 Q4 (NEAT): Investigating the cometary origin of H_2CO. Astrophys J 2006;649:1169–77. http://dx.doi.org/10.1086/506501.

[346] Aikawa Y, Momose M, Thi W-F, van Zadelhoff G-J, Qi C, Blake GA, et al. Interferometric observations of formaldehyde in the protoplanetary disk around LkCa 15. Publ Astron Soc Japan 2003;55(1):11–5. http://dx.doi.org/10.1093/pasj/55.1.11.

[347] Korablev OI, Ackerman M, Krasnopolsky VA, Moroz VI, Muller C, Rodin AV, et al. Tentative identification of formaldehyde in the Martian atmosphere. Planet Space Sci 1993;41(6):441–51. http://dx.doi.org/10.1016/0032-0633(93)90004-L.

[348] Korablev OI. Solar occultation measurements of the martian atmosphere on the phobos spacecraft: Water vapor profile, aerosol parameters, and other results. Sol Syst Res 2002;36:12–34. http://dx.doi.org/10.1023/A:1014269426317.

[349] Al-Refaie AF, Yurchenko SN, Yachmenev A, Tennyson J. ExoMol line lists - VIII: A variationally computed line list for hot formaldehyde. Mon Not R Astron Soc 2015;448(2):1704–14. http://dx.doi.org/10.1093/mnras/stv091.

[350] Al-Derzi AR, Tennyson J, Yurchenko SN, Melosso M, Jiang N, Puzzarini C, et al. An improved rovibrational linelist of formaldehyde, H_2 ^{12}C ^{16}O. J Quant Spectrosc Radiat Transfer 2021;266:107563. http://dx.doi.org/10.1016/j.jqsrt.2021.107563.

[351] Germann M, Hjältén A, Tennyson J, Yurchenko SN, Gordon IE, Pett C, et al. Optical frequency comb Fourier transform spectroscopy of formaldehyde in the 1250 to 1390 cm^{-1} range: Experimental line list and improved MARVEL analysis. J Quant Spectrosc Radiat Transfer 2024;312:108782. http://dx.doi.org/10.1016/j.jqsrt.2023.108782.

[352] Jacquemart D, Laraia A, Tchana FK, Gamache RR, Perrin A, Lacome N. Formaldehyde around 3.5 and 5.7-μm: Measurement and calculation of broadening coefficients. J Quant Spectrosc Radiat Transfer 2010;111(9):1209–22. http://dx.doi.org/10.1016/j.jqsrt.2010.02.004.

[353] Nadler S, Reuter DC, Daunt SJ, Johns JWC. The ν_3, ν_4, and ν_6 bands of formaldehyde: A spectral catalog from 900 cm^{-1} to 1580 cm^{-1}. Tech. Rep., NASA Technical Memorandum 100709, Greenbelt, Maryland, USA: NASA Goddard Space Flight Center; 1988, URL https://ntrs.nasa.gov/citations/19890010605, NAS/NRC Research Associate at NASA/Goddard; Concordia University; Herzberg Institute of Astrophysics.

[354] Nikitin AV, Rodina AA, Protasevich AE, Manceron L, Rey M, Tyuterev VG. New quantum assignments and analysis of high-resolution H_2 ^{12}CO spectra in the range 3700–4450 cm^{-1}. J Quant Spectrosc Radiat Transfer 2024;329:109180. http://dx.doi.org/10.1016/j.jqsrt.2024.109180.

[355] Rey M. Novel methodology for systematically constructing global effective models from *ab initio*-based surfaces: A new insight into high-resolution molecular spectra analysis. J Chem Phys 2022;156(22):224103. http://dx.doi.org/10.1063/5.0089097.

[356] Nikitin AV, Protasevich AE, Rodina AA, Rey M, Tajti A, Tyuterev VG. Vibrational levels of formaldehyde: Calculations from new high precision potential energy surfaces and comparison with experimental band origins . J Quant Spectrosc Radiat Transfer 2021;260:107478. http://dx.doi.org/10.1016/j.jqsrt.2020.107478.

[357] Azzam AAA, Yurchenko SN, Tennyson J, Naumenko OV. ExoMol molecular line lists – XVI. The rotation–vibration spectrum of hot H_2S. Mon Not R Astron Soc 2016;460(4):4063–74. http://dx.doi.org/10.1093/mnras/stw1133.

[358] Li Q, Palmer PI, Pumphrey HC, Bernath P, Mahieu E. What drives the observed variability of HCN in the troposphere and lower stratosphere? Atmos Chem Phys 2009;9(21):8531–43. http://dx.doi.org/10.5194/acp-9-8531-2009.

[359] Drägerwerk AG& CoKGaA. Understanding the toxic twins: HCN and CO. White Paper/Technical Report, Dräger; 2023, URL https://www.draeger.com/Content/Documents/Products/toxic-twins-wp-9103690-en-us.pdf.

[360] van Loon JT, Marshall JR, Cohen M, Matsuura M, Wood PR, Yamamura I, et al. Very large telescope three micron spectra of dust-enshrouded red giants in the large magellanic cloud. Astron Astrophys 2006;447:971–89. http://dx.doi.org/10.1051/0004-6361:20054222.

[361] Tsiaras A, Rocchetto M, Waldmann IP, Tinetti G, Varley R, Morello G, et al. Detection of an atmosphere around the super-Earth 55 Cancri e. Astrophys J 2016;820:99. http://dx.doi.org/10.3847/0004-637X/820/2/99.

[362] Hawker GA, Madhusudhan N, Cabot SHC, Gandhi S. Evidence for multiple molecular species in the hot jupiter HD 209458b. Astrophys J Lett 2018;863:L11. http://dx.doi.org/10.3847/2041-8213/aac49d.

[363] Cabot SHC, Madhusudhan N, Hawker GA, Gandhi S. On the robustness of analysis techniques for molecular detections using high-resolution exoplanet spectroscopy. Mon Not R Astron Soc 2019;482(4):4422–36. http://dx.doi.org/10.1093/mnras/sty2994.

[364] Mellau GC, Makhnev VY, Gordon IE, Zobov NF, Tennyson J, Polyansky OL. An experimentally-accurate and complete room-temperature infrared HCN line-list for the HITRAN database. J Quant Spectrosc Radiat Transfer 2021;270:107666. http://dx.doi.org/10.1016/j.jqsrt.2021.107666.

[365] Barber RJ, Strange JK, Hill C, Polyansky OL, Mellau GC, Yurchenko SN, et al. ExoMol line lists – III. An improved hot rotation-vibration line list for HCN and HNC. Mon Not R Astron Soc 2013;437(2):1828–35. http://dx.doi.org/10.1093/mnras/stt2011.

[366] van Mourik T, Harris GJ, Polyansky OL, Tennyson J, Császár AG, Knowles PJ. *Ab initio* global potential, dipole, adiabatic, and relativistic correction surfaces for the HCN–HNC system. J Chem Phys 2001;115(8):3706–18. http://dx.doi.org/10.1063/1.1383586.

[367] Harris GJ, Tennyson J, Kaminsky BM, Pavlenko YV, Jones HRA. Improved HCN/HNC linelist, model atmospheres and synthetic spectra for WZ Cas. Mon Not R Astron Soc 2006;367(1):400–6. http://dx.doi.org/10.1111/j.1365-2966.2005.09960.x.

[368] Makhnev VY, Kyuberis AA, Polyansky OL, Mizus II, Tennyson J, Zobov NF. A new spectroscopically-determined potential energy surface and *ab initio* dipole moment surface for high accuracy HCN intensity calculations. J Mol Spectrosc 2018;353:40–53. http://dx.doi.org/10.1016/j.jms.2018.09.002.

[369] Mellau GC, Winnewisser BP, Winnewisser M. Near infrared emission spectrum of HCN. J Mol Spectrosc 2008;249(1):23–42. http://dx.doi.org/10.1016/j.jms.2008.01.006.

[370] Mellau GC. The ν_1 band system of HCN. J Mol Spectrosc 2011;269(1):12–20. http://dx.doi.org/10.1016/j.jms.2011.04.010.

[371] Mellau GC. Complete experimental rovibrational eigenenergies of HCN up to 6880 cm^{-1} above the ground state. J Chem Phys 2011;134(23):234303. http://dx.doi.org/10.1063/1.3598942.

[372] Mellau GC. Rovibrational eigenenergy structure of the [H,C,N] molecular system. J Chem Phys 2011;134(19):194302. http://dx.doi.org/10.1063/1.3590026.

[373] Baraban JH, Changala PB, Mellau GC, Stanton JF, Merer AJ, Field RW. Spectroscopic characterization of isomerization transition states. Science 2015;350(6266):1338–42. http://dx.doi.org/10.1126/science.aac9668.

[374] Mellau GC, Kyuberis AA, Polyansky OL, Zobov N, Field RW. Saddle point localization of molecular wavefunctions. Sci Rep 2016;6:33068. http://dx.doi.org/10.1038/srep33068.

[375] Hardy P, Richard C, Boudon V, Khan MV, Manceron L, Dridi N. High-resolution far-infrared spectroscopy and analysis of the ν_3 and ν_6 bands of chloromethane. J Quant Spectrosc Radiat Transfer 2023;311:108779. http://dx.doi.org/10.1016/j.jqsrt.2023.108779.

[376] Xiao Y, Jacob DJ, Turquety S. Atmospheric acetylene and its relationship with CO as an indicator of air mass age. J Geophys Res (Atmos) 2007;112(D12):D12305. http://dx.doi.org/10.1029/2006JD008268.

[377] Orton GS, Aitken DK, Smith C, Roche PF, Caldwell J, Snyder R. The spectra of Uranus and Neptune at 8-14 and 17-23 μm. Icarus 1987;70(1):1–12. http://dx.doi.org/10.1016/0019-1035(87)90070-4.

[378] Noll KS, Knacke RF, Tokunaga AT, Lacy JH, Beck S, Serabyn E. The abundances of ethane and acetylene in the atmospheres of Jupiter and Saturn. Icarus 1986;65(2–3):257–63. http://dx.doi.org/10.1016/0019-1035(86)90138-7.

[379] Dinelli BM, Puertas ML, Fabiano F, Adriani A, Moriconi ML, Funke B, et al. Climatology of CH_4, HCN and C_2H_2 in Titan's upper atmosphere from Cassini/VIMS observations. Icarus 2019;331:83–97. http://dx.doi.org/10.1016/j.icarus.2019.04.026.

[380] van Dishoeck EF, Grant S, Tabone B, van Gelder M, Francis L, Tychoniec L, et al. The diverse chemistry of protoplanetary disks as revealed by JWST. Faraday Discuss 2023;245:52–79. http://dx.doi.org/10.1039/D3FD00010A, arXiv:2307.11817.

[381] Jacquemart D, Lyulin OM, Solodov AM, Petrova TM, Perevalov V. New acetylene line list near 3.8 μm – Part I: C_2H_2 absorption. J Quant Spectrosc Radiat Transfer 2023;295:108413. http://dx.doi.org/10.1016/j.jqsrt.2022.108413.

[382] Jacquemart D, Lyulin OM, Solodov AM, Petrova TM, Solodov AA. New acetylene line list near 3.8-μm - Part II. J Quant Spectrosc Radiat Transfer 2023;311:108771. http://dx.doi.org/10.1016/j.jqsrt.2023.108771.

[383] Jacquemart D, Lyulin OM, Solodov AM, Petrova TM, Solodov AA. New acetylene line list near 3.8-μm - Part III - $^{12}C^{13}CH_2$ and $^{12}C_2HD$. J Quant Spectrosc Radiat Transfer 2024;316:108904. http://dx.doi.org/10.1016/j.jqsrt.2024.108904.

[384] Lyulin OM, Perevalov VI. ASD-1000: High-resolution, high-temperature acetylene spectroscopic databank. J Quant Spectrosc Radiat Transfer 2017;201:94–103. http://dx.doi.org/10.1016/j.jqsrt.2017.06.032.

[385] Lyulin OM, Perevalov VI. Global modeling of vibration-rotation spectra of the acetylene molecule. J Quant Spectrosc Radiat Transfer 2016;177:59–74. http://dx.doi.org/10.1016/j.jqsrt.2015.12.021.

[386] Lyulin O, Vasilchenko S, Mondelain D, Kassi S, Campargue A. The acetylene spectrum in the 1.45 μm window (6627-7065 cm^{-1}). J Quant Spectrosc Radiat Transfer 2020;253:107057. http://dx.doi.org/10.1016/j.jqsrt.2020.107057.

[387] Lyulin OM, Campargue A. An empirical spectroscopic database for acetylene in the regions of 5850-6341 cm^{-1} and 7000-9415 cm^{-1}. J Quant Spectrosc Radiat Transfer 2017;203:461–71. http://dx.doi.org/10.1016/j.jqsrt.2017.01.036.

[388] Lyulin OM, Kassi S, Campargue A. High sensitivity absorption spectroscopy of acetylene near 1.2 μm. J Quant Spectrosc Radiat Transfer 2021;271:107733. http://dx.doi.org/10.1016/j.jqsrt.2021.107733.

[389] Sakai J, Katayama M. Diode laser spectroscopy of acetylene: $3\nu_1 + \nu_3$ Region at 0.77 μm. J Mol Spectrosc 1992;154(2):277–87. http://dx.doi.org/10.1016/0022-2852(92)90208-6.

[390] Sakai J, Katayama M. Diode Laser Spectroscopy of Acetylene: The $2\nu_1+2\nu_3+\nu_4^1-\nu_5^1$ and $4\nu_1-\nu_5^1$ Interacting Band System. J Mol Spectrosc 1993;157(2):532–5. http://dx.doi.org/10.1006/jmsp.1993.1042.

[391] Zhan XW, Halonen L. High-resolution photoacoustic study of the $\nu_1+3\nu_3$ band system of acetylene with a titanium:Sapphire ring laser. J Mol Spectrosc 1993;160(2):464–70. http://dx.doi.org/10.1006/jmsp.1993.1193.

[392] Hu S-M, Campargue A, Wu Z-Y, Ding Y, Liu A-W, Zhu Q-S. High-resolution Fourier-transform intra-cavity laser absorption spectroscopy: application to $^{12}C_2H_2$ near 12300 cm^{-1}. Chem Phys Lett 2003;372(5):659–67. http://dx.doi.org/10.1016/S0009-2614(03)00476-7.

[393] Campargue A. The absorption spectrum of $^{12}C_2H_2$ between 12800 and 18500 cm^{-1}. Mol Phys 1997;90(5):793–806. http://dx.doi.org/10.1080/002689797172147.

[394] Lyulin OM, Liu GL, Liu AW, Tan Y, Perevalov V, Hu SM. Cavity ring-down spectroscopy of acetylene near 0.8 μm. J Quant Spectrosc Radiat Transfer 2024;328:109169. http://dx.doi.org/10.1016/j.jqsrt.2024.109169.

[395] Lyulin OM, Vasilchenko SS, Perevalov VI. High sensitivity absorption spectroscopy of acetylene near 770 nm. J Quant Spectrosc Radiat Transfer 2023;294:108402. http://dx.doi.org/10.1016/j.jqsrt.2022.108402.

[396] Malathy Devi V, Benner DC, Rinsland CP, Smith MAH, Sams RL, Blake TA, et al. Multispectrum measurements of spectral line parameters including temperature dependences of N_2- and self-broadened half-width coefficients in the region of the ν_9 band of $^{12}C_2H_6$. J Quant Spectrosc Radiat Transfer 2010;111(17):2481–504. http://dx.doi.org/10.1016/j.jqsrt.2010.07.010.

[397] Butler RAH, Sagui L, Kleiner I, Brown LR. The absorption spectrum of phosphine (PH_3) between 2.8 and 3.7 μm: Line positions, intensities, and assignments. J Mol Spectrosc 2006;238(2):178–92. http://dx.doi.org/10.1016/j.jms.2006.04.021.

[398] Nikitin AV, Champion JP, Butler RAH, Brown LR, Kleiner I. Global modeling of the lower three polyads of PH_3: Preliminary results. J Mol Spectrosc 2009;256(1):4–16. http://dx.doi.org/10.1016/j.jms.2009.01.008.

[399] Nikitin AV, Campargue A, Protasevich AE, Rey M, Sung K, Tyuterev VG. Analysis of experimental spectra of phosphine in the Tetradecad range near 2.3 μm using *ab initio* calculations. Spectrochim Acta Part A: Mol Spectrosc 2023;302:122896. http://dx.doi.org/10.1016/j.saa.2023.122896.

[400] Nikitin AV, Holka F, Tyuterev VG, Fremont J. Vibration energy levels of the PH_3, PH_2D, and PHD_2 molecules calculated from high order potential energy surface. J Chem Phys 2009;130(24):244312. http://dx.doi.org/10.1063/1.3156311.

[401] Rey M, Nikitin AV, Tyuterev VG. *Ab initio* ro-vibrational Hamiltonian in irreducible tensor formalism: a method for computing energy levels from potential energy surfaces for symmetric-top molecules. Mol Phys 2010;108(16):2121–35. http://dx.doi.org/10.1080/00268976.2010.506892.

[402] Rey M, Nikitin AV, Tyuterev VG. Complete nuclear motion Hamiltonian in the irreducible normal mode tensor operator formalism for the methane molecule. J Chem Phys 2012;136(24):244106. http://dx.doi.org/10.1063/1.4730030.

[403] Tyuterev V, Tashkun S, Rey M, Kochanov R, Nikitin A, Delahaye T. Accurate spectroscopic models for methane polyads derived from a potential energy surface using high-order contact transformations. J Phys Chem A 2013;117(50):13779–805. http://dx.doi.org/10.1021/jp408116j, PMID: 24131356.

[404] Tyuterev V, Tashkun S, Rey M, Nikitin A. High-order contact transformations of molecular Hamiltonians: general approach, fast computational algorithm and convergence of ro-vibrational polyad models. Mol Phys 2022;120(15–16):e2096140. http://dx.doi.org/10.1080/00268976.2022.2096140.

[405] Nikitin AV, Rey M, Champion JP, Tyuterev VG. Extension of the MIRS computer package for the modeling of molecular spectra: From effective to full ab initio ro-vibrational Hamiltonians in irreducible tensor form. J Quant Spectrosc Radiat Transfer 2012;113(11):1034–42. http://dx.doi.org/10.1016/j.jqsrt.2012.01.027, arXiv:1201.2418.

[406] Nikitin AV, Rey M, Tyuterev VG. High order dipole moment surfaces of PH_3 and *ab initio* intensity predictions in the Octad range. J Mol Spectrosc 2014;305:40–7. http://dx.doi.org/10.1016/j.jms.2014.09.010.

[407] Rey M, Nikitin AV, Babikov YL, Tyuterev VG. TheoReTS - An information system for theoretical spectra based on variational predictions from molecular potential energy and dipole moment surfaces. J Mol Spectrosc 2016;327:138–58. http://dx.doi.org/10.1016/j.jms.2016.04.006.

[408] Malathy Devi V, Kleiner I, Sams RL, Brown LR, Benner DC, Fletcher LN. Line positions and intensities of the phosphine (PH_3) Pentad near 4.5 μm. J Mol Spectrosc 2014;298:11–23. http://dx.doi.org/10.1016/j.jms.2014.01.013.

[409] Nikitin AV, Ivanova YA, Rey M, Tashkun SA, Toon GC, Sung K, et al. Analysis of PH_3 spectra in the Octad range 2733-3660 cm^{-1}. J Quant Spectrosc Radiat Transfer 2017;203:472–9. http://dx.doi.org/10.1016/j.jqsrt.2017.04.032.

[410] Bouanich J-P, Walrand J, Blanquet G. N_2-broadening coefficients in the ν_2 and ν_4 bands of PH_3. J Mol Spectrosc 2005;232(1):40–6. http://dx.doi.org/10.1016/j.jms.2005.02.005.

[411] Salem J, Bouanich J-P, Walrand J, Aroui H, Blanquet G. Hydrogen line broadening in the ν_2 and ν_4 bands of phosphine at low temperature. J Mol Spectrosc 2004;228(1):23–30. http://dx.doi.org/10.1016/j.jms.2004.06.015.

[412] Guest ER, Tennyson J, Yurchenko SN. Predicting the rotational dependence of line broadening using machine learning. J Mol Spectrosc 2024;401:111901. http://dx.doi.org/10.1016/j.jms.2024.111901.

[413] Tejwani GD, Fox K. Calculated self- and foreign-gas-broadened linewidths for SF_6. J Quant Spectrosc Radiat Transfer 1987;37(6):541–6. http://dx.doi.org/10.1016/0022-4073(87)90057-4.

[414] Gamache RR, Lacome N, Pierre G, Gabard T. Nitrogen broadening of SF_6 transitions in the ν_3 band. J Mol Struct 2001;599(1):279–92. http://dx.doi.org/10.1016/S0022-2860(01)00831-6.

[415] Dridi N, Boudon V, Faye M, Manceron L. Nitrogen-broadening parameters for atmospheric spectra modelling of the ν_3 band of SF_6. Molecules 2022;27(3):646. http://dx.doi.org/10.3390/MOLECULES27030646.

[416] Yu Q, Wang W, Chang J, Li H, Zhang Z, Ke P, et al. Surface-air exchanges of H_2S and SO_2 in an urban wetland in eastern China. Sci Total Environ 2024;951:175701. http://dx.doi.org/10.1016/j.scitotenv.2024.175701.

[417] Aiuppa A, Inguaggiato S, McGonigle AJS, O'Dwyer M, Oppenheimer C, Padgett MJ, et al. H_2S fluxes from Mt. Etna, Stromboli, and Vulcano (Italy) and implications for the sulfur budget at volcanoes. Geochim Cosmochim Acta 2005;69(7):1861–71. http://dx.doi.org/10.1016/j.gca.2004.09.018.

[418] Llavador Colomer F, Espinós Morató H, Mantilla Iglesias E. Estimation of hydrogen sulfide emission rates at several wastewater treatment plants through experimental concentration measurements and dispersion modeling. J Air Waste Manage Assoc 2012;62(7):758–66. http://dx.doi.org/10.1080/10962247.2012.674008.

[419] Newnham D. Private email communications. 2025.

[420] Thaddeus P, Kutner ML, Penzias AA, Wilson RW, Jefferts KB. Interstellar hydrogen sulfide. Astrophys J 1972;176:L73. http://dx.doi.org/10.1086/181023.

[421] Fu G, Welbanks L, Deming D, Inglis J, Zhang M, Lothringer J, et al. Hydrogen sulfide and metal-enriched atmosphere for a Jupiter-mass exoplanet. Nature 2024;632:752–6. http://dx.doi.org/10.1038/s41586-024-07760-y.

[422] Chubb KL, Naumenko OV, Keely S, Bartolotto S, MacDonald S, Mukhtar M, et al. MARVEL analysis of the measured high-resolution rovibrational spectra of $H_2{}^{32}S$. J Quant Spectrosc Radiat Transfer 2018;218:178–86. http://dx.doi.org/10.1016/j.jqsrt.2018.07.012.

[423] Ulenikov O, Bekhtereva E, Gromova O, Glushkov P, Scherbakov A, Horneman V-M, et al. Extended analysis of the high resolution FTIR spectra of $H_2{}^MS$ ($M = 32, 33, 34, 36$) in the region of the bending fundamental band: The ν_2 and $2\nu_2 - \nu_2$ bands: Line positions, strengths, and pressure broadening widths. J Quant Spectrosc Radiat Transfer 2018;216:76–98. http://dx.doi.org/10.1016/j.jqsrt.2018.05.009.

[424] Ulenikov ON, Bekhtereva ES, Gromova OV, Raspopova NI, Belova AS, Maul C, et al. Experimental line strengths of the $5\nu_2$ band of $H_2{}^{32}S$ in comparison with the results of "variational"' calculation and HITRAN database. J Quant Spectrosc Radiat Transfer 2020;243:106812. http://dx.doi.org/10.1016/j.jqsrt.2019.106812.

[425] Ulenikov ON, Bekhtereva ES, Gromova OV, Zhang F, Maul C, Sydow C, et al. Extended FTIR high resolution analysis of hydrogen sulfide in the region of the second hexad: Line positions and ro–vibrational energies of $H_2{}^MS$ ($M = 32, 33, 34$). J Quant Spectrosc Radiat Transfer 2020;240:106710. http://dx.doi.org/10.1016/j.jqsrt.2019.106710.

[426] Zhang F, Ulenikov O, Bekhtereva ES, Gromova OV, Gappel EV, Sydow C, et al. High-resolution ro-vibrational spectrum of H_2S in highly excited vibrational states: Re-visiting the first decade. J Quant Spectrosc Radiat Transfer 2024;319:108959. http://dx.doi.org/10.1016/j.jqsrt.2024.108959.

[427] Naumenko OV, Polovtseva ER. FTIR spectrum of hydrogen sulfide between 9995 and 10,310 cm^{-1}. J Quant Spectrosc Radiat Transfer 2019;236:106604. http://dx.doi.org/10.1016/j.jqsrt.2019.106604.

[428] Ulenikov ON, Bekhtereva ES, Gromova OV, Zhang F, Raspopova NI, Sydow C, et al. Ro–vibrational analysis of the first hexad of hydrogen sulfide: Line position and strength analysis of the $4\nu_2$ band of $H_2{}^{32}S$ and $H_2{}^{34}S$ for HITRAN applications. J Quant Spectrosc Radiat Transfer 2020;255:107236. http://dx.doi.org/10.1016/j.jqsrt.2020.107236.

[429] Millet DB, Baasandorj M, Farmer DK, Thornton JA, Baumann K, Brophy P, et al. A large and ubiquitous source of atmospheric formic acid. Atmos Chem Phys 2015;15(11):6283–304. http://dx.doi.org/10.5194/acp-15-6283-2015.

[430] Goldstein AH, Shaw SL. Isotopes of volatile organic compounds: An emerging approach for studying atmospheric budgets and chemistry. Chem Rev 2003;103:5025–48. http://dx.doi.org/10.1021/cr0206566.

[431] Western CM, Billinghurst BE. Automatic and semi-automatic assignment and fitting of spectra with PGOPHER. Phys Chem Chem Phys 2019;21(26):13986–99. http://dx.doi.org/10.1039/C8CP06493H.

[432] Zhao J, Billinghurst BE, Raston PL. Synchrotron-based pure rotational spectroscopy of $H^{13}COOH$. J Quant Spectrosc Radiat Transfer 2024;312:108819. http://dx.doi.org/10.1016/j.jqsrt.2023.108819.

[433] Weber WH, Maker PD, Johns JW, Weinberger E. Sub-Doppler laser-Stark and high-resolution Fourier transform spectroscopy of the ν_3 band of formic acid. J Mol Spectrosc 1987;121(2):243–60. http://dx.doi.org/10.1016/0022-2852(87)90048-8.

[434] Vander Auwera J. High-resolution investigation of the far-infrared spectrum of formic acid. J Mol Spectrosc 1992;155(1):136–42. http://dx.doi.org/10.1016/0022-2852(92)90553-Z.

[435] Chang CW, Chen IY, Luo PL. Absolute line strength measurements of HO_2 radical in the OO-stretching fundamental band between 1088 and 1124 cm^{-1} using time-resolved dual-comb spectroscopy. J Chem Phys 2025;162(3):034302. http://dx.doi.org/10.1063/5.0244391.

[436] Zink L, Evenson K, Matsushima F, Nelis T, Robinson R. Atomic oxygen fine-structure splittings with tunable far-infrared spectroscopy. Astrophys J 1991;371(2):L85–6. http://dx.doi.org/10.1086/186008.

[437] De Natale P, Bellini M, Goetz W, Prevedelli M, Inguscio M. Hyperfine-structure and isotope shift in the far-infrared ground-state transitions of atomic oxygen. Phys Rev A 1993;48(5):3757–60. http://dx.doi.org/10.1103/PhysRevA.48.3757.

[438] Drouin BJ, Nemchick DJ, Maestrini A. High precision measurement of the $^3P_0$-$^3P_1$ atomic oxygen fine structure splitting at 2.06 THz. J Quant Spectrosc Radiat Transfer 2025;342. http://dx.doi.org/10.1016/j.jqsrt.2025.109471.

[439] Fathallah OB, Auwera JV, Tudorie M, Boudon V, Richard C, Loroño-Gonzalez M, et al. Analysis of the rotationally-resolved 3.3 μm region of C2H4 in natural isotopic abundance. J Quant Spectrosc Radiat Transfer 2024;323:108995. http://dx.doi.org/10.1016/j.jqsrt.2024.108995, URL https://linkinghub.elsevier.com/retrieve/pii/S002240732400102X.

[440] Fathallah OB, Béguier S, Rey M, Auwera JV, Campargue A. Rovibrational assignments of the ethylene absorption spectrum near 3.3 μm based on variational calculations. J Quant Spectrosc Radiat Transfer 2025;336:109362. http://dx.doi.org/10.1016/J.JQSRT.2025.109362.

[441] Mraidi S, Manceron L, Rey M, Aroui H, Campargue A. High resolution spectroscopy and a theoretical line list of ethylene between 5000 and 9000 cm^{-1}. J Quant Spectrosc Radiat Transfer 2023;310:108734. http://dx.doi.org/10.1016/j.jqsrt.2023.108734, URL https://linkinghub.elsevier.com/retrieve/pii/S0022407323002522.

[442] Fathallah OB, Béguier S, Rey M, Manceron L, Campargue A. The ethylene absorption spectrum between 6075 and 8050 cm^{-1}: Empirical line list and rovibrational assignments. J Quant Spectrosc Radiat Transfer 2024;329:109175. http://dx.doi.org/10.1016/J.JQSRT.2024.109175.

[443] Fathallah OB, Rey M, Campargue A. Analysis of the high resolution absorption spectrum of ethylene between 5800 and 6400 cm^{-1}. J Quant Spectrosc Radiat Transfer 2024;316:108905. http://dx.doi.org/10.1016/J.JQSRT.2024.108905.

[444] Perot S, Lecomte J, Suas-David N, Rutkowski L, Rey M, Kassi S, et al. Jet-cooled ethylene cavity ring-down spectroscopy between 5880 and 6200 cm^{-1}. J Quant Spectrosc Radiat Transfer 2024;324:109065. http://dx.doi.org/10.1016/J.JQSRT.2024.109065.

[445] Wells KC, Millet DB, Hu L, Cady-Pereira KE, Xiao Y, Shephard MW, et al. Tropospheric methanol observations from space: Retrieval evaluation and constraints on the seasonality of biogenic emissions. Atmos Chem Phys 2012;12(13):5897–912. http://dx.doi.org/10.5194/ACP-12-5897-2012.

[446] Booth AS, Wölfer L, Temmink M, Calahan J, Evans L, Law CJ, et al. Ice sublimation in the dynamic HD 100453 disk reveals a rich reservoir of inherited complex organics. Astrophys J Lett 2025;986:L9. http://dx.doi.org/10.3847/2041-8213/ADC7B2.

[447] Spezzano S, Fuente A, Caselli P, Vasyunin A, Navarro-Almaida D, Rodríguez-Baras M, et al. Gas phase elemental abundances in molecular clouds (GEMS) V. Methanol in taurus. Astron Astrophys 2022;657:A10. http://dx.doi.org/10.1051/0004-6361/202141971.

[448] Villanueva GL, DiSanti MA, Mumma MJ, Xu L-H. A quantum band model of the ν_3 fundamental of methanol (CH_3OH) and its application to fluorescence spectra of comets. Astrophys J 2012;747:37. http://dx.doi.org/10.1088/0004-637X/747/1/37.

[449] Brauer CS, Sung K, Pearson JC, Brown LR, Xu LH. Empirical line intensities of methanol in the 300–500 cm^{-1} region. J Quant Spectrosc Radiat Transfer 2012;113(2):128–39. http://dx.doi.org/10.1016/J.JQSRT.2011.09.012.

[450] Lees RM, Baker JG. Torsion–Vibration–rotation interactions in methanol. I. Millimeter wave spectrum. J Chem Phys 1968;48:5299–318. http://dx.doi.org/10.1063/1.1668221.

[451] Lees RM, Xu LH, Billinghurst BE. Patterns in synchrotron near-free-rotor FIR spectra of CH_3OH and CD_3OH – The tau of methanol. J Mol Struct 2020;1209:127960. http://dx.doi.org/10.1016/J.MOLSTRUC.2020.127960.

[452] Dang-Nhu M, Blanquet G, Walrand J, Allegrini M, Moruzzi G. Intensities of the CO stretch band of CH_3OH at 9.7 μm. J Mol Spectrosc 1990;141(2):348–50. http://dx.doi.org/10.1016/0022-2852(90)90172-M.

[453] Xu LH, Fisher J, Lees RM, Shi HY, Hougen JT, Pearson JC, et al. Torsion–rotation global analysis of the first three torsional states (ν_t=0, 1, 2) and terahertz database for methanol. J Mol Spectrosc 2008;251:305–13. http://dx.doi.org/10.1016/J.JMS.2008.03.017.

[454] Gamache RR, Roller C, Lopes E, Gordon IE, Rothman LS, Polyansky OL, et al. Total internal partition sums for 166 isotopologues of 51 molecules important in planetary atmospheres: Application to HITRAN2016 and beyond. J Quant Spectrosc Radiat Transfer 2017;203:70–87. http://dx.doi.org/10.1016/j.jqsrt.2017.03.045.

[455] Moruzzi G, Winnewisser BP, Winnewisser M, Mukhopadhyay I, Strumia F. Atlas of the infrared spectrum of methanol from 0 to 1258 cm^{-1}. In: SPIE's 1995 international symposium on optical science, engineering, and instrumentation. Vol. 2558, SPIE; 1995, p. 285–92. http://dx.doi.org/10.1117/12.224249.

[456] Nickerson S, Rangwala N, Sung K, Huang X, Montiel E, Dewitt C, et al. The discovery of interstellar methanol at 25 micron. In: American astronomical society meeting abstracts #245. American astronomical society meeting abstracts, Vol. 245, 2025, p. 343.04. http://dx.doi.org/10.3847/2041-8213/adf632.

[457] Livesey NJ, Waters JW, Khosravi R, Brasseur GP, Tyndall GS, Read WG. Stratospheric CH_3CN from the UARS microwave limb sounder. Geophys Res Lett 2001;28(5):779–82. http://dx.doi.org/10.1029/2000GL012144.

[458] Kleinböhl A, Toon GC, Sen B, Blavier J-FL, Weisenstein DK, Wennberg PO. Infrared measurements of atmospheric CH_3CN. Geophys Res Lett 2005;32(23):L23807. http://dx.doi.org/10.1029/2005GL024283.

[459] Livesey NJ, Fromm MD, Waters JW, Manney GL, Santee ML, Read WG. Enhancements in lower stratospheric CH_3CN observed by the Upper Atmosphere Research Satellite Microwave Limb Sounder following boreal forest fires. J Geophys Res: Atmos 2004;109(D6):D06308. http://dx.doi.org/10.1029/2003JD004055.

[460] Simpson IJ, Akagi SK, Barletta B, Blake NJ, Choi Y, Diskin GS, et al. Boreal forest fire emissions in fresh Canadian smoke plumes: C_1-C_{10} volatile organic compounds (VOCs), CO_2, CO, NO_2, NO, HCN and CH_3CN. Atmos Chem Phys 2011;11(13):6445–63. http://dx.doi.org/10.5194/acp-11-6445-2011.

[461] Solomon PM, Jefferts KB, Penzias AA, Wilson RW. Detection of millimeter emission lines from interstellar methyl cyanide. Astrophys J 1971;168:L107–10. http://dx.doi.org/10.1086/180794.

[462] Cazaux S, Tielens AGGM, Ceccarelli C, Castets A, Wakelam V, Caux E, et al. The hot core around the low-mass protostar IRAS 16293-2422: Scoundrels rule!. Astrophys J 2003;593(1):L51–5. http://dx.doi.org/10.1086/378038.

[463] Matthews HE, Sears TJ. Detection of the $J = 1 \rightarrow 0$ transition of CH_3CN. Astrophys J 1983;267:L53–7. http://dx.doi.org/10.1086/184001.

[464] Johansson LEB, Andersson C, Elldér J, Friberg P, Hjalmarson Å, Höglund B, et al. Spectral scan of Orion A and IRC +10216 from 72 to 91 GHz. Astron Astrophys 1984;130:227–56, URL https://ui.adsabs.harvard.edu/abs/1984A&A...130..227J.

[465] Öberg KI, Guzmán VV, Furuya K, Qi C, Aikawa Y, Andrews SM, et al. The comet-like composition of a protoplanetary disk as revealed by complex cyanides. Nature 2015;520(7546):198–201. http://dx.doi.org/10.1038/nature14276, arXiv:1505.06347.

[466] Mauersberger R, Henkel C, Walmsley CM, Sage LJ, Wiklind T. Dense gas in nearby galaxies. V. Multilevel studies of CH_3CCH and CH_3CN. Astron Astrophys 1991;247:307, URL https://ui.adsabs.harvard.edu/abs/1991A&A...247..307M.

[467] Bézard B, Marten A, Paubert G. Detection of acetonitrile on Titan. In: AAS/division for planetary sciences meeting abstracts #25. AAS/division for planetary sciences meeting abstracts, Vol. 25, 1993, p. 25.09, URL https://ui.adsabs.harvard.edu/abs/1993DPS....25.2509B.

[468] Rinsland CP, Malathy Devi V, Benner DC, Blake TA, Sams RL, Brown LR, et al. Multispectrum analysis of the ν_4 band of CH_3CN: Positions, intensities, self- and N_2-broadening, and pressure-induced shifts. J Quant Spectrosc Radiat Transfer 2008;109:974–94. http://dx.doi.org/10.1016/j.jqsrt.2007.11.013.

[469] Müller HSP, Belloche A, Lewen F, Drouin BJ, Sung K, Garrod RT, et al. Toward a global model of the interactions in low-lying states of methyl cyanide: Rotational and rovibrational spectroscopy of the $v_4 = 1$ state and tentative interstellar detection of the $v_4 = v_8 = 1$ state in Sgr B2(N). J Mol Spectrosc 2021;378:111449. http://dx.doi.org/10.1016/j.jms.2021.111449, arXiv:2103.07389.

[470] Tolonen AM, Koivusaari M, Paso R, Schroderus J, Alanko S, Anttila R. The infrared spectrum of methyl cyanide between 850 and 1150 cm^{-1}: Analysis of the ν_4, ν_7, and $3\nu_8^1$ bands with resonances. J Mol Spectrosc 1993;160(2):554–65. http://dx.doi.org/10.1006/jmsp.1993.1201.

[471] Pickett HM. The fitting and prediction of vibration-rotation spectra with spin interactions. J Mol Spectrosc 1991;148(2):371–7. http://dx.doi.org/10.1016/0022-2852(91)90393-O.

[472] Drouin BJ, Müller HSP. Special issue dedicated to the pioneering work of Drs. Edward A. Cohen and Herbert M. Pickett on spectroscopy relevant to the Earth's atmosphere and astrophysics. J Mol Spectrosc 2008;251(1–2):1–3. http://dx.doi.org/10.1016/j.jms.2008.05.004.

[473] Novick SE. A beginner's guide to Pickett's SPCAT/SPFIT. J Mol Spectrosc 2016;329:1–7. http://dx.doi.org/10.1016/j.jms.2016.08.015.

[474] Drouin BJ. Practical uses of SPFIT. J Mol Spectrosc 2017;340:1–15. http://dx.doi.org/10.1016/j.jms.2017.07.009.

[475] Müller HSP, Drouin BJ, Pearson JC. Rotational spectra of isotopic species of methyl cyanide, CH_3CN, in their ground vibrational states up to terahertz frequencies. Astron Astrophys 2009;506(3):1487–99. http://dx.doi.org/10.1051/0004-6361/200912932, arXiv:0910.3111.

[476] Cazzoli G, Puzzarini C. The Lamb-dip spectrum of methylcyanide: Precise rotational transition frequencies and improved ground-state rotational parameters. J Mol Spectrosc 2006;240(2):153–63. http://dx.doi.org/10.1016/j.jms.2006.09.013.

[477] Anttila R, Horneman VM, Koivusaari M, Paso R. Ground state constants A_0, D_0^K and H_0^K of CH_3CN. J Mol Spectrosc 1993;157(1):198–207. http://dx.doi.org/10.1006/jmsp.1993.1016.

[478] Müller HSP, Brown LR, Drouin BJ, Pearson JC, Kleiner I, Sams RL, et al. Rotational spectroscopy as a tool to investigate interactions between vibrational polyads in symmetric top molecules: Low-lying states $v_8 \leq 2$ of methyl cyanide, CH_3CN. J Mol Spectrosc 2015;312:22–37. http://dx.doi.org/10.1016/j.jms.2015.02.009, arXiv:1502.06867.

[479] Koivusaari M, Horneman V-M, Anttila R. High-resolution study of the infrared band v_8 of CH_3CN. J Mol Spectrosc 1992;152(2):377–88. http://dx.doi.org/10.1016/0022-2852(92)90076-Z.

[480] Paso R, Anttila R, Koivusaari M. The infrared spectrum of methyl cyanide between 1240 and 1650 cm^{-1}: The coupled band system v_3, $v_6^{\pm1}$, and $v_7+v_8^{\pm2}$. J Mol Spectrosc 1994;165(2):470–80. http://dx.doi.org/10.1006/jmsp.1994.1150.

[481] Gadhi J, Lahrouni A, Legrand J, Demaison J. Dipole moment of CH_3CN. J de Chim Phys 1995;92:1984–92. http://dx.doi.org/10.1051/jcp/1995921984.

[482] Mito A, Sakai J, Katayama M. Laser Stark spectroscopy of the v_4 band of $CH_3C^{15}N$: Fermi resonance with $3v_8^3$. J Mol Spectrosc 1984;103(1):26–40. http://dx.doi.org/10.1016/0022-2852(84)90143-7.

[483] Mito A, Sakai J, Katayama M. Laser stark spectroscopy of the $v_4+v_8-v_8$ band of $CH_3C^{15}N$: Fermi resonances with $4v_8^4$, $4v_8^2$, and $(v_7+v_8)^2$. J Mol Spectrosc 1984;105(2):410–24. http://dx.doi.org/10.1016/0022-2852(84)90230-3.

[484] Dudaryonok AS, Lavrentieva NN, Buldyreva JV. CH_3CN self-broadening coefficients and their temperature dependences for the Earth and Titan atmospheres. Icarus 2015;250:76–82. http://dx.doi.org/10.1016/j.icarus.2014.11.020.

[485] Dudaryonok AS, Lavrentieva NN, Buldyreva JV. N_2-broadening coefficients of CH_3CN rovibrational lines and their temperature dependence for the Earth and Titan atmospheres. Icarus 2015;256:30–6. http://dx.doi.org/10.1016/j.icarus.2015.04.025.

[486] Ma Q, Boulet C. The j and k dependencies of N_2-, O_2-, and air-broadened halfwidths of the CH_3CN molecule. J Quant Spectrosc Radiat Transfer 2025;330:109265. http://dx.doi.org/10.1016/J.JQSRT.2024.109265.

[487] Simon F, Cuisset A, Elmaleh C, Hindle F, Mouret G, Rey M, et al. Unrivaled accuracy in measuring rotational transitions of greenhouse gases: THz CRDS of CF_4. Phys Chem Chem Phys 2024;26:12345–57. http://dx.doi.org/10.1039/D4CP00653D.

[488] Rey M, Chizhmakova IS, Nikitin AV, Tyuterev VG. Understanding global infrared opacity and hot bands of greenhouse molecules with low vibrational modes from first-principles calculations: The case of CF_4. Phys Chem Chem Phys 2018;20(32):21008–33. http://dx.doi.org/10.1039/C8CP03252A.

[489] Domanskaya AV, Berezkin K, Li G, Bohlius H, Kim M, Harrison JJ, et al. Spectral mosaics: Composite absorption cross sections of air-broadened tetrafluoromethane with comparable uncertainty in the measured intensity over orders of magnitude. J Quant Spectrosc Radiat Transfer 2023;311:108790. http://dx.doi.org/10.1016/j.jqsrt.2023.108790.

[490] Jolly A, Manceron L, Kwabia-Tchana F, Benilan Y, Gazeau M-C. Revised infrared bending mode intensities for diacetylene (C_4H_2): application to Titan. Planet Space Sci 2014;97:60–4. http://dx.doi.org/10.1016/j.pss.2014.03.020.

[491] Guelachvili G, Craig AM, Ramsay DA. High-resolution Fourier studies of diacetylene in the regions of the v_4 and v_5 fundamentals. J Mol Spectrosc 1984;105(1):156–92. http://dx.doi.org/10.1016/0022-2852(84)90110-3.

[492] Bizzocchi L, Melosso M, Tamassia F, Taddia M, Tonolo F, Alessandrini S, et al. An improved study of the $2v_5$ band of HC_3N and v_4 band of HC_4H with a detailed analysis of the associated resonances. J Quant Spectrosc Radiat Transfer 2026. submitted for publication.

[493] Tamassia F, Bizzocchi L, Melosso M, Martin-Drumel M-A, Pirali O, Pietropolli Charmet A, et al. Synchrotron-based far-infrared spectroscopy of HC_3N : Extended ro-vibrational analysis and new line list up to 3360 cm^{-1}. J Quant Spectrosc Radiat Transfer 2022;279:108044. http://dx.doi.org/10.1016/j.jqsrt.2021.108044.

[494] Bizzocchi L, Tamassia F, Laas J, Giuliano BM, Degli Esposti C, Dore L, et al. Rotational and high-resolution infrared spectrum of HC_3N: Global ro-vibrational analysis and improved line catalog for astrophysical observations. Astrophys J Suppl Ser 2017;233(1):11. http://dx.doi.org/10.3847/1538-4365/aa9571, arXiv:1711.08592.

[495] Yamada KMT, Moravec A, Niedenhoff M, Bürger H, Winnewisser G. The $2v_5$ overtone band of cyanoacetylene by high resolution FTIR spectroscopy. Z Naturforschung Teil A 1996;51:27–35. http://dx.doi.org/10.1515/zna-1996-1-205.

[496] Jolly A, Benilan Y, Fayt A. New infrared integrated band intensities for HC_3N and extensive line list for the v_5 and v_6 bending modes. J Mol Spectrosc 2007;242(1):46–54. http://dx.doi.org/10.1016/j.jms.2007.01.008.

[497] Jiang N, Melosso M, Tamassia F, Bizzocchi L, Dore L, Canè E, et al. High-resolution infrared spectroscopy of DC_3N in the stretching region. Front Astron Space Sci 2021;8:29. http://dx.doi.org/10.3389/fspas.2021.656295.

[498] Le Bourlot J, Pineau des Forêts G, Flower DR. The cooling of astrophysical media by H_2. Mon Not R Astron Soc 1999;305(4):802–10. http://dx.doi.org/10.1046/j.1365-8711.1999.02497.x.

[499] Dalgarno A. Introductory Lecture: The growth of molecular complexity in the Universe. Faraday Discuss 2006;133:9. http://dx.doi.org/10.1039/b605715b.

[500] Ruaud M. H_2 rovibrational excitation in protoplanetary disks and its effects on the chemistry. Astrophys J 2021;916(2):103. http://dx.doi.org/10.3847/1538-4357/abe712.

[501] Feuchtgruber H, Lellouch E, Orton G, de Graauw T, Vandenbussche B, Swinyard B, et al. The D/H ratio in the atmospheres of Uranus and Neptune from Herschel-PACS observations. Astron Astrophys 2013;551:A126. http://dx.doi.org/10.1051/0004-6361/201220857.

[502] Pierel JDR, Nixon CA, Lellouch E, Fletcher LN, Bjoraker GL, Achterberg RK, et al. D/H ratios on saturn and jupiter from cassini CIRS. Astron J 2017;154(5):178. http://dx.doi.org/10.3847/1538-3881/aa899d.

[503] Wiesemeyer H, Güsten R, Hartogh P, Okada Y, Ricken O, Stutzki J. Revisiting Jupiter2019s deuterium fraction in the rotational ground-state line of HD at high spectral resolution. Astron Astrophys 2024;688:A222. http://dx.doi.org/10.1051/0004-6361/202450115.

[504] Chubb KL, Robert S, Sousa-Silva C, Yurchenko SN, Allard NF, Boudon V, et al. Data availability and requirements relevant for the Ariel space mission and other exoplanet atmosphere applications. RAS Tech Instrum 2024;3(1):636–90. http://dx.doi.org/10.1093/rasti/rzae039.

[505] Pachucki K, Komasa J. Electric dipole rovibrational transitions in the HD molecule. Phys Rev A 2008;78:052503. http://dx.doi.org/10.1103/PhysRevA.78.052503.

[506] Stolarczyk N, Behrendt J, Jóźwiak H, Sł owiński M, J. HR, Gordon IE, et al. Hydrogen molecule spectroscopic data for astrophysical applications: HITRAN2024 update. 2025, (in preparation).

[507] Roueff E, Abgrall H, Czachorowski P, Pachucki K, Puchalski M, Komasa J. The full infrared spectrum of molecular hydrogen. Astron Astrophys 2019;630:A58. http://dx.doi.org/10.1051/0004-6361/201936249.

[508] Jóźwiak H, Cybulski H, Wcisło P. Positions and intensities of hyperfine components of all rovibrational dipole lines in the HD molecule. J Quant Spectrosc Radiat Transfer 2020;253:107171. http://dx.doi.org/10.1016/j.jqsrt.2020.107171.

[509] Jóźwiak H, Cybulski H, Wcisło P. Hyperfine components of all rovibrational quadrupole transitions in the H_2 and D_2 molecules. J Quant Spectrosc Radiat Transfer 2020;253:107186. http://dx.doi.org/10.1016/j.jqsrt.2020.107186.

[510] Komasa J, Puchalski M, Czachorowski P, Łach G, Pachucki K. Rovibrational energy levels of the hydrogen molecule through nonadiabatic perturbation theory. Phys Rev A 2019;100:032519. http://dx.doi.org/10.1103/PhysRevA.100.032519.

[511] Czachorowski P. H2SPECTRE version 7.4: Fortran source code. (Ph.D. thesis), Poland: University of Warsaw; 2022, https://www.fuw.edu.pl/~krp/codes.html, 2019.

[512] Wcisło P, Stolarczyk N, Sł owiński M, Jóźwiak H, Lisak D, Ciuryło R, et al. New beyond-Voigt line-shape profile recommended for the HITRAN database. J Quant Spectrosc Radiat Transfer 2025.

[513] Stolarczyk N, Thibault F, Cybulski H, Jóźwiak H, Kowzan G, Vispoel B, et al. Evaluation of different parameterizations of temperature dependences of the line-shape parameters based on *ab initio* calculations: Case study for the HITRAN database. J Quant Spectrosc Radiat Transfer 2020;240:106676. http://dx.doi.org/10.1016/j.jqsrt.2019.106676.

[514] Thibault F, Patkowski K, Żuchowski PS, Jóźwiak H, Ciuryło R, Wcisło P. Rovibrational line-shape parameters for H_2 in He and new H_2-He potential energy surface. J Quant Spectrosc Radiat Transfer 2017;202:308–20. http://dx.doi.org/10.1016/j.jqsrt.2017.08.014.

[515] Jóźwiak H, Thibault F, Stolarczyk N, Wcisło P. *Ab initio* line-shape calculations for the S and O branches of H_2 perturbed by He. J Quant Spectrosc Radiat Transfer 2018;219:313–22. http://dx.doi.org/10.1016/j.jqsrt.2018.08.023.

[516] Wcisło P, Thibault F, Stolarczyk N, Jóźwiak H, owiński MS, Gancewski M, et al. The first comprehensive dataset of beyond-voigt line-shape parameters from *ab initio* quantum scattering calculations for the HITRAN database: He-perturbed H_2 case study. J Quant Spectrosc Radiat Transfer 2021;260:107477. http://dx.doi.org/10.1016/j.jqsrt.2020.107477.

[517] Thibault F, Martínez RZ, Bermejo D, Wcisło P. Line-shape parameters for the first rotational lines of HD in He. Mol Astrophys 2020;19:100063. http://dx.doi.org/10.1016/j.molap.2020.100063.

[518] Stankiewicz K, Jóźwiak H, Gancewski M, Stolarczyk N, Thibault F, Wcisło P. *Ab initio* calculations of collisional line–shape parameters and generalized spectroscopic cross-sections for rovibrational dipole lines in HD perturbed by He. J Quant Spectrosc Radiat Transfer 2020;254:107194. http://dx.doi.org/10.1016/j.jqsrt.2020.107194.

[519] Stankiewicz K, Stolarczyk N, Jóźwiak H, Thibault F, Wcisło P. Accurate calculations of beyond-Voigt line-shape parameters from first principles for the He-perturbed HD rovibrational lines: A comprehensive dataset in the HITRAN DPL format. J Quant Spectrosc Radiat Transfer 2021;276:107911. http://dx.doi.org/10.1016/j.jqsrt.2021.107911.

[520] Jóźwiak H, Stolarczyk N, Stankiewicz K, Zaborowski M, Lisak D, Wójtewicz S, et al. Accurate reference spectra of HD in an H_2–He bath for planetary applications. Astron Astrophys 2024;687:A69. http://dx.doi.org/10.1051/0004-6361/202449889.

[521] Lamperti M, Rutkowski L, Ronchetti D, Gatti D, Gotti R, Cerullo G, et al. Stimulated Raman scattering metrology of molecular hydrogen. Commun Phys 2023;6(1). http://dx.doi.org/10.1038/s42005-023-01187-z.

[522] Słowiński M, Thibault F, Tan Y, Wang J, Liu A-W, Hu S-M, et al. H_2-he collisions: *Ab initio* theory meets cavity-enhanced spectra. Phys Rev A 2020;101:052705. http://dx.doi.org/10.1103/PhysRevA.101.052705.

[523] Słowiński M, Jóźwiak H, Gancewski M, Stankiewicz K, Stolarczyk N, Tan Y, et al. Collisional line-shape effects in accurate He-perturbed H_2 spectra. J Quant Spectrosc Radiat Transfer 2022;277:107951. http://dx.doi.org/10.1016/j.jqsrt.2021.107951.

[524] Cygan A, Wójtewicz S, Jóźwiak H, Kowzan G, Stolarczyk N, Bielska K, et al. Dispersive heterodyne cavity ring-down spectroscopy exploiting eigenmode frequencies for high-fidelity measurements. Sci Adv 2025;11(5). http://dx.doi.org/10.1126/sciadv.adp8556.

[525] Stolarczyk N, Wcisło P, Ciuryło R. Inhomogeneous broadening, narrowing and shift of molecular lines under frequent velocity-changing collisions. J Quant Spectrosc Radiat Transfer 2022;287:108246. http://dx.doi.org/10.1016/j.jqsrt.2022.108246.

[526] Stolarczyk N, Wcisło P, Ciuryło R. Spectral line shape in the limit of frequent velocity-changing collisions. Phys Rev A 2023;108:032810. http://dx.doi.org/10.1103/PhysRevA.108.032810.

[527] Ben-Reuven A. Spectral line shapes in gases in the Binary2010Collision approximation. Adv Chem Phys 1975;235–93. http://dx.doi.org/10.1002/9780470142523.ch5.

[528] Liu W-K. Symmetrized Liouville basis for indistinguishable particles. application to spectral linewidth. J Chem Phys 1980;72(9):4869–72. http://dx.doi.org/10.1063/1.439743.

[529] Monchick L. Quantum kinetic equations incorporating the Fano collision operator: The generalized hess method of describing line shapes. J Chem Phys 1994;101(7):5566–77. http://dx.doi.org/10.1063/1.467344.

[530] Ben-Reuven A. Resonance broadening of spectral lines. Phys Rev A 1971;4:2115–20. http://dx.doi.org/10.1103/PhysRevA.4.2115.

[531] Sandor BJ, Clancy RT, Moriarty-Schieven G, Mills FP. Sulfur chemistry in the Venus mesosphere from SO_2 and SO microwave spectra. Icarus 2010;208:49–60. http://dx.doi.org/10.1016/j.icarus.2010.02.013.

[532] de Kleer K, de Pater I, Ádámkovics M. Emission from volcanic SO gas on Io at high spectral resolution. Icarus 2019;317:104–20. http://dx.doi.org/10.1016/J.ICARUS.2018.07.012.

[533] Calmonte U, Altwegg K, Balsiger H, Berthelier JJ, Bieler A, Cessateur G, et al. Sulphur-bearing species in the coma of comet 67P/Churyumov-Gerasimenko. Mon Not R Astron Soc 2016;462:253–73. http://dx.doi.org/10.1093/mnras/stw2601.

[534] Western CM. PGOPHER: A program for simulating rotational, vibrational and electronic spectra. J Quant Spectrosc Radiat Transfer 2017;186:221–42. http://dx.doi.org/10.1016/j.jqsrt.2016.04.010.

[535] Bernath PF, Johnson RM, Liévin J. Line lists for $X^3\Sigma^-$ and $a^1\Delta$ vibration-rotation bands of SO. J Quant Spectrosc Radiat Transfer 2022;290:108317. http://dx.doi.org/10.1016/j.jqsrt.2022.108317.

[536] Bernath PF, Johnson R, Liévin J. Line lists for the $b^1\Sigma^+$-$X^3\Sigma^-$ and $a^1\Delta$-$X^3\Sigma^-$ transitions of SO. J Quant Spectrosc Radiat Transfer 2021;272:107772. http://dx.doi.org/10.1016/j.jqsrt.2021.107772.

[537] Le Roy RJ. LEVEL: A computer program for solving the radial Schrödinger equation for bound and quasibound levels. J Quant Spectrosc Radiat Transfer 2017;186:167–78. http://dx.doi.org/10.1016/j.jqsrt.2016.05.028.

[538] Herman R, Wallis RF. Influence of vibration-rotation interaction on line intensities in vibration-rotation bands of diatomic molecules. J Chem Phys 1955;23(4):637–46. http://dx.doi.org/10.1063/1.1742069.

[539] Robichaud DJ, Hodges JT, Brown LR, Lisak D, Masłowski P, Yeung LY, et al. Experimental intensity and lineshape parameters of the oxygen A-band using frequency-stabilized cavity ring-down spectroscopy. J Mol Spectrosc 2008;248(1):1–13. http://dx.doi.org/10.1016/j.jms.2007.10.010.

[540] Brady RP, Yurchenko SN, Tennyson J, Kim G-S. ExoMol line lists - LVI. The SO line list, MARVEL analysis of experimental transition data and refinement of the spectroscopic model. Mon Not R Astron Soc 2024;527(3):6675–90. http://dx.doi.org/10.1093/mnras/stad3508, arXiv:2312.09732.

[541] Bera PP, Francisco JS, Lee TJ. Identifying the molecular origin of global warming. J Phys Chem A 2009;113(45):12694–9. http://dx.doi.org/10.1021/jp905097g, PMID: 19694447.

[542] Khan MV, Jacquemart D, Guinet M, Rey M, Nikitin AV. Line list for the ν_3, $\nu_3+\nu_6-\nu_6$ and $2\nu_3-\nu_3$ bands of methyl fluoride at 9.5 μm. J Quant Spectrosc Radiat Transfer 2025;345:109525. http://dx.doi.org/10.1016/J.JQSRT.2025.109525.

[543] Papoušek D, Pracna P, Winnewisser M, Klee S, Demaison J. Simultaneous rovibrational analysis of the ν_2, ν_3, ν_5, and ν_6 bands of H_3 ^{12}CF. J Mol Spectrosc 1999;196(2):319–23. http://dx.doi.org/10.1006/jmsp.1999.7875.

[544] Papoušek D, Tesař R, Pracna P, Kauppinen J, Belov S, Tretyakov M. High-resolution Fourier transform and submillimeter-wave spectroscopy of the ν_3 and $2\nu_3\leftarrow\nu_3$ bands of $^{13}CH_3F$. J Mol Spectrosc 1991;146(1):127–34. http://dx.doi.org/10.1016/0022-2852(91)90376-L.

[545] Ramchani AB, Jacquemart D, Soulard P, Guinet M. Measurements and modeling of N_2-broadening coefficients for the ν_6 band of CH_3F, comparison with CH_3Cl and CH_3Br molecules. J Quant Spectrosc Radiat Transfer 2017;203:480–9. http://dx.doi.org/10.1016/j.jqsrt.2017.06.013, HITRAN2016 Special Issue.

[546] Lepère M, Blanquet G, Walrand J, Bouanich J-P. K-dependence of broadening coefficients for CH_3F–N_2 and for other systems involving a symmetric top molecule. J Mol Struct 2000;517–518:493–502. http://dx.doi.org/10.1016/S0022-2860(99)00271-9.

[547] Lepère M, Blanquet G, Walrand J, Bouanich J-P. Analysis of O_2-broadening of $^{12}CH_3F$ lines in the 6.8-μm spectral region. J Mol Spectrosc 1998;192(1):17–24. http://dx.doi.org/10.1006/jmsp.1998.7654.

[548] Lerot C, Blanquet G, Bouanich J-P, Walrand J, Lepère M. N_2- and O_2-broadening coefficients in the ν_2 and ν_5 bands of $^{12}CH_3F$ at 183 and 298K. J Mol Spectrosc 2006;235(2):196–205. http://dx.doi.org/10.1016/j.jms.2005.11.004.

[549] Chin M, Davis DD. Global sources and sinks of OCS and CS_2 and their distributions. Glob Biogeochem Cycles 1993;7(2):321–37. http://dx.doi.org/10.1029/93GB00568.

[550] Atreya SK, Edgington SG, Trafton LM, Caldwell JJ, Noll KS, Weaver HA. Abundances of ammonia and carbon disulfide in the Jovian stratosphere following the impact of comet Shoemaker-Levy 9. Geophys Res Lett 1995;22(12):1625–8. http://dx.doi.org/10.1029/95GL01718.

[551] Karlovets E, Gordon I, Hashemi R, Kochanov R, Hargreaves R, Rothman L. Addition of the line list for carbon disulfide to the HITRAN database: line positions, intensities, and half-widths of the $^{12}C^{32}S_2$, $^{32}S^{12}C^{34}S$, $^{32}S^{12}C^{33}S$, and $^{13}C^{32}S_2$ isotopologues. J Quant Spectrosc Radiat Transfer 2021;258:107275. http://dx.doi.org/10.1016/j.jqsrt.2020.107275.

[552] Holmberg M, Madhusudhan N. Possible Hycean conditions in the sub-Neptune TOI-270 d. Astron Astrophys 2024;683:L2. http://dx.doi.org/10.1051/0004-6361/202348238.

[553] Seager S, Bains W, Hu R. Biosignature gases in H_2–dominated atmospheres on rocky exoplanets. Astrophys J 2013;777:95. http://dx.doi.org/10.1088/0004-637X/777/2/95.

[554] Tashkun SA. Global modeling of the $^{12}C^{32}S_2$ line positions within the framework of the non-polyad model of effective Hamiltonian. J Quant Spectrosc Radiat Transfer 2022;279:108072. http://dx.doi.org/10.1016/j.jqsrt.2022.108072.

[555] Huang X, Gordon IE, Tashkun SA, Schwenke DW, Lee TJ. Accurate infrared line lists for 20 isotopologues of CS_2 at room temperature. Astrophys J Suppl Ser 2024;272(1):17. http://dx.doi.org/10.3847/1538-4365/ad3809.

[556] Misago F, Lepère M, Walrand J, Bouanich JP, Blanquet G. Low and room temperature measurements and calculations of O_2-broadening coefficients in the ν_3 band of $^{12}C^{32}S_2$. J Mol Spectrosc 2007;241(1):61–6. http://dx.doi.org/10.1016/j.jms.2006.10.017.

[557] Misago F, Lepère M, Bouanich JP, Blanquet G. Self-broadening coefficients in the ν_3- ν_1 band of CS_2. J Mol Spectrosc 2009;254(1):16–9. http://dx.doi.org/10.1016/j.jms.2008.12.004.

[558] Kongolo Tshikala P, Blanquet G, Lepère M. Study of the effect of perturber mass on collisional broadening coefficients of lines in the ν_3 band of CS_2. J Mol Spectrosc 2012;275(1):48–52. http://dx.doi.org/10.1016/j.jms.2012.04.010.

[559] Kongolo Tshikala P, Populaire JC, Blanquet G, Lepère M. He-, Ne- and Kr-broadening coefficients of lines in the fundamental ν_3 band of $^{12}C^{32}S_2$ at low temperature. J Mol Spectrosc 2014;298:24–30. http://dx.doi.org/10.1016/j.jms.2014.01.008.

[560] Person WB, Hall LC. Absolute infrared intensities of CS_2 fundamentals in gas and liquid phases. An interpretation of the bond moments of CO_2 and CS_2. Spectrochim Acta 1964;20:771–9. http://dx.doi.org/10.1016/0371-1951(64)80076-X.

[561] Drossart P, Maillard JP, Caldwell J, Kim SJ, Watson JKG, Majewski WA, et al. Detection of H_3^+ on jupiter. Nature 1989;340:539–41. http://dx.doi.org/10.1038/340539a0.

[562] Geballe TR, Jagod MF, Oka T. Detection of H_3^+ infrared-emission lines in Saturn. Astrophys J 1993;408:L109–12. http://dx.doi.org/10.1086/186843.

[563] Trafton LM, Geballe TR, Miller S, Tennyson J, Ballester GE. Detection of H_3^+ from Uranus. Astrophys J 1993;405:761–6. http://dx.doi.org/10.1086/172404.

[564] Melin H, Moore L, Fletcher LN, Hammel HB, O'Donoghue J, Stallard TS, et al. Discovery of H_3^+ and infrared aurorae at Neptune with JWST. Nat Astron 2025;9:666–71. http://dx.doi.org/10.1038/s41550-025-02507-9.

[565] Miller S, Geballe TR, Stallard T, Tennyson J. Thirty years of H_3^+ astronomy. Rev Modern Phys 2020;92:035003. http://dx.doi.org/10.1103/RevModPhys.92.035003.

[566] Miller S, Tennyson J. Calculated rotational and ro-vibrational transitions in the spectrum of H_3^+. Astrophys J 1988;335:486–90. http://dx.doi.org/10.1086/166941.

[567] Neale L, Miller S, Tennyson J. Spectroscopic properties of the H_3^+ molecule: a new calculated linelist. Astrophys J 1996;464:516–20. http://dx.doi.org/10.1086/177341.

[568] Mizus II, Alijah A, Zobov NF, Kyuberis AA, Yurchenko SN, Tennyson J, et al. ExoMol molecular line lists XX: a comprehensive line list for H_3^+. Mon Not R Astron Soc 2017;468:1717–25. http://dx.doi.org/10.1093/mnras/stx502.

[569] Pavanello M, Adamowicz L, Alijah A, Zobov NF, Mizus II, Polyansky OL, et al. Calibration-quality adiabatic potential energy surfaces for H_3^+ and its isotopologues. J Chem Phys 2012;136:184303. http://dx.doi.org/10.1063/1.4711756.

[570] Petrignani A, Berg M, Wolf A, Mizus II, Polyansky OL, Tennyson J, et al. Visible intensities of the triatomic hydrogen ion from experiment and theory. J Chem Phys 2014;141:241104. http://dx.doi.org/10.1063/1.4904440.

[571] Asvany O, Hugo E, Schlemmer S, Muller F, Kuhnemann F, Schiller S, et al. Overtone spectroscopy of H_2D^+ and D_2H^+ using laser induced reactions. J Chem Phys 2007;127:154317. http://dx.doi.org/10.1063/1.2794331.

[572] Furtenbacher T, Szidarovszky T, Mátyus E, Fábri C, Császár AG. Analysis of the rotational-vibrational states of the molecular ions H_3^+. J Chem Theory Comput 2013;9:5471–8. http://dx.doi.org/10.1021/ct4004355.

[573] Bowesman CA, Mizus II, Zobov NF, Polyansky OL, Sarka J, Poirier B, et al. ExoMol line lists - L: High-resolution line lists of H_3^+, H_2D^+, D_2H^+ and D_3^+. Mon Not R Astron Soc 2023;519:6333–48. http://dx.doi.org/10.1093/mnras/stad050.

[574] Hougen JT. Classification of rotational energy levels for symmetric-top molecules. J Chem Phys 1962;37:1433–41. http://dx.doi.org/10.1063/1.1733301.

[575] Watson JKG. Higher-order vibration-rotation energies of the X_3 molecule. J Mol Spectrosc 1984;103:350–63. http://dx.doi.org/10.1016/0022-2852(84)90062-6.

[576] Gans B, Boyé-Péronne S, Broquier M, Delsaut M, Douin S, Fellows CE, et al. Photolysis of methane revisited at 121.6 nm and at 118.2 nm: quantum yields of the primary products, measured by mass spectrometry. Phys Chem Chem Phys 2011;13:8140–52. http://dx.doi.org/10.1039/C0CP02627A.

[577] Herbst E. The chemistry of interstellar space. Chem Soc Rev 2001;30:168–76. http://dx.doi.org/10.1039/A909040A.

[578] Bézard B, Feuchtgruber H, Moses JI, Encrenaz T. Detection of methyl radicals (CH_3) on Saturn. Astron Astrophys 1998;334:L41–4, URL https://ui.adsabs.harvard.edu/abs/1998A&A...334L..41B.

[579] Fletcher LN, King ORT, Harkett J, Hammel HB, Roman MT, Melin H, et al. Saturn's atmosphere in northern summer revealed by JWST/MIRI. J Geophys Res: Planets 2023;128(9). http://dx.doi.org/10.1029/2023JE007924, e2023JE007924.

[580] Bézard B, Romani PN, Feuchtgruber H, Encrenaz T. Detection of the methyl radical on neptune*. Astrophys J 1999;515(2):868. http://dx.doi.org/10.1086/307070.

[581] Feuchtgruber H, Helmich FP, van Dishoeck EF, Wright CM. Detection of interstellar CH_3*. Astrophys J 2000;535(2):L111. http://dx.doi.org/10.1086/312711.

[582] van den Bekerom D, Richards C, Huang E, Adamovich I, Frank JH. 2D imaging of absolute methyl concentrations in nanosecond pulsed plasma by photo-fragmentation laser-induced fluorescence. Plasma Sources Sci Technol 2022;31(9):095018. http://dx.doi.org/10.1088/1361-6595/ac8f6c.

[583] Herzberg G. The bakerian lecture. The spectra and structures of free methyl and free methylene. Proc R Soc Lond Ser A 1961;262(1310):291–317. http://dx.doi.org/10.1098/rspa.1961.0120.

[584] Adam AY, Yachmenev A, Yurchenko SN, Jensen P. Variationally computed IR line list for the methyl radical CH_3. J Phys Chem A 2019;123(22):4755–63. http://dx.doi.org/10.1021/acs.jpca.9b02919.

[585] Egorov O, Rey M, Nikitin AV, Viglaska D. New theoretical infrared line list for the methyl radical with accurate vibrational band origins from high-level ab initio calculations. J Phys Chem A 2022;126(37):6429–42. http://dx.doi.org/10.1021/acs.jpca.2c04822.

[586] Rey M, Viglaska D, Egorov O, Nikitin AV. A numerical-tensorial "hybrid" nuclear motion Hamiltonian and dipole moment operator for spectra calculation of polyatomic nonrigid molecules. J Chem Phys 2023;159(11):114103. http://dx.doi.org/10.1063/5.0166657.

[587] Hirota E, Yamada C. Intramolecular motions and molecular structure of the CH_3 radical. J Mol Spectrosc 1982;96(1):175–82. http://dx.doi.org/10.1016/0022-2852(82)90223-5.

[588] Yamada C, Hirota E, Kawaguchi K. Diode laser study of the ν_2 band of the methyl radical. J Chem Phys 1981;75(11):5256–64. http://dx.doi.org/10.1063/1.441991.

[589] Robinson GN, Zahniser MS, Freedman A, David D. Nelson J. Pressure-broadened linewidth measurements in the ν_2 band of the CH_3 radical. J Mol Spectrosc 1996;176:337–41. http://dx.doi.org/10.1006/jmsp.1996.0095.

[590] A'Hearn MF, Schleicher DG, Feldman PD. The discovery of S_2 in comet IRAS-Araki-Alcock 1983d. Astrophys J 1983;274:L99–103. http://dx.doi.org/10.1086/184158.

[591] Laffont C, Boice D, Moreels G, Clairemidi J, Rousselot P, Andernach H. Tentative identification of S_2 in the IUE spectra of comet Hyakutake (C/1996 B2). Geophys Res Lett 1998;25(14):2749–52. http://dx.doi.org/10.1029/98GL01953.

[592] Spencer JR, Jessup KL, McGrath MA, Ballester GE, Yelle R. Discovery of gaseous S_2 in io's pele plume. Science 2000;288:1208–10. http://dx.doi.org/10.1126/science.288.5469.1208.

[593] Kasting JF, Zahnle KJ, Pinto JP, Young AT. Sulfur, ultraviolet radiation, and the early evolution of life. Orig Life Evol Biosph 1989;19:95–108. http://dx.doi.org/10.1007/BF01808144.

[594] Shingledecker CN, Lamberts T, Laas JC, Vasyunin A, Herbst E, Kästner J, et al. Efficient production of s_8 in interstellar ices: The effects of cosmic-ray-driven radiation chemistry and nondiffusive bulk reactions. Astrophys J 2020;888(1):52. http://dx.doi.org/10.3847/1538-4357/ab5360, arXiv:1911.01239.

[595] Gomez FM, Hargreaves RJ, Gordon IE. A HITRAN-formatted UV line list of S_2-containing transitions involving $X\,^3\Sigma_g^-$, $B\,^3\Sigma_u^-$, and $B''\,^3\Pi_u$ electronic states. Mon Not R Astron Soc 2024;528(2):3823–32. http://dx.doi.org/10.1093/mnras/stae246.

[596] Stark G, Herde H, Lyons J, Heays A, de Oliveira N, Nave G, et al. Fourier-transform-spectroscopic photoabsorption cross sections and oscillator strengths for the $S_2B^3\Sigma_u^-$-$X^3\Sigma_g^-$ system. J Chem Phys 2018;148:244302. http://dx.doi.org/10.1063/1.5029929.

[597] Lewis B, Gibson S, Stark G, Heays A. Predissociation of the $B^3\Sigma_u^-$ state of S_2: A coupled-channel model. J Chem Phys 2018;148(24):244303. http://dx.doi.org/10.1063/1.5029930.

[598] Green ME, Western CM. A deperturbation analysis of the $B^3\Sigma_u^-$ (v'=0-6) and the $B''^3\Pi_u$ (v'=2-12) states of S_2. J Chem Phys 1996;104. http://dx.doi.org/10.1063/1.470810.

[599] Wheeler MD, Newman SM, Orr-Ewing AJ. Predissociation of the $b^3\ \Sigma_u^-$ state of S_2. J Chem Phys 1998;108:6594–605. http://dx.doi.org/10.1063/1.476074.

[600] Green M, Western C. Upper vibrational states of the $B''^3\Pi_u$ state of $^{32}S_2$. J Chem Soc Faraday Trans 1997;93(3):365–72. http://dx.doi.org/10.1039/A606591K.

[601] Tuttle S, Matsumura M, Ardila DR, Chen P, Davis M, Ertley C, et al. Ultraviolet technology to prepare for the habitable worlds observatory. 2024, http://dx.doi.org/10.48550/arXiv.2408.07242, arXiv e-prints arXiv:2408.07242.

[602] Tsai S-M, Lee EKH, Powell D, Gao P, Zhang X, Moses J, et al. Direct evidence of photochemistry in an exoplanet atmosphere. 2022, http://dx.doi.org/10.1038/s41586-023-05902-2, arXiv e-prints arXiv:2211.10490.

[603] Fu D, Boone CD, Bernath PF, Weisenstein DK, Rinsland CP, Manney GL, et al. First global observations of atmospheric COClF from the Atmospheric Chemistry Experiment mission. J Quant Spectrosc Radiat Transfer 2009;110:974–85. http://dx.doi.org/10.1016/J.JQSRT.2009.02.018.

[604] Perrin A, Flaud J-M, Bürger H, Pawelke G, Sander S, Willner H. First High-Resolution Analysis of the Six Fundamental Bands ν_1, ν_2,ν_3, ν_4, ν_5, and ν_4, of $COF^{35}Cl$ in the 340 to 2000-cm^{-1} Region. J Mol Spectrosc 2001;209:122–32. http://dx.doi.org/10.1006/jmsp.2001.8415.

[605] Perrin A, Demaison J, Toon G. The ν_1, ν_2, and ν_3 bands of carbonyl chlorofluoride (COFCl) at 5.3, 9.1, and 13.1μm: position and intensity parameters and their use for atmospheric studies. J Quant Spectrosc Radiat Transfer 2011;112:1266–79. http://dx.doi.org/10.1016/j.jqsrt.2011.01.003.

[606] Demaison J, Perrin A, Bürger H. Ab initio anharmonic force field and equilibrium structure of carbonyl chlorofluoride. J Mol Spectrosc 2003;221:47–56. http://dx.doi.org/10.1016/S0022-2852(03)00169-3.

[607] Spataro F, Ianniello A, Esposito G, Allegrini I, Zhu T, Hu M. Occurrence of atmospheric nitrous acid in the urban area of Beijing (China). Sci Total Environ 2013;447:210–24. http://dx.doi.org/10.1016/J.SCITOTENV.2012.12.065.

[608] Kleffmann J, Gavriloaiei T, Hofzumahaus A, Holland F, Koppmann R, Rupp L, et al. Daytime formation of nitrous acid: A major source of OH radicals in a forest. Geophys Res Lett 2005;32. http://dx.doi.org/10.1029/2005GL022524.

[609] Coutens A, Ligterink NFW, Loison JC, Wakelam V, Calcutt H, Drozdovskaya MN, et al. The ALMA-PILS survey: First detection of nitrous acid (HONO) in the interstellar medium. Astron Astrophys 2019;623:L13. http://dx.doi.org/10.1051/0004-6361/201935040, arXiv:1903.03378.

[610] Betnga WT, Tchana FK, Perrin A, Manceron L, Auwera JV, Hindle F, et al. New line intensities for the far infrared bands of the Trans- and Cis-conformer of nitrous acid (HONO), new determination of the Trans-Cis conformer barrier and its impact on the astrophysical detection of nitrous acid in protostellar clouds. J Quant Spectrosc Radiat Transfer 2023;310:108727. http://dx.doi.org/10.1016/j.jqsrt.2023.108727.

[611] Dehayem-Kamadjeu A, Pirali O, Orphal J, Kleiner I, Flaud PM. The far-infrared rotational spectrum of nitrous acid (HONO) and its deuterated species (DONO) studied by high-resolution Fourier-transform spectroscopy. J Mol Spectrosc 2005;234(1):182–9. http://dx.doi.org/10.1016/j.jms.2005.09.006.

[612] Allegrini M, Johns JWC, McKellar ARW, Pinson P. Stark spectroscopy with the CO laser: The ν_2 fundamental bands of trans- and cis-nitrous acid, HNO_2, in the 6-μm region. J Mol Spectrosc 1980;79(2):446–54. http://dx.doi.org/10.1016/0022-2852(80)90225-8.

[613] Crevoisier C, Clerbaux C, Guidard V, Phulpin T, Armante R, Barret B, et al. Towards IASI-New generation (IASI-NG): Impact of improved spectral resolution and radiometric noise on the retrieval of thermodynamic, chemistry and climate variables. Atmos Meas Tech 2014;7:4367–85. http://dx.doi.org/10.5194/AMT-7-4367-2014.

[614] Betnga WT, Perrin A, Manceron L, Vander Auwera J, Hindle F, Cuisset A, et al. New line list for the ν_4 bands of the trans (790.117 cm^{-1}) and cis (851.943 cm^{-1}) conformers of nitrous acid (HONO): Accurate positions and absolute intensities. J Quant Spectrosc Radiat Transfer 2024;325:109082. http://dx.doi.org/10.1016/j.jqsrt.2024.109082.

[615] Perrin A, Miljanic S, Dehayem-Kamadjeu A, Chélin P, Orphal J, Demaison J. The 14-22 μm absorption spectrum of nitrous acid studied by high-resolution Fourier-transform spectroscopy: New analysis of the ν_5 and ν_6 interacting bands of trans-HONO and first analysis of the ν_6 band of cis-HONO. J Mol Spectrosc 2007;245(2):100–8. http://dx.doi.org/10.1016/j.jms.2007.07.007.

[616] Lee B, Wood E, Wormhoudt J, Shorter J, Herndon S, Zahniser M, et al. Effective line strengths of trans-nitrous acid near 1275 cm^{-1} and cis-nitrous acid at 1660 cm^{-1}. J Quant Spectrosc Radiat Transfer 2012;113:1905–12. http://dx.doi.org/10.1016/j.jqsrt.2012.06.004.

[617] Finlayson-Pitts BJ, Ezell MJ, Pitts JN. Formation of chemically active chlorine compounds by reactions of atmospheric NaCl particles with gaseous N_2O_5 and $ClONO_2$. Nat 1989;337:241–4. http://dx.doi.org/10.1038/337241a0.

[618] Behnke W, Scheer V, Zetzsch C. Formation of $ClNO_2$ and HNO_3 in the presence of N_2O_5 and wet pure NaCl- and wet mixed $NaCl/Na_2SO_4$- aerosol. J Aerosol Sci 1993;24:S115–6. http://dx.doi.org/10.1016/0021-8502(93)90150-8.

[619] Leu M-T. Heterogeneous reactions of N_2O_5 with H_2O and HCl on ice surfaces: Implications for Antarctic ozone depletion. Geophys Res Lett 1988;15:851–4. http://dx.doi.org/10.1029/GL015I008P00851.

[620] Tolbert MA, Rossi MJ, Golden DM. Antarctic ozone depletion chemistry: Reactions of N_2O_5 with H_2O and HCl on ice surfaces. Science 1988;240:1018–21. http://dx.doi.org/10.1126/SCIENCE.240.4855.1018.

[621] Osthoff HD, Roberts JM, Ravishankara AR, Williams EJ, Lerner BM, Sommariva R, et al. High levels of nitryl chloride in the polluted subtropical marine boundary layer. Nat Geosci 2008;1:324–8. http://dx.doi.org/10.1038/ngeo177.

[622] Yun H, Wang W, Wang T, Xia M, Yu C, Wang Z, et al. Nitrate formation from heterogeneous uptake of dinitrogen pentoxide during a severe winter haze in southern China. Atmos Chem Phys 2018;18:17515–27. http://dx.doi.org/10.5194/ACP-18-17515-2018.

[623] Wong JP, Carslaw N, Zhao R, Zhou S, Abbatt JP. Observations and impacts of bleach washing on indoor chlorine chemistry. Indoor Air 2017;27:1082–90. http://dx.doi.org/10.1111/INA.12402.

[624] Mattila JM, Lakey PS, Shiraiwa M, Wang C, Abbatt JP, Arata C, et al. Multiphase chemistry controls inorganic chlorinated and nitrogenated compounds in indoor air during bleach cleaning. Environ Sci Technol 2020;54:1730–9. http://dx.doi.org/10.1021/ACS.EST.9B05767.

[625] Flaud JM, Anantharajah A, Tchana FK, Manceron L, Orphal J, Wagner G, et al. High-resolution analysis of the 12.6 μm spectral region of the nitryl chloride $ClNO_2$ molecule. J Quant Spectrosc Radiat Transfer 2019;224:217–21. http://dx.doi.org/10.1016/J.JQSRT.2018.11.020.

[626] Ridolfi M, Bianco SD, Di Roma A, Castelli E, Belotti C, Dandini P, et al. FORUM Earth explorer 9: Characteristics of level 2 products and synergies with IASI-NG. Remote Sens 2020;12:1496. http://dx.doi.org/10.3390/rs12091496.

[627] Orphal J, Morillon-Chapey M, Klee S, Mellau GC, Winnewisser M. The far-infrared spectrum of $ClNO_2$ studied by high-resolution Fourier-transform spectroscopy. J Mol Spectrosc 1998;190:101–6. http://dx.doi.org/10.1006/jmsp.1998.7570.

[628] Anantharajah A, Tchana FK, Manceron L, Orphal J, Flaud JM. New analysis of line positions of the ν_3 bands of $^{35}ClNO_2$ and $^{37}ClNO_2$ around 370 cm^{-1}. J Quant Spectrosc Radiat Transfer 2020;253:107078. http://dx.doi.org/10.1016/j.jqsrt.2020.107078.

[629] Ngo N, Lisak D, Tran H, Hartmann J-M. An isolated line-shape model to go beyond the Voigt profile in spectroscopic databases and radiative transfer codes. J Quant Spectrosc Radiat Transfer 2013;129:89–100. http://dx.doi.org/10.1016/j.jqsrt.2013.05.034.

[630] Loos J, Birk M, Wagner G. New multispectrum fitting software used at DLR for analysis of laboratory Fourier-transform molecular spectra. 2014, http://dx.doi.org/10.5281/zenodo.11156, The 13th Biennial HITRAN Conference (HITRAN13), Harvard-Smithsonian Center for Astrophysics, Cambridge, MA, USA.

[631] Adkins EM. MATS: Multi-spectrum analysis tool for spectroscopy. 2020, http://dx.doi.org/10.18434/M32200.

[632] Kochanov RV, Gordon IE, Rothman LS, Shine KP, Sharpe SW, Johnson TJ, et al. Infrared absorption cross-sections in HITRAN2016 and beyond: Expansion for climate, environment, and atmospheric applications. J Quant Spectrosc Radiat Transfer 2019;230:172–221. http://dx.doi.org/10.1016/j.jqsrt.2019.04.001.

[633] Johnson TJ, Profeta LTM, Sams RL, Griffith DWT, Yokelson RL. An infrared spectral database for detection of gases emitted by biomass burning. Vib Spectrosc 2010;53(1):97–102. http://dx.doi.org/10.1016/j.vibspec.2010.02.010.

[634] Hodnebrog Ø, Etminan M, Fuglestvedt JS, Marston G, Myhre G, Nielsen CJ, et al. Global warming potentials and radiative efficiencies of halocarbons and related compounds: A comprehensive review. Rev Geophys 2013;51(2):300–78. http://dx.doi.org/10.1002/rog.20013.

[635] Hargreaves RJ, et al. Overview of the absorption cross-section additions for HITRAN2024. J Quant Spectrosc Radiat Transfer 2025. in preparation.

[636] Harrison JJ. New infrared absorption cross sections of difluoromethane (HFC-32) for atmospheric remote sensing. J Quant Spectrosc Radiat Transfer 2021;270:107639. http://dx.doi.org/10.1016/j.jqsrt.2021.107639.

[637] Harrison JJ. New infrared absorption cross sections of pentafluoroethane (HFC-125) for atmospheric remote sensing. J Quant Spectrosc Radiat Transfer 2025;346:109600. http://dx.doi.org/10.1016/J.JQSRT.2025.109600.

[638] Godin PJ, Johnson H, Piunno R, Le Bris K, Strong K. Conformational analysis and global warming potentials of 1,1,1,2,3,3-hexafluoropropane and 1,1,2,2,3-pentafluoropropane from absorption spectroscopy. J Quant Spectrosc Radiat Transfer 2019;225:337–50. http://dx.doi.org/10.1016/j.jqsrt.2019.01.003.

[639] Le Bris K, DeZeeuw J, Godin PJ, Strong K. Radiative efficiency and global warming potential of the hydrofluoroether HFE-356mec3 ($CH_3OCF_2CHFCF_3$) from experimental and theoretical infrared absorption cross-sections. J Mol Spectrosc 2020;367:111241. http://dx.doi.org/10.1016/j.jms.2019.111241.

[640] Le Bris K, Yeo MacDougall C, Godin PJ, Strong K. Absorption cross-sections, radiative efficiency and global warming potential of HFE-347pcf2 (1,1,2,2-tetrafluoroethyl 2,2,2-trifluoroethyl ether). J Mol Spectrosc 2021;379:111494. http://dx.doi.org/10.1016/j.jms.2021.111494.

[641] Ishtiak MO, Colebatch O, Le Bris K, Godin PJ, Strong K. Measurements of infrared absorption cross-sections for 1H-perfluorohexane and perfluoro-2-methyl-2-pentene from 300 to 340 K. Journal of Quantitative Spectroscopy and Radiative Transfer 2025;342:109469. http://dx.doi.org/10.1016/J.JQSRT.2025.109469.

[642] Ishtiak MO, Colebatch O, Le Bris K, Godin PJ, Strong K. Measurements of infrared absorption cross-sections for n-C_3F_8, c-C_4F_8, n-C_4F_{10}, and n-C_5F_{12} from 298 to 350 K. J Mol Spectrosc 2024;401:111900. http://dx.doi.org/10.1016/j.jms.2024.111900.

[643] Ishtiak MO, Colebatch O, Le Bris K, Godin PJ, Strong K. Measurements of perfluoro-n-hexane and perfluoro-2-methylpentane infrared absorption cross-sections from 298 to 350 K. J Mol Spectrosc 2023;397:111835. http://dx.doi.org/10.1016/j.jms.2023.111835.

[644] Ishtiak MO, Colebatch O, Le Bris K, Godin PJ, Strong K. Measurements of perfluoro-n-heptane and perfluoro-n-octane absorption cross-sections from 300 to 350 K. J Mol Spectrosc 2023;392:111747. http://dx.doi.org/10.1016/j.jms.2023.111747.

[645] Espinosa S, Asensio M, Antiñolo M, Albaladejo J, Jiménez E. Atmospheric chemistry of $CF_3CHFCF_2OCH_3$ (HFE-356mec3) and $CHF_2CHFOCF_3$ (HFE-236ea1) initiated by OH and Cl and their contribution to global warming. Environ Sci Pollut Res Int 2024;31:50347–58. http://dx.doi.org/10.1007/s11356-024-34374-8.

[646] Blázquez S, Papadimitriou VC, Albaladejo J, Jiménez E. Atmospheric reaction of $CH_2=CHCH_2OCF_2CHF_2$ with OH radicals and Cl atoms, UV and IR absorption cross sections, and global warming potential. Environ Sci Pollut Res Int 2024;31:66827–41. http://dx.doi.org/10.1007/s11356-024-35536-4.

[647] Blázquez S, Espinosa S, Antiñolo M, Albaladejo J, Jiménez E. Kinetics of $CF_3CH_2OCH_3$ (HFE-263fb2), $CHF_2CF_2CH_2OCH_3$ (HFE-374pcf), and $CF_3CF_2CH_2OCH_3$ (HFE-365mcf3) with OH radicals, IR absorption cross sections, and global warming potentials. Phys Chem Chem Phys 2022;24:14354–64. http://dx.doi.org/10.1039/D2CP00160H.

[648] Cuisset A, Coeur C, Mouret G, Ahmad W, Tomas A, Pirali O. Infrared spectroscopy of methoxyphenols involved as atmospheric secondary organic aerosol precursors: Gas-phase vibrational cross-sections. J Quant Spectrosc Radiat Transfer 2016;179:51–8. http://dx.doi.org/10.1016/j.jqsrt.2016.03.020.

[649] Jacquemart D, Tremblay B, Soulard P, Krim L, Guillemin JC, Coustenis A, Encrenaz T, Lavvas P, Greathouse TK, Giles R. Near- and mid-infrared spectroscopy of isobutyronitrile and cyanopropyne: absorption cross-sections for quantitative detection in astrophysical objects. Journal of Quantitative Spectroscopy and Radiative Transfer 2025;341:109466. http://dx.doi.org/10.1016/J.JQSRT.2025.109466.

[650] Sulbaek Andersen MP, Frausig M, Nielsen OJ. Atmospheric chemistry of $CCl_2FCH_2CF_3$ (HCFC-234fb): Kinetics and mechanism of reactions with Cl atoms and OH radicals. Int J Chem Kinet 2023;55(2):63–71. http://dx.doi.org/10.1002/kin.21615.

[651] Sulbaek Andersen MP, Borcher JE, Nielsen OJ. Atmospheric chemistry of (Z)-$CF_2HCF=CHCl$: Kinetics and products of reaction with Cl atoms and OH radicals. Int J Chem Kinet 2025;57(2):108–16. http://dx.doi.org/10.1002/kin.21763.

[652] Kjærgaard ER, Vogt E, Møller KH, Nielsen OJ, Kjaergaard HG. Correction to "atmospheric chemistry of $CH_3OCF_2CHF_2$". J Phys Chem A 2023;127(25):5520–1. http://dx.doi.org/10.1021/acs.jpca.3c03255, PMID: 37315189.

[653] Trisna BA, Park S, Park I, Lee J, Lim JS. Measurement report: Radiative efficiencies of $(CF_3)_2CFCN$, CF_3OCFCF_2, and $CF_3OCF_2CF_3$. Atmos Chem Phys 2023;23(7):4489–500. http://dx.doi.org/10.5194/acp-23-4489-2023.

[654] Domanskaya AV, Berezkin K, Li G, Bohlius H, Kim M, Harrison JJ, et al. Intensities in the composite infrared spectrum of SF_6 in mixtures with air at 296 K. J Quant Spectrosc Radiat Transfer 2024;317:108922. http://dx.doi.org/10.1016/j.jqsrt.2024.108922.

[655] Muraviev A, Konnov D, Vodopyanov KL. High-resolution mid-IR spectra of methanol and dimethyl sulfide obtained with interleaved subharmonic OPO combs. In: CLEO 2023. Optica Publishing Group; 2023, p. ATh1K.5. http://dx.doi.org/10.1364/CLEO_AT.2023.ATh1K.5.

[656] Vasilyev S, Muraviev A, Konnov D, Mirov M, Smolski V, Moskalev I, et al. Longwave infrared (6.6-11.4 μm) dual-comb spectroscopy with 240,000 comb-mode-resolved data points at video rate. Opt Lett 2023;48(9):2273. http://dx.doi.org/10.1364/OL.477346.

[657] Konnov D, Muraviev A, Vasilyev S, Vodopyanov K. High-resolution frequency-comb spectroscopy with electro-optic sampling and instantaneous octave-wide coverage across mid-IR to THz at a video rate. APL Photon 2023;8(11):110801. http://dx.doi.org/10.1063/5.0165879.

[658] Konnov D, Muraviev A, Vodopyanov K. High-resolution (< 10 MHz) ro-vibrational spectra of low-pressure methanol, ethanol, isoprene, and dimethyl sulfide measured with the dual-comb spectroscopy at 800-1350 cm^{-1}. J Quant Spectr Radiat Transf 2025;347:109690. http://dx.doi.org/10.1016/J.JQSRT.2025.109690.

[659] Dodangodage R, Bernath PF, Zhao J, Billinghurst B. Absorption cross sections for ethane broadened by hydrogen and helium in the 3.3 micron region. J Quant Spectrosc Radiat Transfer 2020;253:107131. http://dx.doi.org/10.1016/j.jqsrt.2020.107131.

[660] Wong A, Hargreaves RJ, Billinghurst B, Bernath PF. Infrared absorption cross sections of propane broadened by hydrogen. J Quant Spectrosc Radiat Transfer 2017;198:141–4. http://dx.doi.org/10.1016/j.jqsrt.2017.05.006.

[661] Wong A, Billinghurst B, Bernath PF. Helium broadened propane absorption cross sections in the far-IR. Mol Astrophys 2017;8:36–9. http://dx.doi.org/10.1016/j.molap.2017.06.003.

[662] Wong A, Appadoo DRT, Bernath PF. IR absorption cross sections of propane broadened by H_2 and He between 150 K and 210 K. J Quant Spectrosc Radiat Transfer 2018;218:68–71. http://dx.doi.org/10.1016/j.jqsrt.2018.06.026.

[663] Hewett DM, Bernath PF, Billinghurst BB. Infrared absorption cross sections of isobutane with hydrogen and nitrogen as broadening gases. J Quant Spectrosc Radiat Transfer 2019;227:226–9. http://dx.doi.org/10.1016/j.jqsrt.2019.02.008.

[664] Hewett D, Bernath PF, Wong A, Billinghurst BE, Zhao J, Lombardo NA, et al. N_2 and H_2 broadened isobutane infrared absorption cross sections and butane upper limits on Titan. Icarus 2020;344:113460. http://dx.doi.org/10.1016/j.icarus.2019.113460.

[665] Bernath P, Dodangodage R, Dulick M, Zhao J, Billinghurst B. Absorption cross sections for neopentane broadened by nitrogen in the 3.3 μm region. J Quant Spectrosc Radiat Transfer 2020;251:107034. http://dx.doi.org/10.1016/j.jqsrt.2020.107034.

[666] Bernath P, Sibert EL, LaBelle K, Zhao J, Billinghurst B. Absorption cross sections and local mode analysis for neopentane. J Quant Spectrosc Radiat Transfer 2022;293:108390. http://dx.doi.org/10.1016/j.jqsrt.2022.108390.

[667] Dodangodage R, Bernath PF, Zhao J, Billinghurst B. Absorption cross sections in the CH stretching region for propene broadened by helium and nitrogen. J Quant Spectrosc Radiat Transfer 2021;271:107738. http://dx.doi.org/10.1016/j.jqsrt.2021.107738.

[668] Bernath PF, Dodangodage R, Zhao J, Billinghurst B. Infrared absorption cross sections for propene broadened by N_2 (450-1250 cm^{-1}) and by H_2 (2680-3220 cm^{-1}). J Quant Spectrosc Radiat Transfer 2023;296:108462. http://dx.doi.org/10.1016/j.jqsrt.2022.108462.

[669] Sorensen JJ, Bernath PF, Johnson RM, Dodangodage R, Cameron WD, LaBelle K. Absorption cross sections of n-butane, n-pentane, cyclopentane and cyclohexane. J Quant Spectrosc Radiat Transfer 2022;290:108284. http://dx.doi.org/10.1016/j.jqsrt.2022.108284.

[670] Steffens BL, Sung K, Malaska MJ, Lopes RMC, Toon GC, Nixon CA. Mid-infrared cross-sections and pseudoline parameters for trans-2-butene (2-C_4H_8). J Quant Spectrosc Radiat Transfer 2023;310:108730. http://dx.doi.org/10.1016/j.jqsrt.2023.108730.

[671] Bernath P, Fernando AM. Infrared absorption cross sections for hot isobutane in the CH stretching region. J Quant Spectrosc Radiat Transfer 2021;269:107644. http://dx.doi.org/10.1016/j.jqsrt.2021.107644.

[672] Es-sebbar E-t, Benilan Y, Farooq A. Temperature-dependent absorption cross-section measurements of 1-butene (1-C_4H_8) in VUV and IR. J Quant Spectrosc Radiat Transfer 2013;115:1–12. http://dx.doi.org/10.1016/j.jqsrt.2012.09.014.

[673] Alrefae M, Es-sebbar E-t, Farooq A. Absorption cross-section measurements of methane, ethane, ethylene and methanol at high temperatures. J Mol Spectrosc 2014;303:8–14. http://dx.doi.org/10.1016/j.jms.2014.06.007.

[674] Es-sebbar E-t, Alrefae M, Farooq A. Infrared cross-sections and integrated band intensities of propylene: Temperature-dependent studies. J Quant Spectrosc Radiat Transfer 2014;133:559–69. http://dx.doi.org/10.1016/j.jqsrt.2013.09.019.

[675] Es-sebbar E, Jolly A, Benilan Y, Farooq A. Quantitative mid-infrared spectra of allene and propyne from room to high temperatures. J Mol Spectrosc 2014;305:10–6. http://dx.doi.org/10.1016/j.jms.2014.09.004.

[676] Strand CL, Ding Y, Johnson SE, Hanson RK. Measurement of the mid-infrared absorption spectra of ethylene (C_2H_4) and other molecules at high temperatures and pressures. J Quant Spectrosc Radiat Transfer 2019;222–223:122–9. http://dx.doi.org/10.1016/j.jqsrt.2018.10.030.

[677] Ding Y, Strand CL, Hanson RK. High-temperature mid-infrared absorption spectra of methanol (CH_3OH) and ethanol (C_2H_5OH) between 930 and 1170 cm^{-1}. J Quant Spectrosc Radiat Transfer 2019;224:396–402. http://dx.doi.org/10.1016/j.jqsrt.2018.11.034.

[678] Ding Y, Peng WY, Strand CL, Hanson RK. Quantitative measurements of broad-band mid-infrared absorption spectra of formaldehyde, acetaldehyde, and acetone at combustion-relevant temperatures near 5.7 μm. J Quant Spectrosc Radiat Transfer 2020;248:106981. http://dx.doi.org/10.1016/j.jqsrt.2020.106981.

[679] Ding Y, Su WW, Johnson SE, Strand CL, Hanson RK. Temperature-dependent absorption cross section measurements for propene, 1-butene, cis-/trans-2-butene, isobutene and 1,3-butadiene in the spectral region 8.4–11.7 μm. J Quant Spectrosc Radiat Transfer 2020;255:107240. http://dx.doi.org/10.1016/j.jqsrt.2020.107240.

[680] Su WW, Ding Y, Strand CL, Hanson RK. Experimental temperature- and pressure-dependent absorbance cross sections and a pseudo-line-list model for methyl formate near 5.7 μm. J Quant Spectrosc Radiat Transfer 2024;327:109128. http://dx.doi.org/10.1016/J.JQSRT.2024.109128.

[681] Adil M, Giri BR, Mai TVT, Szőri M, Huynh LK, Farooq A. High-temperature mid-IR absorption spectra and reaction kinetics of 1,3-dioxolane. Proc Combust Inst 2023;39(1):621–31. http://dx.doi.org/10.1016/j.proci.2022.08.019.

[682] Adil M, Giri BR, Mai TV-T, Szőri M, Huynh LK, Farooq A. High-temperature mid-IR absorption and reaction kinetics of 2-methyl-1, 3-dioxolane: An experimental and theoretical study. J Photochem Photobiol 2023;13:100165. http://dx.doi.org/10.1016/j.jpap.2023.100165.

[683] Adil M, Giri BR, Elkhazraji A, Farooq A. Mid-IR absorption spectra of C1-C4 alkyl acetates at high temperatures. J Quant Spectrosc Radiat Transfer 2023;300:108522. http://dx.doi.org/10.1016/j.jqsrt.2023.108522.

[684] Adil M, Farooq A. Shock tube/laser absorption measurements of the high-temperature spectra and decomposition of propyl ethers. J Phys Chem A 2023;127(37):7764–71. http://dx.doi.org/10.1021/acs.jpca.3c04446.

[685] Vasilchenko S, Solodov A, Egorov O, Tyuterev V. Accurate absolute absorption cross-sections of the ozone Wulf bands at 1 μm range: measurements with high-resolution cw-CRDS laser techniques. J Quant Spectrosc Radiat Transfer 2024;312:108817. http://dx.doi.org/10.1016/j.jqsrt.2023.108817.

[686] Vasilchenko SS, Solodov AA, Egorov OV, Tyuterev VG. Experimental study and simulation of singlet-triplet rovibronic ozone bands in the 11 900-12 800 cm^{-1} region. Atmos Ocean Opt 2024;37(2):123–31. http://dx.doi.org/10.1134/S1024856024700155.

[687] Volkamer R, Spietz P, Burrows J, Platt U. High-resolution absorption cross-section of glyoxal in the UV–vis and IR spectral ranges. J Photochem Photobiol A: Chem 2005;172(1):35–46. http://dx.doi.org/10.1016/j.jphotochem.2004.11.011.

[688] Alvarado-Jiménez D, Pietropolli Charmet A, Stoppa P, Tasinato N. The radiative efficiency and global warming potential of HCFC-132b. ChemPhysChem 2025;26(1):e202400632. http://dx.doi.org/10.1002/cphc.202400632, arXiv:https://chemistry-europe.onlinelibrary.wiley.com/doi/pdf/10.1002/cphc.202400632, URL https://chemistry-europe.onlinelibrary.wiley.com/doi/abs/10.1002/cphc.202400632.

[689] Karman T, Gordon IE, van der Avoird A, Baranov YI, Boulet C, Drouin BJ, et al. Update of the HITRAN collision-induced absorption section. Icarus 2019;328:160–75. http://dx.doi.org/10.1016/j.icarus.2019.02.034.

[690] Richard C, Gordon I, Rothman L, Abel M, Frommhold L, Gustafsson M, et al. New section of the HITRAN database: Collision-induced absorption (CIA). J Quant Spectrosc Radiat Transfer 2012;113(11):1276–85. http://dx.doi.org/10.1016/j.jqsrt.2011.11.004.

[691] Terragni J, Gordon IE, Adkins EM, Boulet C, Campargue A, Chistikov D, et al. Collision induced absorption in HITRAN2024: Enhanced and improved data for atmospheric and planetary studies. J Quant Spectrosc Radiat Transfer 2025;347:109631. http://dx.doi.org/10.1016/J.JQSRT.2025.109631.

[692] Lorenz RD, McKay CP, Lunine JI. Photochemically driven collapse of titan's atmosphere. Science 1997;275(5300):642–4. http://dx.doi.org/10.1126/science.275.5300.642.

[693] Forget F, Wordsworth R, Millour E, Madeleine J-B, Kerber L, Leconte J, et al. 3D modelling of the early martian climate under a denser CO_2 atmosphere: Temperatures and CO_2 ice clouds. Icarus 2013;222(1):81–99. http://dx.doi.org/10.1016/j.icarus.2012.10.019.

[694] Wordsworth RD. The climate of early mars. Annu Rev Earth Planet Sci 2016;44:381–408. http://dx.doi.org/10.1146/annurev-earth-060115-012355.

[695] Trafton L. Planetary atmospheres: The role of collision-induced absorption. In: Molecular complexes in earth's, planetary, cometary, and interstellar atmospheres. 1998, p. 177–93. http://dx.doi.org/10.1142/9789812812155_0006.

[696] Meadows VS, Reinhard CT, Arney GN, Parenteau MN, Schwieterman EW, Domagal-Goldman SD, et al. Exoplanet biosignatures: Understanding oxygen as a biosignature in the context of its environment. Astrobiology 2018;18(6):630–62. http://dx.doi.org/10.1089/ast.2017.1727.

[697] Fauchez TJ, Villanueva GL, Schwieterman EW, Turbet M, Arney G, Pidhorodetska D, et al. Sensitive probing of exoplanetary oxygen via mid-infrared collisional absorption. Nat Astron 2020;4(4):372–6. http://dx.doi.org/10.1038/s41550-019-0977-7.

[698] Wei C, Klingberg A, Strand CL, Hanson RK. Measurement of hydrogen and nitrogen via collision-induced infrared absorption. Int J Hydrog Energy 2024;93:364–73. http://dx.doi.org/10.1016/j.ijhydene.2024.10.318.

[699] Hübert T, Boon-Brett L, Black G, Banach U. Hydrogen sensors – a review. Sensors Actuators 2011;157(2):329–52. http://dx.doi.org/10.1016/j.snb.2011.04.070.

[700] Samuelson RE, Nath NR, Borysow A. Gaseous abundances and methane supersaturation in Titan's troposphere. Planet Space Sci 1997;45(8):959–80. http://dx.doi.org/10.1016/S0032-0633(97)00090-1.

[701] Borysow A, Frommhold L. Collision-induced rototranslational absorption spectra of CH_4-CH_4 pairs at temperatures from 50 to 300 K. Astrophys J 1987;318:940. http://dx.doi.org/10.1086/165426.

[702] Taylor RH, Borysow A, Frommhold L. Concerning the rototranslational absorption spectra of He-CH_4 pairs. J Mol Spectrosc 1988;129(1):45–58. http://dx.doi.org/10.1016/0022-2852(88)90257-3.

[703] Odintsova T, Serov E, Balashov A, Koshelev M, Koroleva A, Simonova A, et al. CO_2–CO_2 and CO_2–Ar continua at millimeter wavelengths. J Quant Spectrosc Radiat Transfer 2021;258:107400. http://dx.doi.org/10.1016/j.jqsrt.2020.107400.

[704] Fakhardji W, Boulet C, Tran H, Hartmann J-M. Direct calculations of the CH_4+CO_2 far infrared collision-induced absorption. J Quant Spectrosc Radiat Transfer 2022;283:108148. http://dx.doi.org/10.1016/j.jqsrt.2022.108148.

[705] Wordsworth R, Kalugina Y, Lokshtanov S, Vigasin A, Ehlmann B, Head J, et al. Transient reducing greenhouse warming on early Mars. Geophys Res Lett 2017;44(2):665–71. http://dx.doi.org/10.1002/2016GL071766.

[706] Turbet M, Boulet C, Karman T. Measurements and semi-empirical calculations of CO_2+CH_4 and CO_2+H_2 collision-induced absorption across a wide range of wavelengths and temperatures. Application for the prediction of early Mars surface temperature. Icarus 2020;346:113762. http://dx.doi.org/10.1016/j.icarus.2020.113762.

[707] Gruszka M, Borysow A. Roto-translational collision-induced absorption of CO_2 for the atmosphere of venus at frequencies from 0 to 250 cm^{-1}, at temperatures from 200 to 800 K. Icarus 1997;129(1):172–7. http://dx.doi.org/10.1006/icar.1997.5773.

[708] Baranov YI, Lafferty W, Fraser G. Infrared spectrum of the continuum and dimer absorption in the vicinity of the O_2 vibrational fundamental in O_2/CO_2 mixtures. J Mol Spectrosc 2004;228(2):432–40. http://dx.doi.org/10.1016/j.jms.2004.04.010, Special Issue Dedicated to Dr. Jon T. Hougen on the Occasion of His 68th Birthday.

[709] Terragni J, Kohler E, Kofman V, Anderson S, Villanueva GL, Faggi S. New measurements of high-temperature CO_2–CO_2 collision-induced absorption in the 1100–1800 cm^{-1} range. J Quant Spectrosc Radiat Transfer 2025;346:109595. http://dx.doi.org/10.1016/j.jqsrt.2025.109595.

[710] Baranov YI, Fraser GT, Lafferty WJ, Vigasin AA. Collision-induced absorption in the CO_2 Fermi triad for temperatures from 211 K to 296 K. In: Camy-Peyret C, Vigasin AA, editors. Weakly interacting molecular pairs: unconventional absorbers of radiation in the atmosphere. Dordrecht: Springer Netherlands; 2003, p. 149–58. http://dx.doi.org/10.1007/978-94-010-0025-3_12.

[711] Tran H, Hartmann J, Rambinison E, Turbet M. Collision-induced absorptions by pure CO_2 in the infrared: New measurements in the 1150–4500 cm^{-1} spectral range and empirical modeling for applications. Icarus 2024;422:116265. http://dx.doi.org/10.1016/j.icarus.2024.116265.

[712] Baranov YI. Collision-induced absorption in the region of the $\nu_2 + \nu_3$ band of carbon dioxide. J Mol Spectrosc 2018;345:11–6. http://dx.doi.org/10.1016/j.jms.2017.11.005.

[713] Fleurbaey H, Mondelain D, Fakhardji W, Hartmann J, Campargue A. Simultaneous collision-induced transitions in H_2O+CO_2 gas mixtures. J Quant Spectrosc Radiat Transfer 2022;285:108162. http://dx.doi.org/10.1016/j.jqsrt.2022.108162.

[714] Bar-Ziv E, Weiss S. Translational spectra due to collision-induced overlap moments in mixtures of he with CO_2, N_2, CH_4, and C_2H_6. J Chem Phys 1972;57(1):34–7. http://dx.doi.org/10.1063/1.1677970.

[715] Borysow A, Frommhold L. Theoretical collision-induced rototranslational absorption spectra for the outer planets: H_2-CH_4 pairs. Astrophys J 1986;304:849. http://dx.doi.org/10.1086/164221.

[716] Gustafsson M, Frommhold L. The H_2–H infrared absorption bands at temperatures from 1000 K to 2500 K. Astron Astrophys 2003;400(3):1161–2. http://dx.doi.org/10.1051/0004-6361:20030100.

[717] Abel M, Frommhold L, Li X, Hunt KLC. Collision-induced absorption by H_2 pairs: From hundreds to thousands of kelvin. J Phys Chem A 2011;115(25):6805–12. http://dx.doi.org/10.1021/jp109441f.

[718] Fletcher LN, Gustafsson M, Orton GS. Hydrogen dimers in giant-planet infrared spectra. Astrophys J Suppl Ser 2018;235(1):24. http://dx.doi.org/10.3847/1538-4365/aaa07a.

[719] Vitali F, Stefani S, Piccioni G, Snels M, Grassi D, Biondi D, et al. New experimental measurements of the Collision Induced Absorptions of H_2-H_2 and H_2-He in the 3600-5500 cm^{-1} spectral range from 120 to 500 K. J Quant Spectrosc Radiat Transfer 2025;330:109255. http://dx.doi.org/10.1016/j.jqsrt.2024.109255.

[720] Koroleva A, Kassi S, Fleurbaey H, Campargue A. The collision-induced absorption of H_2 near 1.20 μm: Subatmospheric measurements and validation tests of calculations. J Quant Spectrosc Radiat Transfer 2024;318:108948. http://dx.doi.org/10.1016/j.jqsrt.2024.108948.

[721] Abel M, Frommhold L, Li X, Hunt KLC. Infrared absorption by collisional H_2–He complexes at temperatures up to 9 000 K and frequencies from 0 to 20 000 cm^{-1}. J Chem Phys 2012;136(4):044319. http://dx.doi.org/10.1063/1.3676405.

[722] Borysow J, Frommhold L, Birnbaum G. Collision-induced rototranslational absorption spectra of H 2-He pairs at temperatures from 40 to 3000 K. Astrophys J 1988;326:509. http://dx.doi.org/10.1086/166112.

[723] Gustafsson M, Frommhold L. Infrared absorption spectra of collisionally interacting He and H atoms. Astrophys J 2001;546(2):1168. http://dx.doi.org/10.1086/318311.

[724] Baranov Y, Lafferty W, Fraser G. Investigation of collision-induced absorption in the vibrational fundamental bands of O_2 and N_2 at elevated temperatures. J Mol Spectrosc 2005;233(1):160–3. http://dx.doi.org/10.1016/j.jms.2005.06.008.

[725] Menoux V, Doucen RL, Boulet C, Roblin A, Bouchardy AM. Collision-induced absorption in the fundamental band of N_2: temperature dependence of the absorption for N_2-N_2 and N_2-O_2 pairs. Appl Opt 1993;32(3):263–8. http://dx.doi.org/10.1364/AO.32.000263.

[726] Lafferty WJ, Solodov AM, Weber A, Olson WB, Hartmann J-M. Infrared collision-induced absorption by N_2 near 4.3μm for atmospheric applications: measurements and empiricalmodeling. Appl Opt 1996;35(30):5911–7. http://dx.doi.org/10.1364/AO.35.005911.

[727] Hartmann J-M, Boulet C, Toon GC. Collision-induced absorption by N_2 near 2.16 μm: Calculations, model, and consequences for atmospheric remote sensing. J Geophys Res: Atmos 2017;122(4):2419–28. http://dx.doi.org/10.1002/2016JD025677.

[728] Serov E, Galanina T, Koroleva A, Makarov D, Amerkhanov I, Koshelev M, et al. Continuum absorption in pure N_2 gas and in its mixture with Ar. J Quant Spectrosc Radiat Transfer 2024;328:109172. http://dx.doi.org/10.1016/j.jqsrt.2024.109172.

[729] Moreau G. étude en température et modélisation de l'absorption induite par collision dans les régions des bandes fundamentales pour les mélanges des gaz N_2−Ar et O_2 (Ph.D. thesis), Université de Rennes; 1999.

[730] Finenko AA, Bézard B, Gordon IE, Chistikov DN, Lokshtanov SE, Petrov SV, et al. Trajectory-based simulation of far-infrared collision-induced absorption profiles of CH_4–N_2 for modeling titan's atmosphere. Astrophys J Suppl Ser 2022;258(2):33. http://dx.doi.org/10.3847/1538-4365/ac36d3.

[731] Borysow A, Tang C. Far infrared CIA spectra of N_2-CH_4 pairs for modeling of titan's atmosphere. Icarus 1993;105(1):175–83. http://dx.doi.org/10.1006/icar.1993.1117.

[732] Borysow A, Frommhold L. Theoretical collision-induced rototranslational absorption spectra for modeling titan's atmosphere: H_2-N_2 pairs. Astrophys J 1986;303:495. http://dx.doi.org/10.1086/164096.

[733] Hartmann J-M, Boulet C, Tran DD, Tran H, Baranov Y. Effect of humidity on the absorption continua of CO_2 and N_2 near 4 μm: Calculations, comparisons with measurements, and consequences for atmospheric spectra. J Chem Phys 2018;148(5):054304. http://dx.doi.org/10.1063/1.5019994.

[734] Chistikov DN, Finenko AA, Lokshtanov SE, Petrov SV, Vigasin AA. Simulation of collision-induced absorption spectra based on classical trajectories and ab initio potential and induced dipole surfaces. I. Case study of N_2–N_2 rototranslational band. J Chem Phys 2019;151(19):194106. http://dx.doi.org/10.1063/1.5125756.

[735] Sung K, Wishnow E, Venkataraman M, Brown LR, Ozier I, Benner DC, et al. Progress in the measurement of temperature-dependent N_2-N_2 collision-induced absorption and H_2-broadening of cold and hot CH_4. In: AGU fall meeting abstracts. AAS/division for planetary sciences meeting abstracts, Vol. 48, 2016, p. 424.11, URL https://ui.adsabs.harvard.edu/abs/2016DPS....4842411S/abstract.

[736] Thibault F, Menoux V, Doucen RL, Rosenmann L, Hartmann J-M, Boulet C. Infrared collision-induced absorption by O_2 near 6.4 μm for atmospheric applications: measurements and empiricalmodeling. Appl Opt 1997;36(3):563–7. http://dx.doi.org/10.1364/AO.36.000563.

[737] Orlando JJ, Tyndall GS, Nickerson KE, Calvert JG. The temperature dependence of collision-induced absorption by oxygen near 6 μm. J Geophys Res: Atmos 1991;96(D11):20755–60. http://dx.doi.org/10.1029/91JD02042.

[738] Mondelain D, Kassi S, Campargue A. Accurate laboratory measurement of the O_2 collision-induced absorption band near 1.27 μm. J Geophys Res: Atmos 2019;124(1):414–23. http://dx.doi.org/10.1029/2018JD029317.

[739] Kassi S, Guessoum S, Abanto JCA, Tran H, Campargue A, Mondelain D. Temperature dependence of the collision-induced absorption band of O_2 near 1.27 μm. J Geophys Res: Atmos 2021;126(13). http://dx.doi.org/10.1029/2021JD034860, e2021JD034860.

[740] Adkins EM, Karman T, Campargue A, Mondelain D, Hodges JT. Parameterized model to approximate theoretical collision-induced absorption band shapes for O_2-O_2 and O_2-N_2. J Quant Spectrosc Radiat Transfer 2023;310:108732. http://dx.doi.org/10.1016/j.jqsrt.2023.108732.

[741] Karman T, Koenis MA, Banerjee A, Parker DH, Gordon IE, van der Avoird A, et al. O_2-O_2 and O_2-N_2 collision-induced absorption mechanisms unravelled. Nat Chem 2018;10(5):549–54. http://dx.doi.org/10.1038/s41557-018-0015-x.

[742] Spiering FR, van der Zande WJ. Collision induced absorption in the $a^1\Delta(v = 2) \leftarrow X^3\Sigma_g^-(v = 0)$ band of molecular oxygen. Phys Chem Chem Phys 2012;14:9923–8. http://dx.doi.org/10.1039/C2CP40961E.

[743] Tran H, Boulet C, Hartmann J-M. Line mixing and collision-induced absorption by oxygen in the A band: Laboratory measurements, model, and tools for atmospheric spectra computations. J Geophys Res: Atmos 2006;111(D15). http://dx.doi.org/10.1029/2005JD006869.

[744] Drouin BJ, Benner DC, Brown LR, Cich MJ, Crawford TJ, Devi VM, et al. Multispectrum analysis of the oxygen A-band. J Quant Spectrosc Radiat Transfer 2017;186:118–38. http://dx.doi.org/10.1016/j.jqsrt.2016.03.037, Satellite Remote Sensing and Spectroscopy: Joint ACE-Odin Meeting, October 2015.

[745] Banerjee A, Mandon J, Harren F, Parker DH. Collision-induced absorption between O_2–CO_2 for the $a^1\Delta(v = 1) \leftarrow X^3\Sigma_g^-(v = 0)$ transition of molecular oxygen at 1060 nm. Phys Chem Chem Phys 2019;21:1805–11. http://dx.doi.org/10.1039/C8CP06778C.

[746] Vangvichith M, Tran H, Hartmann J-M. Line-mixing and collision induced absorption for o_2–CO_2 mixtures in the oxygen A-band region. J Quant Spectrosc Radiat Transfer 2009;110(18):2212–6. http://dx.doi.org/10.1016/j.jqsrt.2009.06.002.

[747] Spiering FR, Kiseleva MB, Filippov NN, van Kesteren L, van der Zande WJ. Collision-induced absorption in the O_2 B-band region near 670 nm. Phys Chem Chem Phys 2011;13:9616–21. http://dx.doi.org/10.1039/C1CP20403C.

[748] Thalman R, Volkamer R. Temperature dependent absorption cross-sections of O_2–O_2 collision pairs between 340 and 630 nm and at atmospherically relevant pressure. Phys Chem Chem Phys 2013;15:15371–81. http://dx.doi.org/10.1039/C3CP50968K.

[749] Finkenzeller H, Volkamer R. O_2–O_2 CIA in the gas phase: Cross-section of weak bands, and continuum absorption between 297–500 nm. J Quant Spectrosc Radiat Transfer 2022;279:108063. http://dx.doi.org/10.1016/j.jqsrt.2021.108063.

[750] Jakobsen P, Ferruit P, Alves de Oliveira C, Arribas S, Bagnasco G, Barho R, et al. The near-infrared spectrograph (NIRSpec) on the james webb space telescope - I. Overview of the instrument and its capabilities. Astron Astrophys 2022;661:A80. http://dx.doi.org/10.1051/0004-6361/202142663.

[751] Kendrew S, Scheithauer S, Bouchet P, Amiaux J, Azzollini R, Bouwman J, et al. The mid-infrared instrument for the james webb space telescope, IV: The low-resolution spectrometer. Publ Astron Soc Pac 2015;127(953):623. http://dx.doi.org/10.1086/682255.

[752] Nicholls H, Lichtenberg T, Bower DJ, Pierrehumbert R. Magma ocean evolution at arbitrary redox state. J Geophys Res: Planets 2024;129(12). http://dx.doi.org/10.1029/2024JE008576, e2024JE008576.

[753] Zahnle K, Arndt N, Cockell C, Halliday A, Nisbet E, Selsis F, et al. Emergence of a habitable planet. Space Sci Rev 2007;129:35–78. http://dx.doi.org/10.1007/s11214-007-9225-z.

[754] Hartmann J-M, Tran H, Armante R, Boulet C, Campargue A, Forget F, et al. Recent advances in collisional effects on spectra of molecular gases and their practical consequences. J Quant Spectrosc Radiat Transfer 2018;213:178–227. http://dx.doi.org/10.1016/j.jqsrt.2018.03.016.

[755] Blouin S, Dufour P, Allard NF, Kilic M. A new generation of cool white dwarf atmosphere models. II. A DZ Star with collision-induced absorption. Astrophys J 2018;867(2):161. http://dx.doi.org/10.3847/1538-4357/aae53a.

[756] Fauchez TJ, Rackham BV, Ducrot E, Stevenson KB, de Wit J. Stellar models also limit exoplanet atmosphere studies in emission. Astrophys J 2025;989(2):170. http://dx.doi.org/10.3847/1538-4357/adf068, arXiv:2502.19585.

[757] Stamnes K, Thomas GE, Stamnes JJ. Radiative transfer in the atmosphere and ocean. second ed.. Cambridge: Cambridge University Press; 2017, http://dx.doi.org/10.1017/9781316148549.

[758] Brasseur GP, Solomon S. Aeronomy of the middle atmosphere: chemistry and physics of the stratosphere and mesosphere. Springer Science & Business Media; 2005.

[759] Fenn R, Clough S, Gallery W, Good R, Kneizys F, Mill J, et al. Optical and infrared properties of the atmosphere. In: Handbook of geophysics and the space environment. US Air Force Geophysics Laboratory, Hanscom Air Force Base, Bedford, Mass; 1985, p. 1–71.

[760] Downing HD, Williams D. Optical constants of water in the infrared. J Geophys Res 1975;80(12):1656–61. http://dx.doi.org/10.1029/JC080i012p01656.

[761] Wagner R, Benz S, Möhler O, Saathoff H, Schnaiter M, Schurath U. Mid-infrared extinction spectra and optical constants of supercooled water droplets. J Phys Chem A 2005;109(32):7099–112. http://dx.doi.org/10.1021/jp051942z.

[762] Warren SG, Brandt RE. Optical constants of ice from the ultraviolet to the microwave: A revised compilation. J Geophys Res: Atmos 2008;113(D14). http://dx.doi.org/10.1029/2007JD009744.

[763] Clapp ML, Worsnop DR, Miller RE. Frequency-dependent optical constants of water ice obtained directly from aerosol extinction spectra. J Phys Chem 1995;99(17):6317–26. http://dx.doi.org/10.1021/j100017a010.

[764] Tisdale RT, Glandorf DL, Tolbert MA, Toon OB. Infrared optical constants of low-temperature H_2SO_4 solutions representative of stratospheric sulfate aerosols. J Geophys Res: Atmos 1998;103(D19):25353–70. http://dx.doi.org/10.1029/98JD02457.

[765] Lund Myhre CE, Christensen DH, Nicolaisen FM, Nielsen CJ. Spectroscopic study of aqueous H_2SO_4 at different temperatures and compositions: Variations in dissociation and optical properties. J Phys Chem A 2003;107(12):1979–91. http://dx.doi.org/10.1021/jp026576n.

[766] Lund Myhre CE, Grothe H, Gola AA, Nielsen CJ. Optical constants of HNO_3/H_2O and $H_2SO_4/HNO_3/H_2O$ at low temperatures in the infrared region. J Phys Chem A 2005;109(32):7166–71. http://dx.doi.org/10.1021/jp0508406.

[767] Niedziela RF, Miller RE, Worsnop DR. Temperature- and frequency-dependent optical constants for nitric acid dihydrate from aerosol spectroscopy. J Phys Chem A 1998;102(32):6477–84. http://dx.doi.org/10.1021/jp981299z.

[768] Richwine LJ, Clapp ML, Miller RE, Worsnop DR. Complex refractive indices in the infrared of nitric acid trihydrate aerosols. Geophys Res Lett 1995;22(19):2625–8. http://dx.doi.org/10.1029/95GL02650.

[769] Toon OB, Tolbert MA, Koehler BG, Middlebrook AM, Jordan J. Infrared optical constants of H_2O ice, amorphous nitric acid solutions, and nitric acid hydrates. J Geophys Res: Atmos 1994;99(D12):25631–54. http://dx.doi.org/10.1029/94JD02388.

[770] Wagner R, Ajtai T, Kandler K, Lieke K, Linke C, Müller T, et al. Complex refractive indices of Saharan dust samples at visible and near UV wavelengths: a laboratory study. Atmos Chem Phys 2012;12(5):2491–512. http://dx.doi.org/10.5194/acp-12-2491-2012.

[771] Di Biagio C, Formenti P, Balkanski Y, Caponi L, Cazaunau M, Pangui E, et al. Global scale variability of the mineral dust long-wave refractive index: a new dataset of in situ measurements for climate modeling and remote sensing. Atmos Chem Phys 2017;17(3):1901–29. http://dx.doi.org/10.5194/acp-17-1901-2017.

[772] Grainger RG, Peters DM, Thomas GE, Smith AJA, Siddans R, Carboni E, et al. Measuring volcanic plume and ash properties from space. In: Pyle DM, Mather TA, Biggs J, editors. Remote sensing of volcanoes and volcanic processes: integrating observation and modelling. vol. 380, Geological Society of London; 2013, http://dx.doi.org/10.1144/SP380.7.

[773] Deguine A, Petitprez D, Clarisse L, Guđmundsson S, Outes V, Villarosa G, et al. Complex refractive index of volcanic ash aerosol in the infrared, visible, and ultraviolet. Appl Opt 2020;59(4):884–95. http://dx.doi.org/10.1364/AO.59.000884.

[774] Reed BE, Peters DM, McPheat R, Grainger RG. The complex refractive index of volcanic ash aerosol retrieved from spectral mass extinction. J Geophys Res: Atmos 2018;123(2):1339–50. http://dx.doi.org/10.1002/2017JD027362.

[775] Liu PF, Abdelmalki N, Hung H-M, Wang Y, Brune WH, Martin ST. Ultraviolet and visible complex refractive indices of secondary organic material produced by photooxidation of the aromatic compounds toluene and *m*-xylene. Atmos Chem Phys 2015;15(3):1435–46. http://dx.doi.org/10.5194/acp-15-1435-2015.

[776] Liu P, Zhang Y, Martin ST. Complex refractive indices of thin films of secondary organic materials by spectroscopic ellipsometry from 220 to 1200 nm. Environ Sci Technol 2013;47(23):13594–601. http://dx.doi.org/10.1021/es403411e.

[777] He Q, Tomaz S, Li C, Zhu M, Meidan D, Riva M, et al. Optical properties of secondary organic aerosol produced by nitrate radical oxidation of biogenic volatile organic compounds. Environ Sci Technol 2021;55(5):2878–89. http://dx.doi.org/10.1021/acs.est.0c06838.

[778] Fang Z, Li C, He Q, Czech H, Gröger T, Zeng J, et al. Secondary organic aerosols produced from photochemical oxidation of secondarily evaporated biomass burning organic gases: Chemical composition, toxicity, optical properties, and climate effect. Environ Int 2021;157:106801. http://dx.doi.org/10.1016/j.envint.2021.106801.

[779] Hashemi VH, Galpin T, Greenslade ME. Complex refractive index of vanillic acid aerosol retrieved from 270–600 nm using aerosol extinction and solution phase absorption measurements. Aerosol Sci Technol 2024;58(5):569–83. http://dx.doi.org/10.1080/02786826.2024.2332636.

[780] Lund Myhre CE, Nielsen CJ. Optical properties in the UV and visible spectral region of organic acids relevant to tropospheric aerosols. Atmos Chem Phys 2004;4(7):1759–69. http://dx.doi.org/10.5194/acp-4-1759-2004.

[781] Alexander DTL, Crozier PA, Anderson JR. Brown carbon spheres in East Asian outflow and their optical properties. Science 2008;321(5890):833–6. http://dx.doi.org/10.1126/science.1155296.

[782] Sutherland RA, Khanna RK. Optical properties of organic-based aerosols produced by burning vegetation. Aerosol Sci Technol 1991;14(3):331–42. http://dx.doi.org/10.1080/02786829108959495.

[783] Shepherd RH, King MD, Marks AA, Brough N, Ward AD. Determination of the refractive index of insoluble organic extracts from atmospheric aerosol over the visible wavelength range using optical tweezers. Atmos Chem Phys 2018;18(8):5235–52. http://dx.doi.org/10.5194/acp-18-5235-2018.

[784] Magi BI, Fu Q, Redemann J. A methodology to retrieve self-consistent aerosol optical properties using common aircraft measurements. J Geophys Res: Atmos 2007;112(D24). http://dx.doi.org/10.1029/2006JD008312.

[785] Stagg BJ, Charalampopoulos TT. Refractive indices of pyrolytic graphite, amorphous carbon, and flame soot in the temperature range 25° to 600°C. Combust Flame 1993;94(4):381–96. http://dx.doi.org/10.1016/0010-2180(93)90121-I.

[786] Chang H-c, Charalampopoulos TT. Determination of the wavelength dependence of refractive indices of flame soot. Proc R Soc Lond Ser A: Math Phys Sci 1990;430(1880):577–91. http://dx.doi.org/10.1098/rspa.1990.0107.

[787] Querry MR. Optical constants of minerals and other materials from the millimeter to the ultraviolet. Aberdeen Proving Ground, Md.: Chemical Research, Development & Engineering Center, U.S. Army Armament Munitions Chemical Command; 1987.

[788] Toon OB, B. Pollack J, Sagan C. Physical properties of the particles composing the Martian dust storm of 1971–1972. Icarus 1977;30(4):663–96. http://dx.doi.org/10.1016/0019-1035(77)90088-4.

[789] Chehab M, Herbin H, Deguine A, Gosselin S, Bizet V, Petitprez D. First complex refractive indices retrieval from FIR to UV: Application to kaolinite particles. Aerosol Sci Technol 2024;58(5):498–511. http://dx.doi.org/10.1080/02786826.2024.2318371.

[790] Herbin H, Deschutter L, Deguine A, Petitprez D. Complex refractive index of crystalline quartz particles from UV to thermal infrared. Aerosol Sci Technol 2023;57(3):255–65. http://dx.doi.org/10.1080/02786826.2023.2165899.

[791] Khare BN, Sagan C, Arakawa ET, Suits F, Callcott TA, Williams MW. Optical constants of organic tholins produced in a simulated Titanian atmosphere: From soft X-ray to microwave frequencies. Icarus 1984;60(1):127–37. http://dx.doi.org/10.1016/0019-1035(84)90142-8.

[792] Ramirez SI, Coll P, da Silva A, Navarro-González R, Lafait J, Raulin F. Complex refractive index of Titan's aerosol analogues in the 200–900 nm domain. Icarus 2002;156(2):515–29. http://dx.doi.org/10.1006/icar.2001.6783.

[793] Imanaka H, Cruikshank DP, Khare BN, McKay CP. Optical constants of Titan tholins at mid-infrared wavelengths (2.5–25 μm) and the possible chemical nature of Titan's haze particles. Icarus 2012;218(1):247–61. http://dx.doi.org/10.1016/j.icarus.2011.11.018.

[794] Jovanović L, Gautier T, Broch L, Protopapa S, Bertrand T, Rannou P, et al. Optical constants of Pluto aerosol analogues from UV to near-IR. Icarus 2021;362:114398. http://dx.doi.org/10.1016/j.icarus.2021.114398.

[795] Henning T, Mutschke H. Low-temperature infrared properties of cosmic dust analogues. Astron Astrophys 1997;327:743–54, URL https://ui.adsabs.harvard.edu/abs/1997A%26A...327..743H/abstract.

[796] Zeidler S, Posch T, Mutschke H. Optical constants of refractory oxides at high temperatures - Mid-infrared properties of corundum, spinel, and α-quartz, potential carriers of the 13 μm feature. Astron Astrophys 2013;553:A81. http://dx.doi.org/10.1051/0004-6361/201220459.

[797] Begemann B, Dorschner J, Henning T, Mutschke H, Gürtler J, Kömpe C, et al. Aluminum oxide and the opacity of oxygen-rich circumstellar dust in the 12–17 micron range. Astrophys J 1997;476(1):199. http://dx.doi.org/10.1086/303597.

[798] Henning T, Begemann B, Mutschke H, Dorschner J. Optical properties of oxide dust grains. Astron Astrophys Suppl Ser 1995;112:143, URL https://ui.adsabs.harvard.edu/abs/1995A%26AS..112..143H/abstract.

[799] Posch T, Kerschbaum F, Fabian D, Mutschke H, Dorschner J, Tamanai A, et al. Infrared properties of solid titanium oxides: Exploring potential primary dust condensates. Astrophys J Suppl Ser 2003;149(2):437. http://dx.doi.org/10.1086/379167.

[800] Triaud AH. Iron oxides. 2026, https://www2.astro.uni-jena.de/Laboratory/OCDB/mgfeoxides.html, Unpublished data.

[801] Fabian D, Henning T, Jäger C, Mutschke H, Dorschner J, Wehrhan O. Fayalite in the UV-VIS-NIR. 2026, https://www2.astro.uni-jena.de/Laboratory/OCDB/crsilicates.html, Unpublished.

[802] Fabian D, Henning T, Jäger C, Mutschke H, Dorschner J, Wehrhan O. Steps toward interstellar silicate mineralogy - VI. Dependence of crystalline olivine IR spectra on iron content and particle shape. Astron Astrophys 2001;378(1):228–38. http://dx.doi.org/10.1051/0004-6361:20011196.

[803] Fabian D, Posch T, Mutschke H, Kerschbaum F, Dorschner J. Infrared optical properties of spinels - A study of the carrier of the 13, 17 and 32 μm emission features observed in ISO-SWS spectra of oxygen-rich AGB stars. Astron Astrophys 2001;373(3):1125–38. http://dx.doi.org/10.1051/0004-6361:20010657.

[804] Jäger C, Dorschner J, Mutschke H, Posch T, Henning T. Steps toward interstellar silicate mineralogy - VII. Spectral properties and crystallization behaviour of magnesium silicates produced by the sol-gel method. Astron Astrophys 2003;408(1):193–204. http://dx.doi.org/10.1051/0004-6361:20030916.

[805] Zeidler S, Posch T, Mutschke H, Richter H, Wehrhan O. Near-infrared absorption properties of oxygen-rich stardust analogs - The influence of coloring metal ions. Astron Astrophys 2011;526:A68. http://dx.doi.org/10.1051/0004-6361/201015219.

[806] Posch T, Kerschbaum F, Mutschke H, Fabian D, Clément D, Dorschner J. Features of oxide dust particles in circumstellar shells of AGB stars. In: Exploiting the ISO data archive. infrared astronomy in the internet age. 511, 2003, p. 141.

[807] Kou L, Labrie D, Chylek P. Refractive indices of water and ice in the 0.65- to 2.5-μm spectral range. Appl Opt 1993;32(19):3531–40. http://dx.doi.org/10.1364/AO.32.003531.

[808] Sinyuk A, Torres O, Dubovik O. Combined use of satellite and surface observations to infer the imaginary part of refractive index of Saharan dust. Geophys Res Lett 2003;30(2). http://dx.doi.org/10.1029/2002GL016189.

[809] Dingle JH, Zimmerman S, Frie AL, Min J, Jung H, Bahreini R. Complex refractive index, single scattering albedo, and mass absorption coefficient of secondary organic aerosols generated from oxidation of biogenic and anthropogenic precursors. Aerosol Sci Technol 2019;53(4):449–63. http://dx.doi.org/10.1080/02786826.2019.1571680.

[810] Zarzana KJ, De Haan DO, Freedman MA, Hasenkopf CA, Tolbert MA. Optical properties of the products of α-Dicarbonyl and amine reactions in simulated cloud droplets. Environ Sci Technol 2012;46(9):4845–51. http://dx.doi.org/10.1021/es2040152.

[811] Niedziela RF, Norman ML, DeForest CL, Miller RE, Worsnop DR. A temperature- and composition-dependent study of H_2SO_4 aerosol optical constants Using Fourier transform and tunable diode laser infrared spectroscopy. J Phys Chem A 1999;103(40):8030–40. http://dx.doi.org/10.1021/jp991323o.

[812] Biermann UM, Luo BP, Peter T. Absorption spectra and optical constants of binary and ternary solutions of H_2SO_4, HNO_3, and H_2O in the mid infrared at atmospheric temperatures. J Phys Chem A 2000;104(4):783–93. http://dx.doi.org/10.1021/jp992349i.

[813] Palmer KF, Williams D. Optical constants of sulfuric acid; application to the clouds of venus? Appl Opt 1975;14(1):208–19. http://dx.doi.org/10.1364/AO.14.000208.

[814] Norman ML, Qian J, Miller RE, Worsnop DR. Infrared complex refractive indices of supercooled liquid HNO_3/H_2O aerosols. J Geophys Res: Atmos 1999;104(D23):30571–84. http://dx.doi.org/10.1029/1999JD900902.

[815] Querry MR, Tyler IL. Reflectance and complex refractive indices in the infrared for aqueous solutions of nitric acid. J Chem Phys 1980;72(4):2495–9. http://dx.doi.org/10.1063/1.439445.

[816] Remsberg EE, Lavery D, Crawford BJ. Optical constants for sulfuric and nitric acids. J Chem Eng Data 1974;19(3):263–5. http://dx.doi.org/10.1021/je60062a003.

[817] Hasenkopf CA, Beaver MR, Trainer MG, Langley Dewitt H, Freedman MA, Toon OB, et al. Optical properties of Titan and early Earth haze laboratory analogs in the mid-visible. Icarus 2010;207(2):903–13. http://dx.doi.org/10.1016/j.icarus.2009.12.015.

[818] Bohren CF, Huffman DR. Absorption and scattering of light by small particles. Weinheim: Wiley-VCH; 1983.

[819] Wakeford HR, Sing DK. Transmission spectral properties of clouds for hot Jupiter exoplanets. Astron Astrophys 2015;573:A122. http://dx.doi.org/10.1051/0004-6361/201424207.

[820] Massie ST, Hervig M. HITRAN 2012 refractive indices. J Quant Spectrosc Radiat Transfer 2013;130:373–80. http://dx.doi.org/10.1016/j.jqsrt.2013.06.022.

[821] Mlawer EJ, Payne VH, Moncet JL, Delamere JS, Alvarado MJ, Tobin DC. Development and recent evaluation of the MT_CKD model of continuum absorption. Philos Trans R Soc Lond Ser A 2012;370(1968):2520–56. http://dx.doi.org/10.1098/rsta.2011.0295.

[822] Mlawer EJ, Mascio J, Turner DD, Payne VH, Flynn CJ, Pincus R. A more transparent infrared window. J Geophys Res: Atmos 2024;129. http://dx.doi.org/10.1029/2024JD041366, e2024JD041366.

[823] Mondelain D, Vasilchenko S, Kassi S, Campargue A. The water vapor foreign-continuum in the 1.6 μm window by CRDS at room temperature. J Quant Spectrosc Radiat Transfer 2020;246:106923. http://dx.doi.org/10.1016/J.JQSRT.2020.106923.

[824] Mondelain D, Vasilchenko S, Čermák P, Kassi S, Campargue A. The self- and foreign-absorption continua of water vapor by cavity ring-down spectroscopy near 2.35 μm. Phys Chem Chem Phys 2015;17:17762–70. http://dx.doi.org/10.1039/C5CP01238D.

[825] Vasilchenko S, Campargue A, Kassi S, Mondelain D. The water vapour self- and foreign-continua in the 1.6 μm and 2.3 μm windows by CRDS at room temperature. J Quant Spectrosc Radiat Transfer 2019;227:230–8. http://dx.doi.org/10.1016/J.JQSRT.2019.02.016.

[826] Fleurbaey H, Campargue A, Silva YCMD, Grilli R, Kassi S, Mondelain D. Characterization of the H_2O+CO_2 continuum within the infrared transparency windows. J Quant Spectrosc Radiat Transfer 2022;282:108119. http://dx.doi.org/10.1016/J.JQSRT.2022.108119.

[827] Koroleva A, Kassi S, Mondelain D, Campargue A. The water vapor foreign continuum in the 8100 – 8500 cm^{-1} spectral range. J Quant Spectrosc Radiat Transfer 2023;108432. http://dx.doi.org/10.1016/J.JQSRT.2022.108432.

[828] Liuzzi G, Masiello G, Serio C, Palchetti L, Bianchini G. Validation of H_2O continuum absorption models in the wave number range 180-600 cm^{-1} with atmospheric emitted spectral radiance measured at the Antarctica Dome-C site. Opt Express 2014;22(14):16784. http://dx.doi.org/10.1364/OE.22.016784.

[829] Simonova AA, Ptashnik IV, Shine KP. Semi-empirical water dimer model of the water vapour self-continuum within the IR absorption bands. J Quant Spectrosc Radiat Transfer 2024;329:109198. http://dx.doi.org/10.1016/J.JQSRT.2024.109198.

[830] Schulze R, Schreiber T, Yatsishin I, Dahimene R, Milovidov A. ClickHouse - lightning fast analytics for everyone. Proc the VLDB Endow 2024;17(12):3731–44. http://dx.doi.org/10.14778/3685800.3685802.

[831] Tashkun SA, Perevalov VI. CDSD-4000: High-resolution, high-temperature carbon dioxide spectroscopic databank. J Quant Spectrosc Radiat Transfer 2011;112(9):1403–10. http://dx.doi.org/10.1016/j.jqsrt.2011.03.005.

[832] Hargreaves RJ, Gordon IE, Rey M, Nikitin AV, Tyuterev VG, Kochanov RV, et al. An accurate, extensive, and practical line list of methane for the HITEMP database. Astrophys J Suppl Ser 2020;247:55. http://dx.doi.org/10.3847/1538-4365/ab7a1a, http://arxiv.org/abs/2001.05037, https://iopscience.iop.org/article/10.3847/1538-4365/ab7a1a.

[833] HITRAN group. HITRANonline GitHub repositories: HAPI, HAPIEST, and related tools. 2025, Open-source Python interfaces for accessing and processing HITRAN database (e.g., HAPI, HAPI2, HAPIEST), various spectral tools, https://github.com/hitranonline/.

[834] van den Bekerom D, Pannier E. A discrete integral transform for rapid spectral synthesis. J Quant Spectrosc Radiat Transfer 2021;261:107476. http://dx.doi.org/10.1016/j.jqsrt.2020.107476.

[835] Laraia AL, Gamache RR, Lamouroux J, Gordon IE, Rothman LS. Total internal partition sums to support planetary remote sensing. Icarus 2011;215(1):391–400. http://dx.doi.org/10.1016/j.icarus.2011.06.004.

[836] Gamache RR, Orphanos NG. Thermodynamic functions for N_2 from the total partition sum and its moments. J Phys Chem Ref Data 2023;52:023101. http://dx.doi.org/10.1063/5.0137083.

[837] Gamache RR, Orphanos NG, Qu Q, Yurchenko SN, Tennyson J. Ideal gas thermodynamic functions for NO from the total partition sum and its moments. J Phys Chem Ref Data 2024;53:033103. http://dx.doi.org/10.1063/5.0209834.

[838] Tiesinga E, Mohr PJ, Newell DB, Taylor BN. CODATA recommended values of the fundamental physical constants: 2018. J Phys Chem Ref Data 2021;50:033105. http://dx.doi.org/10.1063/5.0064853.

[839] Skinner F, Gordon I, Hill C, Hargreaves R, Lockhart K, Rothman L. Referencing sources of molecular spectroscopic data in the era of data science: Application to the HITRAN and AMBDAS databases. Atoms 2020;8:16. http://dx.doi.org/10.3390/atoms8020016.

[840] Boudon V, Richard C, Manceron L. High-resolution spectroscopy and analysis of the fundamental modes of $^{28}SiF_4$. Accurate experimental determination of the Si-F bond length. J Mol Spectrosc 2022;383:111549. http://dx.doi.org/10.1016/j.jms.2021.111549.

[841] Kamel R, Boudon V, Richard C, Raddaoui E, Landsheere X, Manceron L, et al. New experimental spectra and quantitative modeling of the bending dyad of silane in the 900 cm^{-1} region for its 3 isotopologues. Molecules 2025;30(9). http://dx.doi.org/10.3390/molecules30091992.

[842] Bertin T, Vander Auwera J. CO_2 collision-induced line parameters for the ν_3 band of $^{12}CH_4$ measured using a hard-collision speed-dependent line shape and the relaxation matrix formalism. J Quant Spectrosc Radiat Transfer 2024;324:109069. http://dx.doi.org/10.1016/j.jqsrt.2024.109069.

[843] Tran H, Li G, Ngo NH, Elbert V. Pressure dependence of the measured line intensity and super-Lorentzian effects in the absorption spectra of pure HCl. Phys Chem Chem Phys 2023;25:10343–52. http://dx.doi.org/10.1039/d2cp04892b.

[844] Tran H, Li G, Ngo NH, Elbert V. Non-impact effects in the absorption spectra of HCl diluted in CO_2, air, and He: Measurements and predictions. J Chem Phys 2023;158:184301. http://dx.doi.org/10.1063/5.0147916.

[845] Reed ZD, Tran H, Ngo HN, Hartmann JM, Hodges JT. Effect of non-Markovian collisions on measured integrated line shapes of CO. Phys Rev Lett 2023;130:143001. http://dx.doi.org/10.1103/PHYSREVLETT.130.143001.

[846] Niraula P, de Wit J, Gordon IE, Hargreaves RJ, Sousa-Silva C, Kochanov RV. The impending opacity challenge in exoplanet atmospheric characterization. Nat Astron 2022;6:1–9. http://dx.doi.org/10.1038/s41550-022-01773-1.

[847] Gharib-Nezhad ES, Batalha NE, Chubb K, Freedman R, Gordon IE, Gamache RR, et al. The impact of spectral line wing cut-off: recommended standard method with application to MAESTRO opacity data base. RAS Tech Instrum 2024;3:44–55. http://dx.doi.org/10.1093/RASTI/RZAD058.

[848] Kim J, Jeong U, Ahn M-H, Kim JH, Park RJ, Lee H, et al. New era of air quality monitoring from space: Geostationary environment monitoring spectrometer (GEMS). Bull Am Meteorol Soc 2020;101(1):E1–22. http://dx.doi.org/10.1175/BAMS-D-18-0013.1.

[849] Lustrement B, Bertran S, Rouanet N, Damián AD, Hassen-Khodja R, Montaron C, et al. Design of the VenSpec-U instrument: a double UV imaging spectrometer to analyze sulfured gases in the Venusian atmosphere. In: Strojnik M, Helbert J, editors. Infrared remote sensing and instrumentation XXXII. Vol. 13144, SPIE, International Society for Optics and Photonics; 2024, p. 131440K. http://dx.doi.org/10.1117/12.3028252.

[850] Muslimov E, Neiner C, Bouret J-C. Optical design options for pollux: UV spectropolarimeter project for the habitable worlds observatory. In: den Herder J-WA, Nikzad S, Nakazawa K, editors. Space telescopes and instrumentation 2024: ultraviolet to Gamma ray. Society of photo-optical instrumentation engineers (SPIE) conference series, Vol. 13093, 2024, p. 130933D. http://dx.doi.org/10.1117/12.3020175.

[851] Dudhia A. The reference forward model (RFM). J Quant Spectrosc Radiat Transfer 2017;186:243–53. http://dx.doi.org/10.1016/j.jqsrt.2016.06.018, http://linkinghub.elsevier.com/retrieve/pii/S0022407316301029, https://linkinghub.elsevier.com/retrieve/pii/S0022407316301029.